VARIATIONS IN POTENTIAL VORTICITY STREAMER ACTIVITY: DEVELOPMENT PATHWAYS, ENVIRONMENTAL IMPACTS, AND LINKS TO TROPICAL CYCLONE ACTIVITY IN THE NORTH ATLANTIC BASIN

By

Philippe. P. Papin

A Dissertation
Submitted to the University at Albany, State University of New York
in Partial Fulfillment, of
the Requirements for the Degree of
Doctor of Philosophy

College of Arts & Sciences
Department of Atmospheric and Environmental Sciences
2017

ABSTRACT

This dissertation examines the climatological occurrence of potential vorticity streamers (PVSs) during the tropical cyclone (TC) season that occur in the upper troposphere in the North Atlantic (NATL) basin, assessing how their variations in frequency, area, and intensity impact the synoptic environment, how they are induced by different synoptic-dynamic patterns, and how they modify TC activity and genesis pathways.

A climatology of PVSs is constructed for June–November 1979–2015 by identifying PVS along the 2-PVU contour on the 350-K isentropic surface. A novel aspect of this PVS climatology is that PVSs are categorized by intensity, area, and tilt. PVSs mainly occur in a positively tilted southwest to northeast axis across the NATL basin, along where the time mean tropical upper-tropospheric trough (TUTT) is present, with overall activity peaking in July. Seasonal variations in PVS intensity, area, and tilt are prevalent, prompting the development of a seasonal PVS activity index (PVSI). After accounting for PVS area and intensity, the PVSI demonstrates that TC seasons with the most PVSs are not necessarily associated with the highest PVSI.

Composite analysis is preformed to evaluate how the intensity of PVSs impact the large-scale environment. Strong PVSs are characterized by higher magnitude and larger area vertical wind shear (VWS) anomalies southeast of the PVS axis and reduced precipitable water anomalies within and poleward of the axis, both of which are unfavorable for TC activity. Prior to occurrence, strong PVSs possess earlier upstream ridge building linked with greater mid-level diabatic heating and negative PV advection by the irrotational wind. Prior PVS occurrence aids in the development of strong PVSs, where their positive PV anomaly works constructively with the negative PV anomaly in the upstream ridge to advect high PV air into the strong PVS trough axis. By contrast, weak PVSs have delayed upstream ridge building and no pre-existing positive PV anomalies where they develop, which reduces the advection of high PV air into the weak PVS trough axis.

Seasonal PVS activity is compared to TC activity using accumulated cyclone energy (ACE). In general, PVS occurrence is negatively correlated to ACE, though the strength of the relationship is dependent on PVS intensity. Incorporating PVS area and intensity differences, PVSI has the largest negative correlation with ACE, and high values of PVSI ($> 65\times10^4\sigma$) always result in below mean ACE in the NATL basin. Reduced TC activity in top PVSI years is linked to seasonal increases in VWS and sea level pressure, but reduced precipitable water and upper-tropospheric thickness at low-latitudes. Composites of TC position relative to PVS centroids show the tendency for TCs to occur in the ridge upstream of PVSs, where VWS is lower and precipitable water is higher. In top PVSI years, non-baroclinic tropical cyclogenesis (TCG) occurrence is reduced, resulting in a decrease and poleward shift in ACE, which is mainly due to baroclinic TCG.

ACKNOWLEGEMENTS

First and foremost, I'd like to thank my academic co-advisors, Drs. Ryan Torn and Lance Bosart, for their constant aid and dedication to stimulate my development over the past six years to become a better atmospheric scientist. It has been an honor to be advised by two of the leading experts in our discipline that helped me grow as a scientist, whether or not that be through attending numerous conferences on their dime, or through stimulating discussions in our numerous group meetings. Additional thanks goes to my Ph.D. committee, which includes Kristen Corbosiero, Ron McTaggart-Cowan, and Chris Thorncroft. To have such a top-notch committee to review and critique my work, while providing helpful insight, is something that not all students have the privilege to receive, and I am grateful for the opportunities this committee has provided me.

There are a slew of people I would like to thank from the large student and faculty body at the University at Albany. I'm grateful to the work that Annette Audi, Chaina Porter, Ashley Turski, and Barbara Zampella do to ensure that grants are processed, flights and hotels to conferences are booked, and so many other tasks that go on behind the scenes that keep our department the well-oiled machine it is. Special thanks also goes out to our technical support team, Kevin Tyle and David Knight, that keep our servers and computer clusters running in tip top shape, that without this dissertation would not be possible. I must give a shout out to all the grad students that have enriched my life in Albany, especially Alicia Bentley, Kevin Biernat, Alan Brammer, Pamela Eck, Michael Fisher, Larry Gloeckler, Kyle Griffin, Bill Lamberson, Ben Moore, Bob Setzenfand, Matt Janiga, and Stephanie Stevenson. These people all deserve special recognition because they either provided me with technical assistance when I was still just trying to get started in grad school, or have been my friend along the way making my time in Albany a wonderful experience.

I have to thank my family for being my constant cheerleader through the dissertation writing process, always keeping my priories on the straight and narrow. I love my mom and dad with all my heart, and I would I have never made it this far without the help and guiding principles growing up and even now from afar. And finally, the biggest thank you goes to my girlfriend Ajda Savarin. She will most likely have to go through this process in a couple of years, and I hope that I can give her the patience and positive reinforcement that she has provided me through this grueling process. She was great to bounce off most mundane to radical research ideas with only a tiny amount of resentment. Thanks for being my sunflower Ajda, and I’m looking forward to starting the next sunny chapter of our lives on the west coast.

Financial support for this research was provided by National Science Foundation Grant AGS-1656406, AGS-1239787, and NOAA Grant S1512.

TABLE OF CONTENTS

1. Introduction

1.1 Motivation and purpose

Tropical cyclones (TCs) are a major natural hazard in the United States and worldwide, where they frequently cause substantial socioeconomic impacts and threat to human life in the regions they traverse (Peduzzi et al. 2012). Due to their devastating effects, accurate TC activity forecasts are desired at time-scales ranging from days to months in advance (Klotzbach and Gray 2008; Rapport et al. 2009; Vecchi and Villarini 2014). Numerous environmental factors affect TC activity at these varied time-scales, but among the most important are vertical wind shear (VWS) and deep-layer moisture (i.e., precipitable water), which appear critical to the formation and maintenance of TCs (e.g., Gray 1968; Zehr 1992; Knaff 1997; DeMaria et al. 2001). These factors are also seen as critical forecast challenges for TCs (e.g., Fitzpatrick et al. 1995; Rapport et al. 2009; Kaplan et al. 2010). Understanding all the underlying features that modify VWS and deep-layer moisture in regions where significant TC activity is observed is of critical importance, given the hazards that TCs possess.

On seasonal time-scales in the North Atlantic (NATL) basin, the tropical upper tropospheric trough (TUTT; Sadler 1967) is an underlying feature that can modify the VWS and moisture profile of the Atlantic basin (e.g., Whitfield and Lyons 1992; Fitzpatrick et al. 1995; Knaff 1997; Ferreira and Schubert 1999; Patla et al. 2009). TC seasons with a stronger magnitude TUTT feature higher VWS and lower tropospheric moisture along its axis, which inhibit low-latitude TC activity (Fitzpatrick et al. 1995; Knaff 1997). Only limited research has been performed, however, on what modulates the seasonal TUTT intensity. Recently, Zhang et al. (2017) showed that seasonal Rossby wave breaking (RWB) frequency, occurring where the time-mean TUTT is located, could negatively impact seasonal TC activity, due to characteristic increases in VWS and decreases in precipitable water in active RWB years in the NATL basin. In the NATL TC season, RWB occurs most often as anticyclonic wave breaking (AWB), which is initiated by upstream Rossby wave amplification (e.g., McIntyre and Palmer 1983; Hoskins et al. 1985 [Hereafter, HMR]; Thorncroft et al. 1993; Postel and Hitchman 1999; Holton 2004) and results in a trough of high potential vorticity (PV) air downstream, often referred to as a PV streamer (PVS). The downstream PVS is the feature responsible for VWS increases and precipitable water decreases noted in Zhang et al. (2016, 2017).

While the seasonal frequency of RWB and PVS events demonstrate important relationships with VWS, precipitable water, and overall TC activity, individual RWB and PVS events can exhibit large variations in intensity, area, and tilt, with recent research showing that these differences can result in positive or negative impacts on TC activity (e.g., Galarneau et al. 2015; Peirano et al. 2016; Fischer et al. 2017). A PVS climatology that also investigates PVS intensity, area, and tilt could provide added value on how VWS, precipitable water, and TC activity changes when these PVS attributes change.

The intensity of a PVS is governed by changes in the PV anomaly within the PVS trough axis (HMR). Since PV is calculated as the product of absolute vorticity and static stability, larger positive PV anomalies are associated with larger absolute vorticity anomalies, larger static stability anomalies, or both (Ertel 1942, HMR, Martin 2006). Differences in the PVS intensity, area, and tilt also modify the magnitude of its three-dimensional circulation (Martin 2006; Masarik and Schubert 2013), where changes in this circulation may affect VWS and moisture in the troposphere below. An exploration into how PVS intensity (using PV anomaly) alters nearby VWS and moisture has not been conducted in a climatology. Moreover, it is not known how differences in the upstream synoptic-dynamic pattern before AWB affect the intensity of PVSs downstream, though previous research conducted using idealized modeling and case studies suggest the importance of dry and moist dynamics occurring with ridge building before AWB (e.g., Thorncroft et al. 1993; Massacand et al. 2001; Knippertz and Martin 2005; Meir and Knippertz 2009; Grams et al. 2011; Teubler and Riemer 2016).

The principal goal of this dissertation is to investigate the factors and impacts that are associated with different categories of PVS activity in the Atlantic basin. The following questions will be addressed:

1) What is the climatological distribution of PVSs in the Atlantic basin, emphasizing differences in intensity, area, and tilt?
2) How do PVSs of different intensity, area, and tilt modify environmental variables at the time of PVS identification, and what are the synoptic-dynamic differences in the upstream environment that precede strong versus weak PVSs?
3) How does PVS activity (combining frequency, area, and intensity) influence TC genesis, spatial distribution, and overall activity in the Atlantic basin?

The dissertation is organized as follows: The remainder of Chapter 1 presents a literature review. Chapter 2 describes the algorithm used to deduce intensity, area, and tilt differences of PVSs, highlighting important datasets and methods, while Chapter 3 presents the climatology of PVS occurrence using two reanalysis datasets, focusing on variations in intensity, area, and tilt. Chapter 4 contains composite differences in PVS intensity, emphasizing upstream differences that relate to strong versus weak PVSs before formation, and their environmental impacts after formation. Chapter 5 contains a comparison of PVS activity with TC activity, illustrating their relationship statistically and spatially. Chapter 6 presents a summary of the key findings and highlights additional research pathways beyond this dissertation.

1.2. Literature review

1.2.1 Potential vorticity

PV is an atmospheric quantity that combines vorticity with vertical stratification, and was independently developed by Carl-Gustaf Rossby (Rossby 1940) and Hans Ertel (Ertel 1942). Thorpe and Volkert (1997) provide background into the early development of PV and its potential uses. The Ertel (1942) version of PV for an isentropic surface is defined as:

$$PV_\theta = -g(\xi_\theta + f)\frac{\partial\theta}{\partial p} \tag{1.1}$$

where g is gravity, ξ_θ is relative vorticity on an isentropic surface, f is planetary vorticity, and $\frac{\partial\theta}{\partial p}$ is the static stability. The dimensions of PV are K kg^{-1} m^{2} s^{-1}. There are several advantages to using PV to identify features compared to vorticity. First, PV is a conserved quantity in adiabatic, frictionless motion on isentropic surfaces, meaning PV in the dry, frictionless atmosphere can only be modified by parcel changes in latitude and static stability (Eliassen and Kleinschmidt 1957, Thorpe and Volkert 1997, Martin 2006). Second, changes in PV can indicate the transition into different air masses, especially between the troposphere (low PV air) and stratosphere (high PV air). This PV air mass distinction is possible due to changes in static stability between the troposphere (low static stability) and stratosphere (high static stability) via the changing vertical temperature gradient. Therefore, PV is an excellent quantity to observe atmospheric waves (i.e., Rossby waves; Rossby 1939) occurring at the tropopause, the interface between the troposphere and stratosphere.

1.2.2 Potential vorticity streamers

PVSs are a related feature to Rossby waves that are defined as elongated filaments of high PV air (e.g., Appenzeller and Davies 1992), which have high length to width aspect ratio. The boundary of a PVS is typically determined by following a PV contour that is roughly approximate to the tropopause. The concept of this "dynamical tropopause" was first devised by Reed (1955), and is typically defined as the 2-PV unit (PVU; where 1 PVU = 10^{-6} K kg^{-1} m^2 s^{-1}) surface, which separates tropospheric air (< 2-PVU) from stratospheric air (> 2-PVU) (Holton 1995; Kunz et al. 2011). A PVS trough contains stratospheric PV air inside its axis bounded by the 2-PVU contour that separates tropospheric air adjacent to the trough axis. Holton (1995) noted that the climatological location of the 2-PVU contour crosses the 350-K isentropic surface in the subtropics, around 30^{o}N (Fig. 1.1). However, the instantaneous configuration of the 2-PVU contour can become highly deformed in space by synoptic-scale Rossby waves, resulting in irreversible deformation of the tropopause-based PV. The occurrence of PVSs is fundamentally linked to these instances where Rossby waves grow non-linearly along a waveguide (i.e., a narrow band of enhanced meridional tropopause-based PV gradient; Schwierz et al. 2004; Martius et al. 2010) and undergo RWB.

1.2.3 Processes leading to RWB and PVS formation.

Numerous studies have discussed features that excite Rossby waves along a waveguide that may facilitate amplification and breaking of Rossby waves. These features include recurving TCs (e.g., Riemer et al. 2008; Riemer and Jones 2010; Torn 2010; Grams et al. 2011; Grams and Archambault 2016; Archambault et al. 2013, 2015; Bosart et al. 2017), broadly organized regions of tropical convection (e.g., Sardeshmukh and Hoskins 1988; Moore et al. 2010, MacRitchie and Roundy 2016), tropopause-level vortices (e.g., Schwierz et al. 2004), and extratropical baroclinic cyclones (e.g., Davies et al. 1991; Orlanski and Sheldon 1993; Teubler and Riemer 2016). These features are associated with baroclinic and/or diabatic processes (i.e., latent heat release [LHR]), which amplify the incipient Rossby wave to the point at which it becomes significant to the time-mean state of the waveguide, allowing RWB to occur (e.g., Holton 2004).

Rossby waves can break either anticyclonically (i.e., AWB) or cyclonically (i.e., cyclonic wave breaking, CWB), depending on the background meridional barotropic shear (e.g., LC1 and LC2; Thorncroft et al. 1993, Fig. 1.2). AWB, where low PV folds poleward over high PV air, is most common at higher isentropic surfaces in the subtropics (Ndarana and Waugh 2011; Homeyer and Bowman 2013), because meridional anticyclonic shear is typically observed equatorward of the climatological jet wind-maximum associated with the mid-latitude waveguide (e.g., Thorncroft et al. 1993; Postel and Hitchman 1999; Fig. 1.2a). This research emphasizes the AWB pathway of PVS formation because it occurs an order of magnitude more frequently than cyclonic RWB in the subtropical Atlantic basin during the warm season (Homeyer and Bowman 2013). AWB may occur via dry baroclinic dynamics (Thorncroft et al. 1993, Fig. 1.2), where Rossby waves amplify due to a combination of the background flow plus the flow associated with pre-existing PV anomalies located along the waveguide (e.g., HMR; Nielsen-Gammon and Lefevre 1996).

However, diabatic processes (i.e., LHR) occurring in TCs, large-scale convection, and the moist ascending branch of baroclinic cyclones (i.e., “warm conveyor belts” [WCBs; Wernli and Davies 1997; Ralph et al. 2011; Grams et al. 2011; Madonna et al. 2014a,b; Martinez-Alvarado et al. 2014; Methven 2015; Hu et al. 2017]) can aid the growth of upstream anticyclonic Rossby wave perturbations that result in AWB. These features often provide a corridor of enhanced moisture along the flank of the building ridge, which supports latent heating. Anticyclonic Rossby wave amplification from these diabatic effects occur through two sequential processes as described in Stoelinga (2003) and illustrated in Fig. 1.3. First, mid-tropospheric diabatic heating (through cloud LHR) results in negative PV tendencies that lower PV in the upper-troposphere above the level of maximum heating (direct effect in Fig. 1.3). Second, the diabatically generated, low PV air is advected by the divergent convective outflow (indirect effect in Fig. 1.3). Negative PV advection from the divergent outflow both slows the upstream Rossby wave progression, and increases anticyclonic PV anomalies in the ridge apex.

Teubler and Riemer (2016) recently investigated the cumulative effects of radiation, LHR, and flow from quasi-barotropic, baroclinic, and divergent components in the upper-troposphere on the waveguide in an early fall case study in the North Pacific basin (Fig. 1.4). In this case study, the downstream trough that results in the development of a PVS is primarily a consequence of downstream development, where positive PV tendency is mostly aided by the quasi-barotropic flow of the upstream ridge advecting positive PV anomalies into the trough axis (Fig. 1.4a,c). The positive PV tendency from quasi-barotropic flow is greater than the positive PV tendency associated with radiation (Fig. 1.4e), but both effects work constructively to generate a positive PV tendency that strengthens the PVS (Fig. 1.4c,e). The upstream ridge is aided by divergent outflow that results in the greatest negative PV tendency in the poleward flank of the upstream ridge (Fig. 1.4b,d). The negative PV tendency from the indirect effect of divergent outflow is greater than the direct effect of LHR from condensation that flanks the ridge (Fig. 1.4f), but both effects work constructively to promote a negative PV tendency that leads to ridge growth (Fig. 1.4d,f).

Additional case studies have also highlighted linkages between stronger upstream ridge amplification tied to greater moisture that enhances diabatic processes (e.g., Massacand et al. 2001; Knippertz and Martin 2005; Grams et al. 2011 [Fig. 1.5]; Pantillon et al. 2013, 2015; Grams and Archambault 2016). The development of larger, negative PV anomalies in the ridge also allows tightening of the meridional PV gradient poleward of the ridge, which accelerates the tropopause-based jet streak. When RWB occurs, this stronger jet streak often results in greater equatorward advection of high PV air that characterizes the PVS downstream.

Grams et al. (2011) demonstrated this effect by running two simulations on the extratropical transition (ET) of TC Hannah in 2008. One simulation was run as a control run, without modifying the initial conditions, while another simulation was run after removing the circulation of TC Hannah via piecewise PV inversion and removing its moisture anomalies. The latter simulation was effective at removing diabatic effects related to LHR and the subsequent divergent outflow from the TC as it interacted with the waveguide. The removal of LHR and divergent outflow from TC Hannah resulted in the reduced magnitude of low PV air in the upstream ridge relative to the control run (Fig. 1.5a), corresponding to a weaker jet streak along the waveguide (Fig. 1.5b). This weaker jet streak results in less equatorward advection of high PV air downstream of RWB axis, resulting in a weaker PVS (Fig. 1.5b).

The bulk of the literature that describes the adiabatic and diabatic effects related to RWB and PVS formation does so using illustrative case studies and different simulations of individual events. In fact, there is a lack of literature that documents the composite differences (using many cases) in upstream conditions that result in strong versus weak PVSs. The relative importance of diabatic versus dry baroclinic processes governing Rossby wave amplification, resulting in different intensity PVSs remains unknown (e.g., Knippertz 2007; Grams et al. 2011), especially in scenarios that exhibit enhanced moisture along the waveguide of the ridge that initiates RWB.

1.2.4 PVS intensity relationship with impacts in the troposphere

The occurrence of PVSs at the tropopause are important, because their presence alters the environment of the troposphere below. These alterations can vary depending on differences in PVS characteristics. This section explores the present literature by examining how PVSs can alter the troposphere below, and how these effects may vary based on different PVS size and intensity.

First, PVSs on the 350-K isentropic surface may generate cyclonic, nondivergent winds that maximize in the upper-troposphere. HMR first described how positive PV anomalies, embedded in the PVS trough axis, would modify tropospheric flow, illustrated using isentropic maps and cross-sections (Fig. 1.6 a–b). The positive PV anomalies in the PVS trough axis are associated with cyclonic, nondivergent winds that decay horizontally following the inverse Laplacian relationship used when inverting PV anomalies (HMR). As the width and intensity of the positive PV anomaly in the PVS increases, one would expect the cyclonic, nondivergent winds associated with the positive PV anomaly to increase. The static stability, however, constrains the depth of the cyclonic flow of the PV anomaly, where lower static stability in the troposphere below enables deeper vertical influence of this nondivergent flow, compared to higher static stability found in the stratosphere above.

Juckes (1999) created an idealized framework of two-dimensional shear lines at the tropopause, consistent with PVSs in the real atmosphere, showing that decreasing the size and intensity of the positive PV anomaly results in both weaker and less expansive horizontal flow (his Fig. 9, compare Fig. 1.6b and c). Increasing static stability of the troposphere leads to a similar muted response in the horizontal flow, as expected per HMR. These results were further confirmed in Masarik and Schubert (2013), who isolated the effects of only the positive PV anomaly, keeping static stability outside of the immediate PV anomaly constant. These studies confirm the theoretical understanding that stronger cyclonic PV anomalies result in larger and deeper horizontal regions of cyclonic flow. These changes also result in greater vertical flow gradients that correspond to increases the magnitude and size of VWS corridors.

Prior PVS climatologies (Wernli and Sprenger 2007; Strong and Magnusdottier 2008; Homeyer and Bowman 2013; Kunz et al. 2015) have not investigated if PVS intensity and size impact the wind and VWS relationships detailed above. Zhang et al. (2017) did show that a composite of PVSs downstream of AWB events exhibits positive VWS anomalies downstream of its axis (Fig. 1.7a). This composite, however, combines PVSs of different intensities, areas, and tilts, so it is unknown if differences in VWS exist between intensity subsets in their climatology.

Changes in the intensity and size of PVSs may also impact changes in negative and positive moisture (e.g., precipitable water) perturbations observed upstream and downstream of individual PVS events. Generally, moisture perturbations occur through two complementary mechanisms. The first mechanism is connected to the cyclonic, nondivergent flow associated with the cyclonic PV anomaly of the PVS. As this cyclonic flow approaches lower latitudes, a net poleward integrated flux of moisture from the tropics to subtropics occurs downstream of the positively tilted trough axis of the PVS. This poleward moisture flux has been demonstrated in many different studies (e.g., Waugh and Polvani 2000; Waugh 2005; Knippertz and Martin 2005,2007; Knippertz 2005, 2007; Zhang et al. 2017), and may result in positive moisture anomalies downstream of the PVS trough axis. Concurrently, equatorward flux of drier mid-latitude air often occurs upstream of the positively tilted trough axis of the PVS (e.g., Yoneyama and Parsons 1999; Waugh 2005) resulting in negative moisture anomalies. The second mechanism that assists in the generation of these moisture (precipitable water) anomalies is related to PVS induced quasi-geostrophic (QG) vertical motion, which has been well documented in case studies and climatological composites (Slingo 1998; Waugh and Funatsu 2003; Knippertz 2007; Funatsu and Waugh 2008; Davis 2010; Galarneau et al. 2015; Zhang et al. 2017). Upward QG vertical motion, using the Sutcliffe-Trenberth form (Trenberth 1978; Holton 2004; Martin 2006), results when cyclonic (positive) PV advection by the thermal wind (i.e., VWS) occurs downstream of the PVS, while downward QG vertical motion results when anticyclonic (negative) PV advection by the thermal wind occurs upstream of the PVS. This effect is demonstrated in Davis (2010) in an east–west cross section through a PVS, which shows QG-induced descent upstream of the trough axis and QG-ascent downstream (Fig. 1.8). The downstream portion of the PVS is associated with increased moisture through the tropospheric column (Fig. 1.8b), as well as a developing subtropical cyclone even further downstream associated with deep convective activity (Fig. 1.8a). In particular, Zhang et al. (2017) illustrated the relationship between vertical motion and moisture in PVS events, showing mid-tropospheric descent along and upstream of the PVS axis is associated with a reduction of relative humidity at the same vertical level, with a corresponding region of ascent and enhanced relative humidity downstream of the PVS axis (Fig. 1.7 b,c). These results, however, combine all PVS events observed in the NATL basin, and the question remains as to how intensity and area of the PVS inducing vertical motion alters nearby moisture perturbations.

1.2.5 Connection between seasonal PVS activity and tropical cyclone activity

Since PVSs on the 350-K isentropic surfaces occur most frequently in the warm season in the center of oceanic basins (e.g., Postel and Hitchman 1999; Wernli and Sprenger 2007;

Homeyer and Bowman 2013; Kunz et al 2015; Zhang et al. 2016, 2017), PVS-induced changes in the environment (i.e., VWS, moisture) could affect other oceanic systems, such as TCs, that also occur during the warm season. This section explores how changes in PVS activity may impact changes in TC activity in the NATL basin.

One feature known to influence TC activity in the NATL basin is the TUTT (Sadler 1967, 1976; Whitfield and Lyons 1992), also defined on the time-mean as the mid-ocean trough, which is a warm season, upper-tropospheric trough that influences the climatological westerly VWS corridor in the NATL basin (McTaggart-Cowan et al. 2013; hereafter MC13). The TUTT axis is positively tilted, stretching southwest to northeast across the NATL basin, and generates westerly upper-tropospheric flow equatorward of its axis (Fitzpatrick et al. 1995; Knaff 1997). This westerly upper-tropospheric flow decreases with height, with little impact on the climatological easterly, lower-tropospheric trade winds. While the TUTT is a time-mean feature, its location and strength varies intraseasonally and interannually. Years where the TUTT is more intense have been correlated to increased westerly VWS downstream of its axis, decreased tropospheric moisture upstream of its axis, and higher subtropical sea level pressure across the NATL basin (Knaff 1997). The environmental attributes associated with a stronger TUTT are also similar to effects associated with enhanced PVS activity from AWB (e.g., Davies et al. 1991; Thorncroft et al. 1993; Yoneyama and Parsons 1999; Juckes and Smith 2000; Waugh 2005; Zhang et al. 2017). MC13 suggest that the maintenance of the TUTT is attributed to both radiative and dynamical forcing, with the former forcing associated with diabatic cooling due to longwave radiation (Fig 1.4e), and the latter forcing comprised of repeated AWB and PVS events occurring in the NATL basin that project onto the time-mean TUTT structure. Because PVS activity at least partially affects the organization of the TUTT, we hypothesize that intensity changes in this feature could also result from intensity changes of PVS activity resulting from AWB.

Recent research has looked at how yearly PVS activity affects VWS and moisture (Zhang et al. 2016, 2017), illustrating that seasons with increased PVS activity possess increases in VWS and decreases in precipitable water in the main development region (MDR) for TCs in the NATL basin (Fig. 1.9). Enhanced corridors of VWS and decreased moisture in the MDR often inhibit the development and intensification of non-baroclinic, low-latitude TCs (Gray 1968; Zehr 1992; Kanff 1997; DeMaria et al. 2001). Therefore, increased PVS frequency is negatively correlated with TC activity, when restricting cases to along the TUTT (Zhang et al. 2017). Not all PVSs have the same environmental impact, however, where PVS intensity, area, and tilt variations could be critical to alter environmental variables that affect TC activity in the NATL basin.

The intensity, area, and tilt variations of upper-tropospheric troughs (many of which are PVSs) often result in different outcomes to TCs that develop nearby (Galarneau et al. 2015; Peirano et al. 2016; Fischer et al. 2017). Peirano et al. (2016) found that trough-induced VWS was an important factor in governing TC intensity change near upper-tropospheric troughs (i.e., PVSs), a factor that would likely also be influenced by the intensity and size of the PVS. Fischer et al. (2017) argued for the importance of upshear QG ascent in intensifying TC cases that interacted with upper-tropospheric troughs nearby, another factor that may be influenced by the intensity and size of the nearby upper-tropospheric trough. Galarneau et al. (2015) found, however, that there were only minor differences in QG ascent and VWS in developing versus non-developing TCs near PVSs, instead arguing for the importance of surface latent heat fluxes along the upshear flank of developing TCs.

While it is known that low-latitude, non-baroclinic TCs are negatively impacted by VWS and reduced moisture in the MDR (environmental factors associated with PVSs), this category of TCs represents a minority of cases in the NATL basin (MC13). In fact, nearly half of all TCs in the NATL basin develop in relatively high 200–850-hPa VWS (> 10 m s^{-1}; Bracken and Bosart 2000), which signifies that many TCs develop via a baroclinic pathway (i.e., TCs that develop in the presence of high upper-tropospheric baroclinicity). This pathway has been the source of prolific research the last several decades (e.g., Bosart and Bartlo 1991; Bracken and Bosart 2000; Davis and Bosart 2001, 2002, 2003, 2004, 2006; Davis 2010; McTaggart-Cowan et al. 2006a,b, 2007a,b, 2008, MC13; Galarneau et al. 2015; Bentley and Metz 2016; Bentley et al. 2016, 2017). While common in the NATL basin, baroclinic tropical cyclogenesis (TCG) pathways tend to lead to weaker maximum intensity TCs (McTaggart-Cowan et al. 2008). Nevertheless, this pathway has also resulted in TCs that have produced high societal impact (i.e., TC Katrina in 2005; McTaggart-Cowan et al. 2007a).

Baroclinic TCG can occur when an upper-tropospheric trough (i.e., PVS) interacts with, or induces a surface vortex over open water. This surface vortex may then undergo TCG, which can be summarized in three steps. First, the combination of QG ascent from cyclonic PV advection by the thermal wind (i.e., VWS; Davis and Bosart 2003; McTaggart-Cowan et al. 2007a; Davis 2010) and a reduction in static stability due to cooler upper-tropospheric temperatures in proximity to the PVS (e.g., Juckes and Smith 2000) can both encourage convection to form over the incipient vortex. Second, convection may intensify the surface vortex by generating low-level upward vertical motion that stretches the vortex (e.g., Davis and Galarneau 2009), and also by generating mid-tropospheric LHR, which enhances cyclonic PV anomalies below the level of maximum heating. Finally, the strengthened winds of the intensified surface vortex allow for enhanced surface moisture fluxes that initiate wind-induced surface heat exchange (WISHE; Rotunno and Emanuel 1987), a process by which further intensification of the surface vortex into a TC can occur.

This series of events associated with baroclinic TCG require the initial presence of upper-level temperature gradients (i.e., baroclinicity), which can be provided by PVSs. Several studies have hence linked PVSs to baroclinic TCG, either directly though upper-level baroclinic forcing (i.e., QG ascent; Davis and Bosart 2001, 2002, 2003; McTaggart-Cowan et al. 2006a, 2007a, 2008, MC13; Fischer et al. 2017), or indirectly through enhanced moisture fluxes equatorward of low-level anticyclogenesis (Galarneau et al. 2015), associated with AWB upstream of the PVS (e.g., Davies et al. 1991, Knaff 1997). Thus, an increase in PVS activity in the subtropical NATL basin may allow more opportunities for baroclinc TCG. Given the associated increases in VWS and decreases in moisture in the MDR associated with enhanced PVS activity (Zhang et al. 2017), however, it is possible the increase in baroclinic TCG would come at the expense of non-baroclinic TCG occurrence. Because non-baroclinic TCG typically produces TCs of higher maximum intensity (McTaggart Cowan et al. 2008), the net impact of PVS activity on accumulated cyclone energy (ACE; Bell et al. 2000) is still negative (Zhang et al. 2016, 2017).

1.3 Novel aspects of the dissertation

As discussed in the literature review, previous studies using idealized modeling and individual case studies indicate that PVSs can develop from upstream ridge building induced by both dry baroclinic and moist dynamics. Similar work has also investigated how PVSs modify VWS and moisture anomalies in the NATL basin, which is tied to decreases in TC activity. An investigation looking at how both upstream ridge building and the downstream environment changes due to intensity, area, and tilt differences associated with PVSs has not been yet been performed in a climatology.

This dissertation aims to create a PVS climatology that will compare intensity, area, and tilt differences in PVSs. A novel technique to identify PVSs is created, using an object-based method to construct a 36-year (1979–2015) PVS climatology that quantifies these variables. This study will also assess the unique synoptic-dynamic characteristics that both precede and result from different intensity PVSs. Another unique aspect of this work will be to use the MC13 dataset for baroclincally influenced TCG to determine if seasonal PVS activity influences the quantity of baroclinic and non-baroclinic TC events for a given season. This study complements a small, but growing body of literature that is documenting the importance of mid-latitude influences on seasonal TC activity (e.g., Knaff 1997; Zhang et al. 2016, 2017) by developing a seasonal PVS intensity metric that could be used alongside other predictors that are known to influence seasonal TC activity in the NATL basin (e.g., El Niño Southern Oscillation [ENSO; Gray 1984; Klotzbach 2011], the Madden Julian Oscillation [MJO; Maloney and Hartmann 2000], Atlantic multi-decadal oscillation [AMO; Klotzbach and Gray 2008]).

1.4. Figures

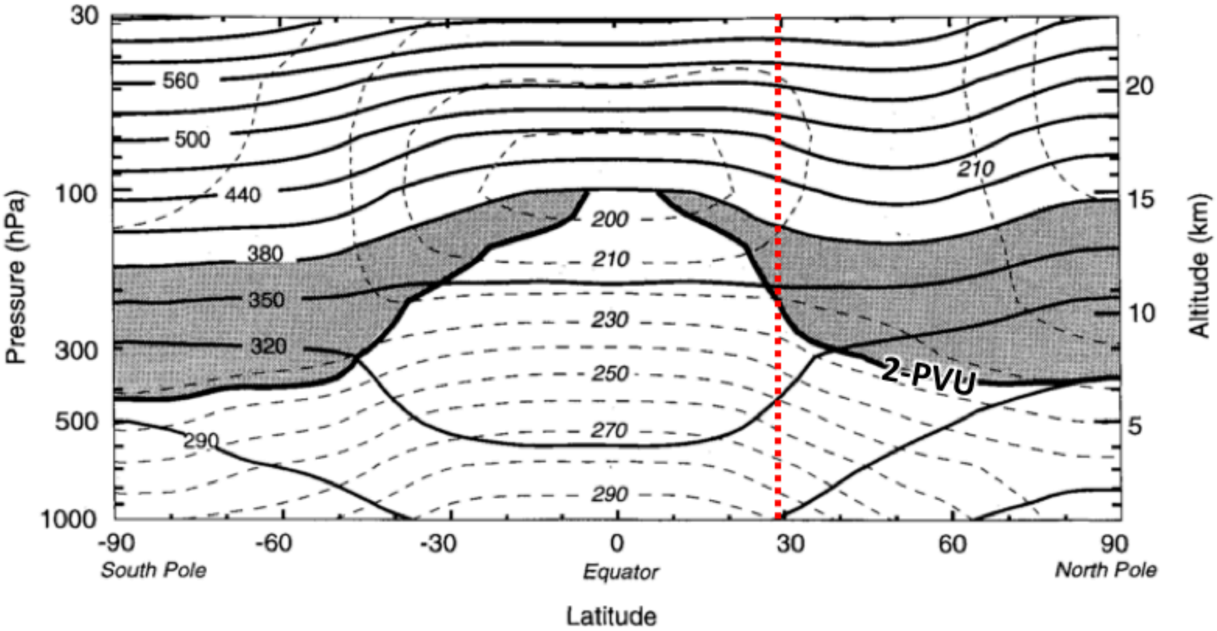

Figure 1.1. Latitude-altitude cross section for January 1993 showing longitudinally averaged potential temperature (solid contours), and temperature (dashed contours). The heavy solid contour (cut off at 380-K isentropic) denotes the 2-PVU potential vorticity contour. The shaded region indicates the lowermost stratosphere. The red dotted line indicates roughly where the 2-PVU contour intersects the 350-K isentrope in the Northern Hemisphere subtropics. [Adapted from Fig. 1 of Holton et al. 1995]

(a) LC1 – Anticyclonic Wave Breaking

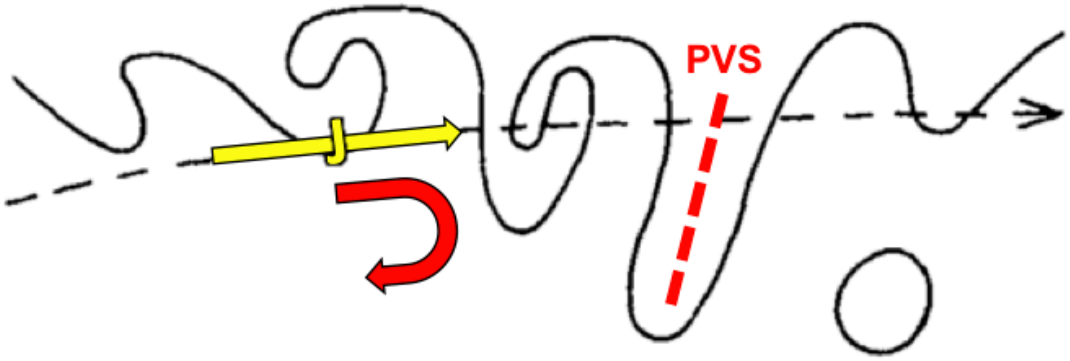

(b) LC2 – Cyclonic Wave Breaking

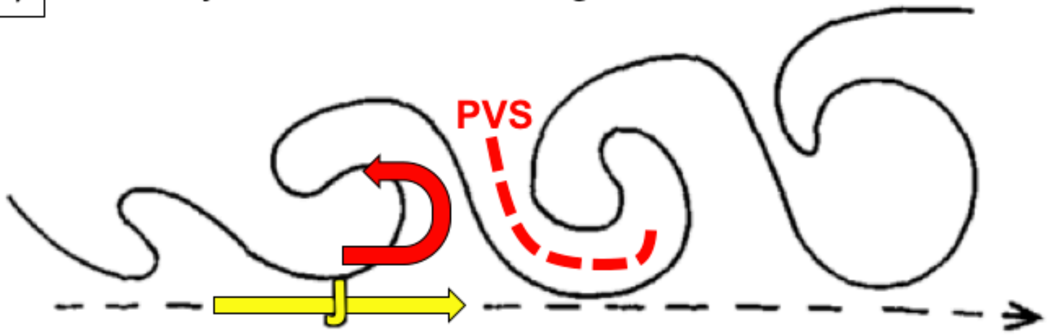

Figure 1.2. Schematic evolution of a tropopause-level PV contour on an isentropic surface associated with (a) an LC1 and (b) an LC2 baroclinic life cycle. The dashed arrow marks the approximate position of the jet stream. The curved red arrows in (a) and (b) indicate barotropic anticyclonic and cyclonic shear, respectively, and the red dotted lines indicate the trough axis of possible PVSs in the schematic. Adapted from Fig. 12 of Thorncroft et al. (1993).

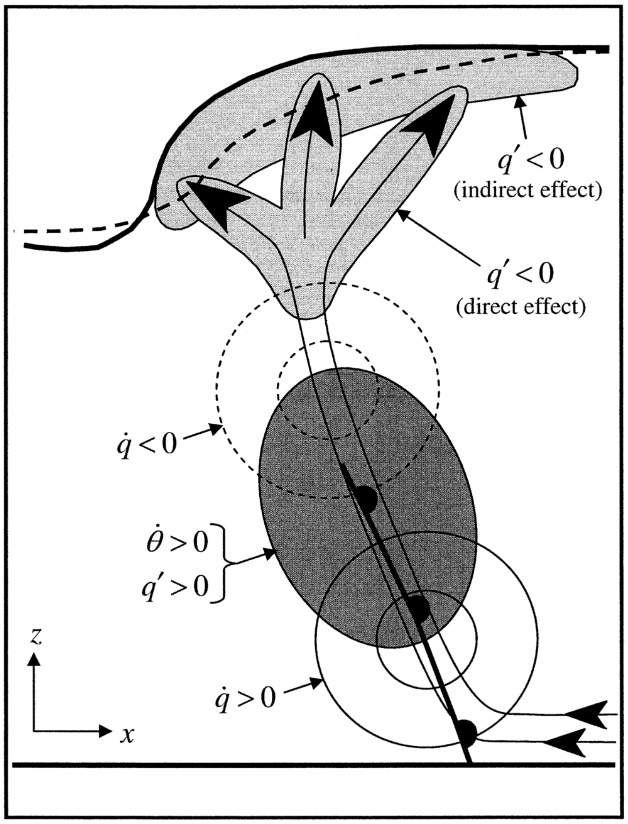

Figure 1.3. Schematic diagram of diabatic effects on the distribution of PV (denoted by q) within the warm ascent region of a baroclinic cyclone (denoted by the warm frontal symbol), also known as the warm conveyer belt (WCB). Curved thin solid lines with arrow heads represent the ascending WCB airstream. Dark-gray shading represents the region of maximum latent heat release ($\dot{\theta}$) in the mid-troposphere, as well as the associated lower-tropospheric positive PV anomaly. Thin solid and dashed contours mark regions of Lagrangian PV increase below the heating maximum and decrease above it, respectively. The heavy solid line represents the position of the tropopause, whereas the heavy dashed line represents the position of the tropopause in the absence of latent heating. Negative anomalous PV created by the direct effect of latent heating (net reduction of PV following the trajectories) is represented by light-gray shaded strands emanating from the mid-troposphere, whereas that created by the indirect effect (enhanced negative PV advection at the tropopause) is shown by the light-gray shaded region bordering the tropopause. Adapted from Fig. 1 of Stoelinga (2003).

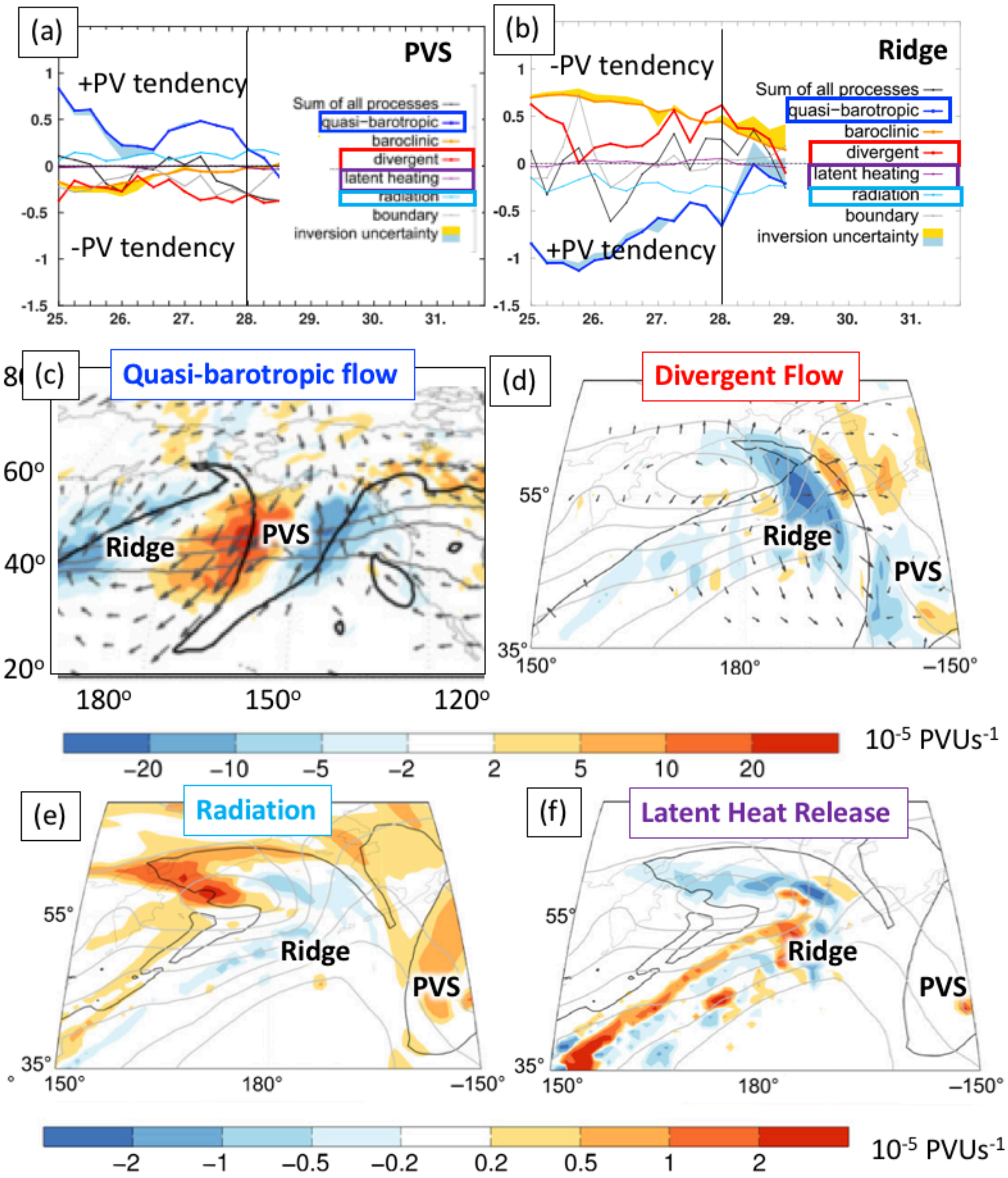

Fig 1.4. Illustration of the processes that lead to upstream ridge and PVS amplification in a Rossby wave train. Panels (a) and (b) show a time series (x-axis) of the individual contributions to the total PV tendency of integrated positive (for the PVS) and negative (for the ridge) PV anomalies (y-axis, 10^8 PVU m^2 s^{-1}). (c) The PV tendency due to quasi-barotropic flow at 330-K (shaded, 10^{-5} PVU s^{-1}). (d) The PV tendency due to the advection of PV anomalies by the divergence term at 330-K (shaded, 10^{-5} PVU s^{-1}). (e) As in (d) except for PV tendency due to radiation (shaded, 10^{-5} PVU s^{-1}). (f) As in (d) except for PV tendency due to direct diabatic modification via latent heat release (shaded, 10^{-5} PVU s^{-1}). The time illustrated in panels (c–f) is 0000 UTC 28 October 2008 and is depicted with a vertical black line in panels (a–b). Arrows in (c–d) denote the respective flow, with values < 3 m s^{-1} omitted. The different term text highlighted in panels (c–f) are colorized by their line plot in panels (a–b). Adapted from Figs. 9–10 of Teubler and Riemer (2016).

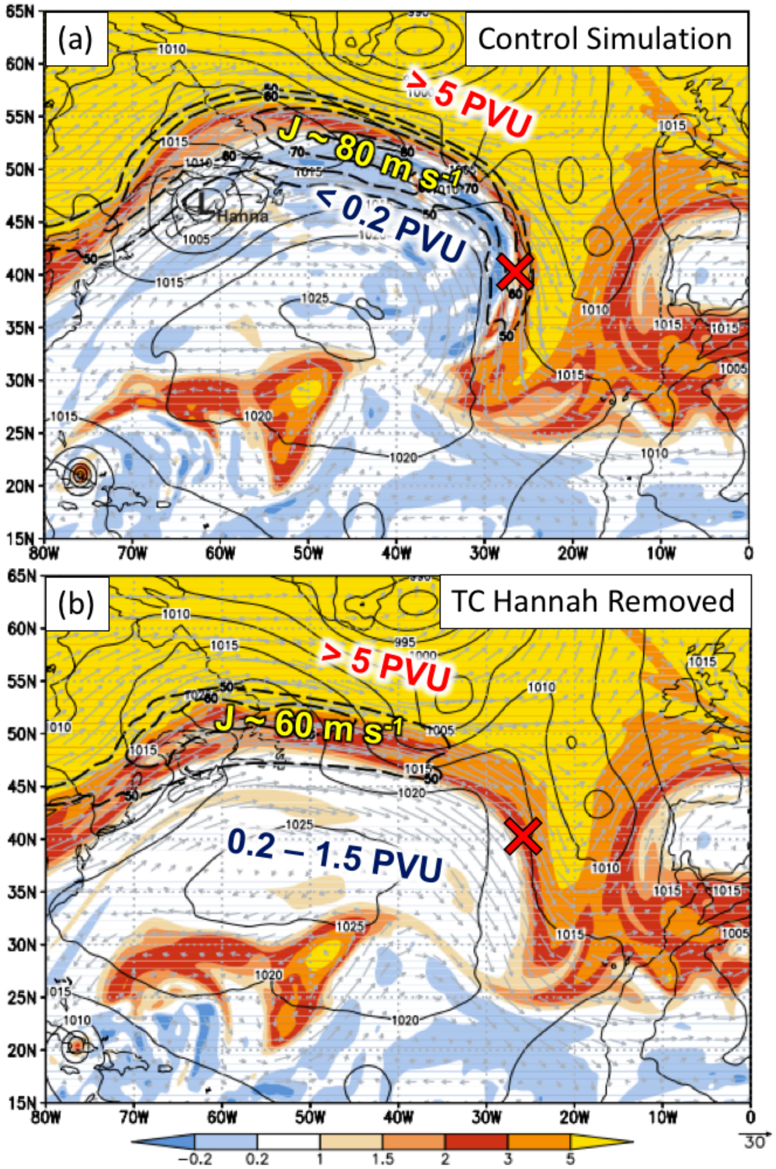

Fig. 1.5. Illustration of two simulations preformed on the extratropical transition of TC Hannah (2008). Panel (a) is a control run with 345-K PV (shaded, PVU), wind speed (black dotted contours, > 50 m s^{-1} at 10 m s^{-1} intervals), wind vectors (gray arrows), and sea level pressure (thin black contours, every 5 hPa). Panel (b) as in (a) except for a modified simulation where PV inversion was used to remove the vortex of TC Hannah, including its moisture anomalies. Both runs are initialized at 0000 UTC 6 September 2008 and the forecast at 0000 UTC 8 September 2008 (+48h) is shown. The location of TC Hannah in (a) is marked by the L_{Hannah}. Estimated jet streak magnitude (m s^{-1}) and PV values (PVU) on the poleward and equatorward side of the jet are given with the reference red X used to depict the axis between the upstream ridge and downstream trough associated with RWB. Adapted from Fig. 6 of Grams et al. (2011).

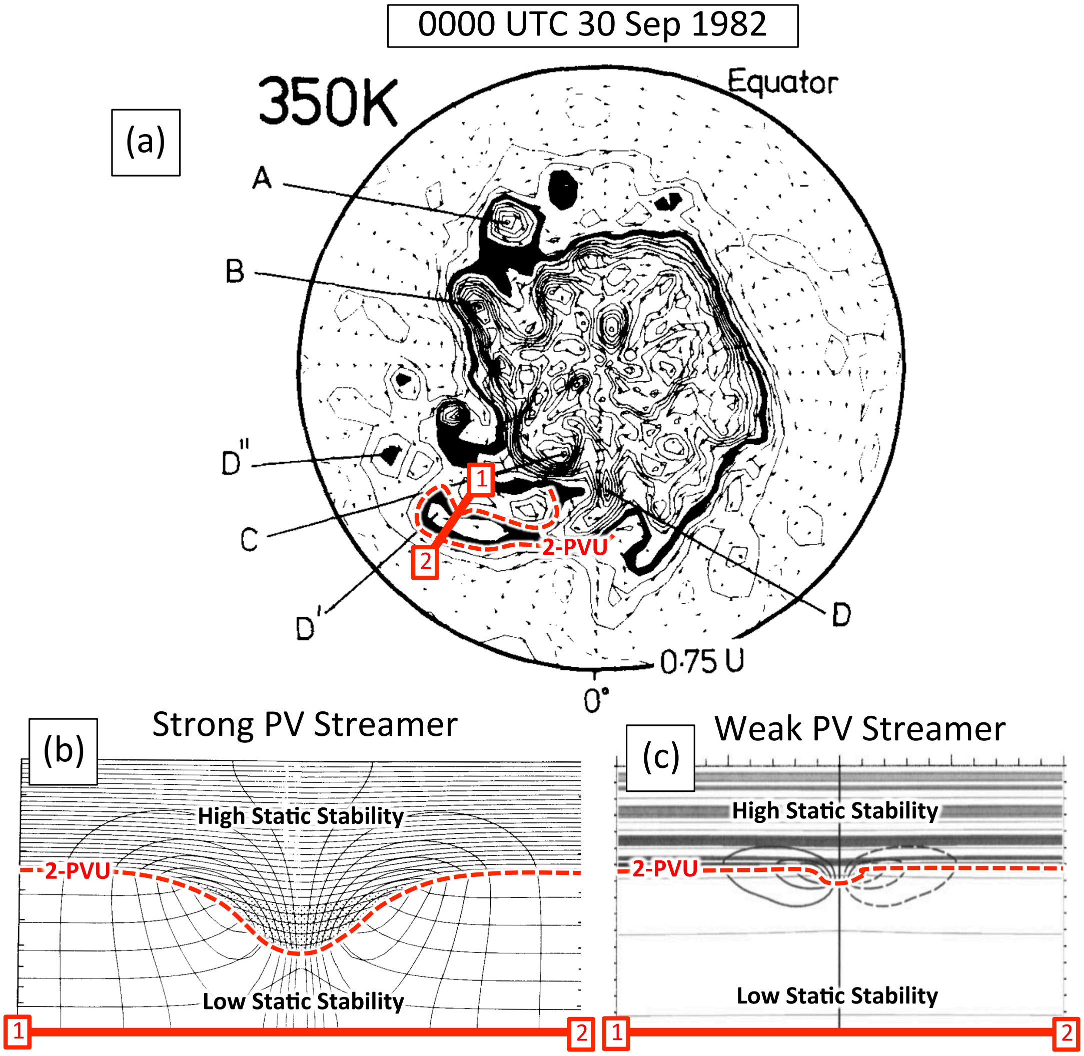

Figure 1.6 Illustration of the concepts described by HMR. (a) Northern Hemispheric polar projection map of 350-K PV (black contours, with 2–3 PVU shaded in black) and 350-K winds (vectors). The 2-PVU contour that outlines the PVS is highlighted by a red dotted line. The line ends marked by 1 and 2 are meant to schematically illustrate the cross-sections that are in (b) and (c). Panel (b) is a cross-section of an idealized, symmetric, strong PVS in HMR. Plotted are potential temperature (horizontal thin black contours, every 5 K), transverse wind velocity (vertical thin black contours, every 3 m s^{-1}, with 0 m s^{-1} isotach omitted), and the dynamic tropopause (red dotted contour, at 2-PVU). The stippled region represents the cyclonic PV anomaly with potential temperature amplitude of 24 K. Panel (c) is a similar cross-section but depicting a weak PVS. Plotted are potential temperature (thin horizontal black contours, every 10 K), transverse wind velocity (thicker black solid and dotted contours, every 1 m s^{-1}) and potential vorticity (alternating black and white shading, 2-PVU contour highlighted in red-dotted line). Adapted from Figs. 2a and 15a of HMR, and Fig. 1 of Juckes and Smith (2000).

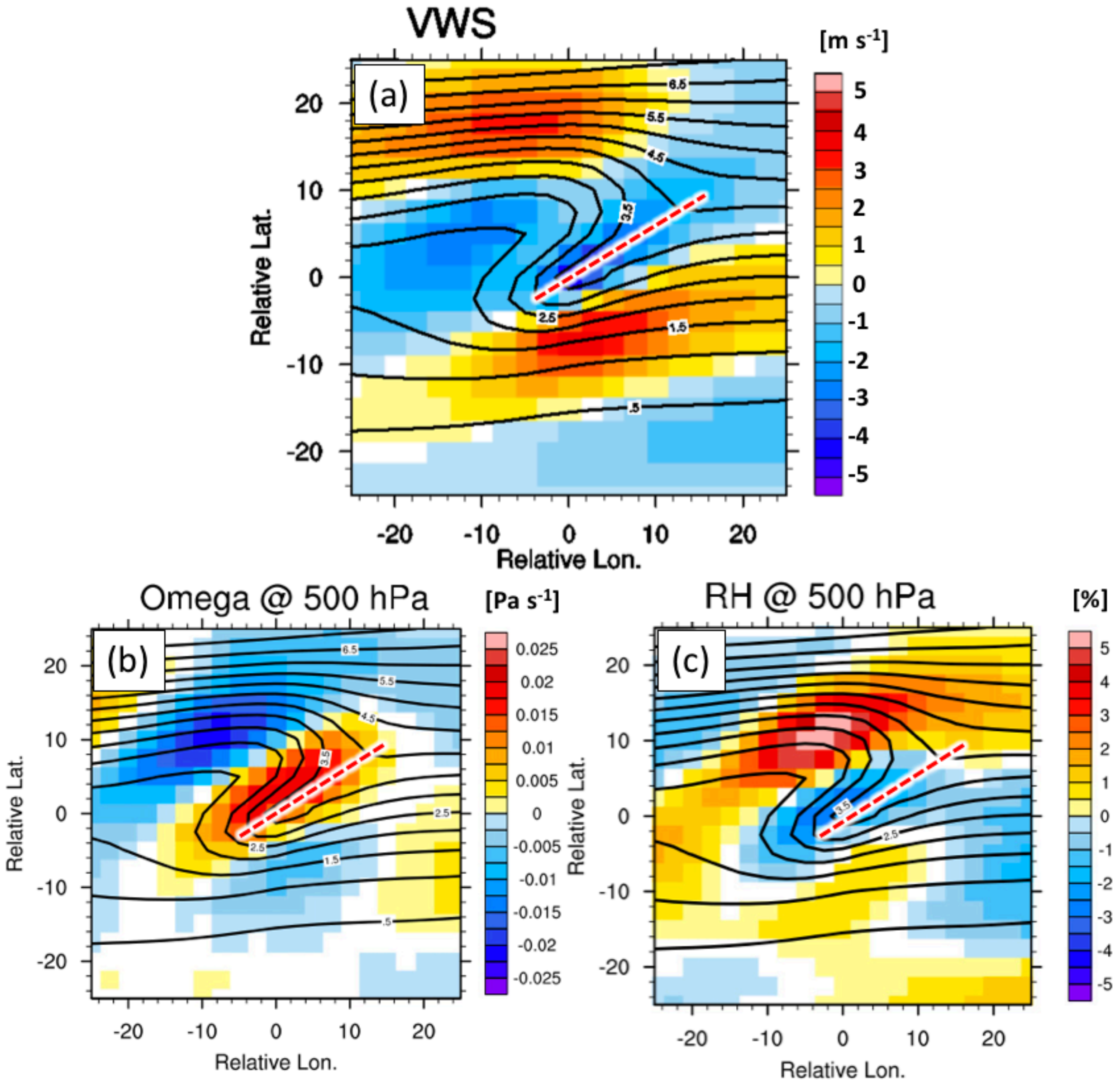

Figure 1.7. Composite environmental characteristics of high-PV tongues (i.e., PVSs) occurring with AWB. Panel (a) depicts 200–850-hPa VWS anomaly (shaded, m s^{-1}). Panel (b) depicts 500-hPa omega anomaly (shaded, Pa s^{-1}). Panel (c) depicts 500-hPa relative humidity anomaly (shaded, %). In all panels, 350-K PV is overlaid (black contours, PVU), while a red dotted line is used to denote where the PVS trough axis lies. Adapted from Figs. 3c, 4a, and 5a of Zhang et al. (2017).

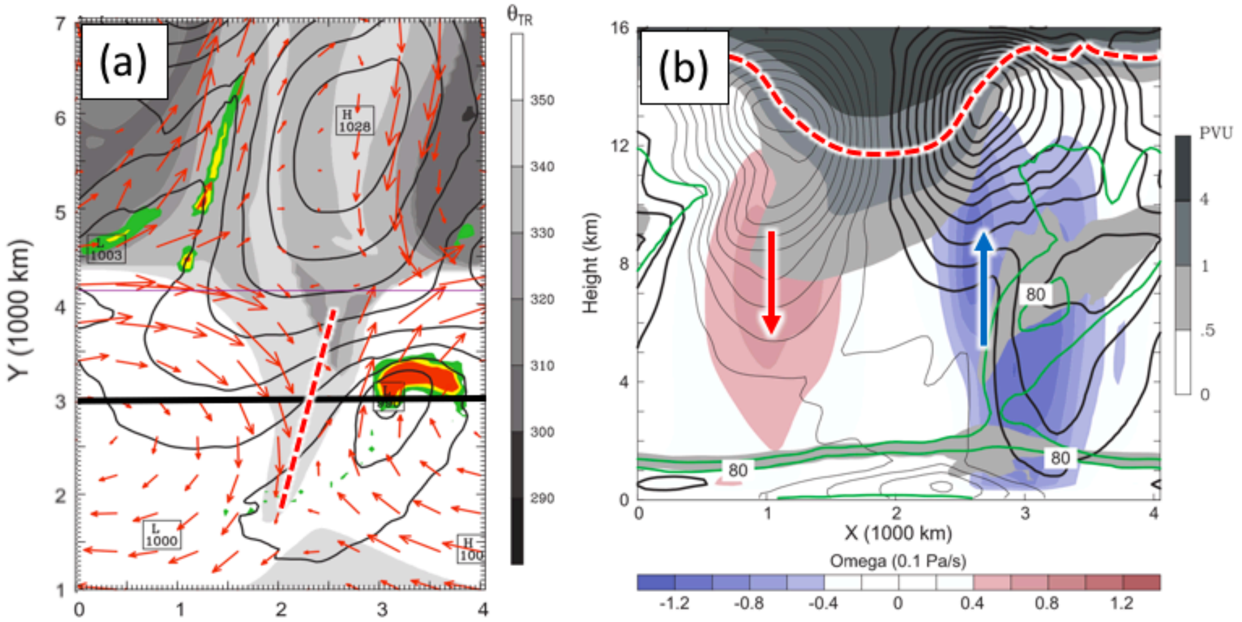

Figure 1.8. Illustration of QG-induced vertical motion associated with a PVS. Panel (a) is a map of theta on the dynamic tropopause (i.e., 2-PVU surface) (gray shading, theta), winds (vectors), and 6-h precipitation (color shading, mm) for the 264-h forecast of simulation S15_U40 in Davis (2010). The red dotted line illustrates the trough axis of the PVS, while the east–west oriented black line depicts the cross-section in (b). Panel (b) is a cross-section depicting PV (gray shading, PVU), QG-induced omega (color shading, Pa s^{-1}), meridional wind (black contours with zero line omitted; heavy lines for positive values, every 2 m s^{-1}), and relative humidity (green contours, > 60%) for the 216-h simulation of S15-U40 in Davis (2010). The red dotted line illustrates the 2-PVU contour associated with the PVS, while the blue and red arrows are used to illustrate upward and downward vertical motion respectively. Adapted from Figs. 7d, and 11 of Davis (2010).

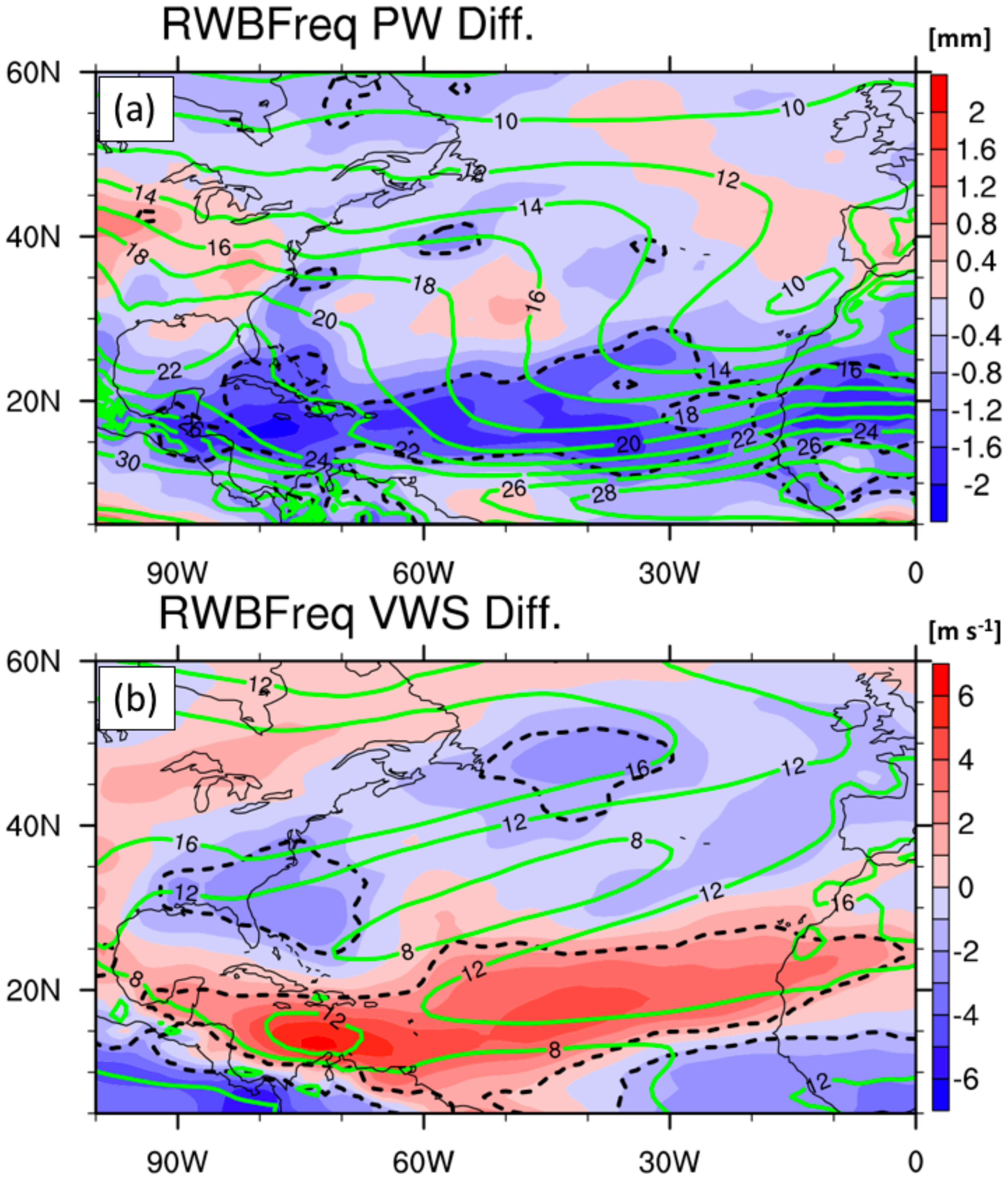

Figure 1.9. Composite seasonal conditions of years with the highest RWB frequency minus years with the lowest RWB frequency. Panel (a) is a map of precipitable water anomaly difference (color shading, mm) and climatological mean (green contours, mm). Panel (b) is a map of 200–850-hPa VWS anomaly difference (color shading, m s^{-1}), with climatological mean (green contours, m s^{-1}). Regions that are statistically significant above the 95% confidence interval are outlined by the black dotted line. Adapted from Fig. 8a,c of Zhang et al. (2017).

2. The PVS algorithm

2.1 Motivation, purpose, and approach

As discussed in Chapter 1, research to date has investigated PVSs through idealized modeling, climatologies, and individual case studies. While idealized modeling studies have looked at the importance of intensity and area variations of PVSs, these aspects of PVS structure have not been investigated in a climatology of PVS events. In this chapter, we will describe the development of a new PVS detection algorithm that will be used to identify different PVS intensities, areas, and tilts from a 36-y (1979–2015) period using two reanalysis datasets. First, a brief overview of the two reanalysis datasets used in this study is presented. Then we will examine the two most prominent methods of RWB and PVS identification used in recent literature, to provide context for the new PVS algorithm developed in this study. Finally, the remainder of this chapter will focus on details of the new methodology that is adapted from these previous methods.

2.2 Datasets

PVS events between 1979–2015 are identified in two reanalysis datasets, the Climate Forecast System Reanalysis (CFSR; Saha et al. 2010) and the ERA-Interim Reanalysis (ERAI; Dee et al. 2011), at 6-h synoptic times (0000, 0600, 1200, and 1800 UTC) from 1 June–30 November. The gridded CFSR dataset has a resolution of 0.5^{o} degrees, the gridded ERAI has a resolution of 0.7^{o}, and both reanalyses have comparable number of vertical levels (64 and 60 vertical levels, respectively). These resolutions are more than sufficient to resolve synoptic-scale PVSs which typically have length scales that exceed these distances by an order of magnitude.

The use of two different reanalysis datasets also allows for an evaluation of the sensitivity of the PVS climatology to different datasets.

There are several differences between the two reanalysis datasets that may potentially affect their ability to depict tropopause-based PV and hence affect the identification of PVSs. First, both the CFSR and ERAI assimilate satellite radiances in the upper-troposphere and lower-stratosphere, but handle radiance observation bias correction differently (e.g., Saha et al. 2010, Dee et al. 2011). In turn, this could impact temperature biases in the upper-troposphere and lower-stratosphere. Given the importance of horizontal and vertical temperature gradients in the calculation of PV, even small differences in the model temperature biases can impact PV values. Second, the CFSR uses a three-dimensional variational analysis scheme (3D-Var) while the ERAI uses a four-dimensional variational analysis scheme (4D-Var). In general, 4D-Var can result in a more effective use of observations, as allowing a time window can enable the extraction of tendencies in the mass field and flow dependent structures that help to constrain the analysis (Thepaut et al., 1996; Rabier et al. 1998, 2000). Due to these advantages, 4D-Var has been shown to outperform 3D-Var in data sparse regions of the globe, such as over oceanic basins (Whitaker et al. 2009). These model differences are useful for understanding the PVS climatology obtained from the two reanalysis datasets.

2.3 Previous PVS identification methods

This section summarizes literature related to algorithms using different methods to identify RWB and PVS occurrence, expressing their advantages and disadvantages. Different methodologies have been used to identify RWB and PVSs in a variety of atmospheric regions for different seasons. To aid the discussion, Tables 2.1 and 2.2 organize the literature into two primary methods; studies that use poleward meridional PV gradient reversals to identify RWB and PVS, and studies that use distance criteria to identify relevant PV filaments that qualify as PVSs. Many of the previous PVS climatologies only focused on boreal winter (December–February; DJF) to identify either RWB or PVS cases. An exception is Zhang et al. (2016, 2017) who investigated RWB events with PVSs during the boreal summer. Zhang et al. (2016, 2017), however, only examined one month (August) and four months (July–October), respectively. RWB and PVS cases used in this dissertation are examined in a longer period that spans the full NATL TC season (1 June–30 November). Moreover, the current study is also the first to compare multiple reanalysis datasets in the identification of PVS events. To explain the rationale for creating a new PVS algorithm, we will compare and contrast the two primary methods, later adapting aspects from these previous methods.

2.3.1 Methodologies using poleward meridional PV gradient reversals

Studies that use a poleward meridional PV gradient reversal for identification of RWB and PVS events appear in Table 2.1. This PV gradient reversal is often attributed to the beginning of overturning PV contours at a specific longitude that signifies the RWB axis. The main advantage of identifying PVSs using a meridional PV gradient reversal is that a downstream PVS area is explicitly tied to a RWB event. There are, however, several drawbacks. First, when identifying PVSs at constant longitude, the entire area of the PVS observed downstream of the AWB axis may not be captured unless it is entirely under the overturning PV contour. The failure to capture the entire area of the PVS then precludes the accurate calculation of the intensity, area, and tilt of the PVS. Second, the dimensions of the high-PV air retained under the meridional PV gradient reversal may not fit the classical definition of a PVS with a high aspect ratio (i.e., a narrow filament where its length is expected to greatly exceed its width). These drawbacks will be addressed when discussing the new methods presented in section 2.4.

Baldwin and Holton (1988) first applied the PV reversal method to identify RWB frequency over the Northern Hemisphere, using isentropic surfaces embedded in the mid-stratosphere (850K) to focus on erosions of the stratospheric polar vortex. A decade later, Postal and Hitchman (1999) updated this method, using a lower isentropic surface (350K) to focus on interactions between the mid-latitudes and tropics. In this study, RWB was identified using PV gradient reversals along the 1.5 PVU contour that covered > 50° swaths in longitude, retaining only the western most point where the reversal occurred. While this method identifies the location of the RWB axis, it does not diagnose the location of the PVS area downstream. Abatzoglou and Magnusdottir (2006) built upon this PV reversal method in two ways. First, in addition to identifying meridional PV gradient reversals, this study also identified localized eastward PV gradients (low to high PV air moving west to east) to classify PVSs occurring from anticyclonic overturning (i.e., AWB). Second, instead of identifying the RWB axis, this study identified the southwestern most point associated with the meridional PV gradient reversal. Only this point is retained, with additional reversal points within 30° of longitude and within four days of the initial identification discarded (refer to section 2a of Abatzoglou and Magnusdottier [2006] for more information). Ndarna and Waugh (2011) also used the method of Abatzoglou and Magnusdottier (2006) except for the Southern Hemisphere. The next incremental method update came from Strong and Magnusdottir (2008). They identified a 350-K PV contour with the longest length that circumnavigated the globe and then detected RWB by identifying points along a constant longitude where the PV contour crosses more than once. These points along the PV contour were used as the start and ending points to create a polygon between the constant longitude and the PV line segment that connects the two points on that constant longitude. Strong and Magnusdottier (2008) used this method to identify low-PV polygons associated with anticyclonic ridging, where the centroid, area, and zonal extent could be obtained (Fig. 2.1). A similar version of this method has been used to identify polygons of high-PV areas that are often consistent with cyclonic troughs of PVSs downstream of AWB events (Song et al. 2011; Homeyer and Bowman 2013; Zhang et al. 2016, 2017).

2.3.2 Methodologies using distance along a PV contour

Studies that used a distance criterion along a PV contour to identify PVS events appear in Table 2.2. These studies identify PVSs by searching along a given PV contour (i.e., 2-PVU) to find locations where the spherical distance between two points on the contour is much smaller than the perimeter between the same two points following along the contour. The primary advantage of this distance method is that it enables the explicit identification of narrow filaments that fit the dimensional criteria of a PVS (e.g., Appenzeller and Davies 1992). This definition assumes, however, that these threshold spherical and perimeter distances are not too restrictive (missing subjectively identified cases) or generous (identifying cases that would not be subjectively identified). In addition, using a distance criterion alone does not explicitly link PVS events with RWB events, since PV gradient reversals are not identified, but rather just elongated corridors along a PV contour. These drawbacks will be addressed when discussing the new methods presented in section 2.4.

Wernli and Sprenger (2007) first used a contour finding algorithm that adapted distance criteria to identify PVS events (Fig. 2.2). First, the 2-PVU contour on an isentropic surface that circumnavigates the globe is identified and split into equally segmented points. For each point, the spherical distance and perimeter following along the contour is calculated for all segmented points. Next, narrow filaments are identified by finding two points where the perimeter distance along the contour is > 1500 km, but the spherical distance is < 800 km. Finally, the grid point areas enclosed by the connection of these two points are retained, with areas containing PV > 2 PVU denoting a PVS. An important caveat to this method is that the distance thresholds chosen by Wernli and Sprenger (2007) were arbitrary because they focused on capturing meso- to synoptic-scale filaments of high PV air. These same distance thresholds were also used in Martius et al. (2007), but additional criteria that identified PVS tilt were added, calculating the angle between a zonally oriented base line and a line that defined the tilt axis of the PVS.

Sprenger et al. (2013) modified the distance criteria for PVSs. They opted for a larger threshold of perimeter distance along the PV contour (> 2000 km) that was required to be at least double the spherical distance, which also used a larger maximum threshold (< 1500 km). Kunz et al. (2015) further refined this method by using a “dynamically relevant PV contour”, which is defined as a seasonal PV contour that exhibits the maximum vertical PV gradient. They also relaxed perimeter and spherical distance criteria at higher isentropic surfaces (350-K and greater) given their observation that PVSs are larger in areal extent on these surfaces.

Because both the poleward meridional PV gradient reversal and contour distance methods have advantages and disadvantages when identifying PVSs events, the methodology used in this study selects aspects from both methodologies to identify PVSs that are tied to RWB, yet are also objectively defined as narrow filaments that can qualitatively be identified as PVSs on isentropic PV maps.

2.4. Methodology of a new PVS detection algorithm

2.4.1. Identification technique

The methodology in this dissertation uses an automated algorithm that adapts methods form previous research so PVSs are identified in association with AWB, and are characterized as elongated filaments of high-PV air, adopting the strengths of the earlier methods. The goal here is to identify PVSs on the circumpolar 2-PVU contour on the 350-K isentropic surface, because this level typically represents the summertime subtropical tropopause where PVSs originate (e.g., Holton 1995; Postel and Hitchman 1999, 2001). The resolution of 350-K PV field is coarsened to 2.5° to remove sub synoptic-scale variability, which is not needed to intensify PVS events. Reducing horizontal resolution is a common practice that has been used in both RWB and PVS identification studies because it can remove small-scale contour undulations (e.g., Postal and Hitchman 1999, Zhang et al. 2016, 2017). Both the CFSR and ERAI datasets are coarsened to this resolution in order to allow for a consistent comparison between the two datasets. After resolution reduction, the first step in the PVS algorithm is to split the circumpolar 2-PVU contour into equally spaced points (Fig. 2.3, white circles) that will be used to calculate both PV gradients and distances along the contour in the PVS algorithm.

Step 2 in the PVS algorithm is the identification of the first consecutive points where a poleward meridional gradient reversal in PV is observed (red circles, Fig. 2.3). This approach is similar to the technique first used by Postel and Hitchman (1999), which has been refined in subsequent studies (e.g., Abatzoglou and Magnusdottier 2006, Homeyer and Bowman 2013). Step 2 also adopts the Abatzoglou and Magnusdottir (2006) criterion that requires an eastward PV gradient along the 2-PVU contour, which helps restrict the points with poleward PV gradient reversals to be associated with AWB events when searching for points from west to east. At least two consecutive points are needed, because a line segment is needed as a baseline to draw an additional line orthogonal to its axis.

When two consecutive points are identified, step 3 involves the construction of an orthogonal line (blue line, Fig. 2.3) from the first point of the contour segment (*A*) until the line crosses the 2-PVU contour eastward and equatorward. Step 4 determines the closest point where this line again intersects the 2-PVU contour (*B*, Fig. 2.3), becoming the ending point that closes a polygon of > 2-PVU air. Steps 3 and 4 in this PVS algorithm are novel, as previous studies only connected points along a constant longitude to create a polygon of high PV air (e.g., Song et al. 2011; Homeyer and Bowman 2013; Zhang et al. 2016, 2017). By using an orthogonal line versus a meridional line, the entire region of the polygon is captured, not just the region folded under the reversal of the poleward PV gradient (e.g., Abatzoglou and Magnusdottir 2006; Zhang et al. 2016), which can omit a significant fraction of the high-PV area associated with a PVS. Capturing the accurate dimensions of the PVS polygon downstream also helps to obtain the correct distances to deduce the area and tilt of the polygon created.

Step 5 uses the orthogonal line that created the PVS polygon to calculate the spatial width (w) between points A and B, which is then compared to the perimeter (p) moving along the 2-PVU contour between A and B (Fig. 2.3). To determine if the polygon identified fits the conceptual definition of a PVS (i.e., a narrow filament of high PV air), distance thresholds between p and w are used. In this study, p is required to be > 3000 km in total distance and p is required to be at least three times larger than w. This results in a 3:1, or greater, aspect ratio between p and w, confirming that the PVS polygon has a high aspect ratio consistent with PVS features (Appenzeller and Davies 1992; Kunz et al. 2015).

Step 5 of the PVS algorithm borrows from previous studies that employed distance criteria to identify PVS polygons (e.g., Wernli and Sprenger 2007; Martus et al. 2007, Sprenger et al. 2013; Kunz et al. 2015) with a few caveats. First, while prior studies used the distance criterion to create the PVS polygon, this study only uses these distances to confirm that the already created polygon is a narrow filament with at least a 3:1 aspect ratio between p and w. Second, the threshold distances used in prior studies vary widely depending on the isentropic surface and the feature scale desired for the study. For example, Wernli and Sprenger (2007) used a maximum w distance of 800 km, which omits larger PVSs that this study would like to identify (Fig. 2.4). As noted by Kunz et al. (2015), PVSs tend to increase in size as the isentropic surface used to identify them increases. Consequently, Kunz et al. (2015) chose maximum w thresholds of 2000–3500 km for PVSs identified on isentropic surfaces between 350–500 K. The methodology used here differs by allowing w to vary using an aspect ratio threshold that is dependent on p. Thus, smaller PVS candidates that barely exceed the p threshold have a more restrictive maximum w threshold in comparison to larger PVSs candidates that have a less restrictive w threshold given the larger size of p. The advantage of a w threshold that varies with p is that PVSs of many different sizes are allowed in the algorithm as long as they satisfy the 3:1 aspect ratio. That said, the minimum p threshold (> 3000 km) used here is still somewhat arbitrarily chosen. This minimum p threshold value also confirms, however, that PVSs identified on a 2.5x2.5° grid will have a perimeter length scale that is at least an order of magnitude larger than the grid spacing resolution (~250 km). Trial and error using different p and w thresholds were tested before settling on the current criteria, which includes the most PVSs events that still faithfully adhere to general PVS characteristics (Appenzeller and Davies 1992; Kunz et al. 2015).

Finally, if a PVS candidate polygon passes the required distance thresholds, step 6a retains all the grid points in the PVS polygon for inclusion into the PVS climatology and also to calculate additional metrics related to the PVS (Fig. 2.3) discussed in the next section (2.4.2). In step 7, the algorithm continues to search for additional PVS candidates starting at the point after *B* not part of the identified PVS (Fig. 2.3). If the PVS candidate polygon does not pass the required distance thresholds, step 6b moves to the next point along the 2-PVU contour (after *A*) and the process begins again (Fig. 2.3). This process continues until each point along the circumpolar 2-PVU contour is accounted for in that time step.

2.4.2 Metrics identified with each PVS

An important component of the PVS climatology created in this study is the ability to compare differences in PVS characteristics, investigating their differences in intensity, area, and tilt. These characteristics are calculated after a PVS is identified (Fig. 2.3, step 6a), and this section will describe how each characteristic is calculated.

An example of a real PVS identified by the algorithm in section 2.4.1 is provided in Fig. 2.5. The 2-PVU contour in this example exhibits a large, poleward, meridional gradient reversal between 40–70°W (red dots, Fig. 2.5a). This feature is denoted a PVS in this climatology because the perimeter (p) between A and B is more than three times greater than the width (w) between A and B. The calculation of the PVS area afterwards is a straightforward exercise once the dimensions of the polygon created between p and w are determined. The PVS identified in Fig. 2.5a is very large, with an area of 5.87×10^6 km^2, placing it in the top 20th percentile of all PVSs in the climatology. The PVS centroid (yellow circle, Fig. 2.5a) is also calculated using all the points located along the p and w of the PVS, and indicates the geometric center of the PVS.

Above this large PVS, there is an additional poleward meridional PV gradient reversal observed near 50°N, 50°W. However, this second feature is too small ($p < 3000$ km) to be considered a PVS.

Computing the tilt of the PVS requires additional calculations (Fig. 2.5b). First, a midpoint between A and B is identified along the orthogonal line (blue circle, Fig. 2.5b). Next, a line is drawn between the midpoint and a point along the PVS that is furthest away in distance from this midpoint (green circle, Fig. 2.5b). Finally, the angle between this line and the nearest meridian is computed. These methods are an update from Martius et al. (2007), which calculated a tilt angle between the midpoint and the southernmost point of the PVS. It is advantageous to use the furthest distance point versus the southernmost point because it better depicts the true tilt of a PVS oriented more east to west. Using the southernmost point in these scenarios may cause the PVS to have greater north to south tilt than what actually occurs. The PVS example in Fig. 2.5b shows a PVS with a positive tilt of 68.3°, which falls in the 40–60th percentile of all cases identified in the PVS climatology. In general, the orientation of PVSs identified in this climatology lie between 0° (oriented north to south) and 90° (oriented east to west), though in rare cases PVSs can exceed these bounds (see the discussion in section 3.2.2 and Fig. 3.9).

Finally, the intensity of the PVS is determined by first identifying all grid points enclosed within the PVS area (Fig. 2.5c). The intensity at each grid point is calculated as a standardized anomaly of the 350-K PV field using the equation below:

$$Z = \frac{x - \bar{x}}{\sigma} \tag{2.1}$$

where x represents the PV for that particular location and time, $\bar{x}$ is the climatological mean, and σ is the climatological standard deviation of 350-K PV for that location and time of year. The climatological mean and standard deviation are defined at 0000, 0600, 1200, and 1800 UTC each calendar day of the year using the first four harmonics of each reanalysis 36-y mean and standard deviation (1979–2015). For all PVS cases, both the average intensity (averaging all grid point values within the PVS) and the summed intensity (adding all grid point values within the PVS) are calculated. The average intensity is used to sort PVSs cases by their intensity in the climatology, while the summed intensity is used to create an activity metric which combines the summed intensity of each PVS case over the entire TC season (June–November). In the example presented in Fig. 2.5c, the PVS identified has an average intensity of $+0.77\sigma$, which falls near the 50th percentile of all PVSs identified in the climatology.

2.5 Tables

Table 2.1 References of RWB and PVS climatological studies where the primarily methodology identifies a poleward meridional PV gradient reversal. Studies are sorted by year, region, period, and isentropic surface used to conduct the climatology.

Reference (Year)	Region of Interest	Period of Study (Season)	Isentropic Surface
Baldwin and Holton (1988)	NH	1964–1982 (DJF)	850-K
Postal and Hitchman (1999)	Globe	1986–1995 (Year)	350-K
Abatzoglou and Magnusdottir (2006)	NH	1958–2003 (Year)	330–360-K
Hitchman and Huesmann (2007)	Globe	1979–2005 (Year)	320–350-K
Strong and Magnusdottir (2008)	NH	1958–2006 (DJF)	350-K
Ndarna and Waugh (2011)	SH	1979–2008 (Year)	350–500-K
Song et al. (2011)	SH	1957–2002 (Year)	300–350-K
Homeyer and Bowman (2013)	Globe	1981–2010 (Year)	350–500-K
Zhang et al. (2016)	NATL	1979–2013 (Aug)	350-K
Zhang et al. (2017)	NATL	1979–2013 (JASO)	350-K

Table 2.2 References of RWB and PVS climatological studies where the primary methodology uses distance thresholds to identify cases. Studies are sorted by year, region, period, and isentropic surface used to conduct the climatology

Reference (Year)	Region of Interest	Period of Study (Season)	Isentropic Surface
Wernli and Sprenger (2007)	NH	1970–1993 (Year)	295–360-K
Martius et al. (2007)	Globe	1958–2002 (DJF)	310–340-K
Sprenger et al. (2013)	SH	1980–2000 (Year)	300–350-K
Kunz et al. (2015)	Globe	1979–2011 (Year)	350–500-K

2.6 Figures

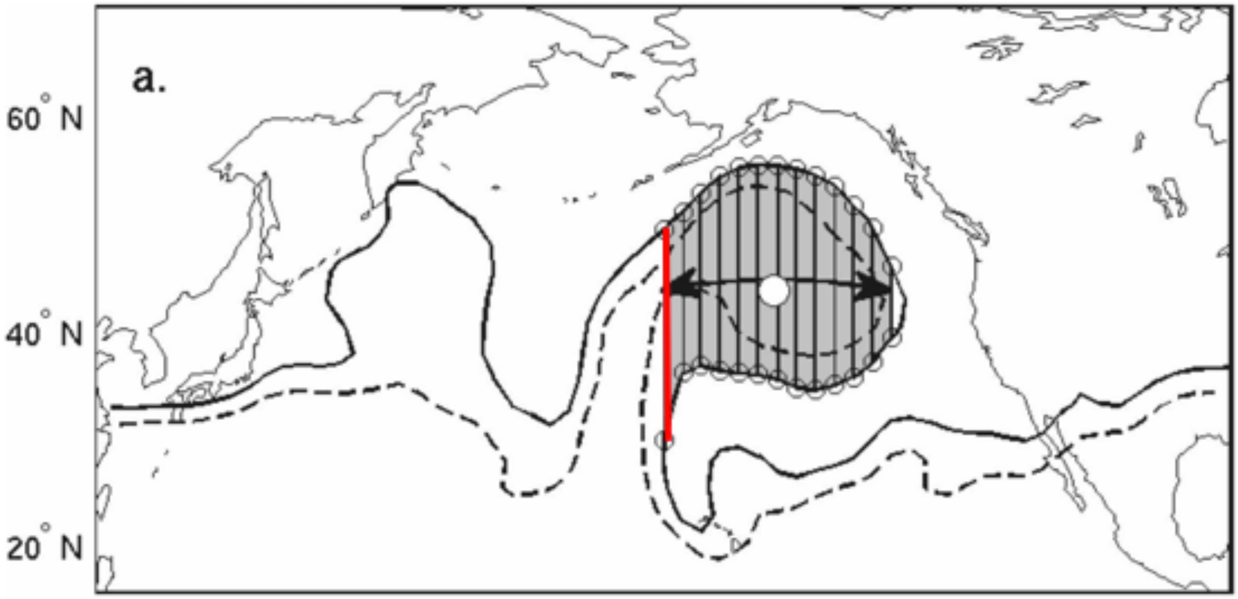

Fig. 2.1. An example of an algorithm identifying a polygon where a poleward PV gradient reversal is observed. The 3 and-5 PVU contours on the 350-K surface are highlighted in dotted and solid lines, respectively. Open circles with lines connecting them identify where the 5-PVU contour has crossed a meridian twice (indicating a PV gradient reversal), the white solid circle indicates the centroid of the polygon, and the black arrow indicates the zonal extent of the PV gradient reversal. The gray shading indicates the total area of the low-PV polygon enclosed by the 5-PVU contour, and the first meridian were a PV gradient reversal was observed (red line). Adapted from Fig. 1 of Strong and Magnusdottir (2008).

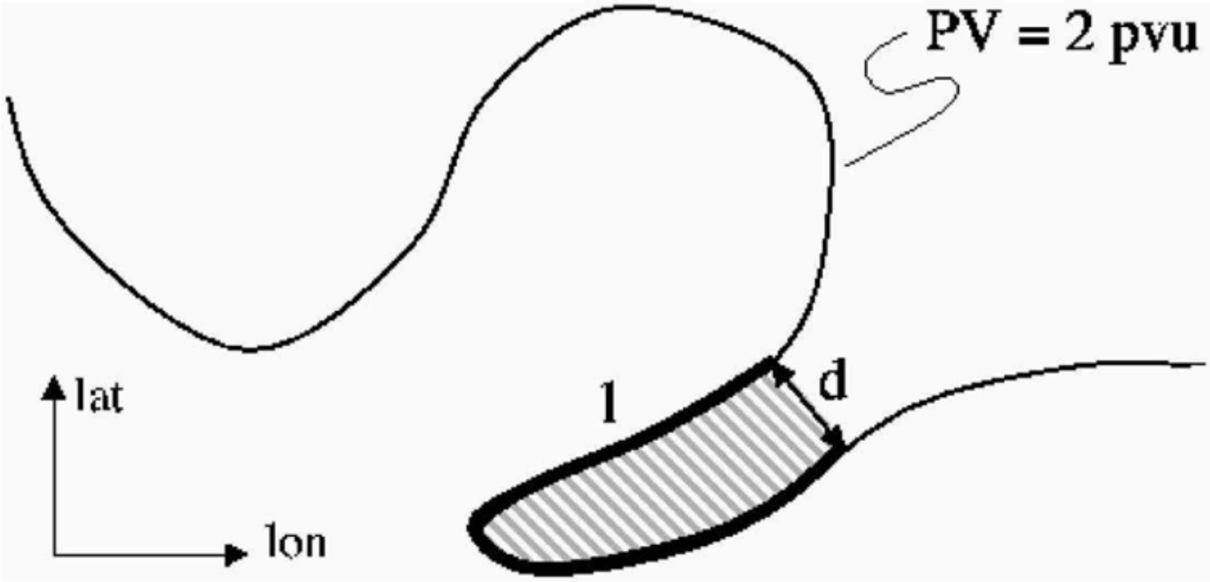

Fig 2.2. An example of an algorithm that identifies a polygon of high-PV air using distance criteria. The black line corresponds to the 2-PVU contour on an isentropic surface. The shaded region indicates a polygon of high-PV air that is identified because the spherical distance (*d*) is <800 km, while the distance along the contour (*l*) is >1500 km. These threshold distances identify meso- to synoptic-scale filaments of high-PV air. Adapted from Fig. 1 of Wernli and Sprenger (2007).

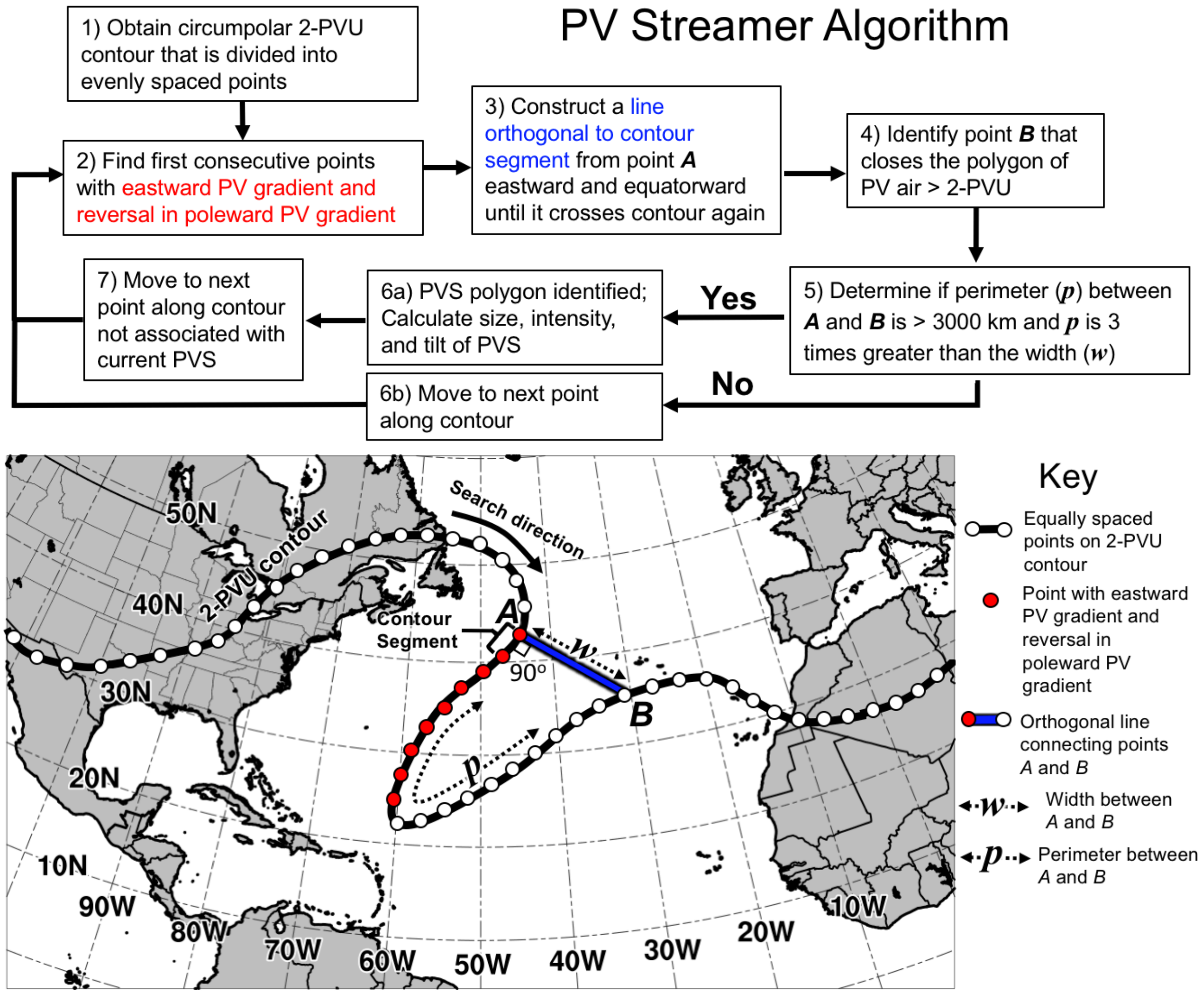

Fig. 2.3. A flowchart and schematic diagram of the PVS algorithm employed in this study to identify a hypothetical PVS. The black arrows in the flowchart indicate the step by step directions the algorithm uses. The process shown here illustrates the algorithm running for one time step (6-h). Note the key to the right that annotates the features embedded in the schematic figure.

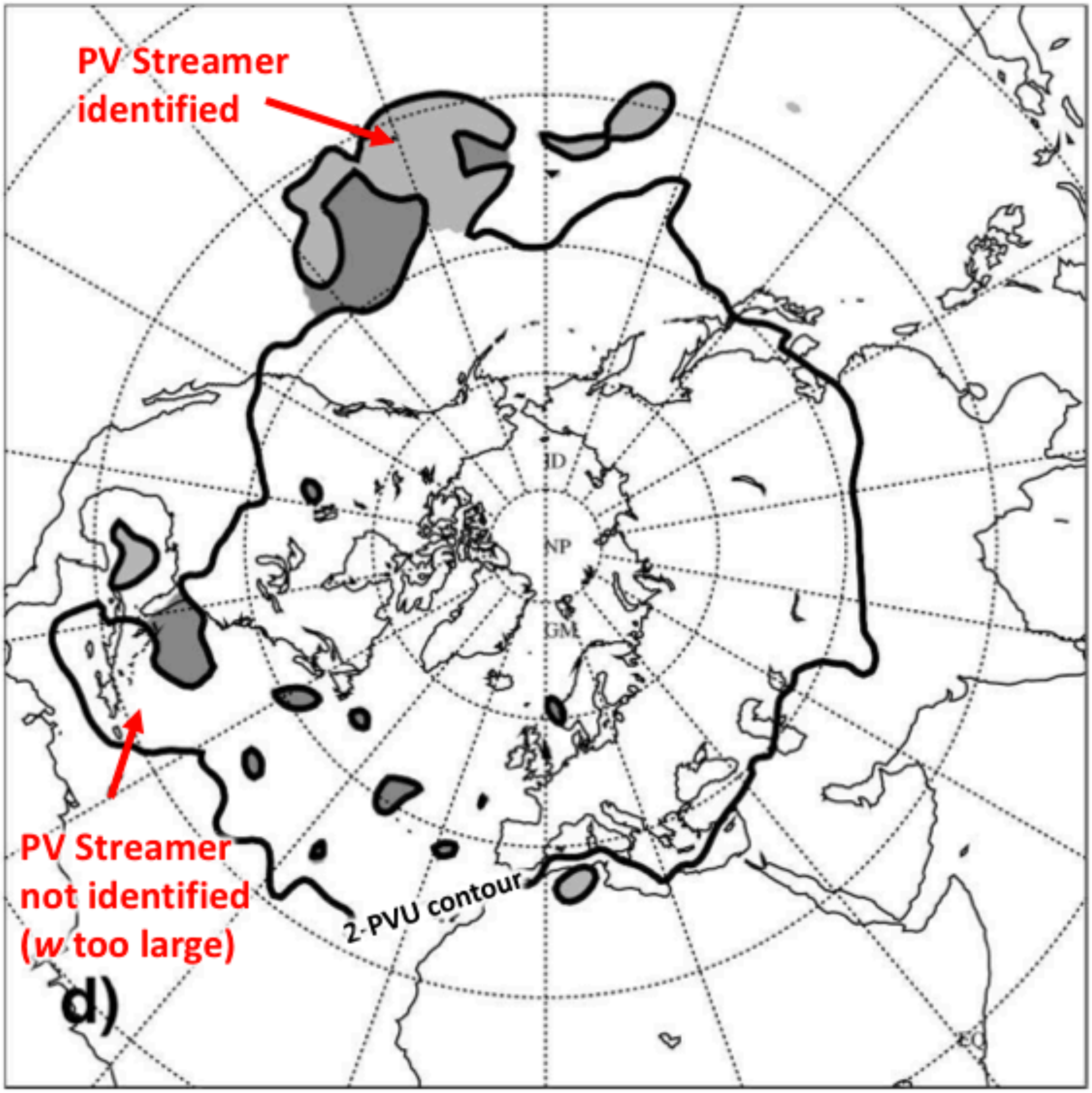

Fig. 2.4. An example of a successful and unsuccessful identification of a PVS using restrictive distance identification criterion. The thick black line represents the 2-PVU contour on the 350-K isentropic surface. Lighter grey shading indicates polygons of high PV air (> 2-PVU), while darker grey shading indicates polygons of low PV air (< 2-PVU). Highlighted by the red arrow near the top in the Pacific basin is a correctly identified PV streamer with a small $w < 800$ km, while highlighted in the red arrow near the bottom in the Caribbean Sea is the failed identification of a PV streamer that has a larger $w > 800$km. Adapted from Fig. 2d of Wernli and Sprenger (2007).

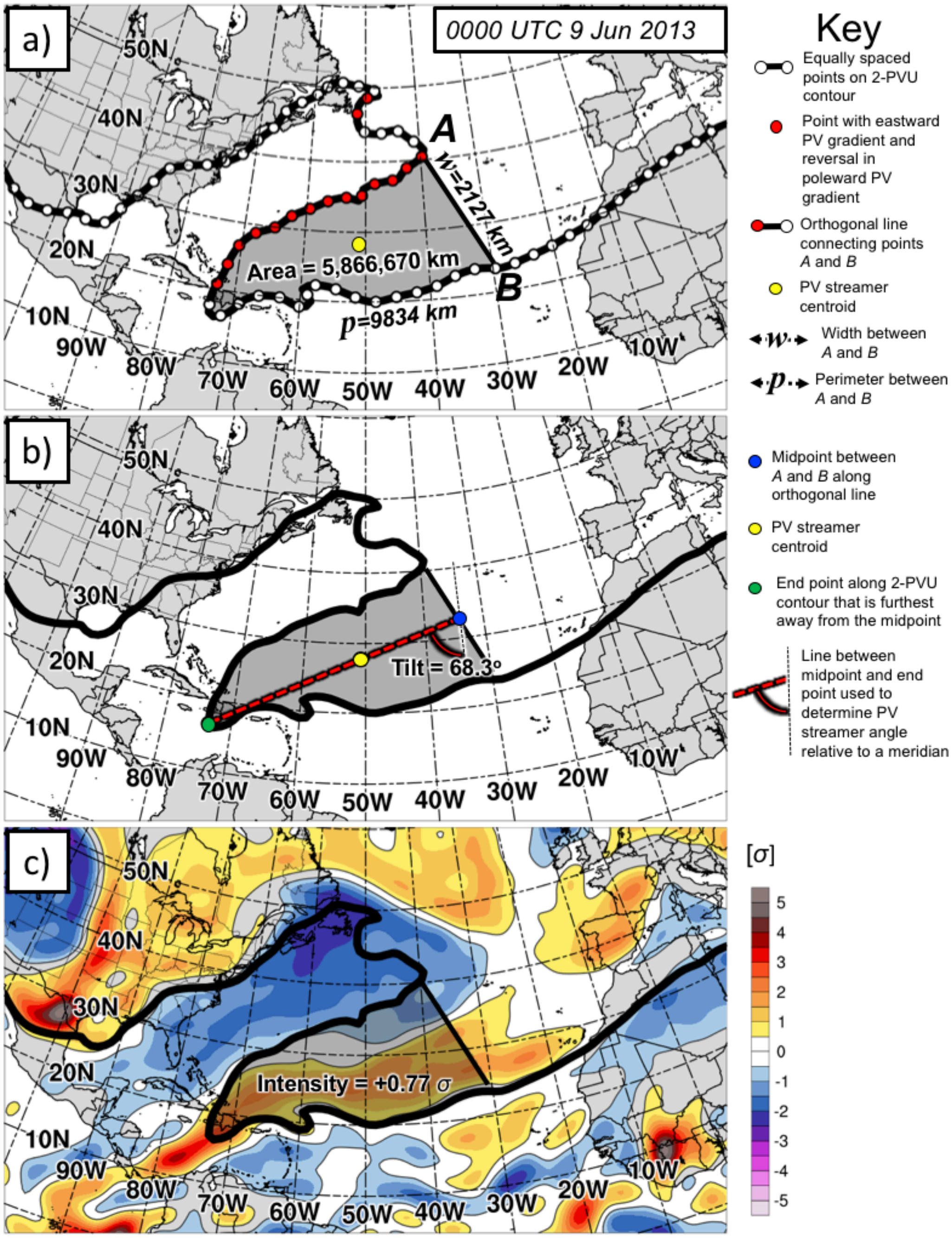

Fig. 2.5. An example of characteristics being identified from a real PVS case on 0000 UTC 9 Jun 2013. Panel (a) depicts a closed polygon of high-PV air (> 2-PVU, gray shading) identified because the perimeter (*p*) is > three times the width (*w*) of the feature. The surface area in km is depicted, as is the centroid of the PVS (yellow circle). Panel (b) illustrates how the orientation angle of the PVS is identified. The red dotted line connects the midpoint (blue circle) with the end point (green circle) of the PVS, with the angle of this line found relative to a longitudinal meridian depicted. The centroid of the PVS is also displayed (yellow circle). Panel (c) illustrates how intensity of the PVS is calculated. The standardized PV anomaly (shaded, σ) is averaged over the grid points within the PVS area (grey shading) with the average value depicted inside. All panels use data from the ERA-Interim.

3. The PVS climatology

3.1 Introduction

Chapters 1 and 2 of this dissertation detailed previous research on AWB, how these events are connected to PVS occurrence, and the various methods used to identify the linked nature of AWB and PVS occurrences. A long-term (1979–2015) climatology of warm season (June–November) PVSs that occur in conjunction with AWB in the Atlantic basin is presented in this chapter. This climatology will highlight PVS frequency, intensity, area, and tilt on a year to year basis, which contribute to differences in environmental variables in the Atlantic basin. In addition to highlighting the interseasonal and intrannual variations of PVS activity, this chapter also investigates differences in PVS activity between the ERAI and CFSR climatologies. We will include possible explanations for these differences. Finally, PVS activity changes will be compared to indices that influence the environment of the NATL basin on interseasonal to intrannual timescales (ENSO, sea surface temperatures [SSTs], MJO).

3.2 PVS climatology in the NATL basin using the ERAI

This section presents the climatological results obtained by applying the PVS algorithm discussed in section 2.4 to June–November from 1979–2015. This analysis extends the previous work that spatially identified regions of AWB in the North Atlantic basin (e.g., Postel and Hitchman 1999; Homeyer and Bowman 2013) and PVSs (e.g., Wernli and Sprenger 2007; Kunz et al. 2015) and is complementary to, but more detailed than, the analysis recently performed in Zhang et al. (2016, 2017). These previous studies emphasized the number of AWB or PVS events spatially on a map by summing their total for a given period, but the study here provides added information on PVS area, intensity, and tilt for an extended climatological period.

3.2.1 Spatial distribution of PVS occurrence

The climatological frequency of PVS occurrence from 1 June–30 November is first assessed spatially on the 350-K surface in Fig. 3.1. Grid points enclosed within an individual PVS are considered part of the same PVS occurrence for a given time. The area of each PVS occurrence is then summed from 1 June–30 November and divided by the total number of 6-h times to provide a frequency percentage of occurrence. The frequency maximum PVS occurrence in the Atlantic basin is 26% at 28.5^{o}N and 47.5^{o}W, though PVS occurrence frequencies between 10–25% stretch from the edge of the Bahamas (25^{o}N, 75^{o}W) northeast to near the Strait of Gibraltar between Africa and Europe (35^{o}N,10^{o}W). We note that the maximum frequency of PVS occurrence in Fig. 3.1 is three times higher than the JJA peak of 9–11% frequency found at 350-K in Wernli and Sprenger (2007). We attribute the large increase in this PVS climatology to differences in our methodology, which allow for wider and larger PVSs to be identified. The southwest to northeast orientation of increased PVS frequencies also lines up with a positively tilted trough axis in the 200-hPa streamlines (black lines, Fig. 3.1). The location of this feature suggests that increased PVS occurrence frequency also corresponds to the position of the traditional, time-mean TUTT (Sadler 1976). In addition, the increased PVS occurrence in the subtropical Atlantic basin is primarily equatorward of the 200-hPa, time-mean wind maximum (yellow contours, Fig 3.1). This result is not surprising given that PVS events in this climatology are linked to anticyclonic RWB, which typically occur equatorward of the mid-latitude jet, where anticyclonic shear in the upper-troposphere is favored (Postel and Hitchman 1999).

Supplementing the full climatology, PVS occurrence frequency plotted for each month of the climatology (June through November) illustrates how PVS activity changes in magnitude and shifts in location across the Atlantic basin during the TC season (Fig. 3.2). In June (Fig. 3.2a) the maximum frequency of PVS occurrence peaks at 30% at 26°N, 49°W, with the highest occurrence oriented west to east along 25°N in the Atlantic basin. In July (Fig. 3.2b), the PVS frequency maximum increases to 46% and shifts poleward and westward to 29°N, 53°W, with the highest occurrence becoming oriented more southwest to northeast across the Atlantic basin. This increase in the PVS frequency maximum also corresponds to a sharpening of the time-mean 200-hPa streamlines across the PVS frequency maximum in the Atlantic basin. In August and September (Fig. 3.2c–d), the PVS frequency maximum axis gradually shifts westward (to 47°W and 42.5°W, respectively) and slowly decreases in total magnitude (maxima of 35% and 34%, respectively) relative to the peak in July. In October and November (Fig. 3.2e–f), PVS frequency rapidly drops off in magnitude (maxima of 27% and 15%, respectively) while shifting further equatorward and eastward. The decrease in overall PVS frequency is at least partially attributed to the increase in magnitude of the 200-hPa time mean jet, which also shifts equatorward during October and November (yellow contours, Fig. 3.2e–f). This time-mean flow along the 350-K waveguide makes it increasingly difficult for perturbations along the waveguide to become significant and grow non-linearly to the point of RWB occurrence (Holton 2004). Since PVS occurrence requires upstream RWB occurrence, the increasing mean jet magnitude may suppress PVS occurrence at 350-K during the latter months of the TC season. Another interpretation of the decreasing PVS occurrence late in the TC season is that PVS occurrence is shifting to lower isentropic surfaces during the winter months in the Northern Hemisphere (Wernli and Sprenger 2007; Martius et al. 2007) as the tropopause decreases in height in correspondence to decreased heating in the cool season. Finally, note that the positively tilted trough in the time-mean 200-hPa streamlines (representing the TUTT) appears to follow the maximum in PVS frequency orientation across the Atlantic basin, becoming more accentuated when PVS frequency increases (July–August, Fig. 3.2b–c) and broader and shifted equatorward later in the TC season (October–November, Fig. 3.2e–f). The association of the positive trough in 200-hPa streamlines with the maxima in PVS frequency provides additional evidence for the link between the TUTT axis and PVS occurrence across the Atlantic basin.

Additional variability is prevalent when looking at the PVS frequency anomaly of individual years relative to the climatological mean from 1 Jun–30 November (Fig. 3.3). For the purposes of brevity, only three years are selected from the larger climatological period: 2013 (Fig. 3.3a–b), 2008 (Fig. 3.3c–d), and 1992 (Fig. 3.3e–f); see Appendix Fig. A1 for all spatial PVS frequency and anomaly plots for 1979–2015. These three years were chosen because they exhibit distinct differences in PVS frequency relative to climatology despite occurring during ENSO-neutral conditions (correlation between PVS activity and ENSO will be discussed in section 3.4). First, 2013 is an example of a year with above normal PVS frequency, where the majority of the Atlantic basin between 80–20^{o}W exhibits positive PVS frequency anomalies up to +20% relative to climatology (Fig. 3.3b). In addition to increased PVS frequency, time-mean, 200-hPa westerly flow is observed across the MDR of the Atlantic basin equatorward of the PVS frequency maximum (Fig. 3.3a). This year is notable because, to date, it is the least active hurricane season observed in the 21st century (ACE = 36 10^4 kt^2). This lack of TC activity occurred despite prediction of above normal activity (ACE >100 10^4 kt^2) by most statistical and dynamical models (Zhang et al. 2016, see Appendix). By contrast, 2008 was an active TC season in the Atlantic basin (ACE = 144 10^4 kt^2), and this season featured anomalously low PVS frequency (-10–15% relative to climatology; Fig. 3.3d). Equatorward of the anomalous reduction in PVS frequency, anticyclonic curving 200-hPa streamlines are observed in the Atlantic basin

MDR, emanating from the west African coastline and the western Caribbean. Finally, 1992 is distinct from the previous two seasons because both positive and negative PVS frequency anomalies are observed equatorward and poleward of the climatological mean, respectively (Fig. 3.3f). This dipole of positive and negative PVS frequency anomalies with latitude is a reflection of an equatorward shift in where PVS activity is occurring relative to climatology. This equatorward shift in PVS frequency also corresponds to an increase in the westerly 200-hPa streamlines in the Atlantic basin MDR (Fig. 3.3e). Consequently, 1992 was a relatively inactive TC season (ACE = 75 10^4 kt^2), which was dominated by TC activity occurring at higher latitudes (>20°N). This brief comparison of TC activity versus PVS frequency for 2013, 2008, and 1992 suggests that a negative relationship may exist. The connections between TC activity and PVS activity are explored in Chapter 5 of this dissertation.

3.2.2 Time series of PVS occurrence and associated attributes

The variability in PVS frequency described in the previous section also extends to the overall climatological period. In total, 21,149 PVS cases[1] (Table 3.1) in the North Atlantic basin were identified from 1 June–30 November over the ERAI climatological period (1979–2015). On average, 571 PVS cases per season occur with the standard deviation of +/- 61 events. This variability can be seen on a year to year basis in Fig. 3.4a where the total number of PVS cases are broken down by month (sorted by color), with their aggregate representing the summed total for each year. Variations in the total number of PVS cases from year to year can be observed (i.e., 1994 to 1995), and these differences may also contrast by month (i.e., increase in June PVSs between 2007 to 2008, despite the decrease in total PVS cases between 2007 to 2008).

---

[1] A PVS "case" is a PV feature identified at a 6-h interval, so these are not 21,149 distinct PVSs

Over the 37-y time series, the ERAI dataset exhibits little to no trend in the number of PVS cases identified each year (Fig. 3.4a; black dotted line; r = -0.04). When averaging the total number of PVS events per month (Fig. 3.4b), both July and August contain the most PVSs (average 125 cases), with the average slowly decreasing during the rest of the season from September–November. These monthly PVS totals match, in general, the seasonal cycle of increasing and decreasing PVS frequency previously discussed in Fig. 3.2 and noted in prior literature (Postel and Hitchman 1999).

Another useful way to sort the total number of PVSs that occur in the ERAI climatology is to sort PVS cases by their intensity, which is calculated as a standardized PV anomaly following the methodology in section 2.4.2 for the area of each PVS. A probability distribution function (PDF) of PVS events sorted by increasing standardized intensity (Fig. 3.5a) shows that their distribution is approximately normal, though some positive skew exists towards higher standardized intensity. The average PVS intensity is 0.85σ, with a standard deviation of +/- 0.62σ. The vast majority of PVS events contain positive standardized intensity, because the PVS climatology only samples the high-PV air (>2-PVU) enclosed within the PVS area, typically characterized as cyclonic troughs with +PV anomalies embedded within. In rare instances (< 10% of all cases), negative standardized PV intensity occurs within a PVSs. To demonstrate how this can occur, Fig. 3.6 shows a PVS example from 1200 UTC 6 September 1998, located near 35°N,25°W, with a negative standardized intensity (average -0.57σ). In this PVS, the area enclosed still contains >2-PVU grid points, but this area is in a location where the climatological PV is higher than the raw PV value, resulting in negative, standardized PV anomalies inside the PVS.

Using the PVS standardized intensity PDF (Fig. 3.5a), PVSs events are sorted into weak (bottom 20th percentile in intensity, blue shading) and strong (top 20th percentile in intensity, red shading) categories. The threshold for the weak PVS category is +0.39σ, and the threshold for the strong PVS category is +1.26σ. These thresholds are first used to show how strong (red), weak (blue), and total PVSs (grey) vary by season (Fig. 3.5b), and later will be used to composite similar events (Chapter 4). In general, years with higher PVSs totals also have more strong PVSs versus weak PVSs, though there are some notable exceptions (i.e., 1994). Moreover, years with similar PVS totals may exhibit large differences in strong versus weak PVS totals (i.e., 2005 versus 2015). This result suggests that seasonal PVS variability should be represented by more than simply the number of cases; it should also include their intensity which has not been investigated in prior PVS climatologies (e.g., Wernli and Sprenger 2007, Zhang et al. 2017).

Figure 3.7a depicts a PDF of PVS cases sorted by their area, which is another PVS attribute that exhibits pronounced year to year variability. The average PVS area is 3.72×10^6 km^2, though there is a large standard deviation (4.22×10^6 km^2) owing to the large variety of sizes. Due to this large range of PVS areas, the x-axis of the area PDF is logarithmic and PVS area is highly positively skewed as small PVSs (~10^6 km^2) occur an order of magnitude more frequently than large PVSs (~10^7 km^2). Thus, the PVS area PDF is most aptly described as a gamma distribution. Due to the highly skewed nature of this distribution, it is also appropriate to sort different categories of PVS area by percentiles (<20%, 20–40%, 40–60%, 60–80%, >80%) in order to infer how PVS area is changing on a yearly basis, noting that the largest PVS quintile (>80%) exhibits a far larger range of PVS areas versus the smallest PVS category (<20%), despite containing the same relative number of cases (Fig. 3.7a). The total number of PVSs in each area category area is plotted from 1979–2015 in Fig. 3.7b from largest to smallest (dark to light shading). Similar to that observed in Fig. 3.5b, years with more PVSs tend to also have an increase in the number of PVS that are in the largest area category (>80%). There are, however, also years that disproportionally have more PVS cases in the largest area category despite having a smaller number of total PVSs (i.e., compare 1994 to 2000 for the >80%). Overall, the 37-y trend in PVS area only exhibits a weak negative correlation (r = -0.14) that only explains 2% of the variance of climatological period using the ERAI (Fig. 3.7b).

Finally, the last attribute explicitly identified with each PVS occurrence in the climatology is its tilt angle. Figure 3.8a depicts the PDF of tilts (x-axis) for all PVSs in the climatology. Note that this distribution has negative skew towards lower tilts with an average of 62.0^{o} and standard deviation of +/- 23.3^{o}. Therefore, PVSs, on average, are tilted more east–west than north–south in the Atlantic basin, though with large case to case variability. Interestingly, a small number of PVS cases (<10%) have a tilt angle exceeding 90^{o}. Figure 3.9 presents an example of a PVS with a tilt angle exceeding 90^{o}. The large tilt angle in this example results from the westernmost portion of the PVS being positioned north of the PVS midpoint, which can occur if the 2-PVU contour is advected by the upstream ridge. The vast majority of PVS tilts identified in this climatology, however, span between 0^{o} to 90^{o}, with these positive tilts consistent with the development of a PVS through AWB along the waveguide upstream. Similar to PVS area, we can sort all PVS tilts into percentile categories from <20% to >80%, spanning the full PDF. Figure 3.8b depicts the breakdown of these tilt percentiles from 1979–2015. As noted previously with intensity and area, some years have proportionally more high tilt categories versus low tilt categories (i.e., see 2002). Interestingly, the 37-y trend shows a moderate negative correlation (r = -0.52) that explains 27% of the variance (Fig. 3.8b), meaning

PVSs are becoming less horizontally tilted over time. However, this decrease in tilt is very small, around 2–3° over the 37-y period (not shown). As will be shown in Chapter 4, the tilt of a PVS event affects the region where environmental variables (i.e., VWS, precipitable water) are modified.

Thus far, the PVS climatology has broken down cases by their number (Fig. 3.4), intensity (Fig. 3.5), area (Fig. 3.7), and tilt (Fig. 3.8). Each of these four PVS attributes is associated with pronounced year to year variability. However, PVS *activity*, in the sense of its impact on the environment of the subtropical Atlantic basin, can be thought of as a combination of the intensity, area, and frequency of all the PVS events that occur in each TC season. Using the attributes that are identified with each PVS case, we can calculate a PVS activity index (PVSI), which integrates the intensity, area, and frequency of PVS events over a given time period. PVSI is defined as:

$$PVSI = \iint PV'_{std} dAdt \tag{3.1}$$

where PV'_{std} represents standardized PV anomalies at each grid point within a PVS. The standardized PV anomalies are then integrated over the total area of each PVS, which is then integrated over the number of PVSs that occur in a specified time span (including PVSs that have net negative standardized PV anomalies). Figure 3.10a presents the PVSI defined from 1 June–30 November for each TC season from 1979–2015. To compare to the PVSI, the number of PVS events (Fig. 3.10b), the average PVS intensity (Fig. 3.10c), and the average PVS area (Fig. 3.10d) are also depicted for each TC season. Predictably, years that exhibit high PVSI (i.e., 1984) typically feature high PVS frequency, intensity, and area. Because, however, these PVS attributes are not always positively correlated to one another, the PVSI is a better measure of net activity, because it incorporates information about the intensity and area of PVSs identified during the TC season. For example, 1994 features the most PVSs identified in the 1979–2015 ERAI climatology, yet the PVSI for this season is only the 13th highest out of the 37-y period, owing to the average intensity and area of PVSs that season running near the climatological mean. In contrast, 2015 featured only the 19th most PVSs identified in the climatology, but the PVSI for the season was the 6th highest, due to the average intensity and area of PVSs occurring in 2015 being much higher than the climatological mean.

The PVSI can also be defined for shorter timespans to assess how PVS activity varies on intraseasonal timescales between the start and end of the TC season. This shorter timespan PVS activity index is of potential interest because PVS frequency varies considerably during the season (Fig. 3.2). Figure 3.11 depicts the PVSI based off a 30-day running sum, centered on the median date of the 30-day period used. Defined this way, PVSI peaks in mid-July (13 July, 16.5×10^4 σ; thick black line, Fig. 3.11), consistent with the highest spatial frequency of PVSs (Fig. 3.2b), and slowly decreases in magnitude over the rest of the TC season, also consistent with the drop off in PVS frequency in the latter half of the TC season (Fig. 3.2d–f). The highest PVSI in July also corresponds to the largest variance in PVSI, with the -/+1 standard deviation over the 37-y climatology ranging from 9.1×10^4 σ to 23.8×10^4 σ (gray shading, Fig. 3.11). Correlating the peak climatological date in PVSI with other dates during the TC season also reveals a moderate positive correlation with PVSI over the remainder of the TC season (+0.3 to +0.6, blue line, Fig. 3.11). This demonstrates that TC seasons that have high PVSI in July are more likely to experience higher PVSI in subsequent months of the TC season. The possible reasons for this positive correlation are explored later in Chapter 5.

The use of PVSI on seasonal or intraseasonal timescales is a novel technique that combines PVS attributes (frequency, intensity, and area) that are perceived to be important in how PVSs affect their local environment. The following chapter will explore how composite differences in PVS intensity, area, and orientation modulate the environment of the subtropical Atlantic basin (Chapter 4).

3.3. Comparison of PVS climatologies between ERAI and CFSR

This section explores the differences between the ERAI and CFSR PVS climatologies, comparing differences in PVS spatial frequency, count, intensity, and overall activity. At the end of this section, a possible explanation will be presented for why significant differences exist between these two datasets.

A spatial climatology of the PVS frequency using the CFSR dataset is illustrated in Fig. 3.12a (similar to Fig. 3.1). The frequency maximum of PVS activity from 1 June–30 November is 32% at 28°N, 47.5°W, which is close to the same location of the ERAI maximum, but with a 6% increase in frequency. In general, the spatial pattern of PVS activity is similar to the ERAI, with the maximum oriented from southwest to northeast across the NATL basin, which matches the trough axis of time-mean 200-hPa streamlines. The difference between the CFSR PVS climatological frequency and the ERAI PVS climatological frequency (Fig. 3.12b) reveals that the CFSR has basin wide increases relative to the ERAI, especially along the lesser Antilles at 20°N where differences exceed 10%. This positive PVS frequency relative to the ERAI decreases with latitude, with little to no change in PVS frequency poleward of 35°N. One explanation for this increase in PVS frequency equatorward of 35°N is that there are simply more PVS cases being identified in the CFSR (N = 25,673; see Table 3.1). The increase in CFSR PVS climatological frequency, however, mainly equatorward of the ERAI maximum suggests additional differences between the datasets exist.

Figure 3.13 compares a large PVS identified in both the CFSR (Fig. 3.13a) and ERAI (Fig. 3.13b) at 0000 UTC 16 September 1984. At an initial glance, the PVS identified in both the CFSR and ERAI looks similar. The southern extent of the PVS in the CFSR, however, extends equatorward of the ERAI. This greater equatorward extent results in the PVS in the CFSR possessing a larger area (9.3×10^6 km^2) compared to the ERAI (8.1×10^6 km^2). In addition, despite both datasets being coarsened to 2.5^o prior to PVS identification (as discussed in section 2.4), the CFSR 350-K PV field is noisier in comparison to the ERAI 350-K PV field. The noisier CFSR PV field results in more folds of the 2-PVU contour, which inflates the length of the CFSR PVS perimeter (13,270 km) relative to the ERAI (10,454 km), despite the widths closing the poleward end of the PVS in both datasets being similar (CFSR: 2142 km, ERAI: 2137 km). This increase in the CFSR perimeter cannot be solely attributed to the increase in the PVS area, since the CFSR PVS perimeter increases by 27% relative to the ERAI, but the PVS area only increases by 15% relative to the ERAI.

The PVS case in Fig. 3.13 is representative of the differences between PVSs in the CFSR and ERAI in the overall climatology, as seen in Table 3.1. Overall, the average perimeter for ERAI PVSs is 9000 km, while the average perimeter for CFSR PVSs is 10,150 km (+12.7%). Similarly, the average area of ERAI PVSs is 3.72×10^6 km^2, while the average area for CFSR PVSs is 4.05×10^6 km^2 (+8.9%). The increase in area for CFSR PVSs, primarily on their equatorward flank, as illustrated in Fig. 3.13a, supports the finding in Fig. 3.12b of basin wide increases in PVS frequency equatorward of 30^{o}N. The increase in perimeter for CFSR PVSs also partially explains why there are many more PVS cases identified in the CFSR dataset (Table 3.1), since larger perimeters, without a substantial increase in width (Table 3.1), enable more

PVS candidates to pass the distance criteria imposed in section 2.4.1 to identify PVSs that possess large aspect ratios.

Figure 3.14 also illustrates differences between the CFSR and ERAI in the frequency between weak, strong, and all PVS events. Similar to Fig. 3.5b, CFSR PVS cases are broken down seasonally from 1979–2015, with strong and weak PVSs in the top and bottom 20th percentile of intensity plotted (Fig. 3.14a). Unlike the ERAI distribution, there is a distinct and statistically significant long-term trend towards decreasing PVS frequency overall in the CFSR (r = -0.48, black dotted line; Fig. 3.14a). Even more striking is the change in number of strong and weak PVS cases from the beginning to end of the CFSR climatology, where there is a pronounced decrease in strong PVS cases (Fig. 3.14a; red dotted line, r = -0.71), but an equally pronounced increase in weak PVS cases (Fig. 3.14a; blue dotted line, r = +0.68). These trends in strong and weak PVSs stand out in comparison to the ERAI (Fig. 3.14b), with the CFSR having more strong PVSs especially early in the climatology (1979–1986), but fewer strong PVSs later in the climatology (2005–2015). The opposite is true for weak PVSs in the CFSR relative to the ERAI, with a decrease in weak PVSs early in the climatology, but a large increase later in the climatology. Note, however, that the CFSR still has more PVSs overall each season versus the ERAI (average of +122 cases each season), but the difference between overall PVS counts between the CFSR and ERAI have decreased markedly between 1979 to 2015. All of these results suggest that the CFSR PVS dataset has large long-term changes in PVS counts and intensity, which are in sharp contrast to the relatively stable long-term trend exhibited by the ERAI climatology.

As was performed for the ERAI, we can combine the number, area, and intensity of PVSs in the CFSR to create a seasonal PVSI (equation 3.1). A comparison of the CFSR and ERAI

PVSI is provided in Fig. 3.15. Interannualy, the PVSI between the CFSR and ERAI exhibits a moderate positive correlation (r = +0.62) with similar year to year changes in PVSI (Fig. 3.15, solid lines). The CFSR climatology, however, exhibits a pronounced long-term decreasing trend in seasonal PVSI (blue dashed line, r = -0.67) that explains 45% of the variance in the PVSI. This trend is vastly different to the ERAI PVSI which has very little long-term trend despite the large year-to-year oscillations (red dashed line, r = -0.02). This result is not surprising when you compare the PVSI to the large long-term shifts in strong and weak PVSs per season that were exhibited in Fig. 3.14. Note that the differences between the CFSR and ERAI are most notable early in the climatological period (1979–1986), with a sharp decrease in PVSI in the CFSR occurring in 1987 (Fig. 3.14, Fig. 3.15).

One possible explanation for the large shifts in PVS activity in the CFSR climatology could be associated with changes in temperature anomaly in the upper-troposphere (300–100-hPa) and the stratosphere (100–1-hPa) from 1979–2015. Even subtle changes in temperature in the upper-troposphere and lower-stratosphere are important for the computation of PV, since the vertical gradient of potential temperature increases rapidly beginning in the lower stratosphere where temperatures stop cooling with height. The intensity of PVSs identified in the CFSR and ERAI climatologies rely on PV calculated from grid points in the PVS area, which is in the lower stratosphere above the dynamic tropopause (> 2-PVU). Figure 3.16a depicts a time–pressure plot of global CFSR temperature anomaly from 1979–2010. Between 1986 to 1987, there is a sharp change in the stratospheric temperature anomalies, from primarily positive (> +2^{o}C) to negative (< -2^{o}C). As discussed in Saha et al. (2010), this sharp temperature change occurs at a juncture between two streams, or separate run periods, conducted to put together the CFSR (black line, Fig. 3.16a). In total, six separate streams were performed in order to complete the reanalysis from 1979–2015. Unfortunately, each stream intersection appears to correspond to a sharp change in stratospheric temperature anomalies. This temperature change is attributed to bias correcting the observations from the Stratospheric Sounder Units (SSUs) onboard polar orbiting satellites resulting in a feedback that gradually warmed the upper stratosphere by 10°C over time (Saha et al. 2010). The sharp change from positive to negative temperature anomalies reflects when the biases are reset with the new CFSR model stream (Saha et al 2010).

In comparison, the ERAI was only run in two separate streams (1979–1988 and 1989–current) and uses a more sophisticated 12-h, 4D-Var analysis scheme to assimilate observations (Dee et al. 2011, Simmons et al. 2014). In particular, Simmons et al. (2014) preformed a systematic study of low-frequency temperature variability in the ERAI, concluding that that temperature observations in the upper-troposphere and lower-stratosphere benefited from stable radiance bias correction from SSU and Microwave Sounding Unit (MSU) observations. Even at the location where the two ERAI streams intersect in 1989, there is little discernable discontinuity in temperature anomalies in the upper troposphere or lower stratosphere (Simmons et al. 2014; see their Fig. 7). The lack of temperature anomaly discontinuity is due to the fact that little discontinuity also exists between bias correction of SSU and MSU observations (Simmons et al. 2014; See their Fig. 14).

These ERAI SSU and MSU corrections contrast markedly from the CFSR's bias correction of MSU channel 4 observations (Fig. 3.16b), which exhibit pronounced discontinuities, especially between streams in 1986. MSU channel 4 is particularly sensitive to temperatures in the 200–50-hPa range (Grody et al. 2004), meaning bias correction from these observations could significantly impact isentropic PV values that intersect these pressure levels. As noted in Saha et al. (2010), the discontinuity observed in MSU channel 4 in 1986 is due to a new recalibration algorithm that was only applied after 1986 starting with the National Oceanic and Atmospheric Administration (NOAA) 10 polar orbiter satellite (n10 on the Fig. 3.16b legend). This bias discontinuity likely contributes to the temperature anomaly discontinuity exhibited between 1986–1987 (Fig. 3.16). This CFSR discontinuity is troubling, because this also marks a period where the number of strong PVSs observed dropped sharply in the Atlantic basin from 1986–1987, causing a sharp drop in the PVS activity index (Figs. 3.14, 3.15). While likely not the only contributor to inflated PVS intensity, the positive temperature anomalies exhibited mainly in the stratosphere from 1979–1986 in the CFSR may have contributed to sharper vertical potential temperature gradients that would inflate the raw PV value for that extensive period. This inference is anecdotally confirmed by observing the PV embedded in the PVS identified at 0000 UTC 16 September 1984 (Fig. 3.13), noting the CFSR PV is notably higher in magnitude compared to the ERAI within the PVS area. This systematic higher-magnitude PV in turn affects the long term 1979–2015 CFSR climatological mean PV which is significantly higher in the Atlantic basin in the summer versus the ERAI climatological mean (not shown). The prevalence of weak PV streamers in the latter portion of the CFSR period (2005–2015) and the reduction of the PVS activity index could, therefore, be due to inflated CFSR climatological PV influenced by the 1979–1986 stratospheric warm bias period.

Due to the above concerns with the CFSR, this study will choose to only investigate the ERAI PVS climatology for the rest of the dissertation, given its more reliable temperature record in the stratosphere (Simmons et al. 2014) that exhibits fewer discontinuities and biases that may artificially impact PVS counts and intensities.

3.4. Comparison of PVS activity to atmospheric indices

3.4.1 ENSO

Figure 3.17 presents a subset of years of the 1979–2015 PVS climatology that exhibit El Nino conditions (i.e., June–November Nino 3.4 SST anomalies > 0.5^{o}C) and La Nina conditions (i.e., June-November Nino 3.4 SST anomalies < -0.5^{o}C), using the Ocean Nino Index (ONI) developed by, and available from, the NOAA Climate Prediction Center (CPC) (http://origin.cpc.ncep.noaa.gov/products/analysis_monitoring/ensostuff/detrend.nino34.ascii.txt) . In general, El Nino conditions are associated with an increase in overall PVS frequency relative to climatology across the Atlantic basin, primarily equatorward of 30^{o}N (Fig. 3.17a). This positive anomaly is greatest (maximum +4%) just poleward of the lesser Antilles around 25^{o}N, 65^{o}W. Note that there is also a weak, negative PVS frequency anomaly (minimum -2%) near the Azores. In contrast, La Nina conditions are associated with a near basin wide reduction in PVS frequency relative to climatology, with the maximum negative anomaly (-6%) also located just poleward of the lesser Antilles. One possible explanation for this inverse relationship in PVS frequency relative to ENSO phase may be related to changes in vertical motion induced by the Walker circulation (Bjerknes 1966; Lau and Yang 2002). During El Nino years, enhanced SSTSs in the eastern Pacific enhance convective activity, shifting the ascending branch of the Walker circulation in the eastern Pacific. This movement, in turn, shifts the descending branch of the Walker circulation over the western Atlantic basin, where anomalous upper-tropospheric subsidence can both warm the lower stratosphere and suppressive convective activity. These changes, in theory, could promote more PVS activity, where a warmer lower stratosphere may tighten the vertical potential temperature gradient, boosting PV region-wide; additionally, a suppression of deep convection prevents the erosion of high-PV air that would weaken PVSs at lower latitudes. El Nino is also associated with enhanced convective activity over the eastern Pacific, which may act to perturb the downstream waveguide and encourage AWB downstream in the NATL basin. In La Nina years, an eastward shift in the walker circulation may promote more convection in the NATL, associated with the anomalous ascent and cooler lower-stratospheric temperatures, possibly inhibiting lower latitude PVS occurrence. When comparing Nino region 3.4 SST anomalies versus PVSI on a scatter plot (Fig. 3.18), a weak positive correlation ($r = +0.39$) is revealed. Note, however, that the three highest PVS activity index years occur in ENSO neutral conditions (SST anomalies between -0.5°C to +0.5°C), suggesting that ENSO is not the only governing factor that influences overall PVS activity.

3.4.2 NATL MDR SSTs

Another factor proposed to influence PVS activity in the Atlantic basin is changes in yearly SST anomalies in the Atlantic basin MDR, because SST changes modulate convective activity that can erode the southern extent of low-latitude PVSs. For this investigation, the composite PVS frequency anomaly for the lowest eight SST anomalies and highest eight SST anomalies years (corresponding to the bottom and top 20th percentiles) in the NATL basin MDR are plotted in Fig. 3.19, using SST anomaly data from Kaplan et al. (1998) extended to 2015, where the MDR is defined between 10–20°N and 20–80°W (see Fig. 3.3), a location where TC development is common in the Atlantic basin (e.g., Gray 1968; Zhang et al. 2017). In low SST anomaly years, there is a notable increase in PVS frequency relative to climatology with the greatest anomalies (+4–6%) observed along the equatorward flank of the climatological PVS frequency maximum around 25°N in the Atlantic basin (Fig. 3.19a). The inverse is true for high SST anomaly years, where a -4–6% anomaly relative to climatology is present in roughly the same location in the Atlantic basin (Fig. 3.19b). A possible explanation for this inverse relationship in SST anomaly relative to PVS frequency could be related to the presumption that higher MDR SST anomalies in the Atlantic basin would promote more deep, moist, convection between 10–20°N. The outflow from this convection could, therefore, impinge on PVS activity occurring poleward, and act to destroy upper-tropospheric positive PV anomalies. The opposite would be true for low SST anomaly years, where implied suppressed convective activity may allow PVSs with higher-PV air to penetrate equatorward in the Atlantic basin. When comparing MDR SST anomalies to PVSI, a moderate negative correlation is observed ($r = -0.43$; Fig. 3.20). A large year-to-year spread exists, however, and two of the three highest PVS activity index years feature MDR SST anomalies that are on the warmer end of the 37-y spectrum. Again, PVSs appear to influenced by more than simply MDR SST variations. One additional SST-based index that is explored in chapter 5 is the AMO, where additional context will be provided since the AMO has also been shown to significantly affect TC activity on low frequency timescales (Klotzbach and Gray 2008).

3.4.3 MJO

The Madden Julian Oscillation (MJO; Madden and Julian 1971) is a well-known intraseasonal oscillation that modulates tropical convective activity around the globe. To determine how it related to PVS frequency in the NATL basin, we use the MJO phase determined from the Wheeler and Hendon (2004) Real-time Multivariate MJO (RMM) Index available from the Center for Australian Weather and Climate Research (http://www.bom.gov.au/climate/mjo/graphics/rmm.74toRealtime.txt). To ensure that we only capture robust MJO events, only dates from 1 June–30 November 1979–2015 that possess an amplitude of 1σ, as defined in Wheeler and Hendon (2004), are considered.

Figure 3.21 depicts PVS frequency anomalies for each phase of the MJO relative to the specific climatology associated with the calendar date in which the MJO phase was observed. Progressing from MJO phase 1 to phase 4 (Fig. 3.21a–d), there is a shift from negative to positive PVS frequency anomalies in the eastern NATL basin, but a shift from positive to negative PVS frequency anomalies in the western NATL basin. In general, the increase in positive PVS frequency anomalies in phases 3 and 4 seems to occur where positive 200-hPa velocity potential anomalies that are also typically observed over the NATL basin in phases 3 and 4 (Ventrice et al. 2013). In contrast, MJO phases 5 through 8 (Fig. 3.21e–h) see a notable increase in PVS frequency in the western Atlantic basin, but a decrease in PVS frequency in the eastern Atlantic basin. One possibility for the increase in PVS frequency in the western Atlantic basin may be due to in part enhanced convection ongoing in the eastern Pacific in MJO phases 7 and 8 (Ventrice et al. 2013). Convective, deep-layer ridge building over the eastern Pacific may be able to perturb the subtropical waveguide, enhancing the probability of AWB occurrence downstream, which may promote higher PVS frequency anomalies in the western Atlantic. This hypothesis is supported by the findings in MacRitchie and Roundy (2016), who found AWB occurred more often in the North Pacific downstream of an active MJO in the Indian Ocean. The largest differences in the spatial PVS frequency anomaly pattern for the MJO appear to occur between phases 3–4 and phases 7–8 (Fig. 3.21d,h) which suggests the MJO does impact PVS frequency between inactive (phases 3–4) versus active (phases 7–8) phases in the western hemisphere, respectively.

3.5. Tables

Table 3.1. General PVS statistics for the ERAI and CFSR climatologies

Variable	ERAI	CFSR (% difference)
Total number of cases	21,149	25,673 (+21.4%)
Average width	1698 km	1781 km (+4.9%)
Average perimeter	9000 km	10,150 km (+12.7%)
Average area	3.72×10^{6} km^{2}	4.05×10^{6} km^{2} (+8.9%)
Average standardized intensity	0.85σ	0.76σ (-10.6%)
Average tilt	62.0°	59.5° (-4.0%)
Average seasonal number of cases	572	694 (+21.3%)
Average seasonal PVS activity index	$61.4\times10^{4}\ \sigma$	$71.3\times10^{4}\ \sigma$ (+16.1%)

3.6. Figures

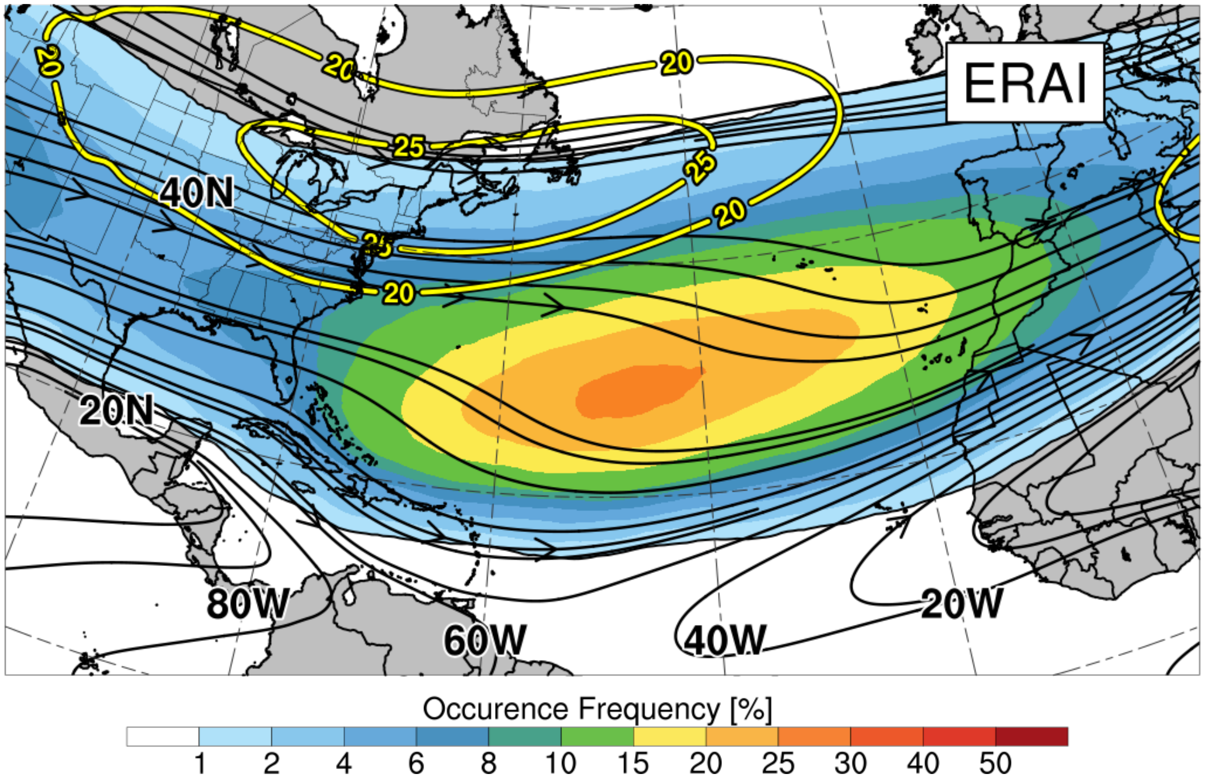

Fig 3.1. Climatological frequency of whether a grid point is embedded within a PVS area (shading, %), 200-hPa wind magnitude (yellow contours, > 20 m s^{-1}) and direction (black streamlines), from 1 June – 30 November.

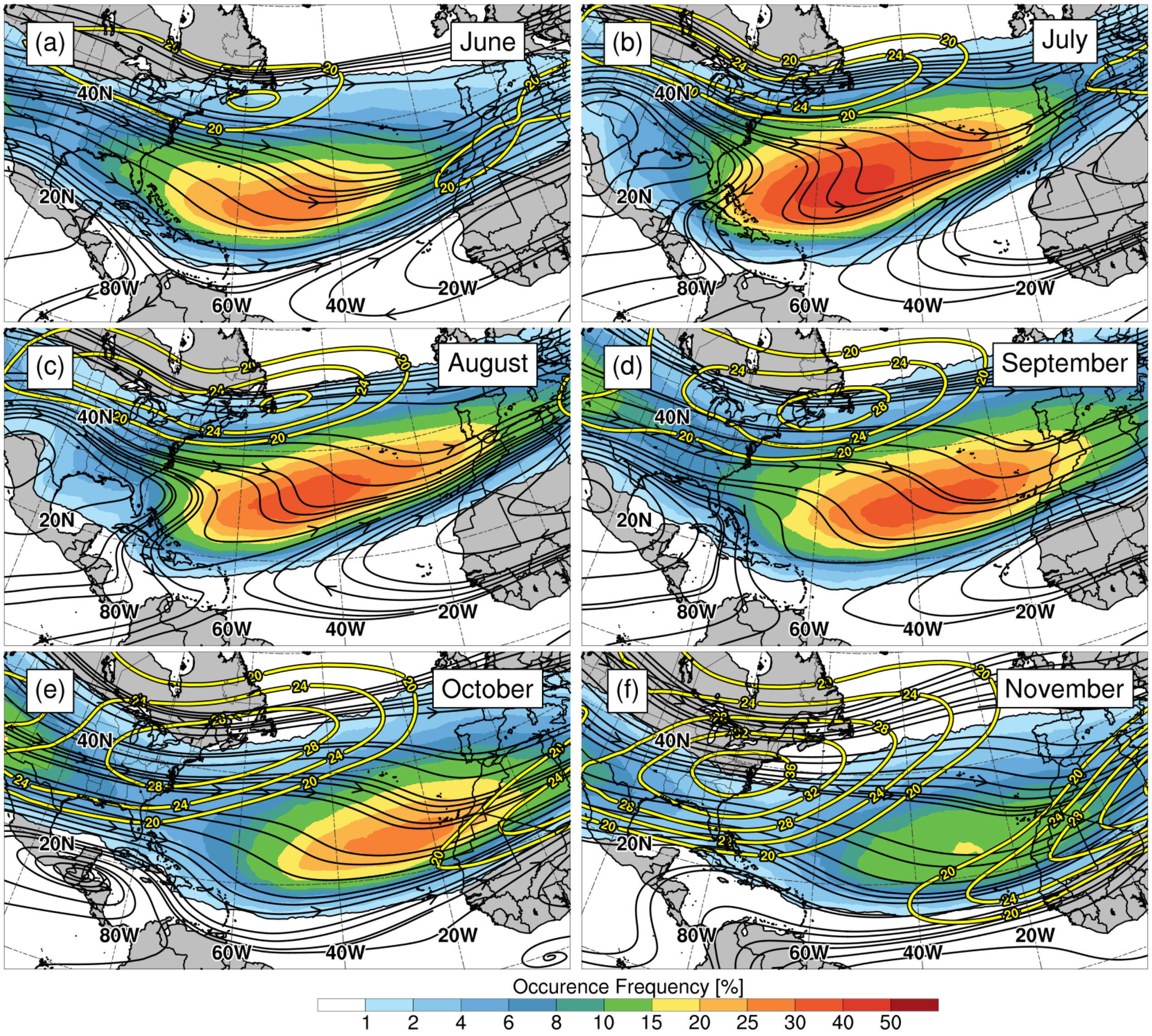

Fig 3.2. As in Fig. 3.1, except divided by month for (a) June, (b), July, (c) August, (d) September, (e) October, and (f) November. Data from the ERAI.

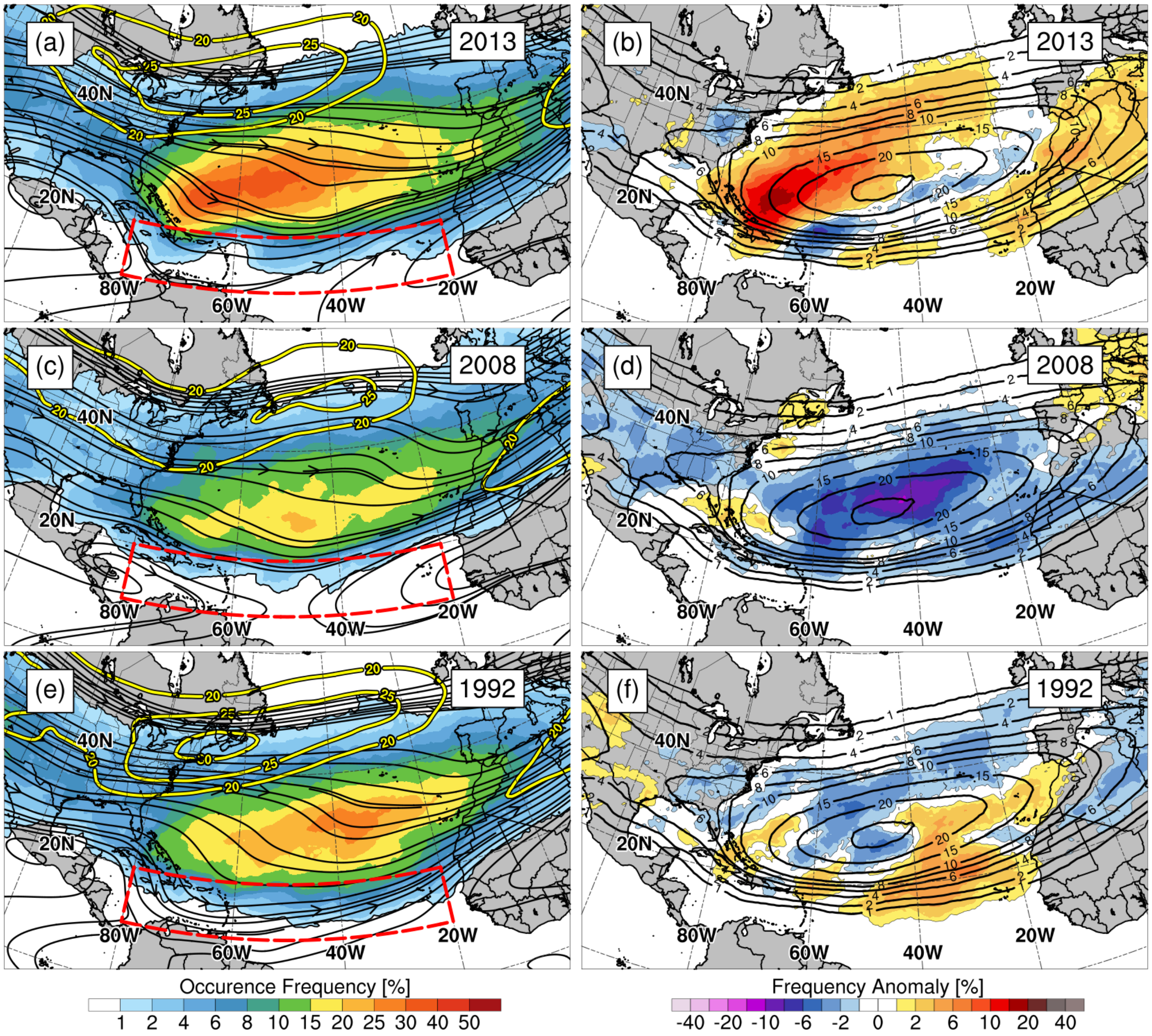

Fig 3.3. (Left) As in Fig. 3.1 except for individual years chosen from the PVS climatology (Right) Yearly PVS frequency anomaly (shading, %) relative to the 1979–2015 climatology (black contours, %). Years selected are 2013 (a–b), 2008 (c–d), and 1992 (e–f). The red dotted line box represents the MDR (10– 20^{o}N, 20–80^{o}W) in (a,c,e). Data from the ERAI.

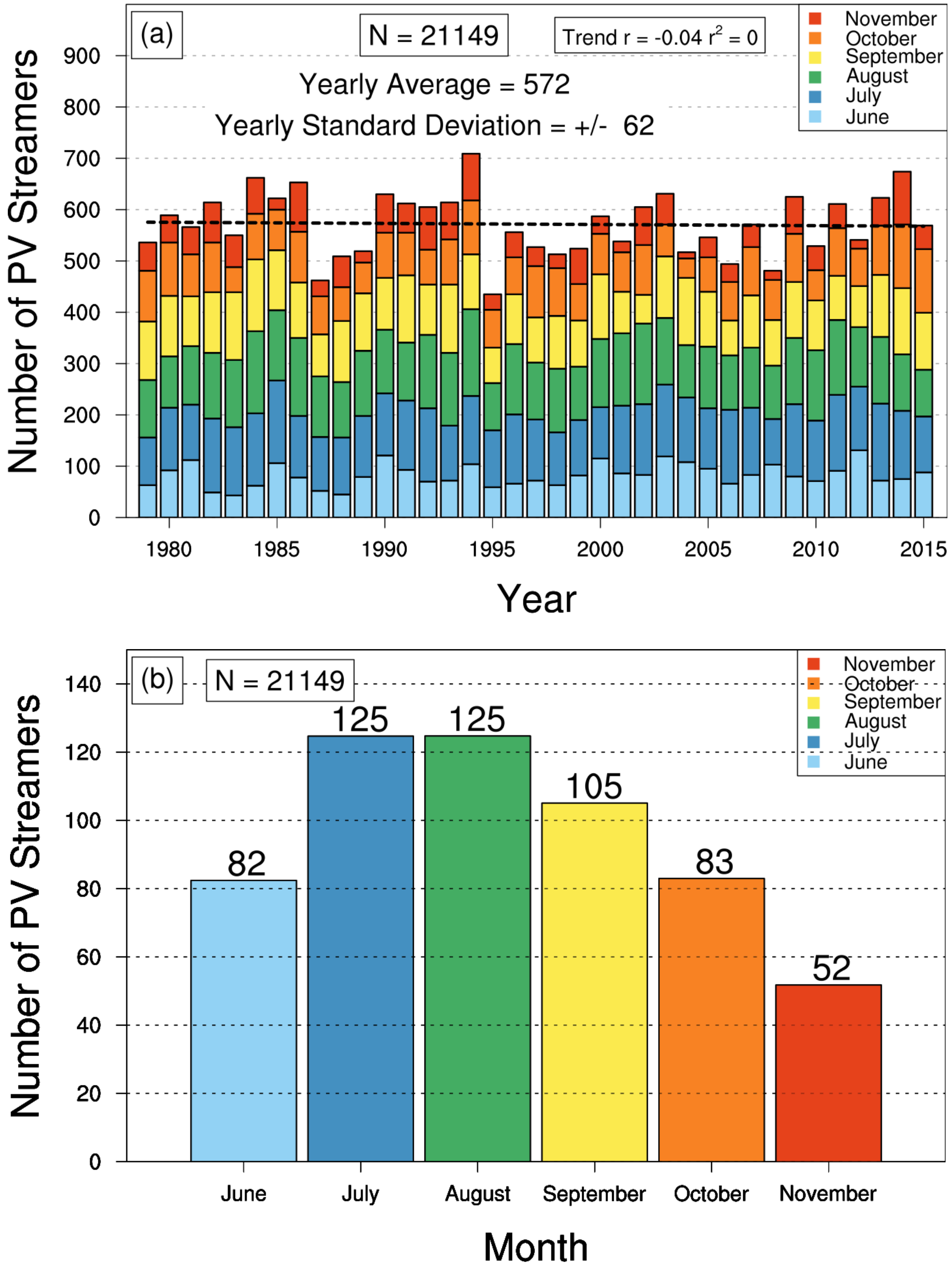

Fig. 3.4. (a) Bar chart of the number of PVSs each year from 1979–2015 (N = 21,149) sorted by month of the TC season (color shading in legend) and 37-y trend (black dotted line). Yearly average, standard deviation, trend line correlation, and r^2 values provided at top of chart. (b) Average number of PVSs that occur each month of the TC season, with numerical value provided at the top of each bar. Data from the ERAI.

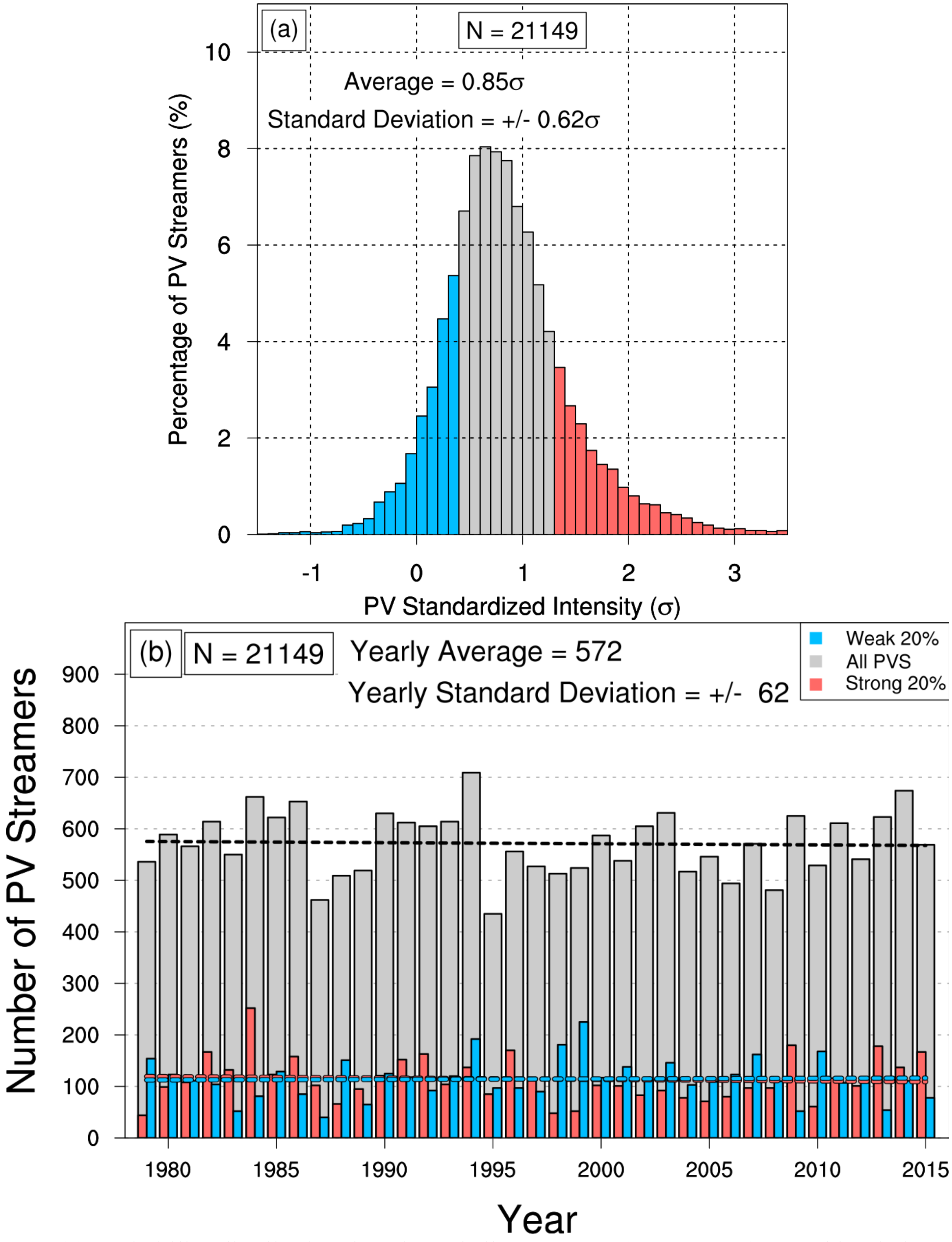

Fig. 3.5. (a) Probability distribution function of all PVS cases (N = 21,149) sorted by their average standardized PV intensity (x-axis, σ) binned every (0.1σ). Percentage is on the y-axis. (b) As in Fig. 3.4a, except the number of strong (top 20% percentile, red) and weak (bottom 20% percentile, blue) PVS depicted inside of the total number of PVSs for a given year. Dotted lines shows the 37-y trend lines for strong, weak and all PVSs events and yearly average and standard deviation for all PVSs provided at top. Data from the ERAI.

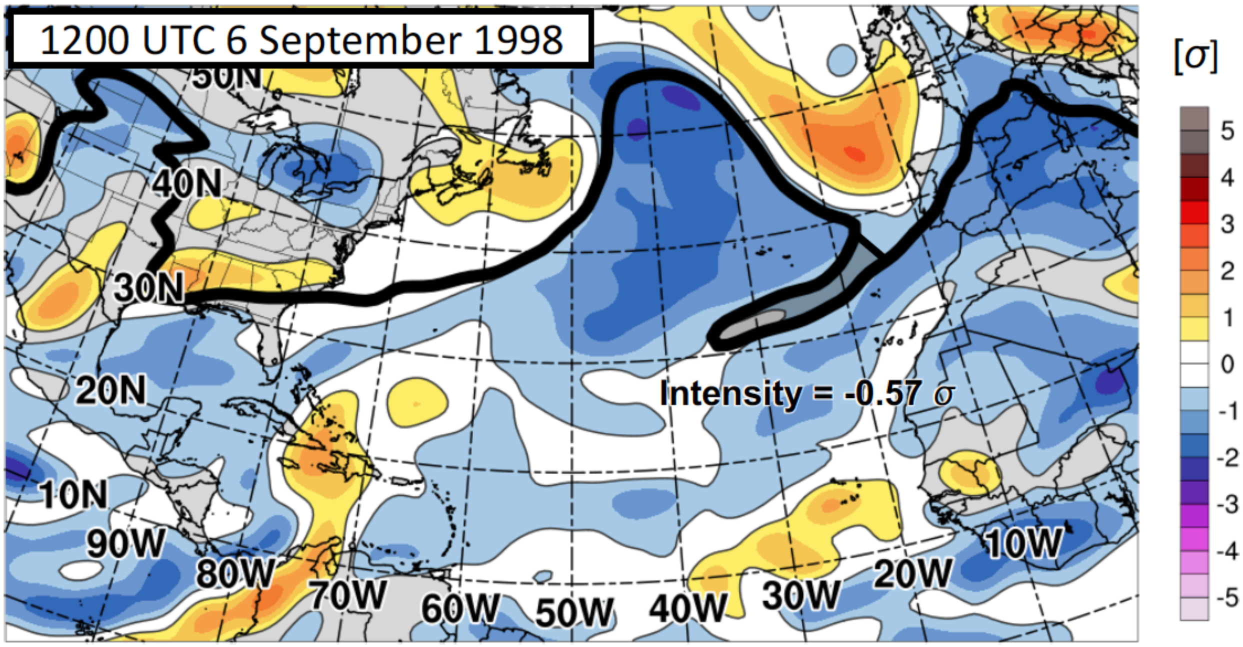

Fig 3.6. Spatial map of a PVS identified on 1200 UTC 6 September 1998 with an average, negative, standardized PV anomaly. Plotted are 350-K standardized PV anomalies (shaded, σ) with the circumpolar 2-PVU contour (black line, 2-PVU). The PVS of interest is located at 32^{o}N,25^{o}W, and the PVS area is lightly shaded in black. Data from the ERAI.

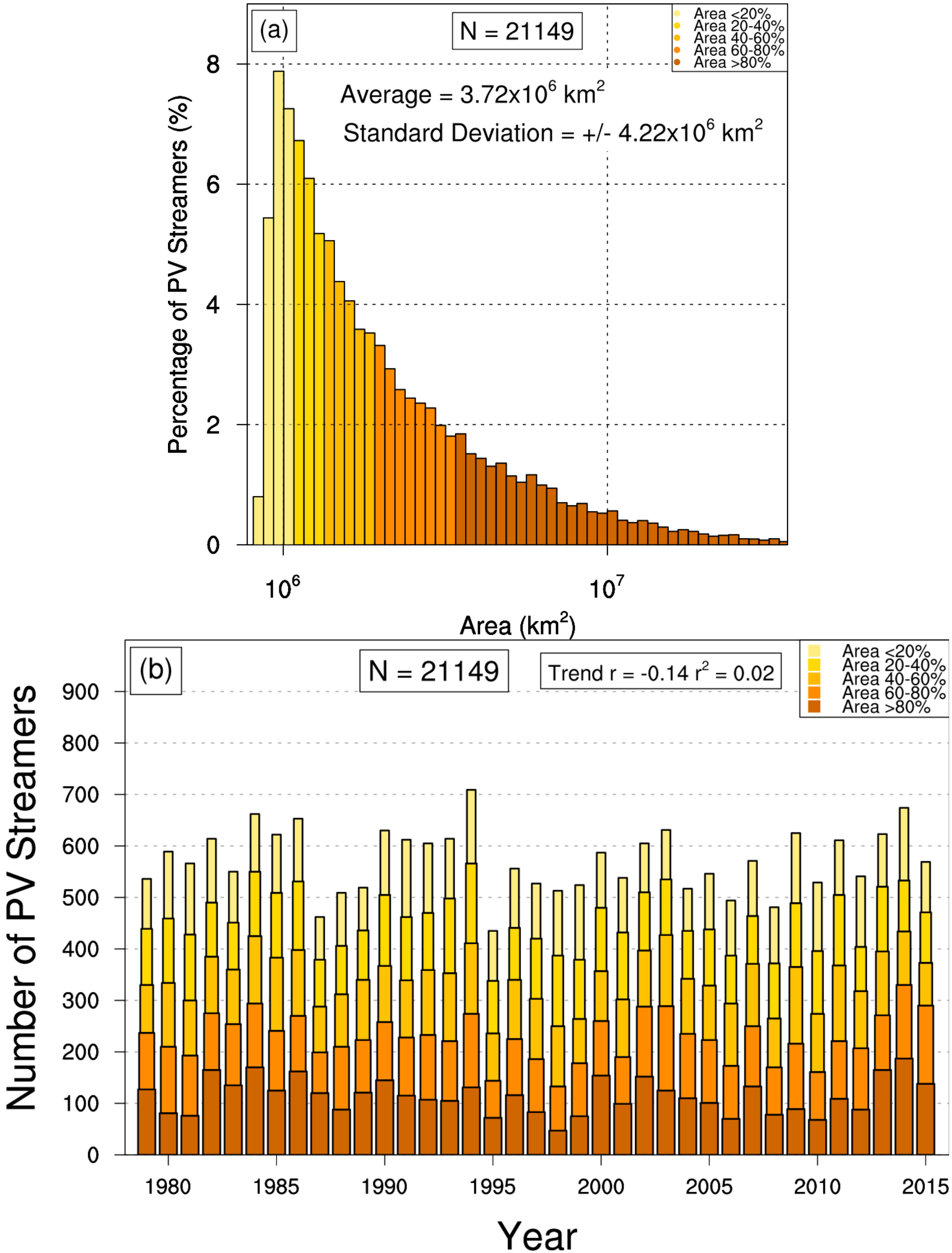

Fig. 3.7. (a) As in Fig. 3.5a., except all PVS cases are sorted by their area (x-axis, km^2) with percentage on the y-axis. (b) As in Fig. 3.5b., except the yearly number of PVSs are sorted by different area percentiles with smaller and light bars indicating smaller area percentiles (see legend at the top right). 37-y PVS area trend line correlation and r^2 provided at top. Data from the ERAI.

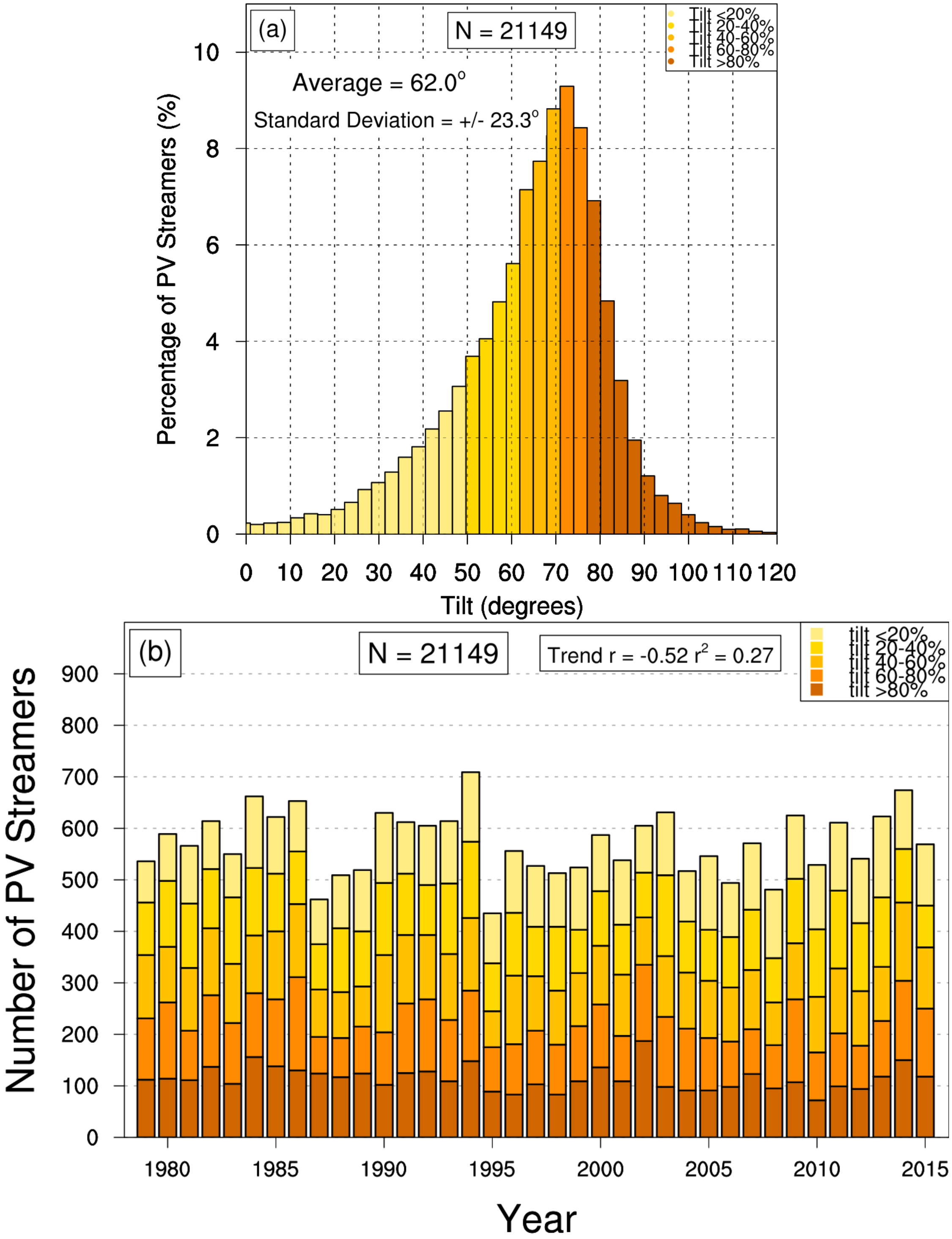

Fig. 3.8. (a) As in Fig. 3.7a., except all PVS cases are sorted by their tilt (x-axis, ^{o}) with percentage on the y-axis. (b) As in Fig. 3.7b., except the yearly number of PVSs are sorted by different tilt percentiles with lighter bars indicating lower tilt percentiles (see legend at the top right). 37-y PVS tilt trend line correlation and r^2 provided at top. Data from the ERAI.

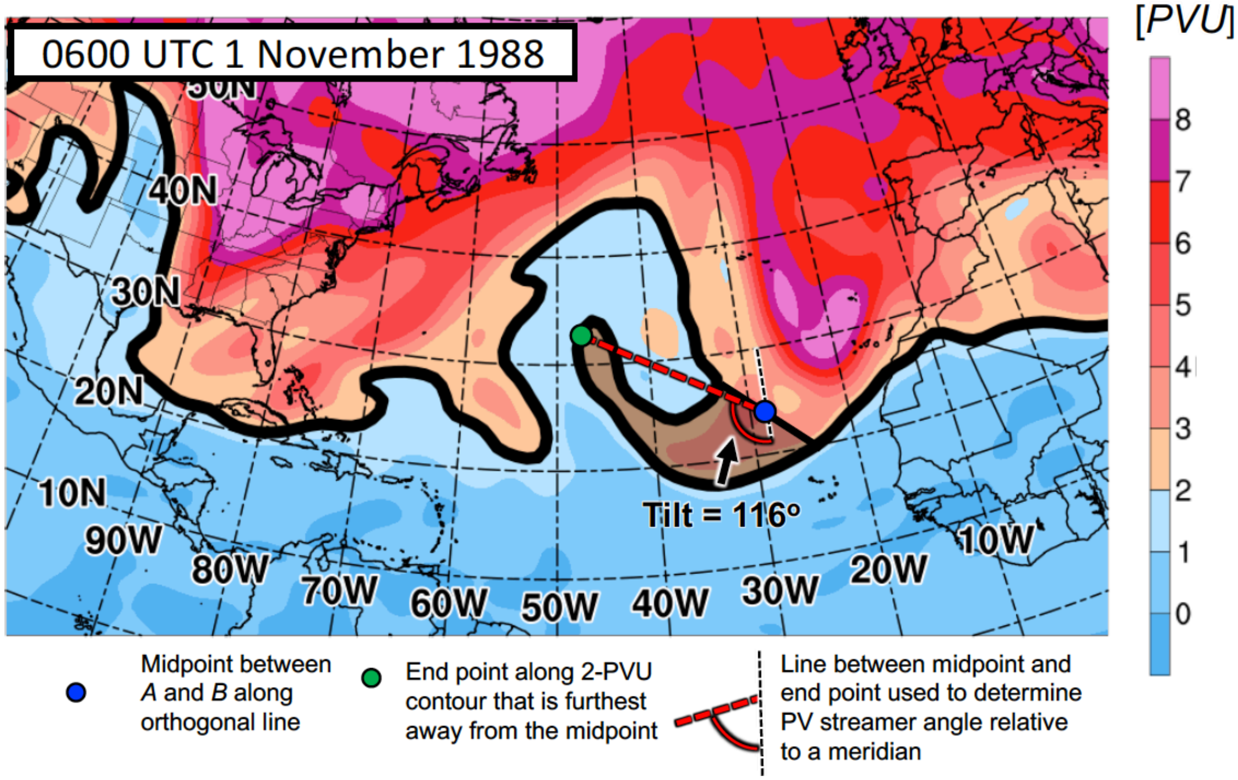

Fig. 3.9. Spatial map of a PVS identified on 0600 UTC 1 November 1988 with a tilt angle > 90°. Plotted is 350-K PV (shaded, PVU) with the circumpolar 2-PVU contour highlighted (black contour, 2-PVU). The PVS of interest in located at 21°N, 34°W and its area is shaded in black. Annotations illustrating how the tilt angle of the PVS is calculated are depicted with a legend below the map. Data from the ERAI.

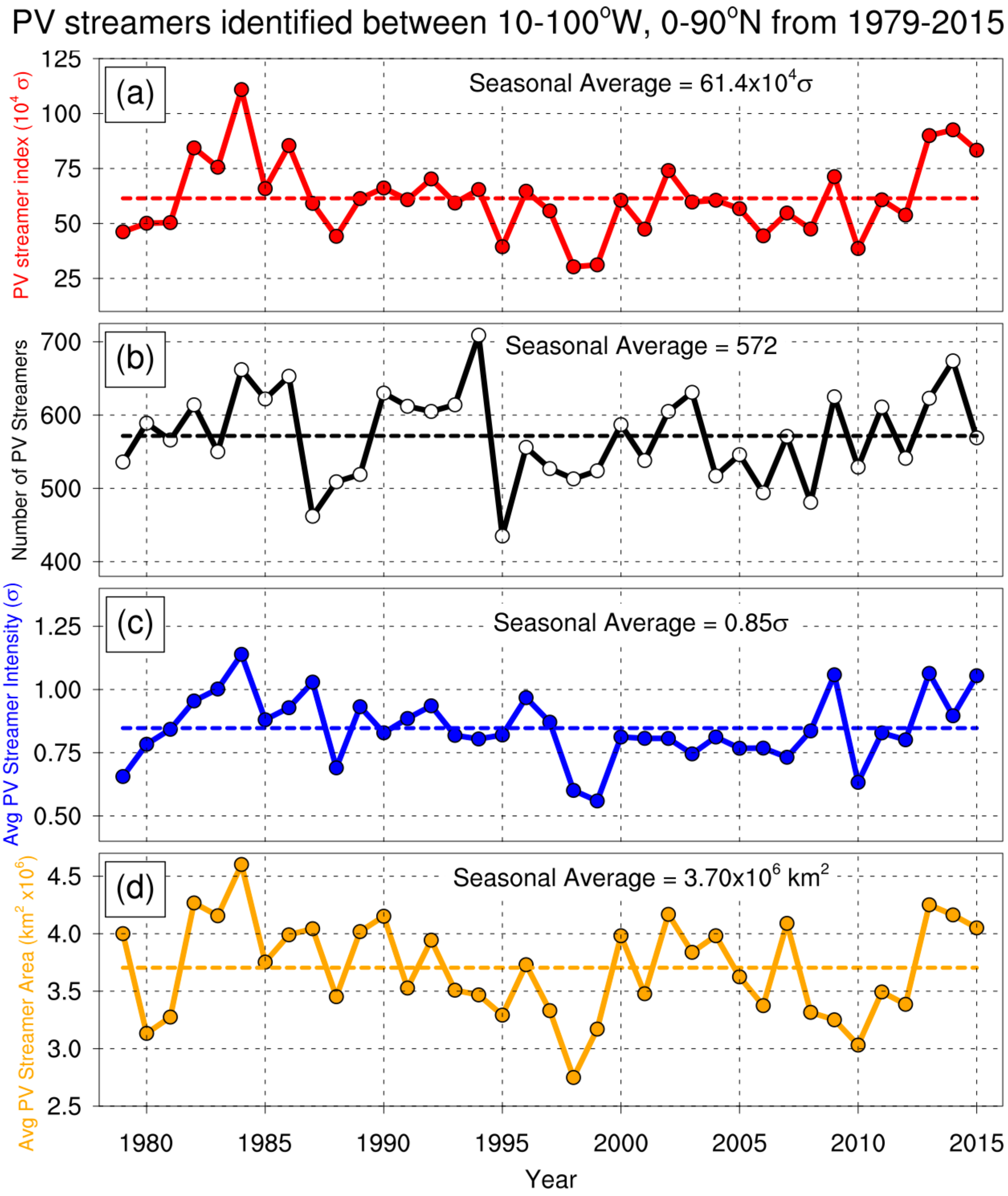

Fig. 3.10. 1979–2015 time series of seasonal PVS attributes including (a) PVS activity index (10^4 σ), (b) total number of PVSs, (c) average intensity (σ), and (d) average area (10^6 km^2). 1979–2015 seasonal averages of each attribute shown by dotted lines, with the numerical value at the top of each plot. Data from the ERAI.

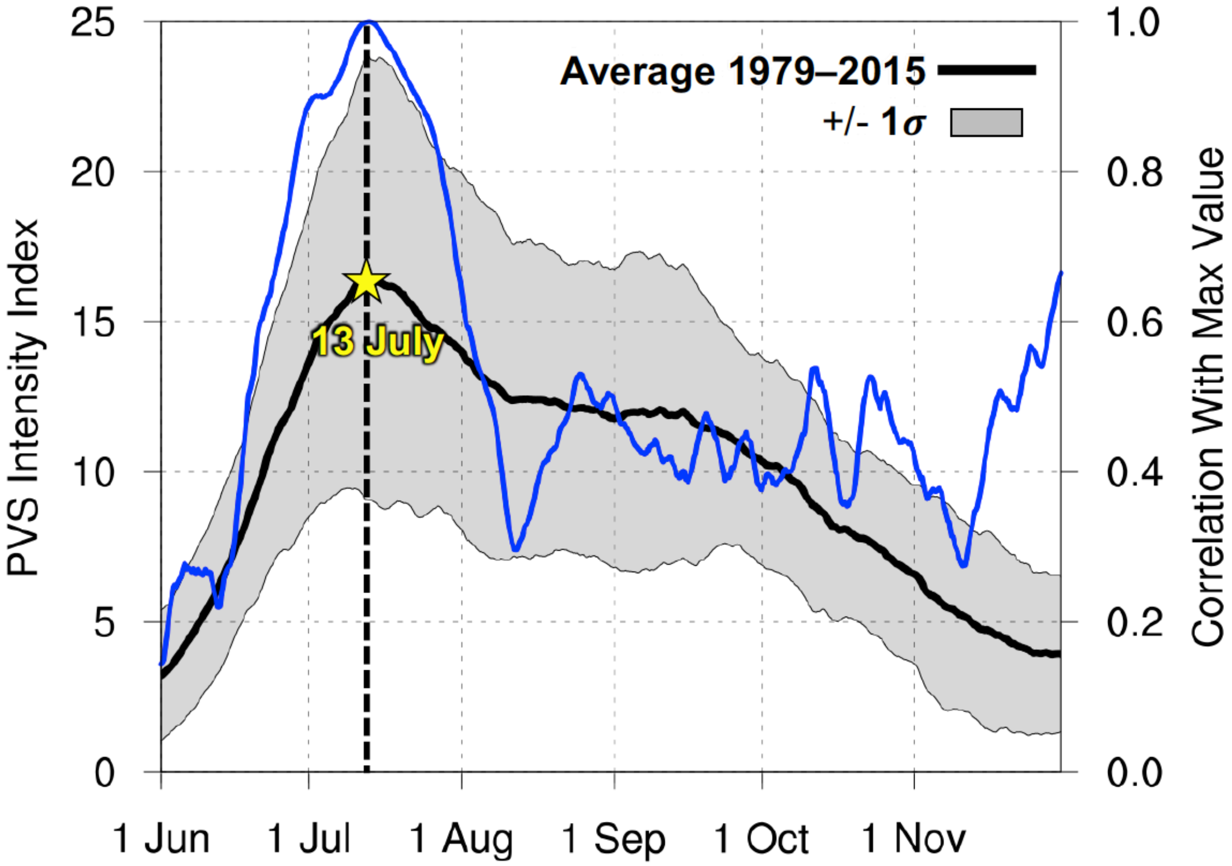

Fig 3.11. 30-day running sum of PVS activity index centered on median date from 1 June–30 November for the 1979–2015 average (black contour, 10^4 σ) and the +/- 1 standard deviation (gray shading, 10^4 σ). The correlation of each date with the maximum average PVS activity on 13 July is also plotted (blue contour). Data from the ERAI.

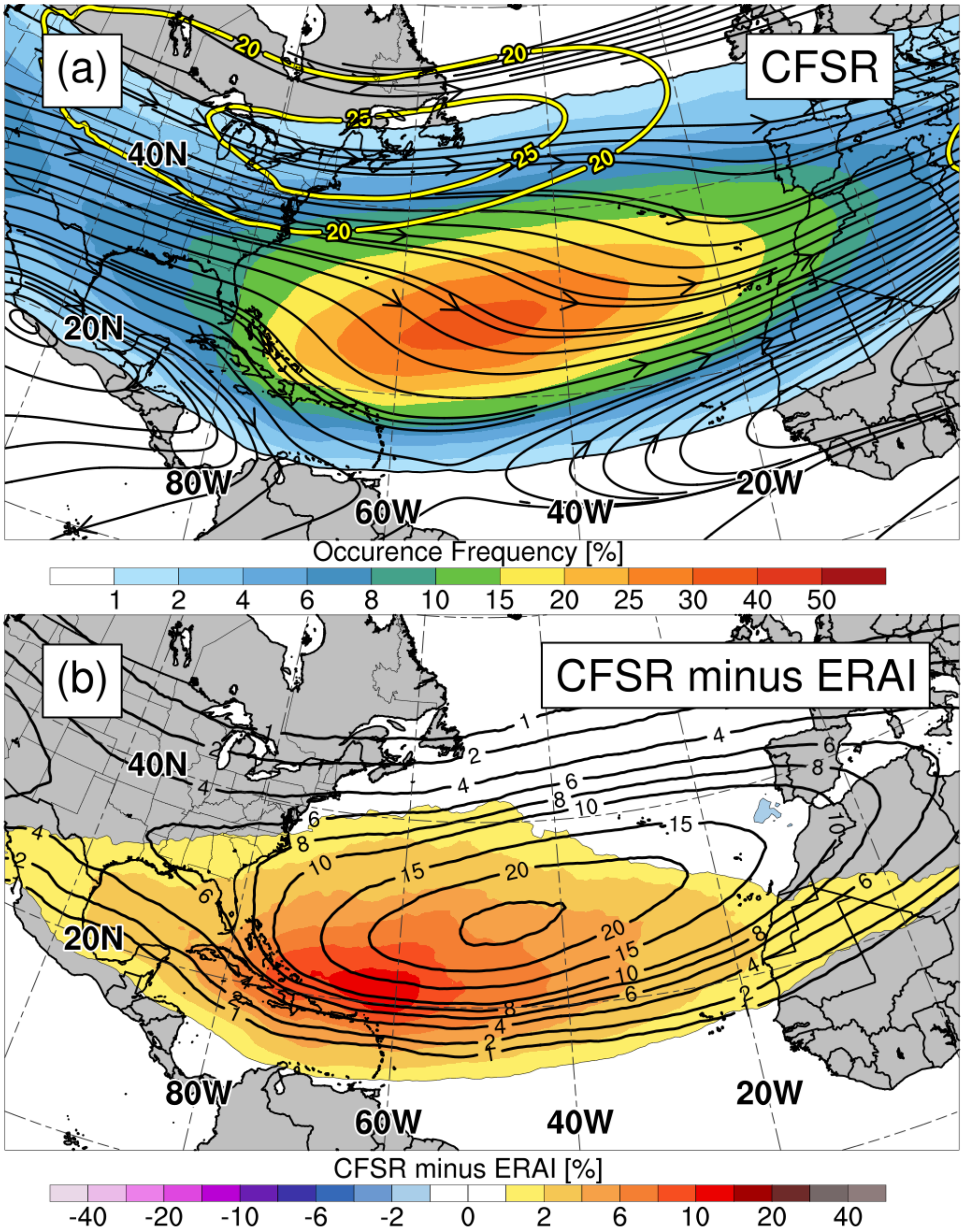

Fig. 3.12. (a) As in Fig. 3.1, except for the CFSR dataset over the same time period. (b) Difference in PVS activity between the CFSR and the ERAI datasets over the same time period (shaded, %) with the ERAI climatology overlaid (black contours, %).

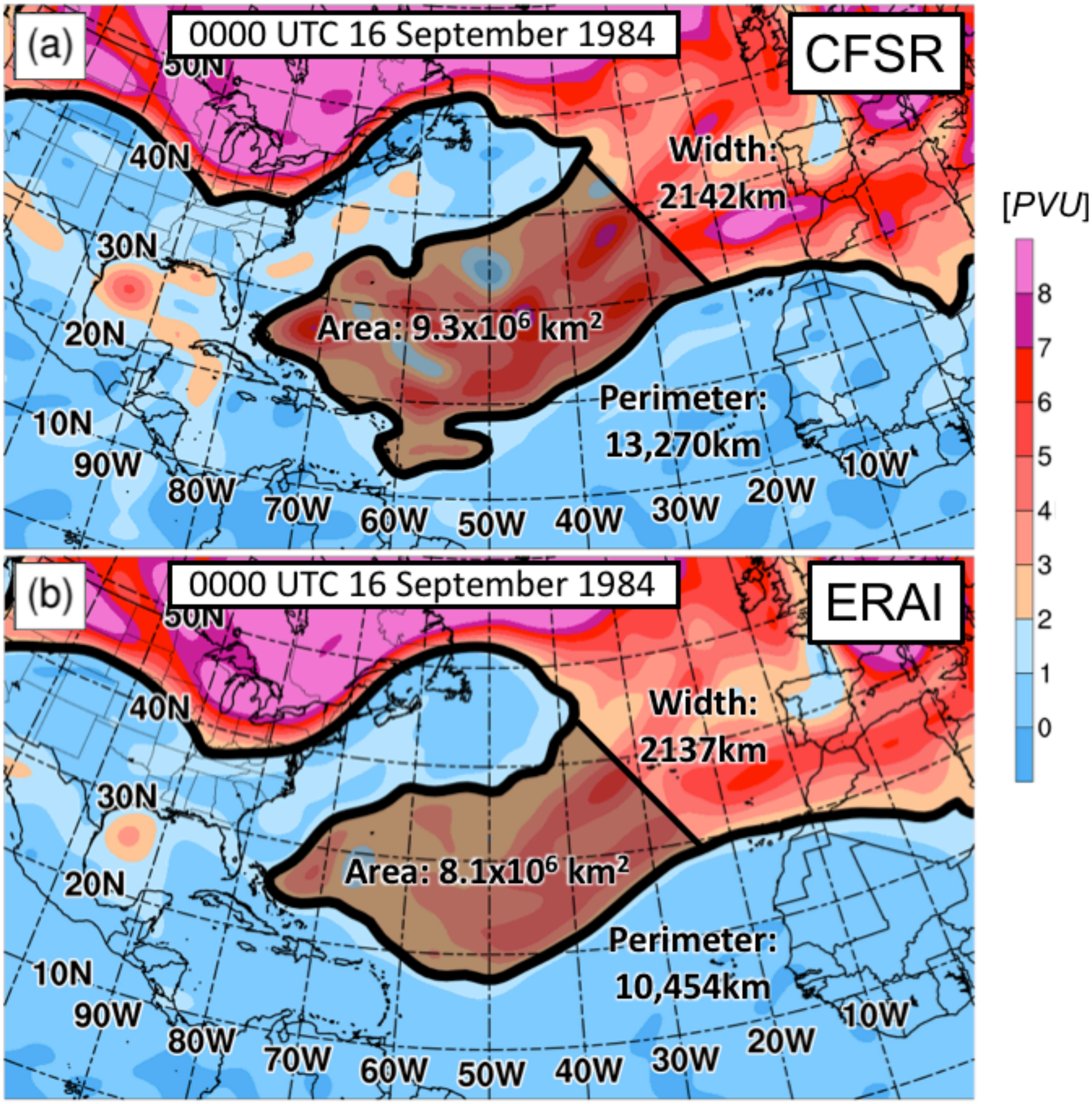

Fig. 3.13. Spatial map of a PVS identified at 0000 UTC 16 September 1984 in both the (a) CFSR and (b) ERAI. Plotted is 350-K PV (shaded, PVU) with the circumpolar 2-PVU contour highlighted (black contour, 2-PVU). The PVS of interest is centered at 30°N, 50°W and its area is shaded in black. Values for the area, perimeter, and width are provided in each panel.

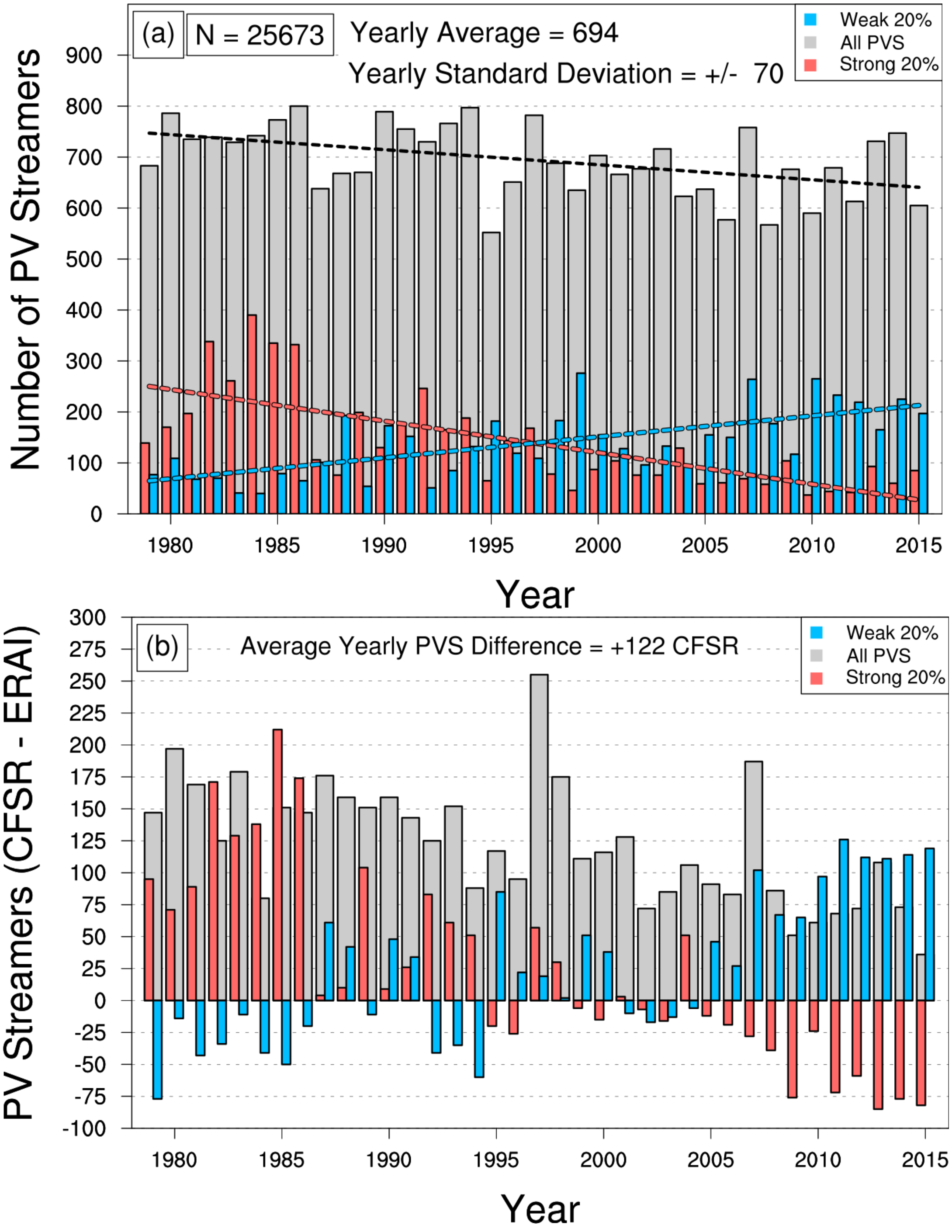

Fig. 3.14. (a) As in Fig. 3.5b, except using the CFSR dataset. Note that the yearly average and standard deviation is provided at the top and dotted lines depict 37-y trend lines for strong, weak and all PVSs events. (b) Time series of differences in strong (red), weak (blue), and total PVS occurrence (gray) between the CFSR minus the ERAI datasets for each TC season. The average yearly difference between the total number of PVS is provided at the top of the plot.

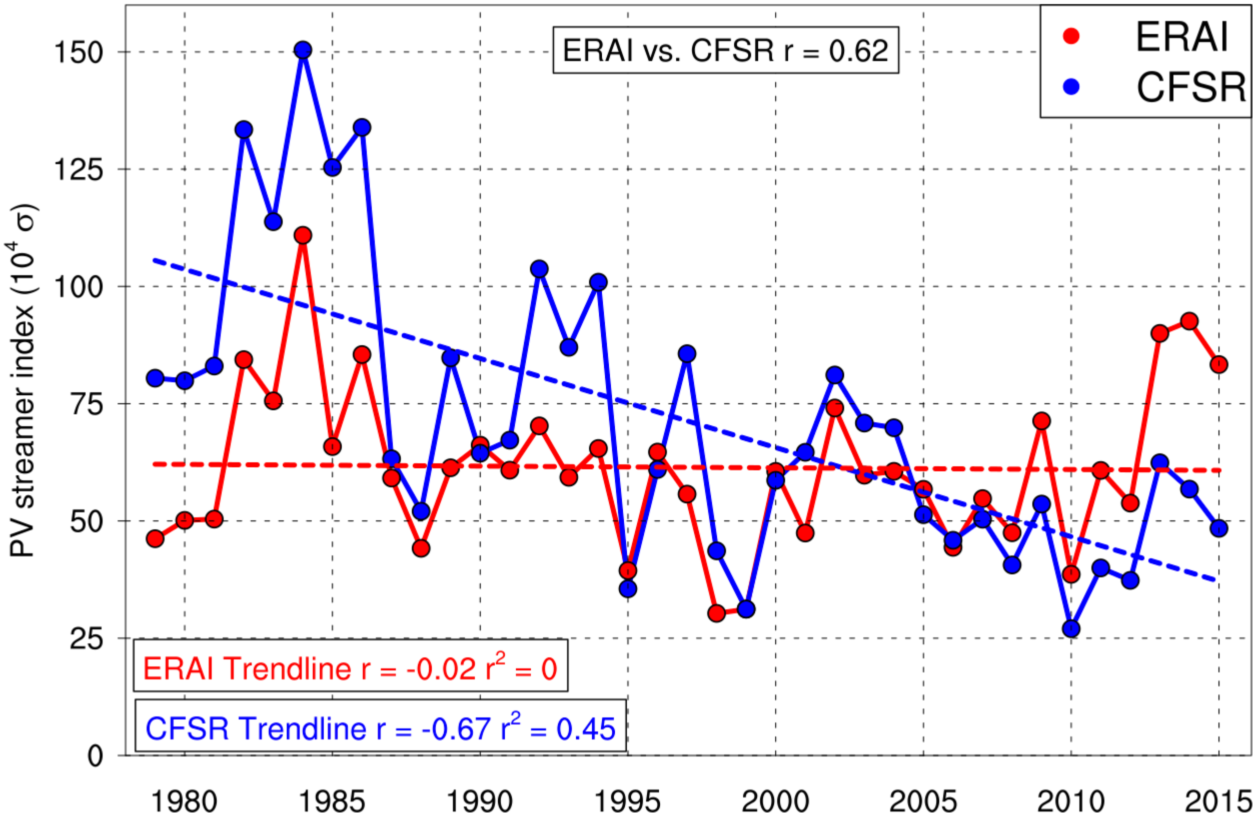

Fig. 3.15. 1979–2015 time series of seasonal PVS activity index for the CFSR (blue line), and the ERAI (red line). Trend lines for the 37-y period are depicted for each dataset (dashed lines). Correlation (r) between the two datasets is depicted at the top, and the correlation and r^2 values for the ERAI and CFSR trend lines are depicted in the bottom left in red and blue, respectively.

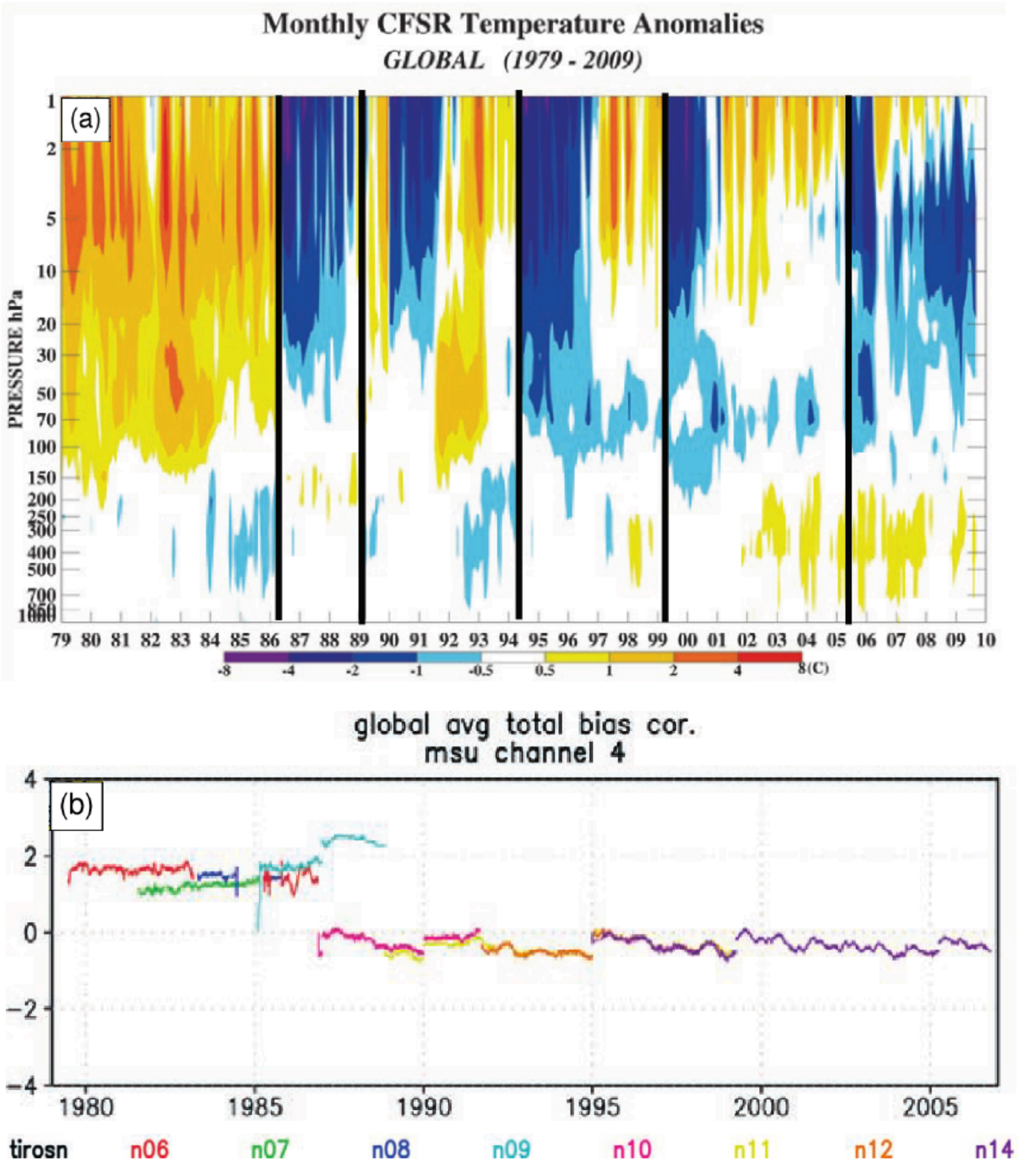

Fig. 3.16. (a) Monthly CFSR temperature anomalies (shading, °C) averaged over the globe from 1979–2010 (x-axis) by vertical pressure level (y-axis). Black lines are used to denote where the CFSR was broken up into separate analysis streams (six in total). (b) Global average temperature bias correction applied to MSU channel 4. The different colors plotted represent different polar orbiting satellites. Adapted from Fig. 7 and 24 of Saha et al. (2010).

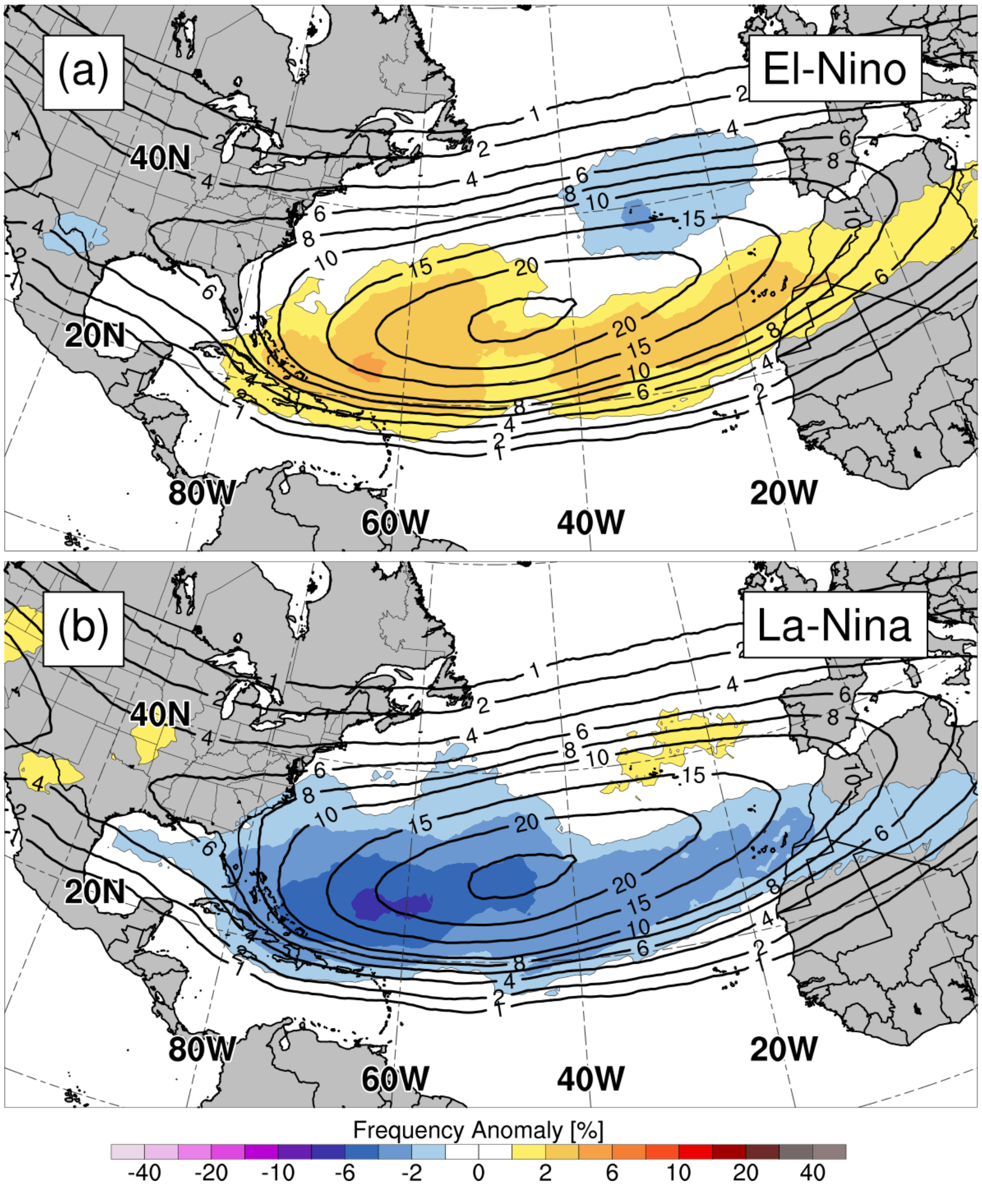

Fig. 3.17. PVS frequency anomalies (shading, %) relative to the 1979–2015 climatology (black contours, %) for (a) El Nino seasons (N = 10) and (b) La Nina seasons (N = 8).

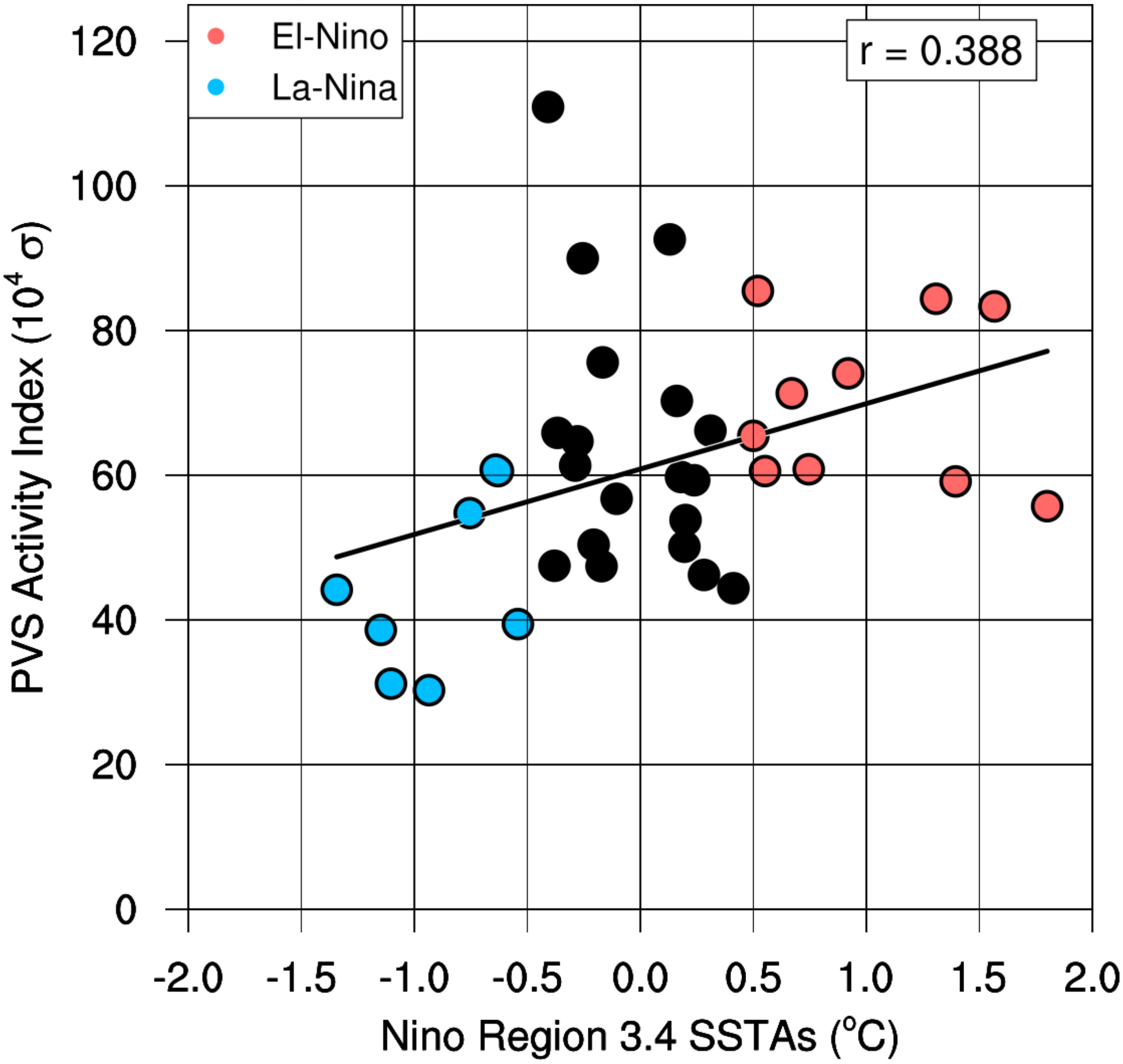

Fig. 3.18. Scatter plot of Nino region 3.4 sea surface temperature anomalies (x-axis, °C) versus PVS activity index (y-axis, 10^4 σ) from 1979–2015. Correlation between the two variables in provided at the top right with the trend line (black line). El Nino and La Nina years are highlighted in red and blue, respectively (see legend at the top left).

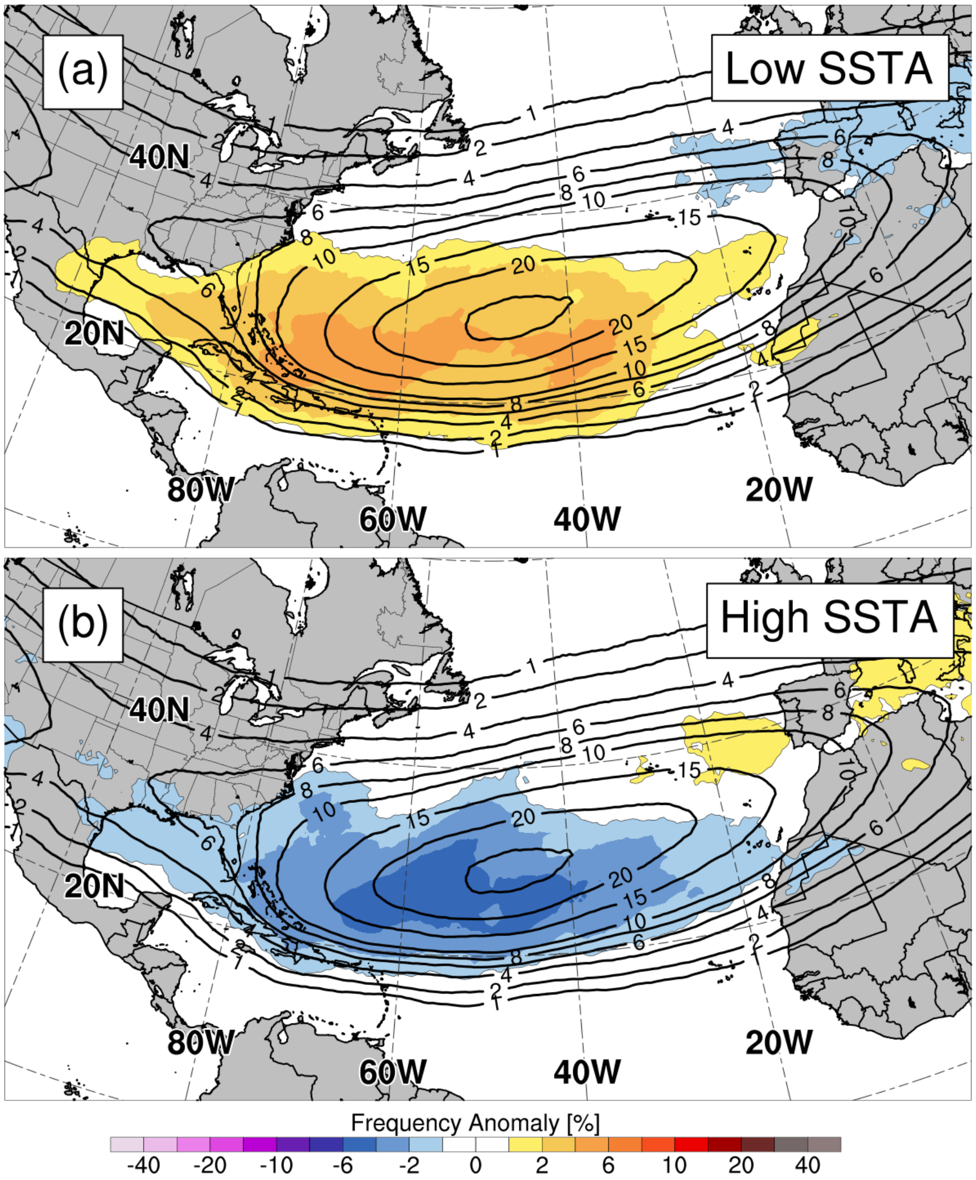

Fig. 3.19. As in Fig. 3.16., except for (a) low sea surface temperature anomaly seasons (N = 8), and (b) high sea surface temperature anomaly seasons (N = 8) in the NATL basin.

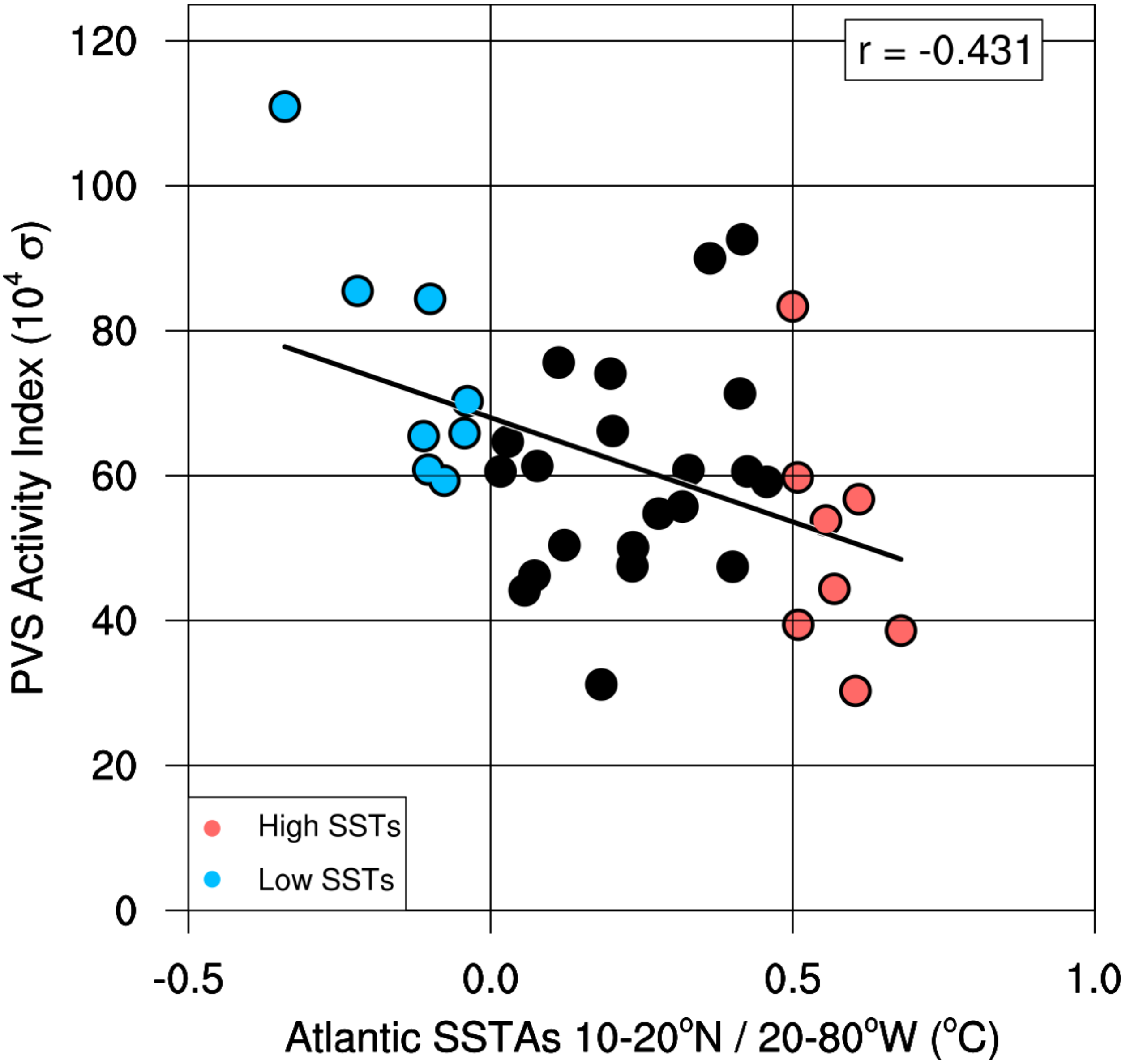

Fig. 3.20. as in Fig. 3.17, except for Atlantic sea surface temperature anomalies (x-axis, °C) versus PVS activity index (y-axis, 10^4 σ). Correlation between the two variables in provided at the top right with the trend line (black line). High and low sea surface temperature seasons are highlighted in red and blue respectively (see legend at the bottom left).

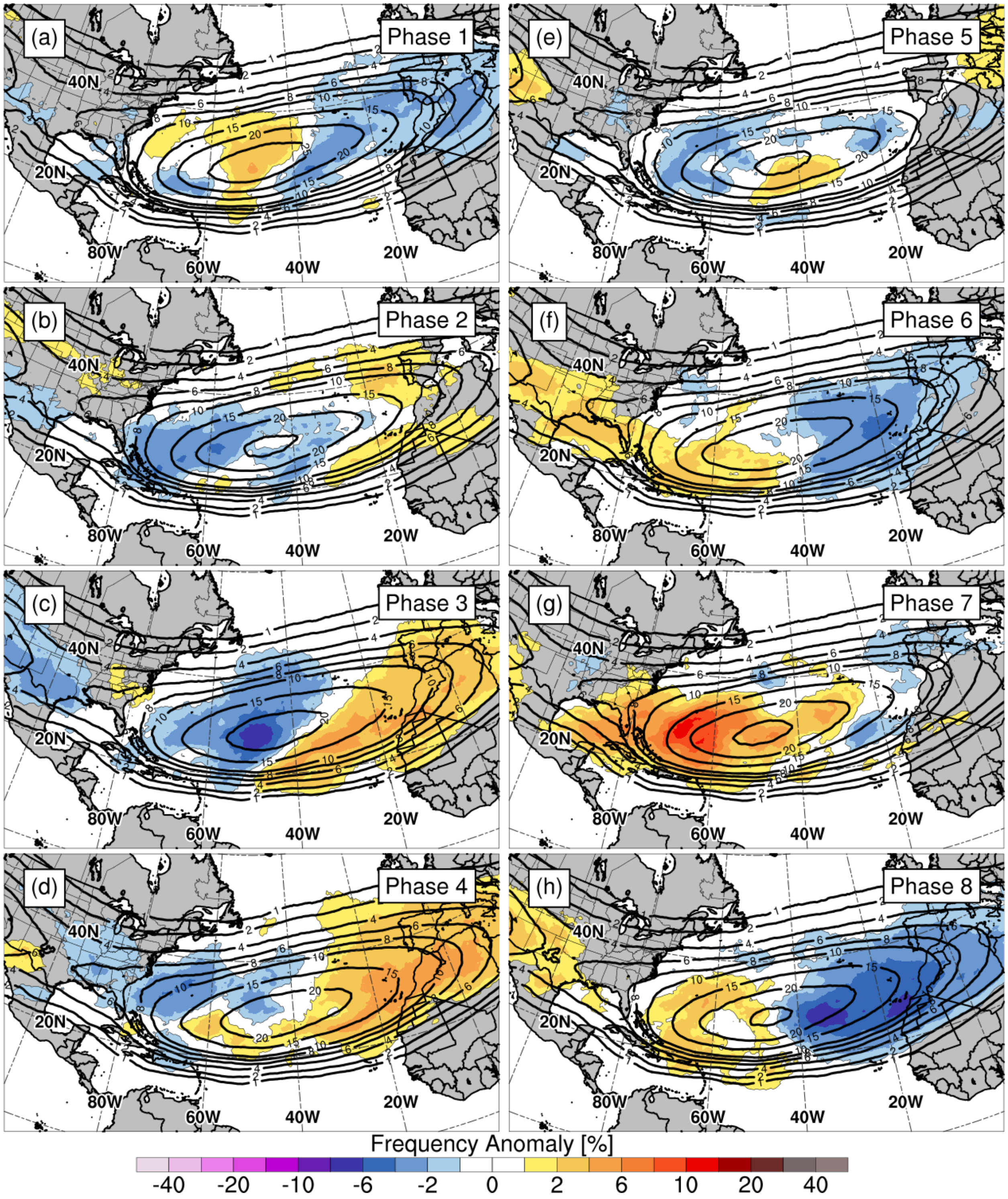

Fig. 3.21. PVS frequency anomalies (shading, %) relative to a climatology (black contours, %) specified for each MJO phase. Panels are for MJO phase (a) 1, (b) 2, (c) 3, (d) 4, (e) 5, (f) 6, (g) 7, and (h) 8. Note that panel order runs down rather than across first in order to allow for a comparison of opposite phases (i.e., d,h for phase 4,8).

4. PVS composites: dynamics and environmental impact

4.1. Introduction

In the previous chapter, the PVS climatology revealed that PVSs occur at a variety of different intensities, areas, and tilts. In this chapter, we test the hypothesis that PVSs of different intensity develop from dynamically distinct environments, and changes in PVS intensity, area, and tilt produce different environmental impacts in the North Atlantic basin. This hypothesis is tested by compositing PVSs of different intensity, area, and tilt to compare their environmental impacts at identification (t_0) and before identification. Individual composites are composed limiting PVS cases to similar areas and tilts in order to focus on intensity differences. Time-lagged composes will also be presented to show differences in the upstream synoptic pattern prior to different intensity PVS occurrence. Environmental variables chosen in these composites illustrate differences that can affect TC activity, and differences in the upstream waveguide that promote weak versus strong PVSs downstream.

4.2 Data and methodology

4.2.1. Compositing technique

Composites of PVS cases are generated using PVS cases from 1 June–30 November between 10^{o}–100^{o}W, so that only cases in the NATL basin during the TC season are considered. Only the top and bottom 20th percentiles of PVS intensities, hereafter referred to as strong and weak PVS events, are used for compositing. Strong and weak PVS composites are generated using the 0.7^{o} 6-h ERAI data (Dee et al. 2011), and are centered on the centroid of each PVS case (PVS-relative) before averaging. Thus, the center of each composite is on the PVS trough axis, noting that this moves grid points occurring in different locations and different times (e.g., Figs. 4.1, 4.2).

To allow for a proper comparison of meteorological variables, standardized anomalies of VWS, precipitable water, and mean sea level pressure are calculated using the method in section 2.4.2. Only regular anomalies (not standardized) were computed of total wind, temperature, thickness, vertical motion, and specific humidity in order to place emphasis on their units (not their sigma anomaly). Some composites will directly compare strong and weak PVSs by differencing their two standardized composite fields, as computed below:

$$\Delta x_{strong-weak} = \left\{\frac{\bar{x}_i{}^{composite} - \bar{x}_i{}^{mean}}{\overline{\sigma_{x_\iota}}}\right\} strong - \left\{\frac{\bar{x}_i{}^{composite} - \bar{x}_i{}^{mean}}{\overline{\sigma_{x_\iota}}}\right\} weak \qquad (4.1)$$

where x represents the variable that is being composited. For these composite difference fields, a bootstrap resampling method (Wilks 1997; Wilks 2006), using 1000-permutations sampling the strong and weak PVS cases, is conducted to determine whether the composite differences between strong and weak PVSs composites are statistically significant to the 95% confidence interval versus zero.

In addition to comparing strong and weak PVS intensity categories, this study also subsets PVSs by different area and tilt, as described in Fig. 3.7 and Fig. 3.8. This subsetting by area and tilt is important to ensure that the composite differences between the strong and weak PVS intensity categories is consistent, and that the composite signal is not being significantly influenced by other attributes (i.e., area and tilt) associated with the PVS. Table 4.1 provides the case counts of strong and weak PVS events divided up into their different area and tilt subsets. In total, nine composite subsets are created, organized by three tilt degree categories (35–55°, 55–75°,75–95°) and three area percentile categories (20–40th percentile, 40–60th percentile, 60–80th percentile) relative to the entire PVS climatology. Table 4.2 shows the average area, tilt, and intensity of composite strong and weak PVS for each composite subset. The differences in average area and tilt between strong and weak PVSs in a specified composite subset is small in comparison to the changes in average intensity between strong and weak PVS composites in the same subset. Changes due to the area and tilt of PVSs are best illustrated by comparing different composite subset categories (see Fig. 4.3).

4.2.2. Computation of unique variables

Additional variables beyond the standard fields provided in the ERAI were computed to deduce synoptic and/or dynamic processes occurring within strong and weak PVS events. To supplement precipitable water, integrated vapor transport (IVT) is used to show instantaneous moisture transport at each grid point. IVT is calculated in the tropospheric column following the calculation below (Neiman et al. 2008):

$$IVT = g^{-1} \int_{1000}^{300} q\vec{V}dp \tag{4.2}$$

where g is the gravitational acceleration, q is the specific humidity, and $\vec{V}$ is the vector wind. Note that this quantity is integrated in 50-hPa increments from 1000–300-hPa, capturing most of the water vapor in the troposphere. While this quantity shows the instantaneous moisture transport, caution is advised when interpreting this quantity in locations where moisture flux convergence or divergence may modify moisture quantity in a location without transport.

This study also uses the flow evolution obtained from composite strong and weak PVS events to calculate the irrotational component of the wind on the isentropic surface (350-K) on which PVSs are identified. Irrotational wind in this study is used to examine negative PV advection by divergent outflow that may be occurring in the amplifying ridges prior to AWB and PVS formation. Calculating irrotational wind requires a Helmholtz partitioning of flow[2] following the technique below (e.g., Bijlsma et al. 1986):

$$\vec{V} = \vec{V}_{\psi} + \vec{V}_{\chi} = \hat{k} \times \nabla\psi + \nabla\chi \tag{4.3}$$

where ψ is the streamfunction and χ is the velocity potential, and $\vec{V}_{\chi}$ indicates irrotational wind. The irrotational wind corresponds to the upper-level divergent outflow that is typically linked to ascent and, in regions of precipitation, to LHR.

Finally, this study uses information from the ERAI horizontal wind, vertical wind, and temperature fields to estimate diabatic heating. Diabatic heating in the 600–400-hPa layer in this study is used as a proxy for LHR to examine its possible role in ridge amplification that occurs prior to AWB and PVS formation. Diabatic heating tendency is calculated using the following equation (e.g., Yanai and Tomita 1998; Ling and Zhang 2013):

$$Q1 = \frac{T}{\theta}\left(\frac{\partial\theta}{\partial t} + u\frac{\partial\theta}{\partial x} + v\frac{\partial\theta}{\partial y} + \omega\frac{\partial\theta}{\partial p}\right) \tag{4.4}$$

where u, v, and ω are the three-dimensional wind components and $\theta = T(p_{00}/p)^{\frac{R}{Cp}}$ is the potential temperature, with T being temperature, p being pressure, p_{00} being surface pressure (usually 1000-hPa), R being the specific gas constant of dry air, and Cp being the specific heat capacity of dry air. It should be noted that diabatic heating, Q1, is an estimate, and not the direct temperature tendency available from microphysical processes parameterized in the ERAI.

---

[2] The irrotational component of the 350-K isentropic flow is computed via Helmholtz partitioning using spherical harmonics functions available in NCL.

4.3 Results: Composite overview

Before strong and weak PVS composite subsets are presented, it is worth providing an overview of the locations and time periods that are associated with strong and weak PVS events across the NATL basin. Figure 4.1 shows a density plot of PVS centroids for strong PVSs (Fig. 4.1a) and weak PVSs (Fig. 4.1b). In general, strong PVSs centroids are positioned in the western NATL basin, though a large range in longitude exists between 90°–40°W, 25°N where more than 150 cases are identified at each grid point (summed over a 500-km radius) are identified. In contrast, weak PVS events are more focused in the eastern NATL basin between 60°–15°W, 30°N. There are also subtle, but still important, differences in latitude, where strong PVSs are generally shifted equatorward by 2°–5°S. These centroid position differences are important, because this indicates strong and weak PVS events are sampling different regions of the NATL basin, which may have different climatological features that influence the anomalies calculated for given variables. Conversely, comparing the months that strong and weak PVSs are observed in (Fig. 4.2) does not reveal substantial differences. In general, similar average number of strong and weak PVSs are identified each month, with a couple exceptions (i.e., June and August). The composites presented subsequently will first be presented as separate strong and weak PVS composites before difference fields are shown. Caution is advised when interpreting these difference fields, since strong and weak PVS centroids are located in different regions that may bias the anomalies in each category to the local climatology used.

Figure 4.3 presents an overview of the nine composite categories used to compare strong and weak PVS composites by depicting their composite 350-K 2-PVU contour as red and blue lines, respectively. Note again that each composite is centered using the average PVS centroid position of the strong and weak PVSs that make up each composite category. The change in PVS area among the nine PVS composite subsets is evident observing the strong and weak 2-PVU contours, where the smaller area PVS subsets (Fig. 4.3g–i) have a smaller trough axis of high PV air in comparison to larger area PVS subsets (Fig. 4.3a–c). The change in PVS tilt among the nine PVS composite subsets is also evident, where low-tilt PVS subsets (Fig. 4.3a,d,g) have their PVS trough axis tilted northeast to southwest, while higher-tilt PVS subsets (Fig. 4.3c,f,i) have their PVS trough axis tilted more east to west. Around the PVS trough axis, the composite 2-PVU contours of the strong and weak PVSs (red and blue contours, Fig. 4.3) line up closely in the same latitude and longitude space in all nine composite subsets, indicating similarities in tilt and area in each subset (despite differences in PVS intensity). In the following section (Section 4.3.2), different atmospheric environmental variables are plotted on top of these nine subsets depicting PVSs at identification (t_0), in order to investigate how PVSs of different intensity modify their local environment at t_0.

Upstream of the PVS trough axis at t_0, the 2-PVU contour of strong PVSs bulges poleward of the 2-PVU contour of weak PVSs in all nine composites (Fig. 4.3). This pattern suggests that, in the aggregate, strong PVS events possess stronger upstream ridges, associated with the 2-PVU contour shifting poleward in the ridge axis. Dynamical and thermodynamic processes leading to stronger ridges in the strong PVS composite may have already occurred by t_0. Thus, time-lagged composites using earlier periods before t_0 are more useful to investigate mechanisms leading to ridge amplification between strong and weak PVSs. Possible mechanisms of ridge amplification in strong and weak PVSs are discussed later in this chapter (Section 4.3.3).

4.4. Results: Composites at identification (t_0) of strong and weak PVSs

4.4.1. VWS and precipitable water

VWS and precipitable water are important variables that impact the formation and maintenance of TCs in the NATL basin (e.g., Gray 1968; Zehr 1992; Knaff 1997; DeMaria et al. 2001). The purpose of this section is to illustrate how VWS and precipitable water anomalies change in the presence of strong and weak PVSs at a variety of different areas and tilts in order to deduce the outstanding differences between the composite subsets.

Figure 4.4 presents 200–850-hPa standardized VWS anomalies for the nine composites in Fig. 4.3, but only for the strong PVS subsets (red contours). Each of these categories show that strong PVSs have a substantial enhancement of VWS between $+1.5\sigma$ to $+2.5\sigma$ (relative to climatology), mainly southeast of the PVS trough axis. For PVS composite tilt angles between 35–55^{o}, this registers as a 5–10-m s^{-1} increase in the southwesterly VWS anomaly (vectors), with the region of standardized VWS enhancement increasing in extent as the PVS categories increase in area percentile (Fig. 4.4a,d,g). The vector magnitude increase in VWS downstream of the strong PVSs is more than double the VWS anomaly magnitude shown in a recent study of PVS features in the Atlantic basin (Zhang et al. 2017; See Fig. 1.5 in Chapter 1), which combine all PVSs into one composite. The maximum magnitude of standardized VWS enhancements decreases slightly moving to medium and high tilt PVSs, and the VWS vector anomaly shifts from southwesterly to westerly (Fig. 4.4 middle and right panels). This shift in the vector direction of the VWS anomaly likely occurs due to tilt changes in the PVS subsets. The overall enhancement of VWS downstream of the PVS trough axis is likely associated with the large magnitude, positive PV anomaly embedded in strong PVSs (Table 4.2), where stronger upper-tropospheric cyclonic flow around the PVS trough axis is consistent with the inversion of stronger, positive PV anomalies (HMR, Martin 2006).

Comparing the standardized VWS anomalies of strong PVSs in Fig. 4.4 to weak PVSs in Fig. 4.5 reveals sharp contrasts in the VWS anomaly magnitudes. For example, the smallest area, weak PVS composite subsets show very little enhancement (0 to +0.25σ) of standardized VWS anomaly southeast of the PVS (Fig. 4.5g–i). There is, however, a significant expansion of positive VWS anomalies in this region as the area of the weak PVS composite increases (Fig. 4.5 middle and top panels). These standardized VWS anomalies correspond to a < 5 m s^{-1} increase in the VWS vector anomaly. Similar to the strong PVS subsets, the anomalous shear vector shifts from southwest to west as tilt angle increases in the PVS composite subsets (Fig. 4.5 left to right panels). These positive VWS anomalies are smaller than those noted in the PVS composites composed in Zhang et al. (2017; See Fig. 1.7 in Chapter 1), who combine all events.

The composite difference in standardized VWS anomalies between strong and weak PVS composites is illustrated in Fig. 4.6. In general, all nine composite subsets show a large region of positive, standardized VWS anomalies, mostly to the south and southeast of the PVS trough axis, indicating strong PVSs possess statistically significant increases in standardized VWS anomalies versus weak PVSs (Fig. 4.6). This region of positive VWS anomalies also appears to scale with the size of the PVS (Fig. 4.6 moving from bottom to top panels). The vector direction of VWS anomaly differences also shifts from southwesterly to westerly as the tilt of the PVS composites shifts from low to high (Fig. 4.6 moving from left to right panels). These composite subsets suggest that strong PVSs produce significantly increased VWS anomalies to their southeast relative to weak PVSs, regardless of the area or tilt of the PVS composite. The reason for large increases in standardized VWS differences is likely associated with strong PVSs having a much higher magnitude positive PV anomaly in their axis versus weak PVSs of the same area and tilt (Table 4.2), which induces greater anomalous cyclonic flow in the upper-troposphere, especially equatorward of the PVS axis.

Notable differences between strong and weak PVS composites are also observed with precipitable water. Figure 4.7 presents the standardized precipitable water anomalies for all strong PVS composites. In general, there is a dipole in moisture anomalies, where weak to moderate negative anomalies (-0.25 to -0.5σ) in standardized precipitable water are present along and just northeast of the PVS trough axis, but positive standardized precipitable water anomalies (+0.5 to +1.0 σ) are observed further northwest along the 2-PVU contour near, and within, the upstream ridge. The spatial extent of negative and positive standardized precipitable water anomalies appears scale with the size of the PVS (Fig. 4.7 bottom to top panels). PVS composites with the lowest tilt have the greatest negative and positive standardized precipitable water anomalies (35–55^{o} tilts, Fig. 4.7a,d,g). These same tilt angles also possess a weak secondary maximum in precipitable water anomaly (+0.25σ) southeast of the PVS trough axis, which is possibly related to some strong PVS cases containing a moist, low-level system or TC interacting near the PVS (see Fig. 5.13a; Galarneau et al. 2015). This positive anomaly of precipitable water, however, is small and is not consistently observed in the remaining strong PVS composites with higher tilt angles (Fig. 4.7 middle and right panels). The negative precipitable water anomalies observed with most of the strong PVS composites may be related to the flux of drier, mid-latitude air upstream of the PVS trough axis, as noted in Yoneyama and Parsons (1999) and Waugh (2005), or increased subsidence induced by QG descent (e.g., Davis 2010; Fig. 1.8b). These mechanisms will be investigated further when looking at vertical cross-section differences between strong and weak PVSs in section 4.4.3.

The precipitable water anomalies noted in the strong PVS composites contrast markedly with the weak PVS composite, presented in Fig. 4.8. For example, there is little to no signature of negative standardized precipitable water anomalies in and just northeast of the PVS trough axis, except for spotty, weak -0.25σ anomalies in Fig. 4.8a,c,d. The lack of negative precipitable water anomalies may be related to less equatorward advection of dry, mid-latitude air or less subsidence (e.g., Yoneyama and Parsons 1999; Waugh 2005; Davis 2010). Instead, the dominant feature is a region of positive standardized precipitable water anomalies (+0.5 to +0.75σ) further north embedded along and poleward of the upstream ridge. Compared to strong PVSs, this region of positive precipitable water anomalies is smaller and positioned more equatorward, closer to the weak PVS trough axis.

Given these differences in moisture between the strong and weak PVS composites, it is not surprising to observe that the composite difference of strong minus weak PVS composites (Fig. 4.9) reveals statistically significant moisture dipoles. Along the 2-PVU contours on the western flank of the PVS difference composites (~80°W), statistically significant positive standardized precipitable water (+0.5 to +0.75σ) differences occur between strong minus weak PVS composites. This result suggests that strong PVSs have greater positive moisture anomalies along the upstream ridge axis, possibly related to greater poleward advection of moisture originating from the tropics in this region (e.g., Knippertz 2005; Zhang et al. 2017; Fig. 1.7c in Chapter 1). Closer to the PVS trough axis, statistically significant negative precipitable water anomalies (-0.25 to -0.5σ) are observed in association with a dip in the composite mean precipitable water. These differences between strong minus weak PVSs are most accentuated in the 35–55° tilts (Fig. 4.9a,d,g). This result suggests that strong PVSs have greater negative moisture anomalies in the PVS trough axis, which may be associated with greater equatorward flux of lower-precipitable water air from higher latitudes (e.g., Waugh and Polvani 2000; Waugh 2005, Zhang et al. 2017), or from greater subsidence that would be favored upstream of the PVS trough axis (e.g., Davis 2010; Zhang et al. 2017; Fig. 1.8 in Chapter 1).

This study is especially interested in how VWS and precipitable water anomalies change equatorward of the PVS trough axis, since this region is where low-latitude TC activity is most common (e.g., the MDR) and TCs are negatively impacted by increases in VWS and decreases in moisture. To place added emphasis of VWS and precipitable water equatorward of PVS events, an average of these anomalous quantities is taken in a PVS-relative box that moves with the location of the PVS centroid (see Fig. 4.10, using the relative box seen in Fig. 4.3h). Anomalies with each PVS subset are organized by tilt angle (x-axis) and area (y-axis), and divided into weak (Fig. 4.10a–b) and strong (Fig. 4.10c–d) PVS cases. Weak PVS subsets have either negative or neutral VWS anomalies, with negative VWS anomalies decreasing as PVS area increases (Fig. 4.10a). In contrast, all strong PVS categories have positive VWS anomalies between +1 to +3.5 m s^{-1}, with positive VWS anomalies increasing as PVS area increases (Fig. 4.10c). For precipitable water anomalies, weak PVS subsets generally have positive or neutral anomalies (Fig. 4.10b). Strong PVS subsets generally have negative precipitable water anomalies with negative precipitable water anomalies decreasing as PVS tilt increases (Fig. 4.10d).

In general, the plots in Fig. 4.10 support the relationship that strong PVSs increase VWS and reduce precipitable water anomalies equatorward of their axis, while weak PVSs are associated with the opposite or neutral anomalies. Higher VWS anomalies in strong PVSs may be related to these cases possessing a higher magnitude, positive PV anomaly, where PV inversion would imply stronger cyclonic flow produced in the upper-troposphere that decays towards the surface (HMR, Martin 2006). Negative precipitable water anomalies in strong PVSs may be related to previously mentioned advection of dry mid-latitude air or subsidence (e.g., Waugh and Polvani 2000; Waugh 2005, Zhang et al. 2017). Noting that TC activity tends to be inhibited by negative precipitable water anomalies and positive VWS anomalies, we can infer that strong PVSs are more likely to inhibit TC activity versus weak PVSs. This inferred relationship will be explored further in Chapter 5 of the dissertation.

4.4.2. Sea level pressure and upper-tropospheric thickness

Next, we investigate changes in mean sea level pressure and upper-troposphere thickness anomalies in different intensity PVS occurrences at identification (t_0). Positive sea level pressure anomalies in the NATL subtropics have been noted to be associated with unfavorable conditions for TC activity in the MDR (Knaff 1997; Klotzbach et al. 2008), since years with higher mean sea level pressure anomalies in the subtropics aid greater northeasterly trade winds, lowering SST anomalies in the tropics. Thickness is also a critical variable that we use to assess how PVSs of different intensity change the upper-tropospheric thermal profile and static stability.

Figure 4.11 shows how composite strong PVSs modify the mean sea level pressure in their vicinity. The standardized mean sea level pressure anomalies, in general, are relatively muted (between -0.5 to +0.5σ in all composite subsets); there is a tendency, however, for enhanced, positive standardized sea level pressure anomalies (+0.25 to +0.5σ) primarily northwest of the PVS trough axis. These positive standardized sea level pressure anomalies appear to increase in spatial extent as the area of the PVS increases in size (Fig. 4.11, moving from bottom to top panels). Weak negative standardized mean sea level pressure anomalies (-0.25 to -0.5σ) are observed even further northwest, mostly poleward and westward of the 2-PVU contour, and are possibly a reflection of a synoptic impulse moving along the waveguide. This signal also appears to increase in spatial extent with increasing PVS area, especially for the low and medium PVS tilt angles (Fig. 4.11, left and middle panels). The broad region of positive sea level pressure anomalies may be associated with subsidence or QG descent, which favor anti-cyclogenesis upstream of the strong PVS trough axis (e.g., Davis 2010; Zhang et al. 2017). Also present around positive sea level pressure anomalies are anticyclonic wind anomalies at 925-hPa, which generally result in northeasterly flow anomalies embedded in the strong PVS trough axis, especially in larger subsets (Fig. 4.11 a–d).

In comparison to the strong PVS composites, the weak PVS composites have a shifted location of positive mean sea level pressure anomalies mainly within the trough axis of the weak PVSs (Fig. 4.12). This signal also appears to increase in spatial extent as the area of the composite PVS increases in size (Fig. 4.12 moving from bottom to top panels). Negative, standardized mean sea level pressure anomalies are mainly observed poleward of the 2-PVU contour both to the east and west of the mean ridge embedded in the PVS trough axis. Characteristic of the enhanced ridging are anticyclonic 925-hPa wind anomalies, resulting in enhanced northeasterly trade winds along and downstream of the larger weak PVS subsets (Fig. 4.12 a–d).

Figure 4.13 presents the composite differences in standardized mean sea level pressure anomalies for strong minus weak PVS composites. In general, the composites are dominated by positive standardized mean sea level pressure anomalies, where these differences between strong minus weak PVSs are most consistent west of the PVS trough axis. One interpretation of the positive mean sea level pressure anomalies in this region is that strong PVSs have stronger forcing for subsidence resulting in surface ridge building (e.g., Davis 2010; Zhang et al. 2017). Vertical motion differences between strong and weak PVSs are explored in a following figure

(Fig. 4.17c). The organization of the sea level pressure anomalies also imply anomalous northerly flow, which is observed just west of the PVS centroids (Fig. 4.17), with these anomalous low-level winds possibly helping to advect drier mid-latitude air resulting in the negative precipitable water anomalies seen in Fig. 4.9. Since, stronger and larger PVSs are most associated with positive, standardized mean sea level pressure anomalies, if these PVSs occur most frequently over a TC season, they could lead to unfavorable feedbacks associated with subsidence and drier mid-latitude air, limiting low-latitude TC activity (Knaff 1997, Klotzbach et al. 2008).

Perhaps the most pronounced differences between the strong and weak PVS composites is exhibited in the upper-tropospheric thickness, defined between 200–500-hPa. Figure 4.14 presents these thickness anomalies for the strong PVS composites. Within the trough axes of the strong PVS composites, negative thickness anomalies between -4 to -10 dm are present, with the spatial region of negative anomalies increasing in size with increasing area of the strong PVS composites (Fig. 4.14 from bottom to top panels), and the negative anomalies increasing in magnitude within the PVS trough axis for lower PVS composite tilt angles (Fig. 4.14 from right to left panels). Upstream of the strong PVS trough axes, however, there is an even larger region of positive thickness anomalies between +2 to +8 dm associated with the upstream ridge that induces AWB. Similar to the negative thickness anomalies, the spatial extent and magnitude of the positive thickness anomalies increase with increasing area and decreasing tilt of the PVS composites (Fig. 4.14 moving from bottom right to top left panels. The positive and negative thickness anomalies are associated with the composite mean thickness ridges and troughs, where the anomalous low thickness in the trough implies that strong PVSs are cold-core in nature, consistent with the inversion of positive PV anomalies (HMR; Martin 2006).

In contrast to the strong PVS composites, upper-tropospheric thicknesses in weak PVS composites exhibit a very different pattern (Fig. 4.15). While there is still a large positive thickness anomaly between +2 to +8 dm mainly positioned near the upstream ridge that induces AWB, this positive anomaly is shifted further east relative to the strong PVS composites. Contrasting further with the strong PVS composites, there is little to no negative thickness anomaly observed in the weak PVS trough axis, but rather a pattern of positive thickness anomalies that surround the PVS trough axis with only climatological thickness values embedded within the PVS trough axis. This lack of negative thickness anomalies in the PVS trough axis are likely a reflection of the shallower penetration depth of the weaker positive PV anomaly associated with weak PVSs (HMR). Weak PVS composites also possess higher mean thickness values in their trough axes compared to the strong PVS composites.

Differencing the strong minus weak PVS composites reveals large regions of statistically significant positive and negative thickness anomalies (Fig. 4.16). The positive thickness anomaly differences (between +2 to +6 dm) are located in the far west, where the 2-PVU contour for strong PVS composites bulges poleward versus the 2-PVU contour for weak PVSs. The negative thickness anomaly differences (between -2 to -8 dm) are focused in the trough axis, where the strong PVS composite has significantly lower thickness anomalies compared to the weak PVS composite. This pattern suggests that strong PVSs have a stronger cold-core circulation in the upper-troposphere, which may generate stronger thermal winds (i.e., VWS) via deeper penetration of the positive PV anomalies in low static stability tropospheric air. While strong PVSs may have deeper penetration of their positive PV anomalies, upstream they also have characteristically higher thickness associated with stronger upper-tropospheric ridging.

While this study has observed subtle changes in the size and magnitude of anomalies in a variety of different variables (VWS, precipitable water, mean sea level pressure, upper-tropospheric thickness), for differences in area and tilt, it is clear the highest sensitivity in these atmospheric fields are found comparing the strong and weak PVS categories. For brevity, the remainder of this chapter will only compare the median composite evolution of strong and weak PVSs, using the 55–75° tilt and 40–60th area percentile (Fig. 4.3e), with the emphasis of the discussion focusing on how PVS intensity differences modify environmental variables.

4.4.3. Vertical differences between strong and weak PVSs

While the previous composite difference fields of strong minus weak PVSs focused on spatial differences in environmental variables, it is also important to observe that large differences occur vertically, associated with differences in VWS, temperature, and moisture. Figure 4.17 illustrates a northwest to southeast cross-section, orthogonally through the composite strong and weak PVSs noted in Fig. 4.3e. All variable quantities are difference fields of strong minus weak PVSs to show their outstanding differences. The wind differences normal to the cross-section axis (Fig. 4.17a) show that at the isentropic level on which the PVS is identified (350-K), strong PVSs possess much higher southwesterly flow (+15 m s^{-1} normal wind) downstream of the PVS axis (right of the black circle) and much higher northeasterly flow (-25 m s^{-1} normal wind) northwest of the PVS axis (left of the black circle). These flow differences in the upper-troposphere are likely a consequence of the higher intensity of strong PVSs versus weak PVSs, where a greater positive PV anomaly is associated with greater cyclonic wind around the strong PVS trough axis. These wind differences decrease in magnitude descending through the troposphere, especially southeast of the PVS axis where differences become negligible (+0–2 m s^{-1} normal wind). This helps explain the significant difference in 200–850-hPa VWS anomalies between strong and weak PVSs (Fig. 4.6), since strong PVSs had much larger differences in the upper-tropospheric wind versus lower-tropospheric wind.

Large vertical differences in temperature anomalies are also observed in the strong minus weak PVSs composites (Fig. 4.17b). Through the tropospheric column (1000–200-hPa), an expansive region of negative temperature anomalies (-1 to -3^{o}C), centered at the PVS trough axis, exist. This result implies that strong PVSs have a stronger, tropospheric-deep, cold-core structure compared to weak PVSs. In the lower stratosphere (200–100-hPa), however, these negative temperature anomalies quickly shift to positive temperature anomalies (+1 to +4^{o}C). This result implies that strong PVSs are also associated with a sharper vertical potential temperature gradient at their isentropic level of identification (350-K). This observation, combined with the much stronger cyclonic flow also observed at this level (Fig. 4.17a), is consistent with strong PVSs possessing a higher +PV anomaly via enhanced relative vorticity and an increased vertical potential temperature gradient at 350-K. These results are also consistent with PV invertability, where greater positive PV anomalies are associated with greater negative geopotential height anomalies, which are characteristically associated with cyclonic wind and negative temperature perturbations (Eliassen and Kleinschmidt 1957, HMR).

Vertical motion anomaly differences between strong minus weak PVSs are also apparent, as illustrated in Fig. 4.17c. Tropospheric-deep ascent anomalies are observed between strong minus weak PVS composites southeast of the PVS trough axis. In contrast, tropospheric-deep descent anomalies are observed between the strong to weak PVS composites northwest of the PVS trough axis. One hypothesis for these differences is ascent and descent, respectively, are simply due to changes in QG-induced vertical motion that would be associated with the greater positive and negative PV advection by the thermal wind (i.e., VWS) in strong minus weak PVSs. Since strong PVSs have greater positive PV anomalies in their trough axes and greater VWS anomalies both upstream and downstream of their trough axes (Fig. 4.6), the changes in upward and downward vertical motion via QG ascent and descent would also be stronger. The anomalous subsidence observed along and northwest of strong PVSs connects back to prior research that has shown subsidence observed upstream of PVSs can dry the tropospheric column (Waugh 2005; Davis 2010; Zhang et al. 2017).

Finally, there are also important differences in specific humidity both upstream and downstream of strong minus weak PVS composites (Fig. 4.17d). Southeast of the PVS trough axis, positive specific humidity anomalies (between +0.1 to +1.0 g kg^{-1}) are observed between 850–300-hPa, though negative specific humidity anomalies (between -0.1 to -0.5 g kg^{-1}) are observed in the boundary layer underneath (1000–850-hPa). These negative to positive specific humidity anomalies with height partially cancel out and may explain why there is only a small region of positive precipitable water anomaly differences in Fig. 4.9e southeast of the PVS trough axis. Northwest of the PVS trough axis, there is an expansive region of negative specific humidity anomalies (between -0.5 to -1.5 g kg^{-1}) in the low- to middle-troposphere (1000–500 hPa). These negative specific humidity anomalies occur under anomalous tropospheric descent (Fig. 4.17c) and where stronger northeasterly flow is observed (Fig. 4.17a). Therefore, we interpret this reduction in specific humidity to both enhanced descent and stronger northeasterly flow advecting drier mid-latitude air in strong PVSs. The negative specific humidity anomaly differences are consistent with the negative standardized precipitable water anomalies observed in Fig. 4.9e northwest of the trough PVS axis.

4.5. Time-lagged composites of strong and weak PVSs

This section explores the synoptic-dynamic conditions that were present prior to PVS identification in order to investigate if there are any synoptic-dynamic differences in evolution prior to the development of strong versus weak PVSs. For the sake of brevity, we will only investigate these time-lagged composites using the 55–75° tilt and 40–60th percentile area composites of strong and weak PVS events. Additionally, PVS events that occurred within 24-h of another event are removed to avoid double counting the same PVS evolution that may dilute the composite. This removal reduces the original strong and weak PVSs counts (see Table 4.1) to $N_{strong} = 170$ and $N_{weak} = 230$. In these composites, we will test the hypothesis that strong PVSs are associated with stronger upstream ridges, that are in turn associated with higher moisture, which induces diabatic processes that aid in upstream ridge building.

4.5.1 PV, winds, and precipitable water

Figure 4.18 shows the time-lagged evolution of strong PVSs (Fig. 4.18a–d) and weak PVSs (Fig. 4.18e–h) from 72-h prior to the time of PVS identification (t_0). Beginning three days prior to PVS formation (t_0-72h) of strong PVSs (Fig. 4.18a), there already exists a distinct positive PV anomaly (between +0.5 to +1.0 PVU) associated with a characteristic cyclonic flow pattern in the 200-hPa wind anomalies near where the PVS is present at t_0. The 200-hPa easterly wind anomalies poleward of this feature may be contributing to weakening the climatological westerly flow along the waveguide (not shown), or that the waveguide itself is weaker in this region. The positive PV anomaly that occurs in Fig. 4.18a may reflect previous PVS events in the composite, which we will explore further near the end of this section.

Moving forward in time to t_0-48h and t_0-24h (Fig. 4.18b–c), the most notable change is the rapid development of a ridge at +10° latitude, -25° longitude which is denoted by negative PV anomalies (between -1 to -2 PVU) and characteristic anticyclonic 200-hPa wind anomalies. This strengthening ridge is associated with a significant enhancement (+10 m s^{-1}) of westerly wind anomalies along its poleward flank, which is a large flow perturbation versus the time-mean waveguide (not shown). The eastern flank of this ridge also begins to interact with the positive PV anomaly in the cyclonic trough downstream, enhancing northeasterly wind anomalies between 5–10 m s^{-1} that likely help advect high-PV air (> 2-PVU) equatorward underneath the ridge. By t_0, the continued northeasterly wind anomalies lead to further equatorward and westward advection of the 2-PVU contour, resulting in the positively-tilted trough of positive PV anomalies (between +1 to +3 PVU) in the PVS trough axis (Fig. 4.18d). Gradually building during this time evolution are enhanced southwesterly 200-hPa wind anomalies equatorward of the developing PVS trough axis, consistent with the enhancement of the positive PV anomalies in the PVS trough axis. This anomalous southwesterly 200-hPa flow is important for generating anomalous southwesterly VWS associated with the strong PVS composites (Fig. 4.4e).

The evolution of the weak PVS composite (Fig. 4.18e–h) contrasts markedly from its strong counterpart. Beginning three days prior to PVS formation (t_0-72h; Fig. 4.18e), the weak PVS composite has a large region of negative PV anomalies (between -0.25 to -1.0 PVU) in the same region where positive PV anomalies were observed in the strong PVS composite (Fig. 4.18a). Broad, anomalous anticyclonic flow is observed with the negative PV anomalies, where the poleward flank of this feature helps to enhance 200-hPa westerly flow (+4-6 m s^{-1}). Moving forward in time to t_0-48h and t_0-24h (Fig. 4.18f–g), this anticyclonic ridge slowly intensifies (-0.5

to -1.5 PVU) as westerly 200-hPa wind anomalies poleward of the ridge also increase and expand eastward. In the absence of a positive PV anomaly east of this ridge, there is much weaker anomalous northeasterly 200-hPa flow occurring downstream of the building ridge. Finally, at t_0, the poleward ridge in the weak PVS composite has reached the same magnitude as the poleward ridge in the strong PVS composite (compare Fig. 4.18d with Fig. 4.18h). There are, however, pronounced differences in the anomalous 200-hPa flow, where the weak PVS composite features a more progressive ridge anomaly as poleward 200-hPa westerly wind anomalies extend further east. Moreover, the 200-hPa anomalous northeasterly winds under the ridge are much weaker. This weaker, anomalous, northeasterly flow, combined with the lack of preexisting positive PV anomalies, is associated with a lack of positive PV anomalies in the weak PVS trough axis, where only a small region of +0.25 PVU is observed in the southern portion of the PVS trough axis. Consequently, the weaker positive PV anomaly in the trough axis is only associated with a slight increase in the anomalous southwesterly flow on its equatorward flank (Fig. 4.18h).

In addition to differences in the upper-tropospheric flow, there exist pronounced differences in the moisture field in the upstream evolution for strong and weak PVSs, as depicted in Fig. 4.19. Starting with the strong PVS evolution at t_0-72h (Fig. 4.19a), there exists an expansive region of positive precipitable water anomalies (+1 to +3 mm) centered along the 2-PVU waveguide 30° west of the strong PVS centroid position. IVT vectors in this location suggest that this enhanced moisture is being transported to the northeast over subsequent time periods. Indeed, this northeastward expansion of positive precipitable water anomalies occurs between t_0-48h and t_0-24h (Fig. 4.19b–c) as the moisture anomalies increase in magnitude (+4 to +6 mm). Note that a confluence axis of IVT is observed equatorward of the greatest positive moisture anomalies in Fig. 4.19b. This location is associated with moisture flux convergence (not shown), which may induce ascent and further enhance moisture anomalies as they are transported downstream. The growing positive moisture anomalies are located along the 2-PVU contour, which is moving poleward and beginning to fold over the equatorward dip in the 2-PVU contour downstream (Fig. 4.19b–c). The folding of the 2-PVU contour also indicates the initiation of AWB that will lead to the downstream, positively-tilted PVS in Fig. 4.19d. Within the developing PVS trough axis, negative precipitable water anomalies are observed (-1 to -3 mm; Fig. 4.19b–c). While IVT vectors in this region are small (due to lower moisture content), the southern extent of the region of negative precipitable water anomalies does have northeasterly IVT vectors, which suggests that this drier region is being transported southwest into lower latitudes. This evolution progresses further by t_0 (Fig. 4.19d), as the region of positive precipitable water anomalies is now moving poleward, up and over the region of negative precipitable water anomalies now primarily located in the PVS trough axis. The IVT vectors in both regions suggest these anomalies will continue to shift northeast and southwest, respectively, on the poleward and equatorward side of the AWB axis (located at +10° latitude, 0° longitude).

In contrast, the weak PVS composite does not begin with a large region of positive or negative precipitable water anomalies at t_0-72h (Fig. 4.19e), though the orientation of IVT vectors near +5° latitude, -20° longitude suggests that transport of moisture from lower latitudes may eventually lead to the development of positive precipitable water anomalies. This enhancement of positive precipitable water anomalies is observed over the subsequent 48-h period in conjunction with a confluence of poleward oriented IVT (Fig. 4.19f–g). During this period, there is also a poleward extension of the 2-PVU contour in the same location where positive precipitable water anomalies are observed, though this poleward extension is smaller and less pronounced then the poleward extension of the 2-PVU contour in the strong PVS evolution (Fig. 4.19b–c). At t_0, the 2-PVU contour and positive precipitable water anomalies continue to move east and are now situated poleward over the weak PVS trough axis that has developed at 0^{o},0^{o} (Fig. 4.19h). There is, however, no corresponding negative precipitable water corridor embedded in the weak PVS trough axis, in stark contrast to the evolution of the strong PVS composite (Fig. 4.19d). One possible explanation for this moisture difference is that the weak PVS trough appears to reside in a region where little in the way of IVT is occurring, consistent with being in the center of a low-level ridge axis, as shown in Fig. 4.12e. In addition, the lack of preexisting negative precipitable water anomalies earlier in the composite evolution may have mitigated the existence of negative precipitable water anomalies in the PVS trough axis. The implied, weaker, anomalous northeasterly flow seen in Fig. 4.18h is also consistent with weaker cyclonic flow around a weaker positive PV anomaly, which is unable to advect as much dry mid-latitude air aloft like seen in the strong PVS composite (Fig. 4.18d, Fig. 4.19d).

4.5.2. PV advection by the irrotational wind and diabatic heating

The differences in precipitable water anomalies observed between strong and weak PVSs (Fig. 4.19) suggest that enhanced moisture in, and upstream of, the ridge axis may aid processes promoting ridge amplification that results in AWB. In Chapter 1 of this dissertation, two of these processes were discussed: the direct effect (LHR) and the indirect effect (divergent outflow; see Fig. 1.3; Stoelinga 2003). This section investigates how LHR and divergent outflow change in strong versus weak PVS evolution.

Figure 4.20 show examples of strong and weak PVS events where PV advection by the 350-K irrotational (i.e., divergent) wind (Fig. 4.20a,c) and 600–400-hPa layer mean diabatic heating (Fig. 4.20b,d) is computed in an upstream box (red lines) tied to the AWB axis (red circle). Only grid points located in the ridge axis (negative PV anomalies in < 2-PVU air) where divergent outflow is observed are integrated, where a total negative PV advection by the irrotational wind indicates ridge building. These same grid points are used to integrate mid-level diabatic heating, which is used as a proxy for LHR since it occurs under divergent outflow (Stoelinga 2003; see Fig. 1.3). Using diabatic heating as a proxy for LHR is necessary since the heating tendencies associated with cloud processes are unavailable for the ERAI climatology (Ling and Zhang 2013). Strong, mid-level, diabatic heating results in a negative stability tendency above the level of maximum heating, directly related to the formation of a negative PV anomaly aloft (i.e., ridge building). In the example plots presented in Fig. 4.20, the strong PVS has greater negative PV advection by the irrotational wind at 350-K and greater mid-level diabatic heating (Fig. 4.20a–b) compared to the weak PVS (Fig. 4.20c–d). These combined processes appear critical to the development of a more amplified ridge upstream of the strong PVSs. We stress that the results presented in this section are qualitative, and do not directly compare to the actual negative PV tendency in the upstream ridge, but rather describe processes that are likely contributing to an enhanced negative PV tendency. A more quantitative approach would involve computing a PV budget to directly deduce which processes result in negative PV anomalies in the upstream ridge, which would be a natural extension of the results presented here.

Figure 4.21 shows integrated PV advection by the irrotational wind (Fig. 4.21a) and integrated diabatic heating (Fig. 4.21b) in the upstream ridge from t_0-72h to t_0, averaged for strong (red) and weak (blue) PVSs. From 54-h to 24-h prior to PVS identification, there is a statistically significant difference in PV advection by the irrotational wind, where strong PVSs have significantly more negative PV advection in comparison to weak PVSs (Fig. 4.21a). In addition, from 60 h to 24 h prior to PVS identification, there is a statistically significant difference in diabatic heating, where strong PVSs have significantly more diabatic heating in comparison to weak PVSs (Fig. 4.21b).

These results suggest that ridge building associated with strong PVSs is associated with diabatic heating that amplifies the ridge two to three days prior to the identification of the PVSs. These results are consistent with the time-lagged composite evolution in Fig. 4.18 and Fig. 4.19, focusing on the changes between t_0–72h to t_0–24h. First, greater precipitable water anomalies along the upstream flank of the ridge in the strong PVS composite (Fig. 4.19 a–c) may promote more condensation leading to greater diabatic heating via LHR (Fig. 4.21b, direct effect in Stoelinga 2003). This occurs in conjunction with greater negative PV advection by the irrotational wind (Fig. 4.21a, indirect effect in Stoelinga 2003). The combination of both processes results greater ridge building in the stronger PVS composite via greater negative PV anomalies in the ridge axis (Fig. 4.18 a–c). In contrast, weak PVSs have lower positive precipitable water anomalies (Fig. 4.19 e–g), more muted diabatic heating and negative PV advection by the irrotational wind (Fig. 4.21), and less ridge amplification (Fig. 4.18 e–g). These results are also consistent with conclusions presented in Teubler and Riemer (2016; See Fig. 1.2), where both LHR and divergent outflow contribute positively to ridge building in the upstream portion of the waveguide, although the implication in this study is that these processes are stronger in cases that lead to strong PVSs formation downstream. Further diagnosis of which of these two features (LHR, irrotational outflow) are more important for upstream ridge building is beyond the scope of this study.

4.5.3. PVS frequency before PVS occurrence

Another observation made in the time-lagged composites presented in Fig. 4.18 was that preexisting positive PV anomalies are observed in the strong PVS composites at t_0-72h, but negative PV anomalies are observed in the weak PVS composites. These different PV patterns suggest the possibility that strong PVSs events are more likely to be preceded by earlier PVS events. These earlier PVSs event may then modify the downstream waveguide to encourage additional AWB and PVSs downstream, as described in Fig. 4.18. Therefore, we will look at how the frequency of PVS events change between strong and weak PVS events before their identification.

Figure 4.22 shows a spatial plot of PVS frequency anomaly (shaded, %) for the 10 days before strong (Fig. 4.22a) and weak (Fig. 4.22b) PVS occurrence, with the climatological PVS frequency also illustrated (black contours, %). The PVS frequency is like that computed in Figs. 3.1–3.3 where each grid point enclosed in a PVS area is counted as an occurrence. Strong PVS events have up to a +6% increase in PVSs occurrence from climatology over the previous 10 days (Fig. 4.22a). While this increase does not appear impressive at first glance, it represents an almost 40% increase in PVS occurrence relative to climatology which is statistically significant. In comparison, there is little change in PVS frequency from climatology for weak PVSs events in the same location (Fig. 4.22b). The climatological PVS frequency for weak PVS events, however, is slightly higher (> 20%) than for strong PVS events (15–20%).

Another way of illustrating the differences in prior PVS activity in strong and weak PVS events is by depicting these anomalies in a Hovmöller diagram from 10 days to 1 day before PVS identification (Fig. 4.23). While both strong and weak PVS events feature an increase in PVS frequency anomaly in the period immediately before PVS identification, only strong PVS events feature a higher frequency of PVS occurrence that stretches as far back as seven days (168 h) before PVS identification (Fig. 4.23a). In the seven to five day (168–120 h) period before PVS identification, strong PVS events have a 2–4% increase in PVS frequency anomaly (4.23a), while weak PVS events have a corresponding 2–4% decrease in PVS frequency anomaly (Fig. 4.23b), with these differences being statistically significant.

The implications of greater PVS activity occurring before strong PVSs events can be discussed using the composite PV and wind anomaly structure in Fig. 4.18. In strong PVS occurrences, a pre-existing positive PV anomaly (associated with a previous PVS event) is associated with anomalous northeasterly flow on its poleward flank. This anomalous flow (i.e., easterly 200-hPa flow Fig. 4.18a–b) may weaken the time-mean waveguide, and allow northeasterly flow enhancement between the upstream ridge (negative PV anomaly) and the downstream trough (positive PV anomaly) (Fig. 4.18b–c). Finally, this enhanced northeasterly flow advects the pre-existing high-PV air equatorward, aiding the development of the strong PVSs (Fig. 4.18d). Without a pre-existing positive PV anomaly (due to reduced prior PVS activity), the weak PVS composite is associated with weaker northeasterly 200-hPa wind anomalies associated with the ridge, which are unable to advect as much high-PV air equatorward, resulting in weaker overall magnitude of the PVS (Fig. 4.18e–h).

4.6. Tables

Table 4.1. Average intensity, area, and tilt of the strong and weak PVS categories used for compositing.

Composite Subset	Strong PVS	Weak PVS
Area 60–80th percentile Tilt 35–55°	55	86
Area 60–80th percentile Tilt 55–75°	187	382
Area 60–80th percentile Tilt 75–95°	57	257
Area 40–60th percentile Tilt 35–55°	216	94
Area 40–60th percentile Tilt 55–75°	341	354
Area 40–60th percentile Tilt 75–95°	84	188
Area 20–40th percentile Tilt 35–55°	361	136
Area 20–40th percentile Tilt 55–75°	372	327
Area 20–40th percentile Tilt 75–95°	75	195

Table 4.2. Average area, tilt, and intensities for strong and weak PVSs that comprise the different composite subsets illustrated in Fig. 4.1.

Composite Subset	PVS Area ($\times 10^6$ km^2) Strong (Weak)	PVS Tilt (^{o}) Strong (Weak)	PVS Intensity(σ) Strong (Weak)
Area 60–80th percentile Tilt 35–55^o	4.15 (4.50)	46.7 (48.0)	+1.69(+0.24)
Area 60–80th percentile Tilt 55–75^o	4.59 (4.58)	66.2 (67.1)	+1.64(+0.21)
Area 60–80th percentile Tilt 75–95^o	4.53 (4.62)	79.7 (80.9)	+1.61(+0.22)
Area 40–60th percentile Tilt 35–55^o	2.59 (2.71)	47.2 (47.4)	+1.88(+0.20)
Area 40–60th percentile Tilt 55–75^o	2.69 (2.70)	64.7 (66.0)	+1.78(+0.18)
Area 40–60th percentile Tilt 75–95^o	2.72 (2.72)	80.6 (82.1)	+1.73(+0.18)
Area 20–40th percentile Tilt 35–55^o	1.58 (1.57)	45.8 (46.8)	+1.99(+0.14)
Area 20–40th percentile Tilt 55–75^o	1.60 (1.58)	63.9 (65.9)	+1.88(+0.08)
Area 20–40th percentile Tilt 75–95^o	1.68 (1.56)	81.0 (82.2)	+1.82(+0.08)

4.7. Figures

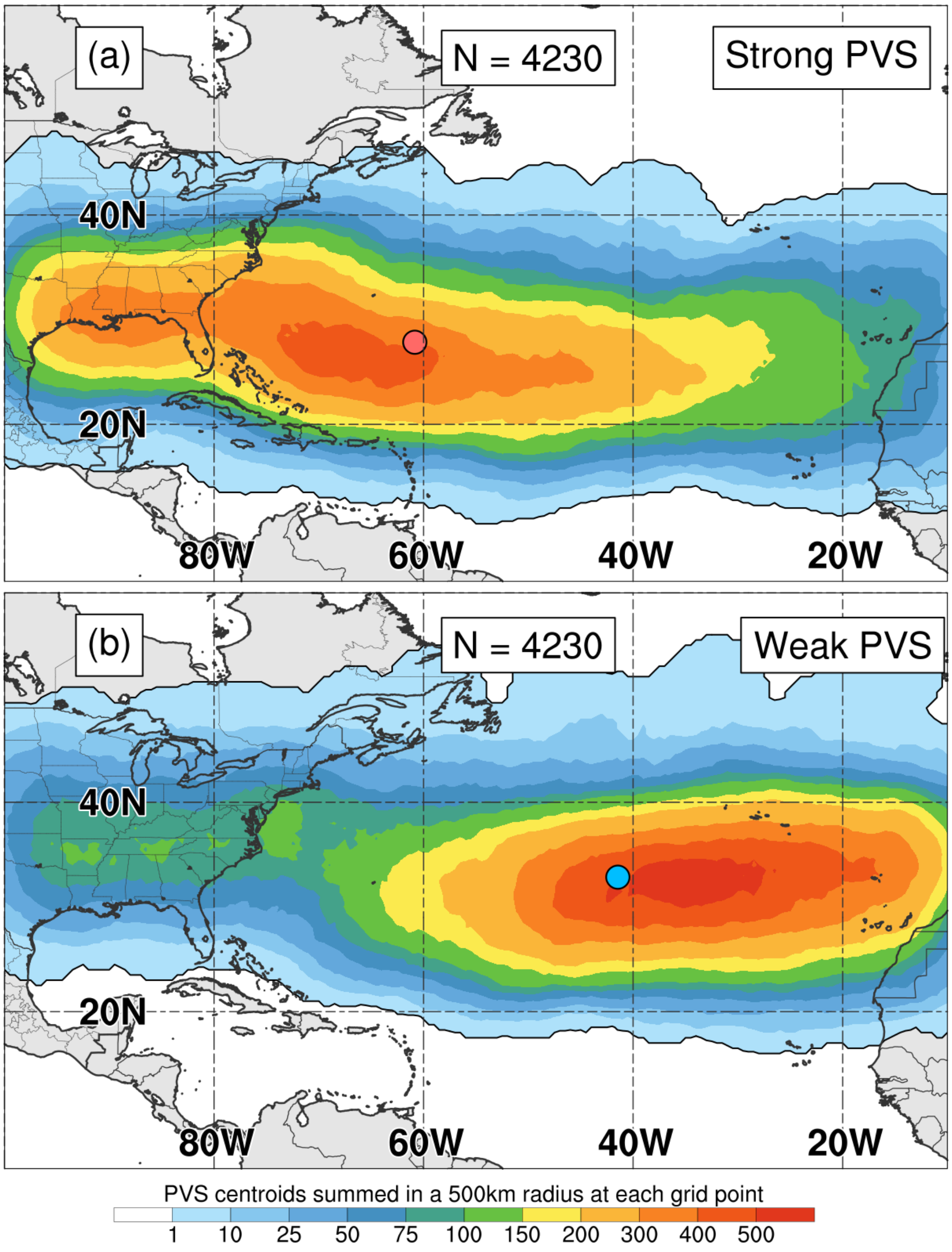

Fig. 4.1. Density plot of PVS centroids summing points in a 500-km radius of each grid point (shaded). Panel (a) is for all strong PVS events with the mean position denoted by a red circle and panel (b) is for all weak PVS events with the mean position denoted by a blue circle. PVS events only selected from 10°–100°W

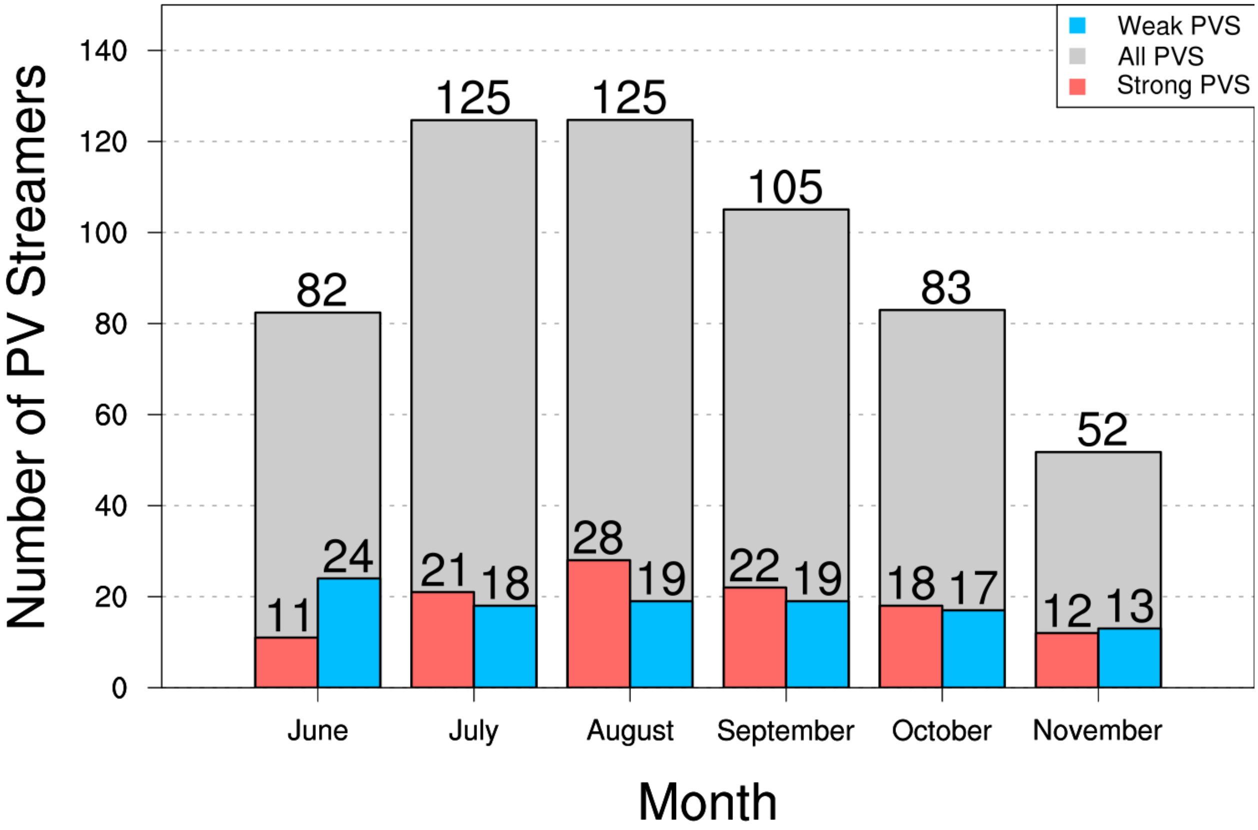

Fig. 4.2. Monthly distribution of all (gray), strong (red), and weak (blue) PVS cases by month from June–November. Quantities are the average number of PVS cases in each month from 1979–2015.

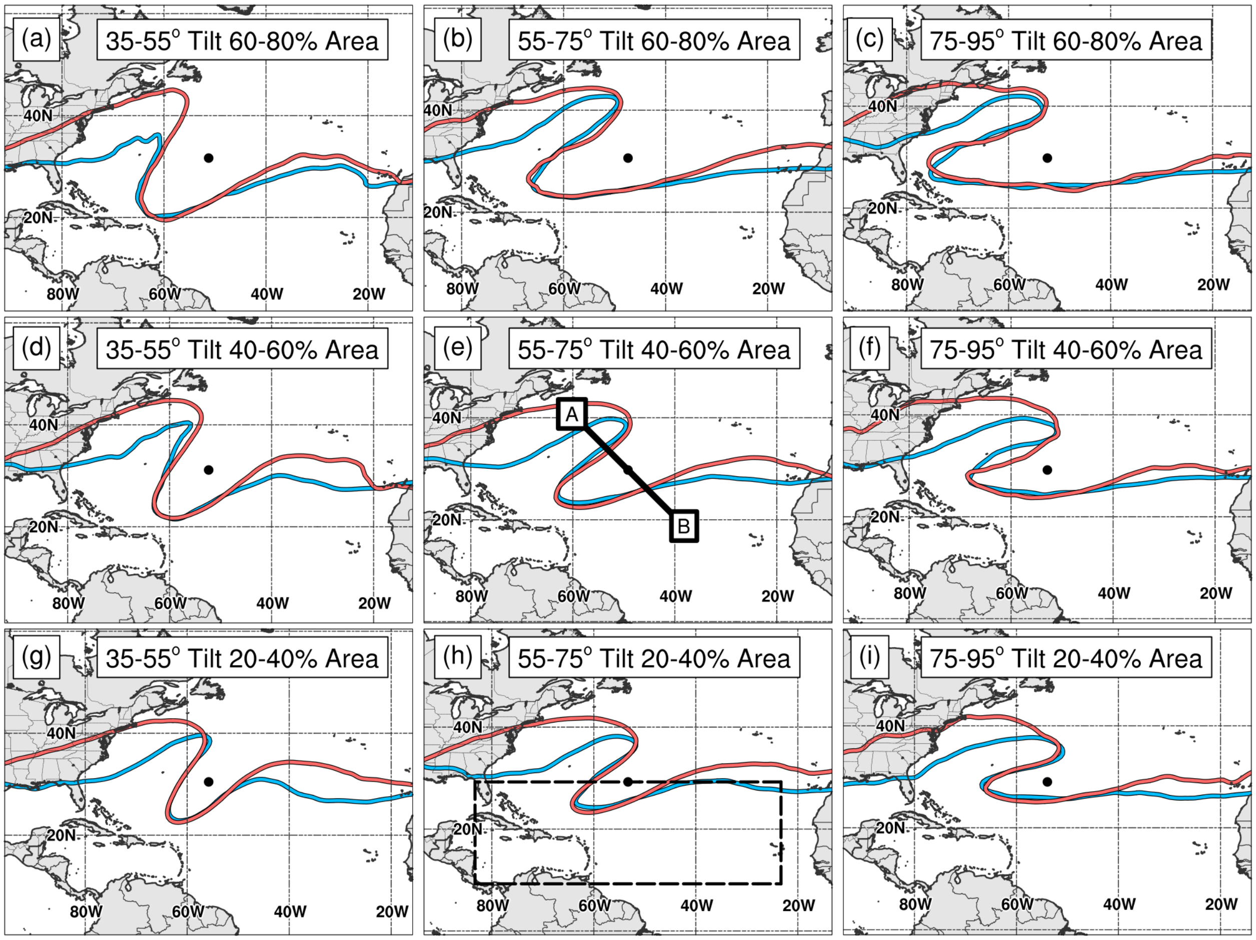

Figure 4.3. Composite 350-K isentropic 2-PVU contour of strong (top 20th percentile, red contour) and weak (bottom 20th percentile, blue contour) PVSs for (a) 35–55° Tilt, 60–80th percentile area, (b) 55–75° Tilt, 60–80th percentile area, (c) 75–95° Tilt, 60–80th percentile area, (d) 35–55° Tilt, 40–60th percentile area, (e) 55–75° Tilt, 40–60th percentile area, (f) 75–95° Tilt, 40–60th percentile area, (g) 35–55° Tilt, 20–40th percentile area, (h) 55–75° Tilt, 20–40th percentile area, (i) 75–95° Tilt, 20–40th percentile area. The composite PVS centroid position is denoted by the black circle in each plot. The thick black line in (e) represents a northwest to southeast cross-section from A to B in that is presented in Fig. 4.15, and the black dotted line box in (h) is used to illustrate the relative area used to average VWS and precipitable water anomalies presented in Fig. 4.8 for each composite subset.

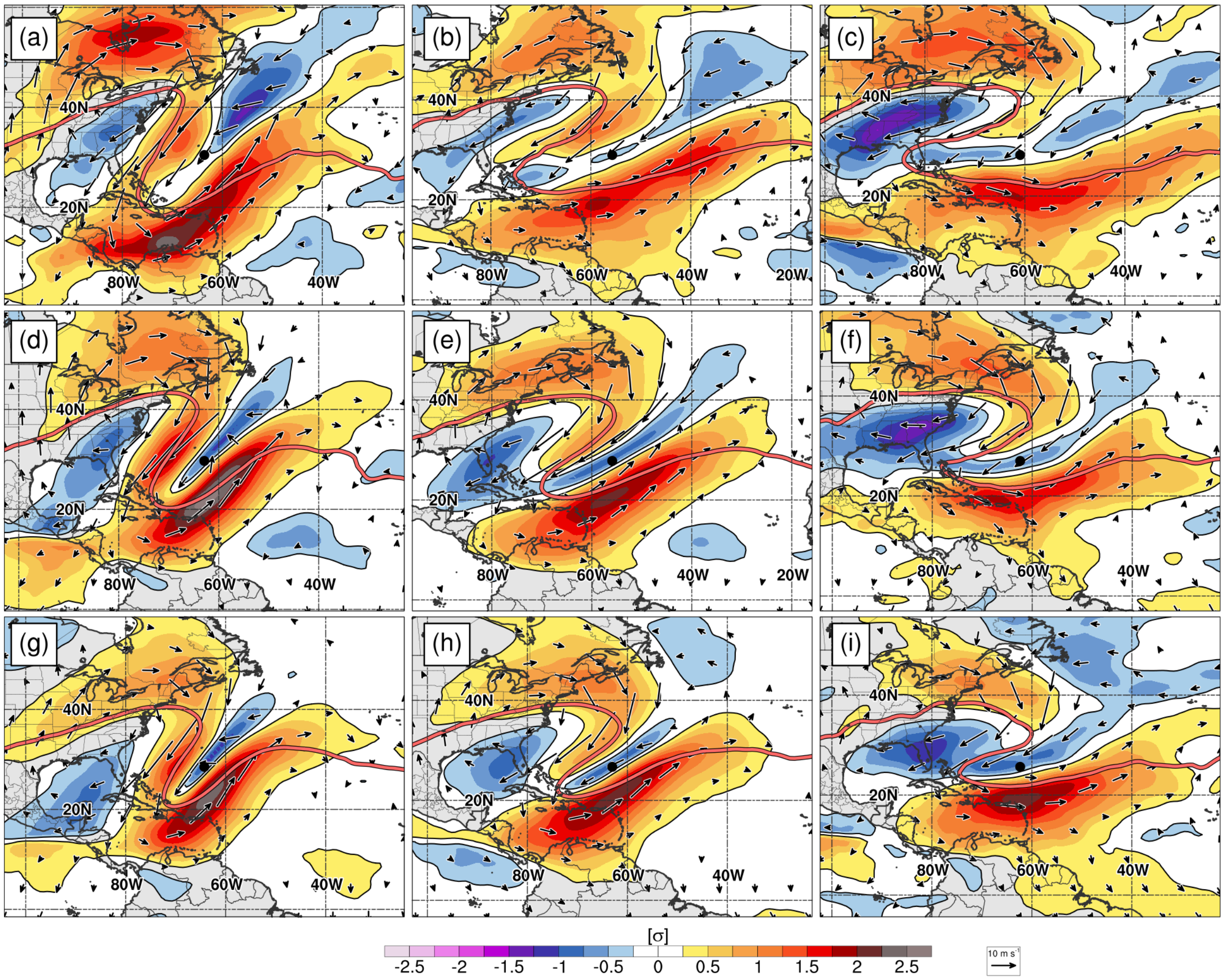

Fig. 4.4. Composite, standardized VWS anomalies (shaded, σ), VWS vector anomaly (vector, m s^{-1}), and the 350-K isentropic 2-PVU contour (red contour, PVU) for strong PVSs. The centroid positions of each strong PVS category denoted by the black circle in center of each plot. The nine composite categories are organized as in Fig. 4.3.

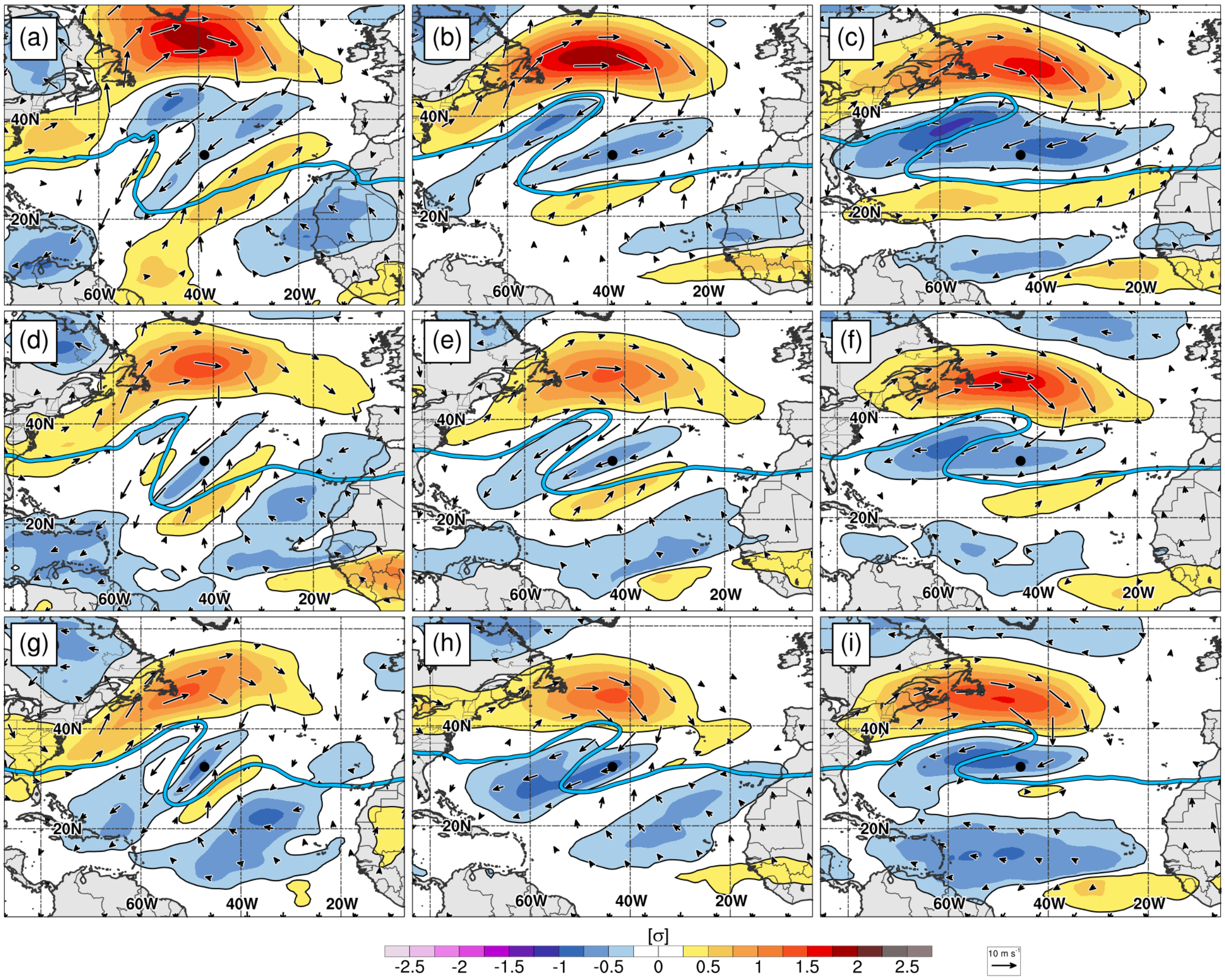

Fig 4.5. As in Fig. 4.4, except for the weak PVSs, where the 350-K isentropic 2-PVU contour is denoted as a blue contour.

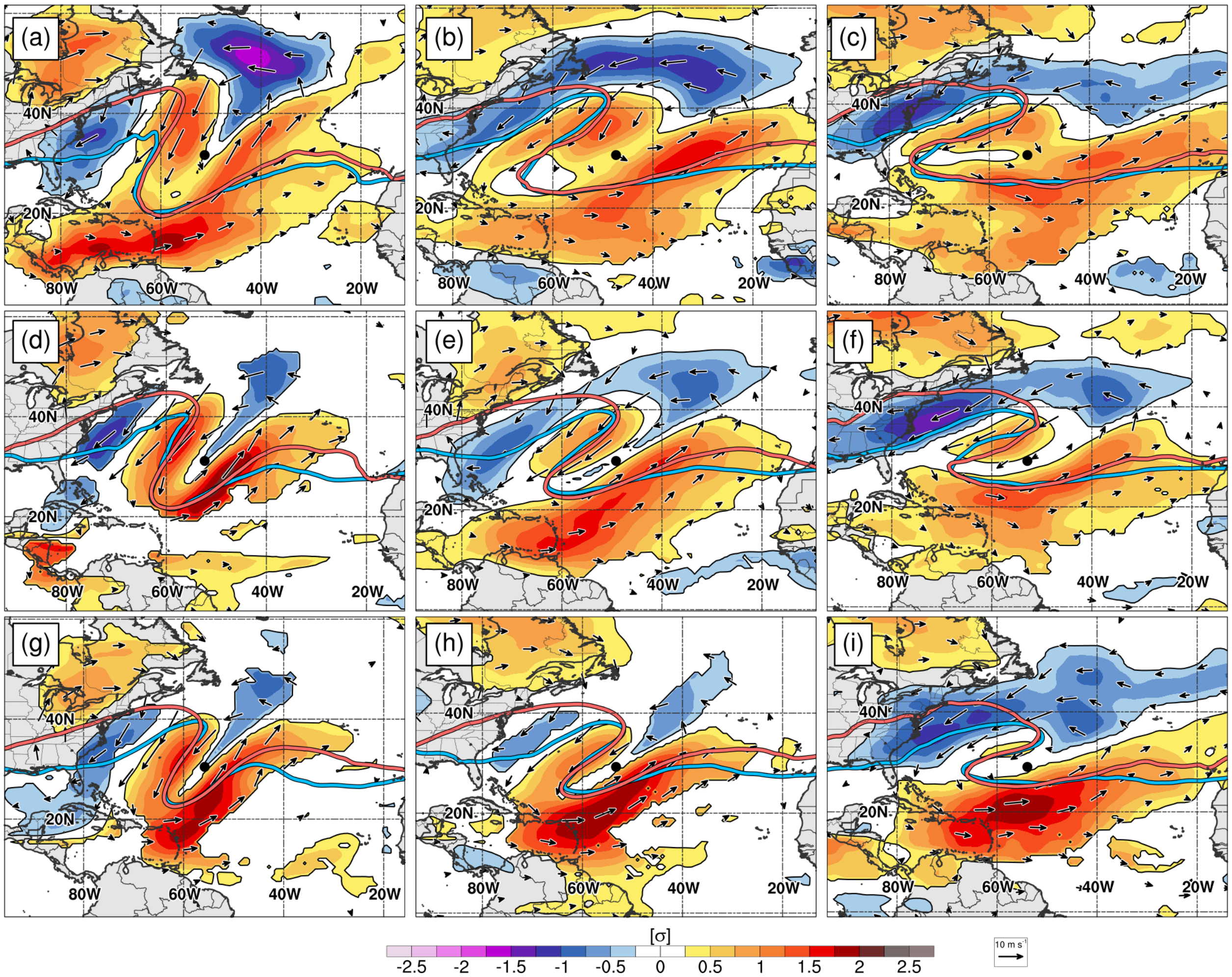

Fig. 4.6. Composite, standardized VWS anomaly difference (shaded, σ) and the VWS vector anomaly difference (vector, m s^{-1}) of strong minus weak PVSs, with the composite 350-K isentropic 2-PVU contour of strong and weak PVSs overlaid (red and blue contours, respectively). Shaded regions also indicate where standardized VWS anomaly differences are statistically significant. The nine composite categories are organized as in Fig. 4.3.

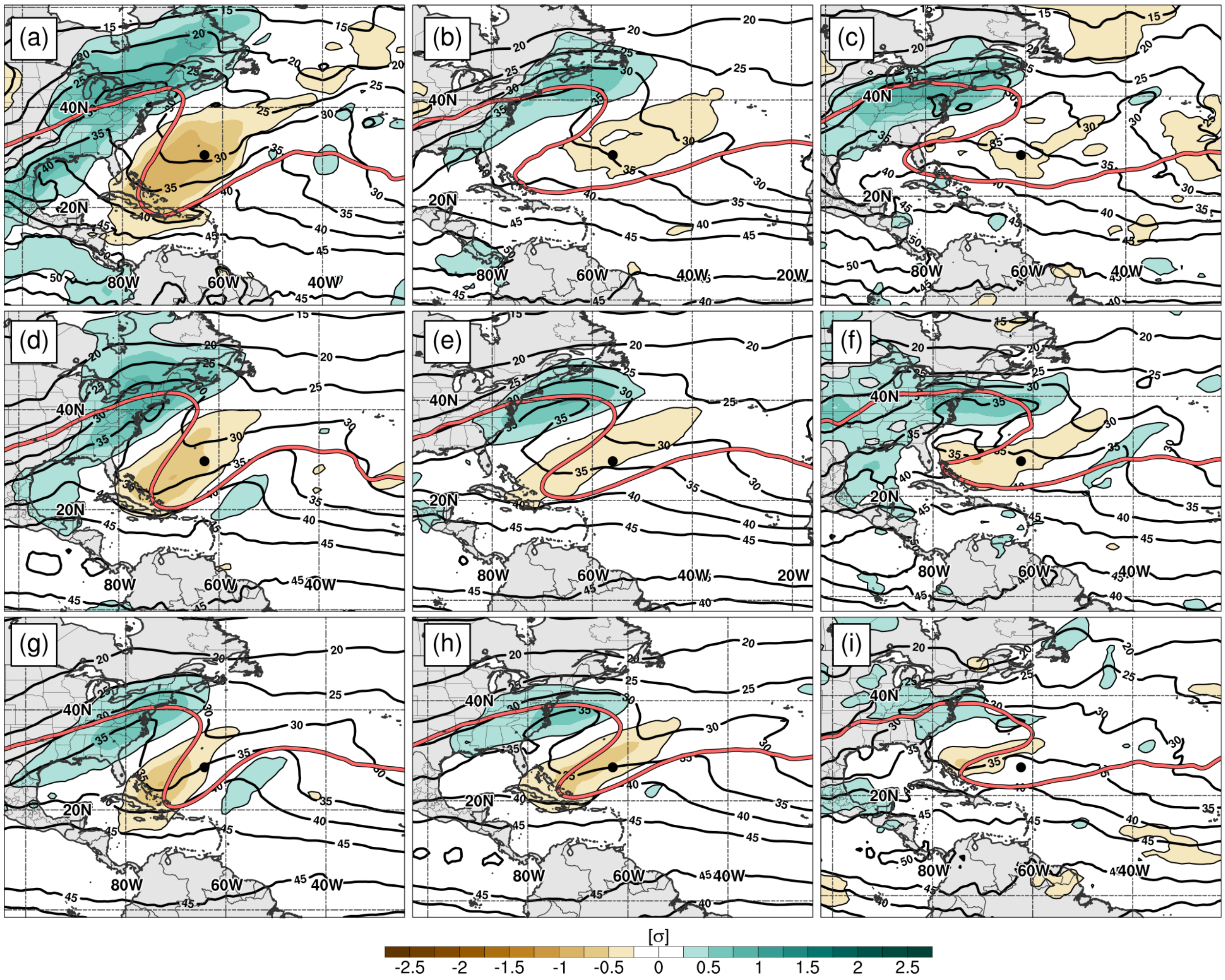

Fig. 4.7. As in Fig. 4.4, except for composite, standardized precipitable water anomalies (shaded, σ), and mean precipitable water (black contours, every 5 mm).

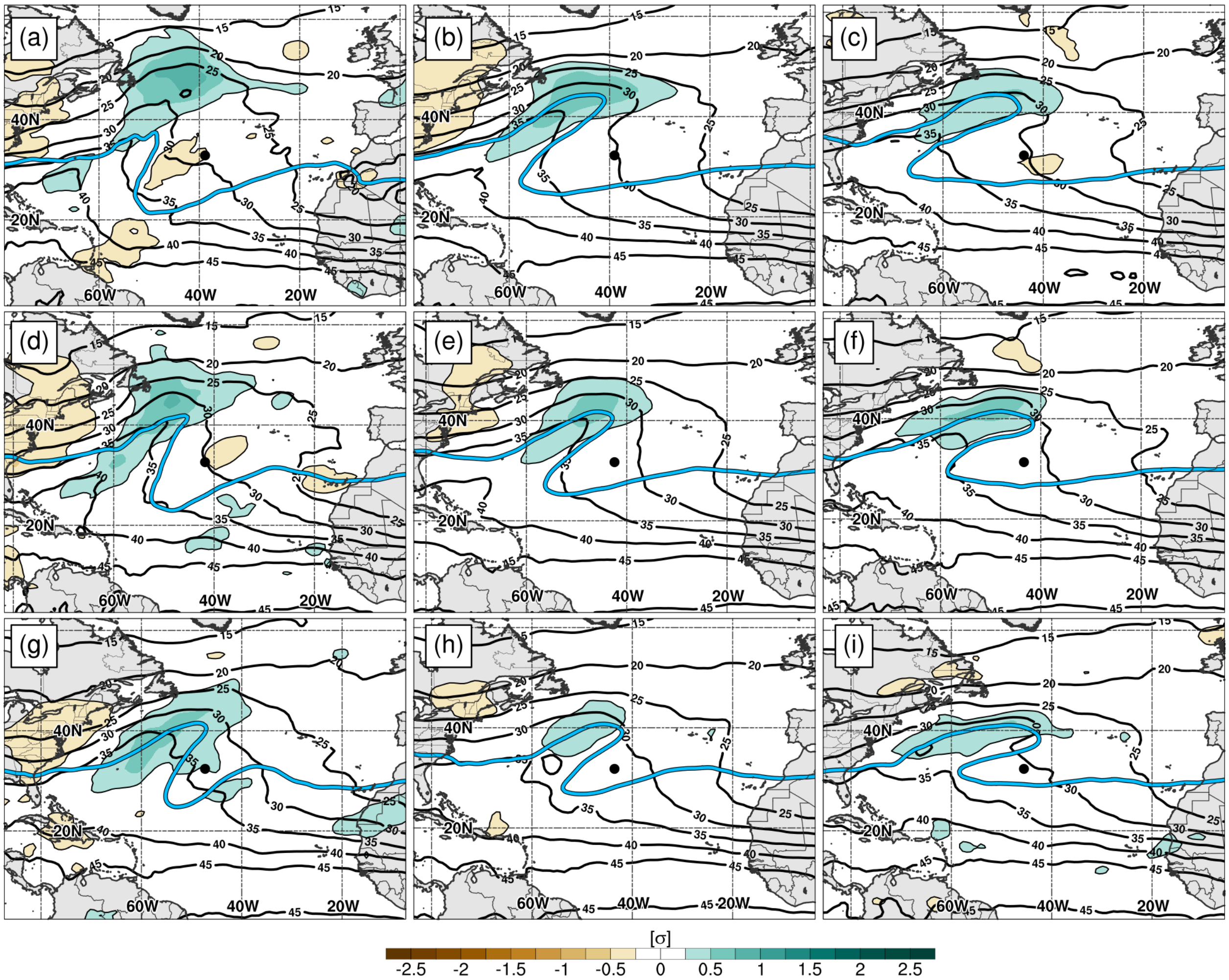

Fig. 4.8. As in Fig. 4.5, except for composite, standardized precipitable water anomalies (shaded, σ), and mean precipitable water (black contours, every 5 mm) for weak PVSs.

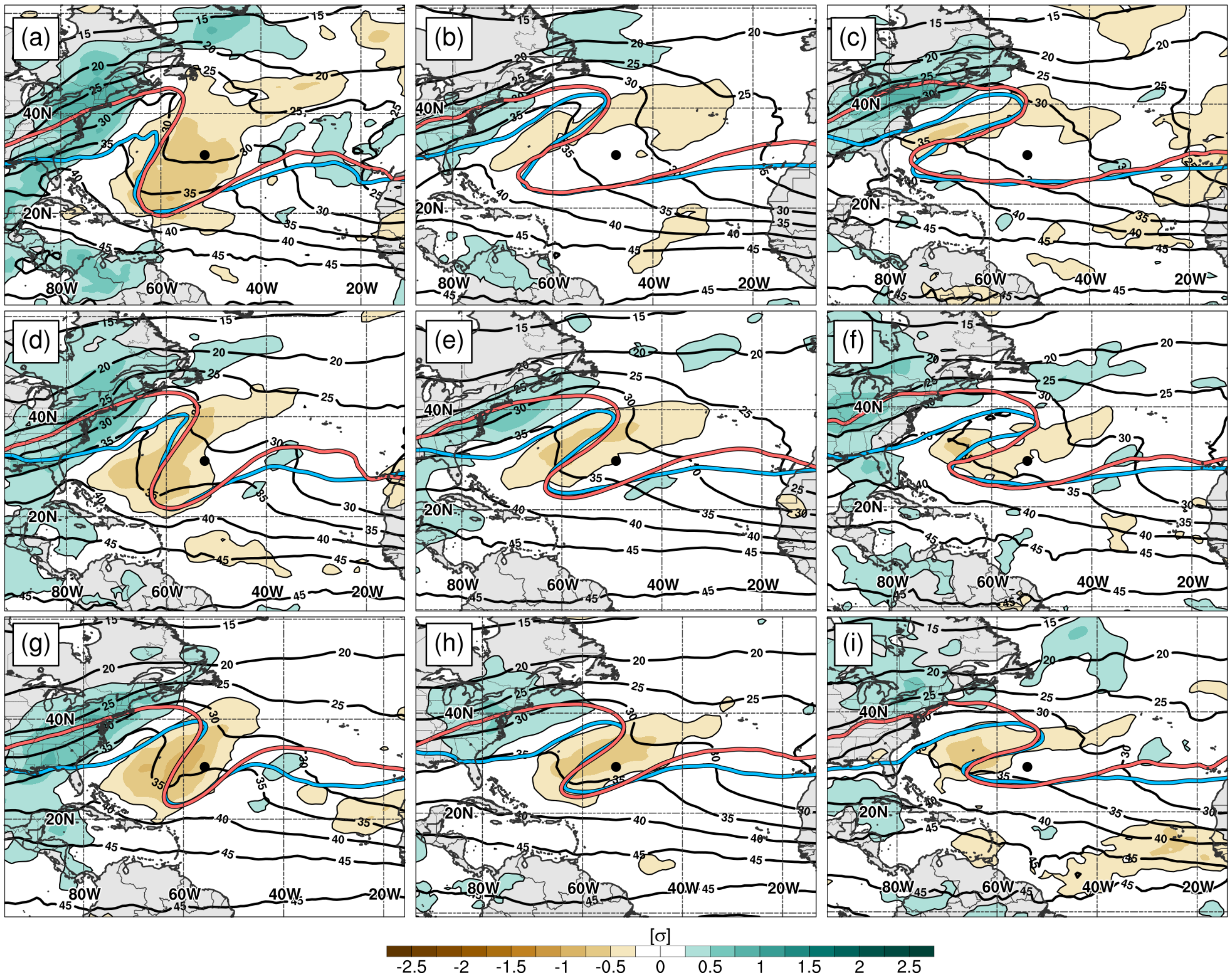

Fig. 4.9. As in Fig. 4.8, except for composite differences in standardized precipitable water anomaly (shaded, σ) and mean precipitable water (black contours, every 5 mm) of combined strong and weak PVSs composites. Shaded regions also indicate where standardized precipitable water anomaly differences are statistically significant.

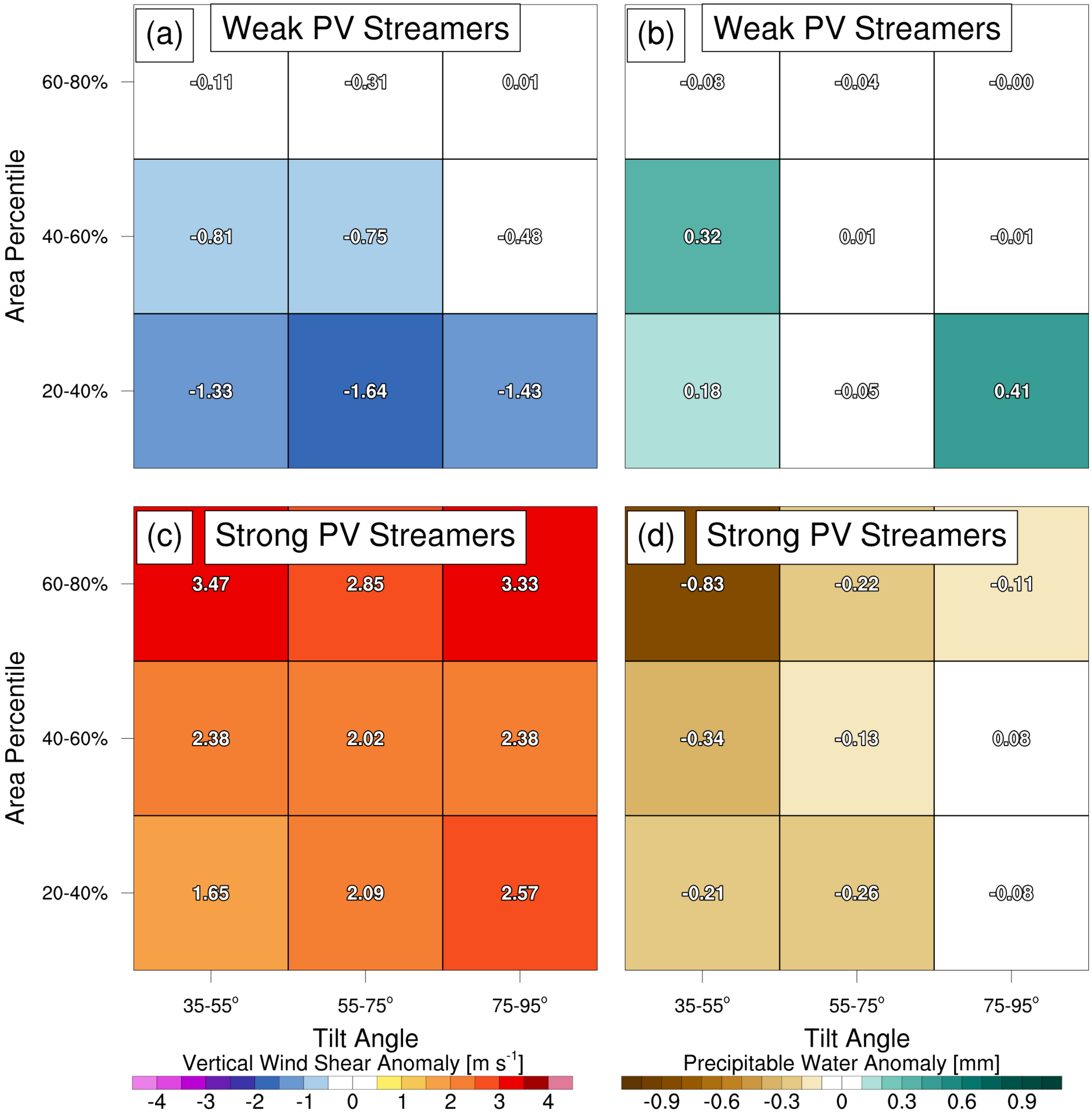

Fig. 4.10. (a,c) Average VWS anomalies (shaded, m s^{-1}) for weak (a) and strong (c) PVS categories sorted by tilt (x-axis) and area (y-axis) categories. (b–d) Average precipitable water anomalies (shaded, mm) for weak (b) and strong (d) PVS categories sorted by tilt (x-axis) and area (y-axis) categories. Raw values are provided within each box category. The region chosen for area averaging is illustrated in Fig. 4.1h where the box covers a region -20° to 0° latitude, and -40° to +40° longitude relative to the centroid of each PVS case.

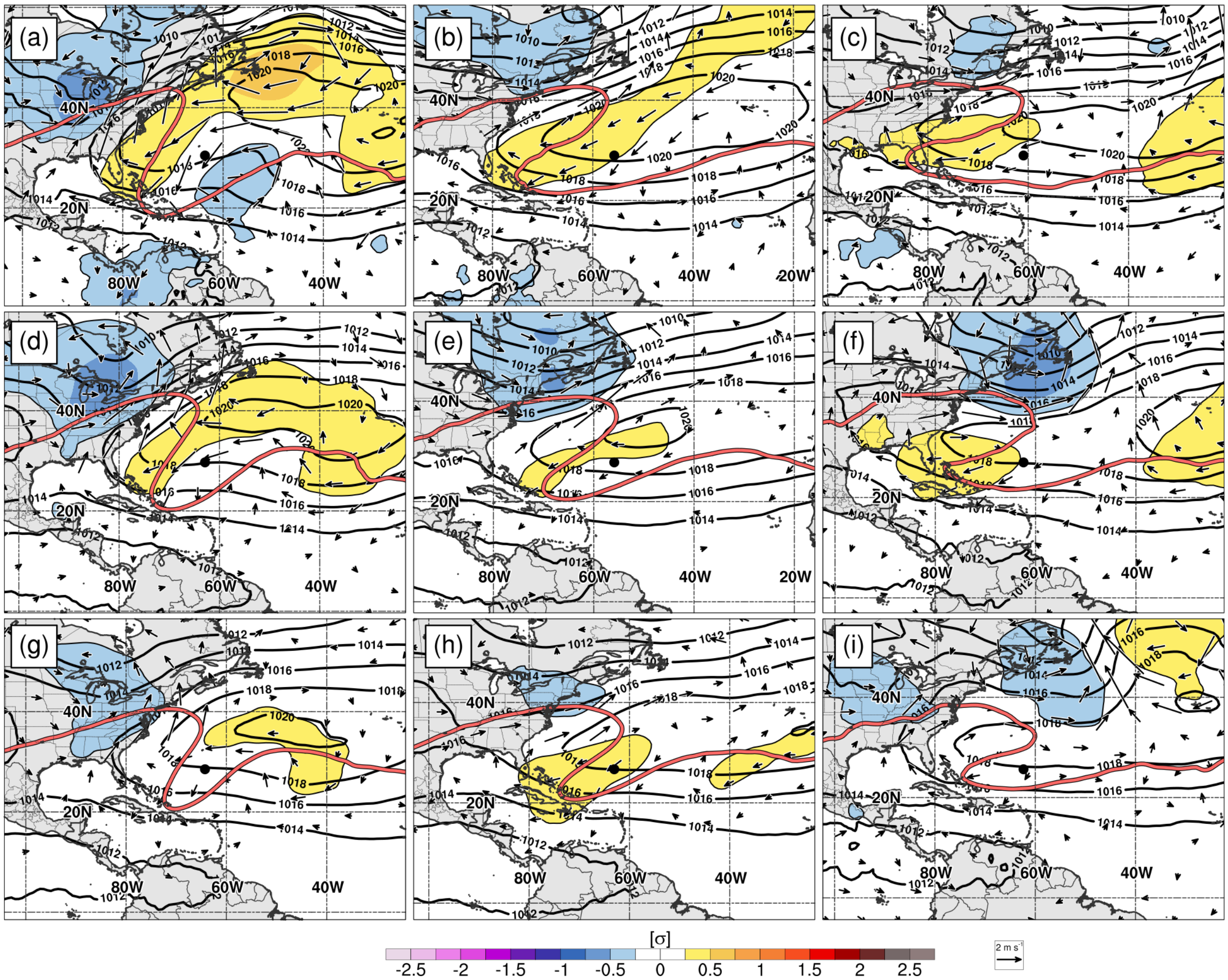

Fig. 4.11. As in Fig. 4.4, except for composite, standardized mean sea level pressure anomaly (shaded, σ), mean sea level pressure (black contours, every 2-hPa), and 925-hPa wind anomalies (vectors, >0.5m s^{-1}) for strong PVSs.

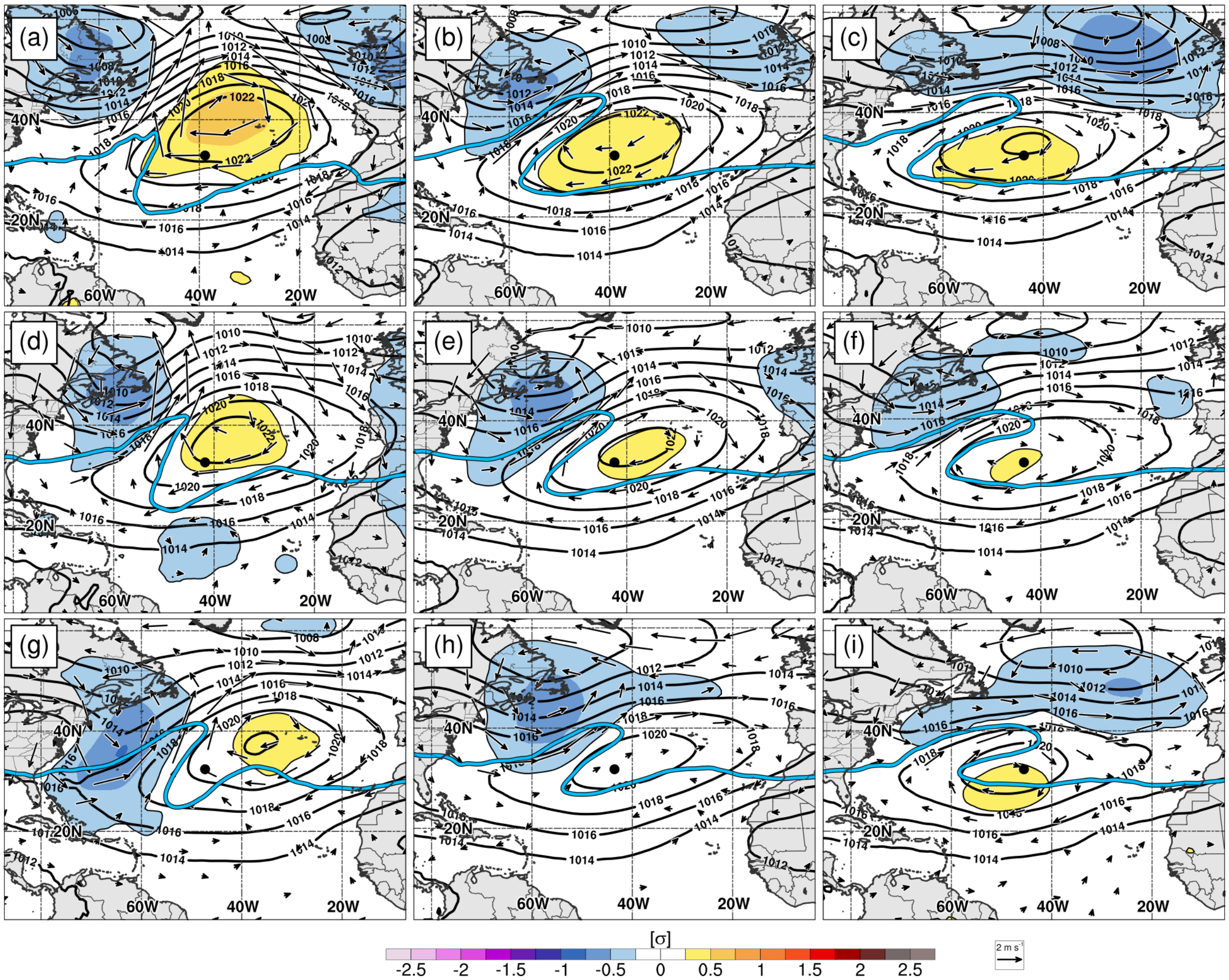

Fig. 4.12. As in Fig. 4.5, except for composite, standardized mean sea level pressure anomaly (shaded, σ), mean sea level pressure (black contours, every 2-hPa), and 925-hPa wind anomalies (vectors, >0.5m s^{-1}) for weak PVSs.

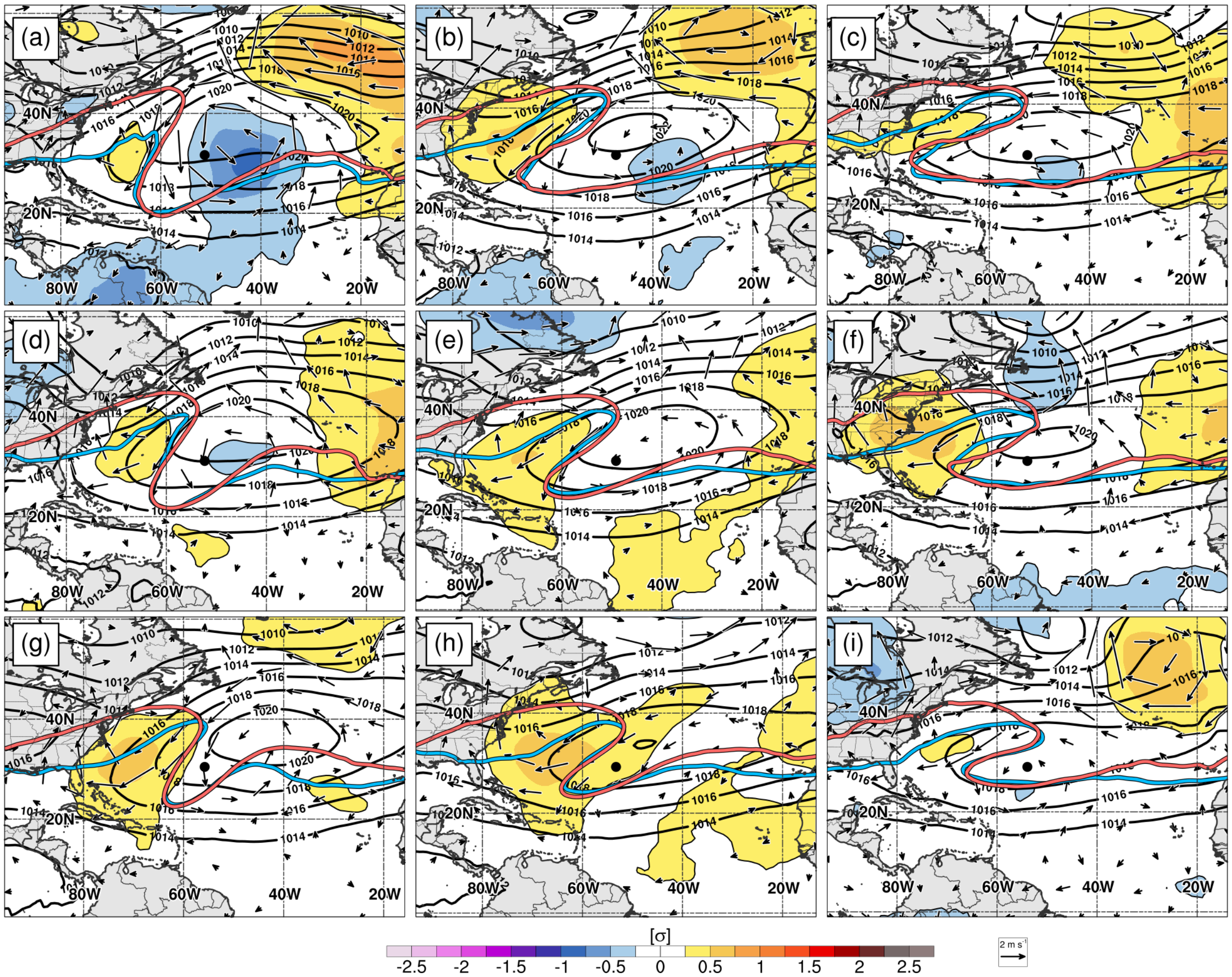

Fig. 4.13. As in Fig. 4.6, except for composite differences in standardized mean sea level pressure (shaded, σ), mean sea level pressure (black contours, every 2-hPa) of combined strong and weak PVSs composites, and 925-hPa wind anomaly differences (vectors, >0.5m s^{-1}). Shaded regions also indicate where standardized mean sea level pressure anomaly differences are statistically significant

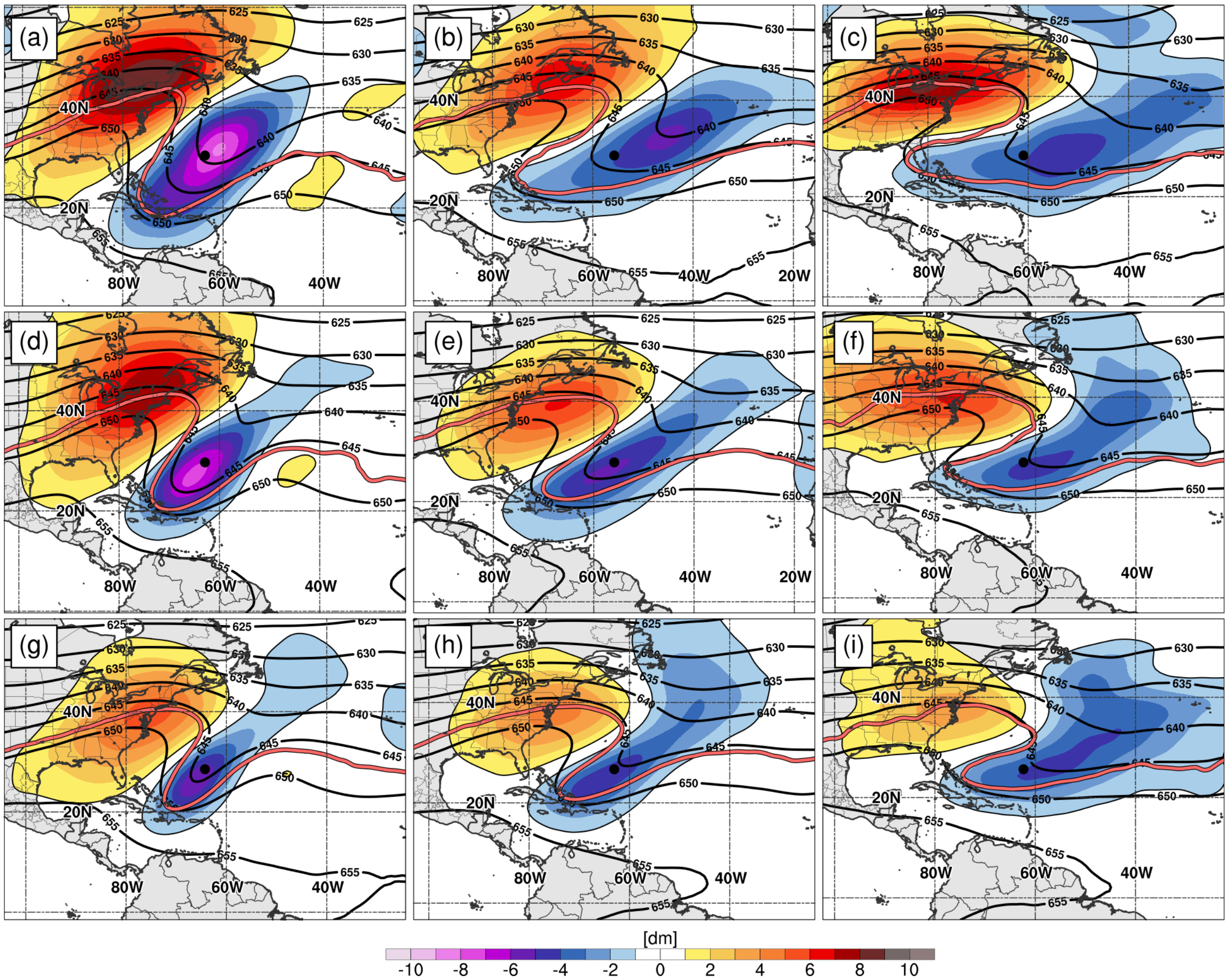

Fig. 4.14. As in Fig. 4.4, except for composite, 200–500-hPa thickness anomalies (shaded, dm), and mean 200–500-hPa thickness (black contours, every 5-dm) for strong PVSs.

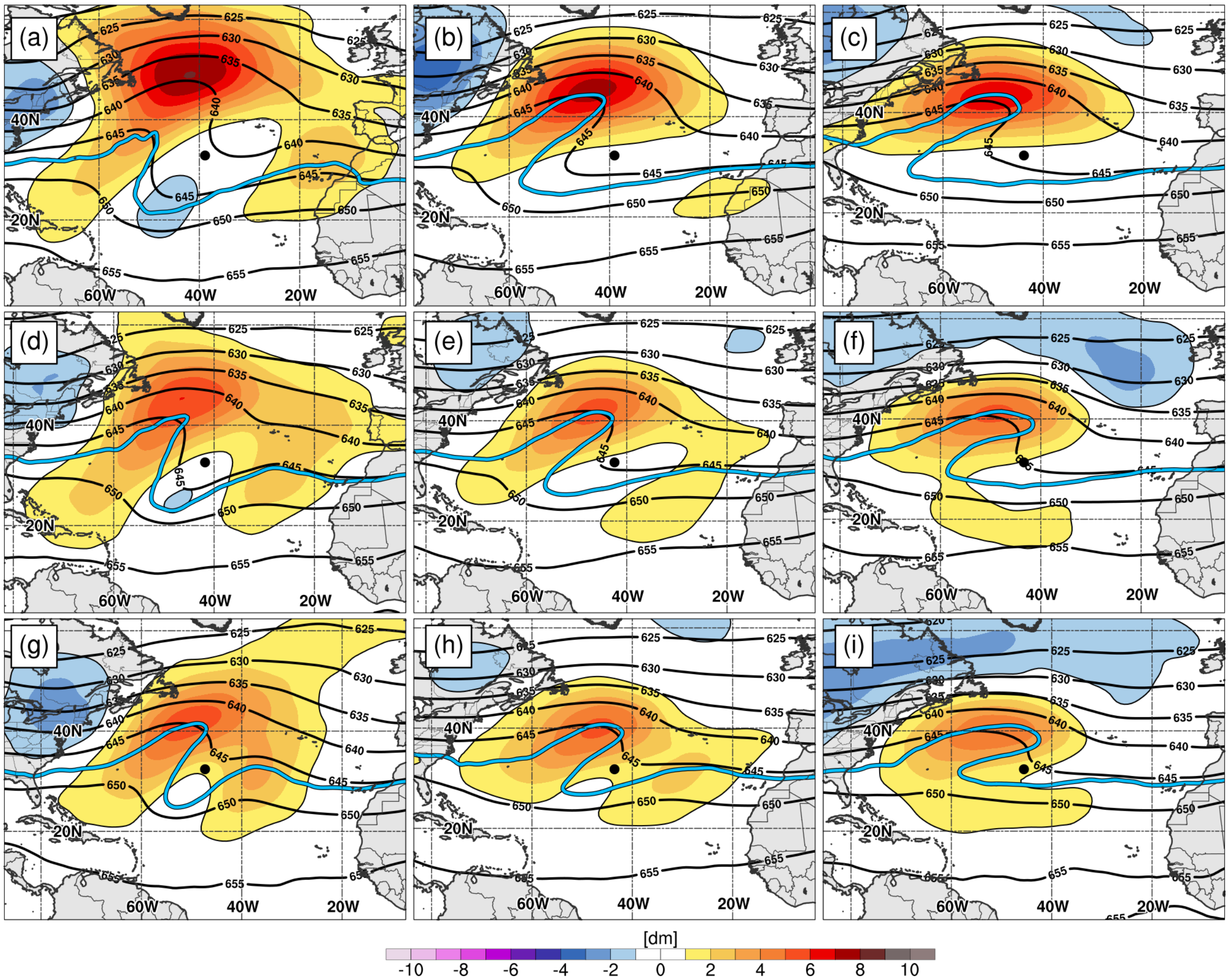

Fig. 4.15. As in Fig. 4.5, except for composite 200–500-hPa thickness anomalies (shaded, dm), and mean 200–500-hPa thickness (black contours, every 5-dm) for weak PVSs.

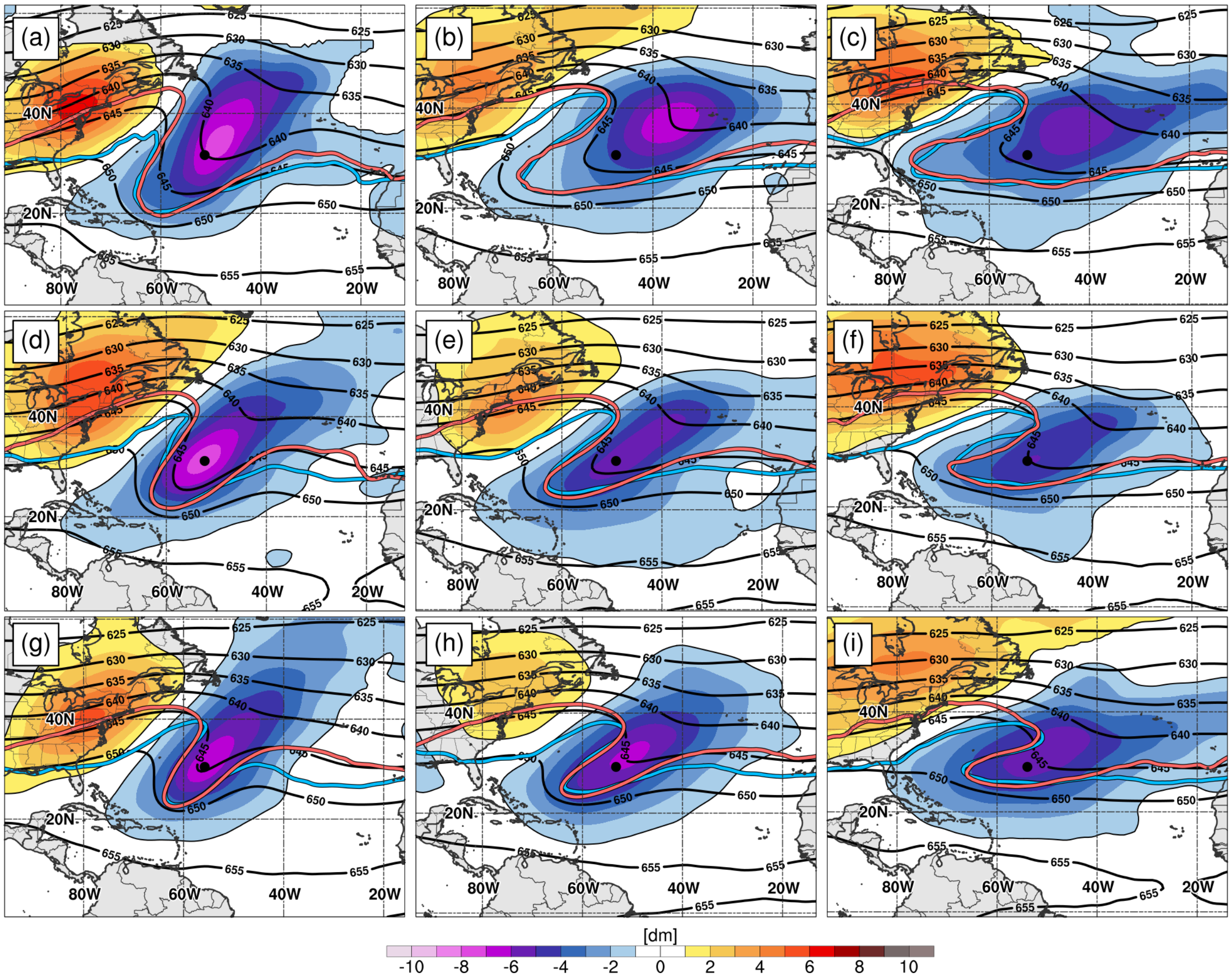

Fig. 4.16. As in Fig. 4.6, except for composite differences in 200–500-hPa thickness (shaded, dm) and mean 200–500-hPa thickness (black contours, every 5-dm) of combined strong and weak PVSs composites. Shaded regions also indicate where thickness anomaly differences are statistically significant.

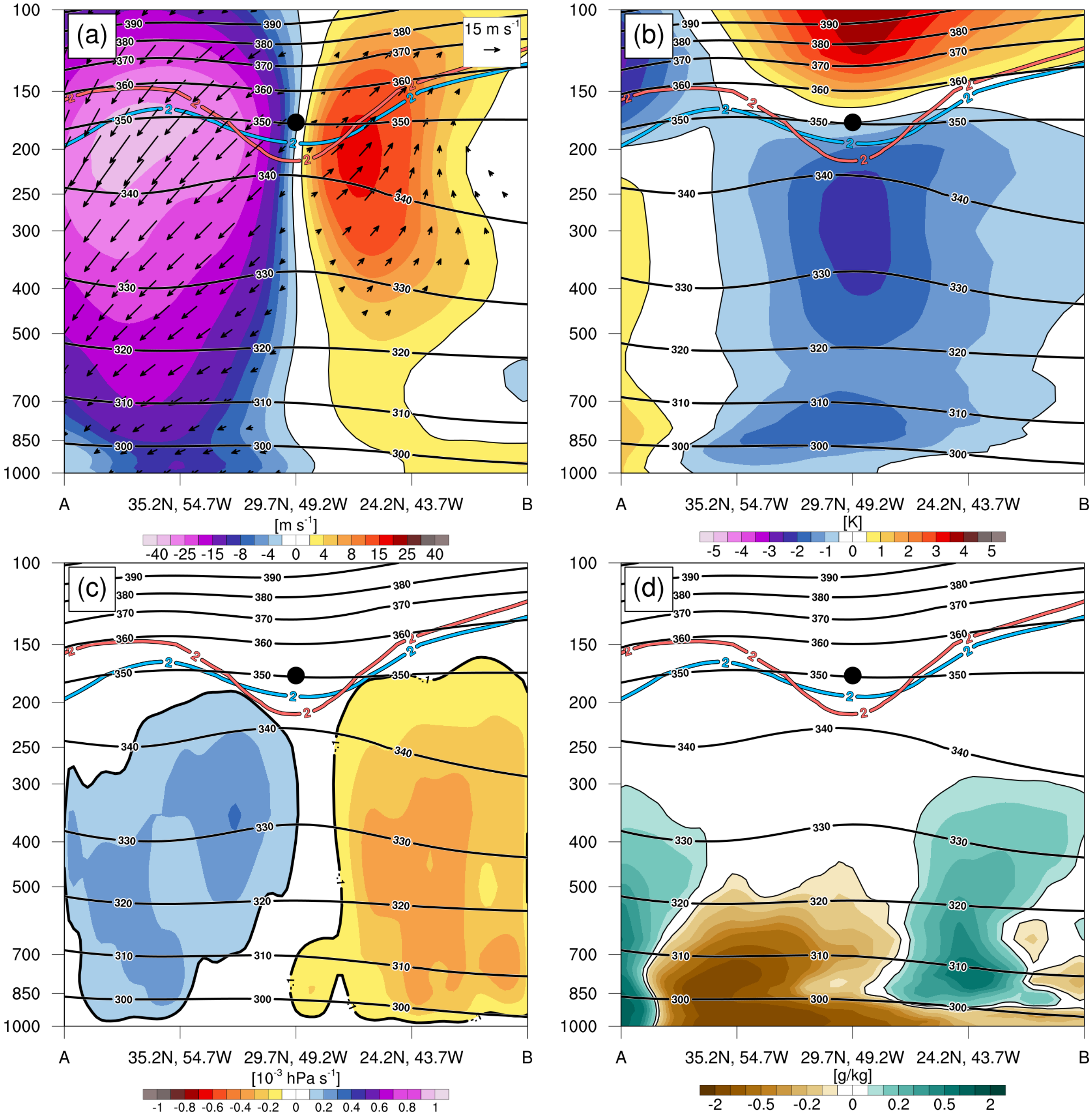

Fig. 4.17. Cross-section composite differences from northwest to southeast through the 55–75° tilt and 40–60th percentile strong minus weak PVS categories (see Fig. 4.1e for illustrated position of cross-section) for (a) wind normal to the cross-section (shaded, m s^{-1}), and actual vector wind direction (vectors, m s^{-1}), (b) temperature anomaly (shaded, K), (c) vertical motion anomaly (shaded, 10^{-3} hPa s^{-1}), and (d) specific humidity anomaly (shaded, g/kg). All panels show potential temperature (black contours, every 10K), the 2-PVU contour for strong and weak PVS composites (red and blue contours, respectively), and the composite centroid position of strong and weak PVSs (black circle).

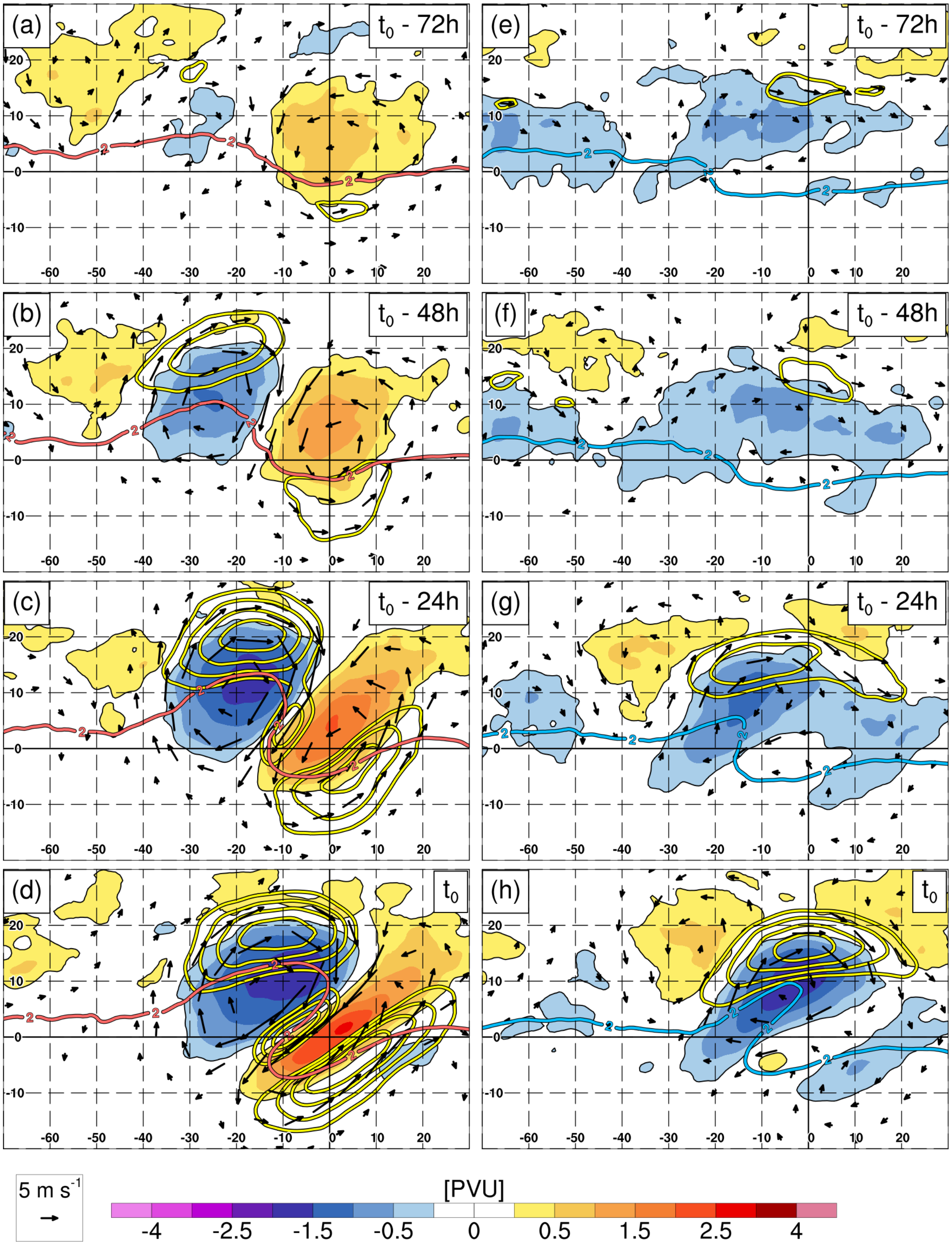

Fig. 4.18. Time-lagged composites of strong (a–d) and weak (e–h) PVSs using the 55–75° and 40–60th percentile category (see Fig. 4.1d). Plotted are 350-K isentropic PV anomalies (shaded, PVU), 200-hPa wind magnitude anomalies, (yellow contours, > 4 m s^{-1} every 2 m s^{-1}), 200-hPa vector wind anomalies (vectors, m s^{-1}), and the 350-K isentropic 2-PVU contour for strong and weak PVSs (red and blue contours, respectively). Latitude and longitude coordinates are relative to the PVS centroid in each figure (at 0,0).

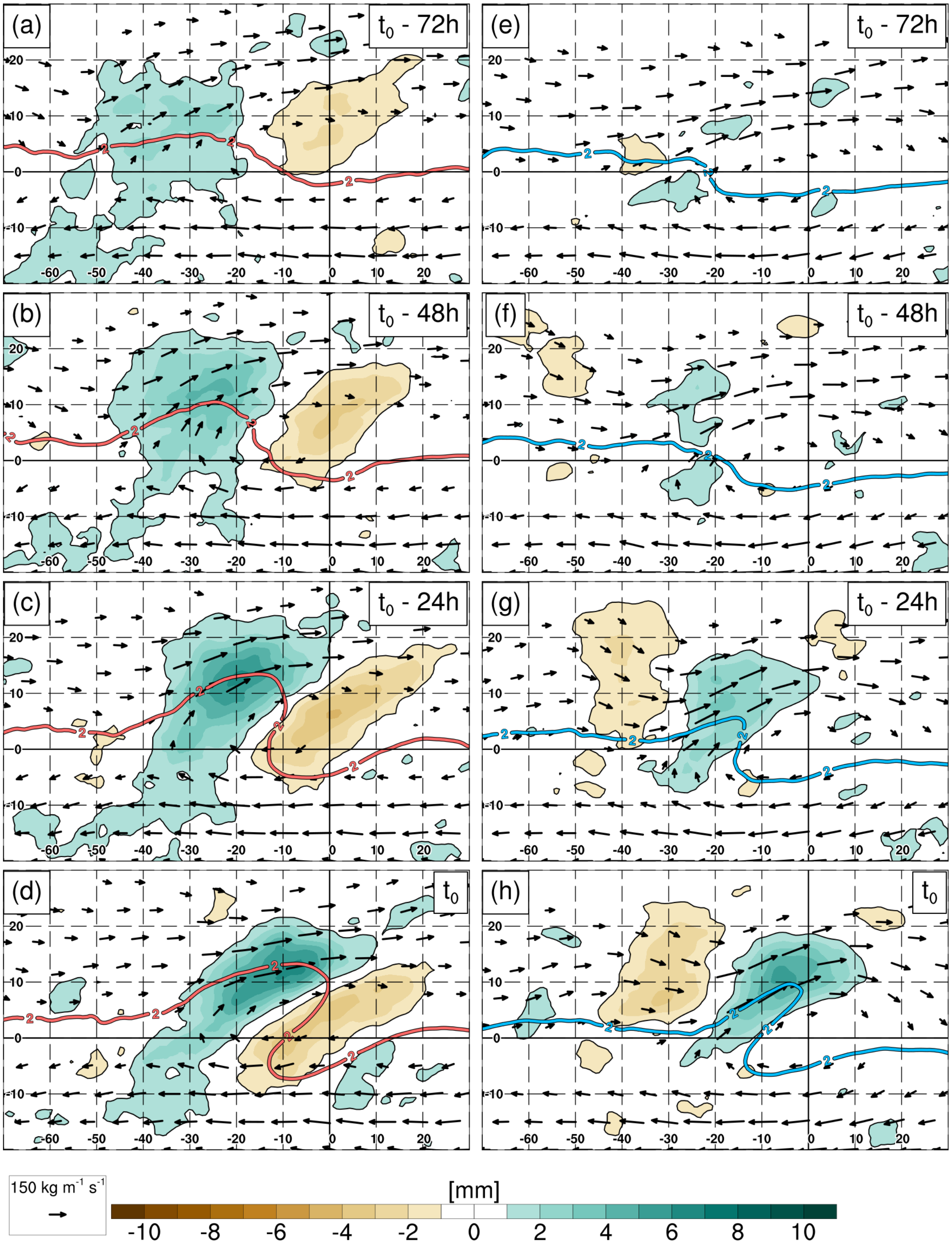

Fig. 4.19. As in Fig. 4.18, except for precipitable water anomalies (shaded, mm), 1000–300-hPa IVT (vectors, kg m^{-1} s^{-1}), and the 350-K isentropic 2-PVU contour for strong and weak PVSs (red and blue contours, respectively)

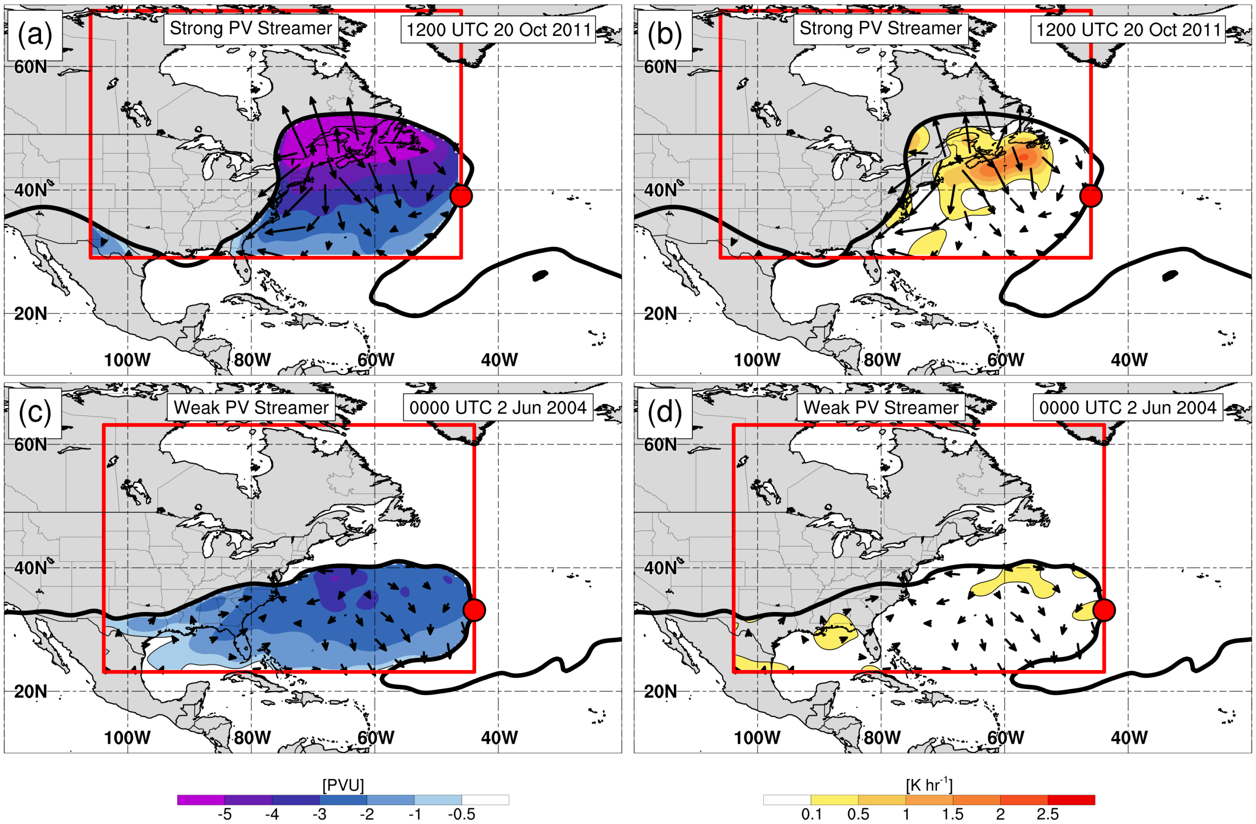

Fig. 4.20. Schematic illustrating how integrated PV advection by the irrotational wind and diabatic heating are computed for an example strong (a–b), and weak (c–d) PVS. Panels on the left (a,c) show negative PV anomalies (shaded, < -0.5 PVU) denoting the ridge. Panels on the right (b,d) show diabatic temperature tendency (shading, > 0.1 K hr^{-1}). All panels illustrate 350-K isentropic irrotational wind (vectors, m s^{-1}) and the 350-K isentropic 2-PVU contour (black contour). The box used for calculations (red line) is oriented from -10° to +30° latitude and -60° to 0° longitude relative to the starting point of the PVSs (red circle), which also denotes the AWB axis. Integrated values are only computed for grid points within the ridge (i.e., negative PV anomalies) in divergent outflow in < 2-PVU air.

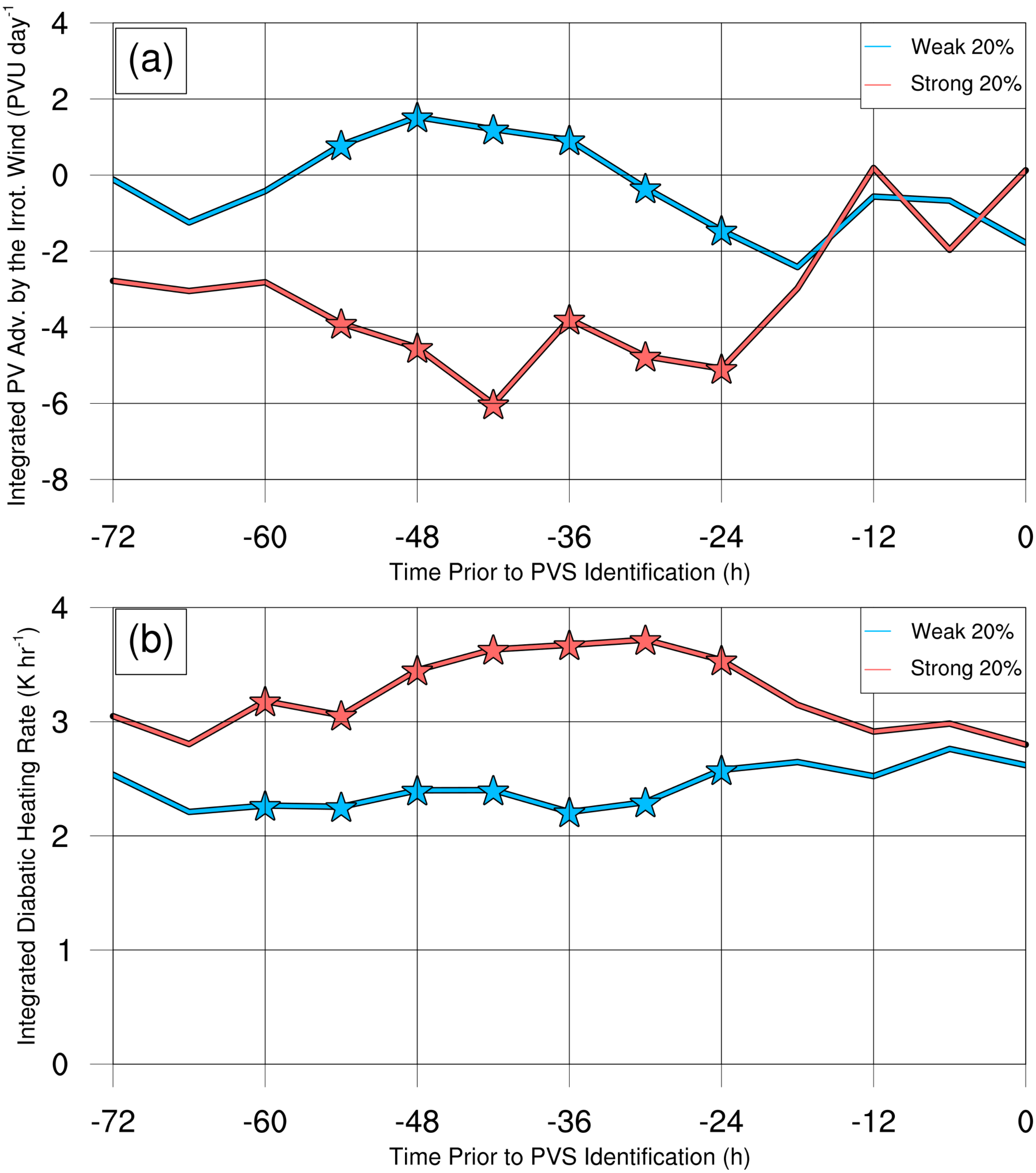

Fig. 4.21. (a) Time-lagged, composite average, integrated 350-K isentropic PV advection by the irrotational wind for strong and weak PVS cases (red and blue lines, respectively) using the regions illustrated in Fig. 4.18. (b) Composite average, integrated 400–600-hPa diabatic heating rate (K hr^{-1}) for strong and weak PVS cases (red and blue lines, respectively). Stars denote time periods where the average differences between strong and weak PVS cases are statistically significant.

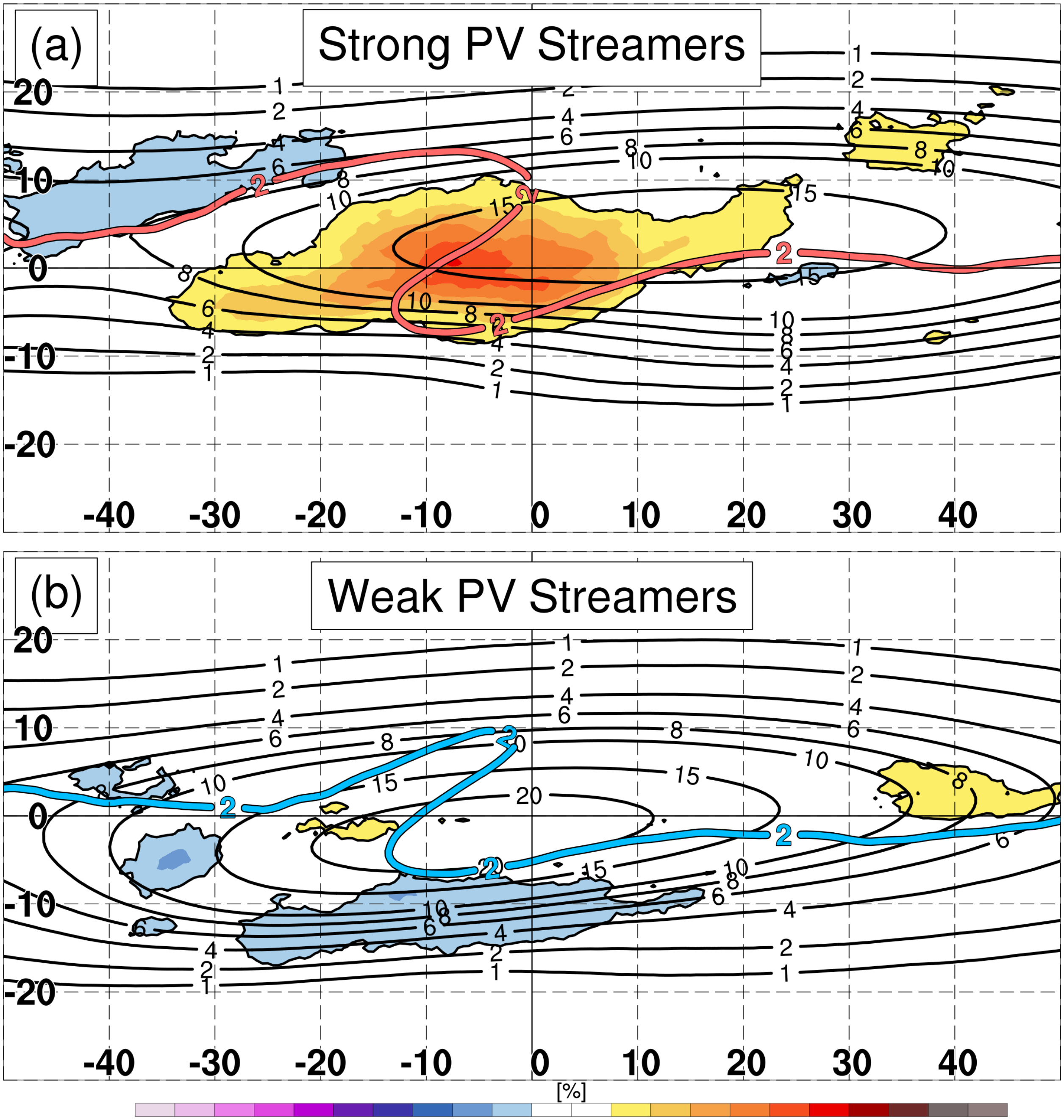

Fig. 4.22. Frequency anomaly of PVS occurrence (shaded, %), and climatological occurrence (black contours, %) in the 10 days before PVS occurrence of (a) strong PVSs and (b) weak PVSs. Latitude and longitude coordinates are all relative to the PVS centroids at t_0, (0,0).

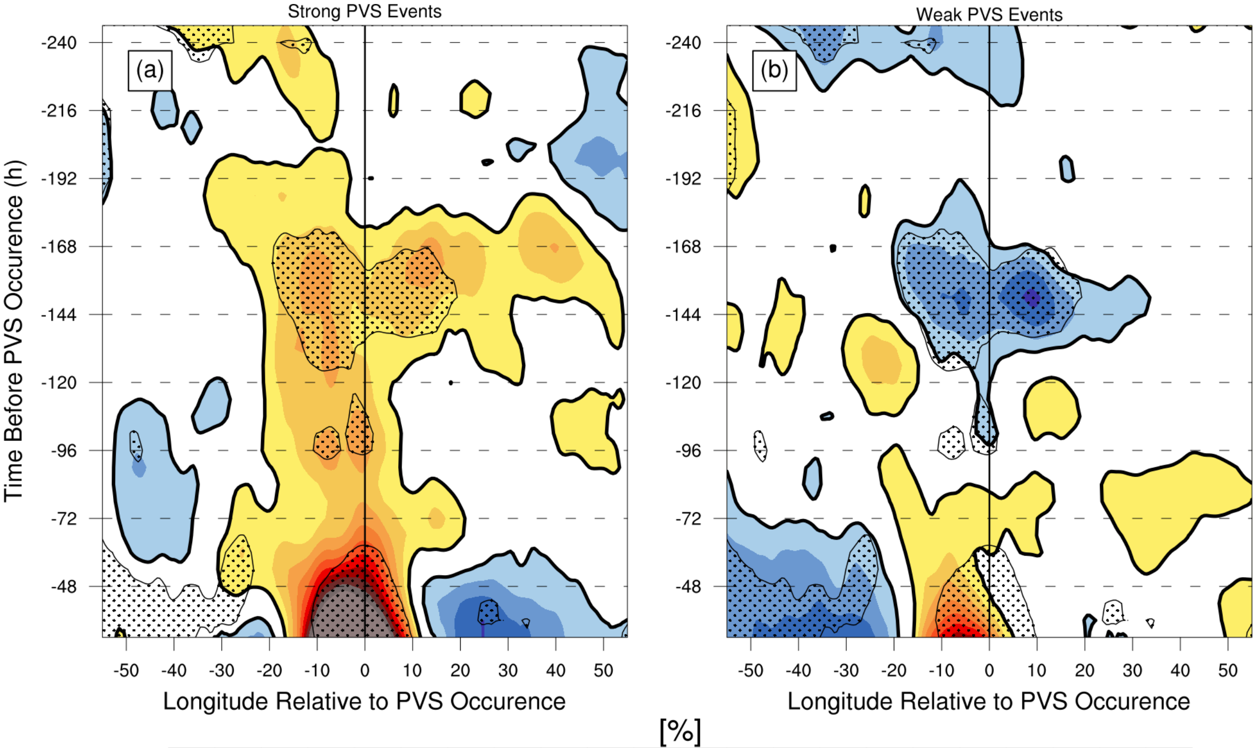

Fig. 4.23. Hovmöller of frequency anomaly of PVS occurrence (shaded, %) for the 10 days before PVS occurrence (t_0) for (a) strong PVSs and (b) weak PVSs. Hovmöllers averaged -10° to +10° latitude relative to the PVS centroids. Statistically significant differences between the strong and weak PVSs are denoted by black stippling.

5. Impacts of PVS activity on TC activity in the NATL basin

5.1 Introduction

The literature reviewed earlier in this dissertation detailed the potential linkages between TC activity and PVS activity. In the previous chapter, PVSs were shown be associated with changes of environmental variables in the NATL basin that impact TC activity (i.e., VWS, precipitable water), suggesting that PVS activity could impact TC activity. This chapter investigates the relationship between PVS activity and TC activity in order to identify how PVSs modify overall TC activity, TC spatial distributions, and TC genesis pathways. The analysis herein uses the PVS climatology in conjunction with several datasets that provide position, intensity, and genesis information for TCs in the NATL basin to investigate how PVSs impact TCs. A brief data and methods section is first presented to discuss the methods used with these datasets. Then, a comparison of PVS activity with TC activity is presented, using statistical and spatial relationships. Composites of TC location relative to PVS location are also presented when these events occur simultaneously. Finally, we will conclude with how PVS activity modifies TCG pathways in the NATL basin.

5.2 Data and methods

5.2.1. Data

This chapter uses the PVS events obtained from the ERAI climatology developed in Chapter 2 of this dissertation and presented in Chapter 3. PVSs of all intensities, areas, and tilts from 10°W–100°W are considered from 1 June–30 November for 1979–2015 to use in comparison with TC activity.

TC position and intensity information in the NATL basin is provided by the International Best Track Archive for Climate Stewardship (IBTrACS, Knapp et al. 2010) version 3 release 9, which includes best-track TC information up to 2015. The data available in IBTrACS is identical to that available from the National Hurricane Center's (NHC's) Atlantic hurricane dataset (HURDAT2), from which we obtain six-hourly information on TC location, maximum sustained winds, and storm type. For this study, we only retain TCs tracks that at reach a maximum wind speed of at least 35 kt. Only tropical and subtropical storm type points are considered.

This study uses the TCG pathway climatology developed by MC13 to categorize different TCG pathways that occur in the NATL basin between 1979–2010. In this pathway climatology, TCG events were categorized using a pair of classification metrics. The first is the *Q-metric*, defined as a 6^o averaged, 400–200-hPa Q vector convergence using the nondivergent wind in place of the traditional geostrophic wind for high Rossby number flows. The second metric is lower-level thickness asymmetry (i.e., the *Th-metric*), defined as the maximum difference in 1000–700-hPa thickness in two hemispheres within 10^o of the TC location.

Using these two metrics, five separate TCG pathway categories were created based on intensity variations in the *Q-metric* and *Th-metric*. The non-baroclinic and low-level baroclinic TCG pathways feature low *Q-metric* values, while the trough-induced, weak TT, and strong TT TCG pathways feature high *Q-metric* values. This change in the *Q-metric* helps to distinguish between TCs that develop in a purely tropical environment (low *Q-metric*) versus TCs that develop where forcing for ascent is associated with an upper-tropospheric trough (high *Q-metric*) (McTaggart Cowan et al. 2008; MC13). This dissertation opts to reorganize these five categories into two more general categories, baroclinic TCG (i.e., high *Q-metric* pathways: including trough induced, weak TT, and strong TT pathways) and non-baroclinic TCG (i.e., low *Q-metric* pathways: including non-baroclinic and low-level baroclinic pathways). The reorganization of the original TCG pathways allow this study to compare TCs that develop near upper-tropospheric troughs that may resemble PVSs (i.e., baroclinic TCG) versus TCs that develop without any upper-tropospheric precursors (i.e., non-baroclinic TCG). The pathway characteristics associated with these TCs are only applicable before and at their genesis (MC13). IBTrACS position and intensity information is used to determine track and intensity information for these TCs after genesis.

5.2.2. Methods used the compare PVS activity to TC activity

PVS activity is quantified using the PVS activity index (PVSI) defined in equation 3.1, which integrates PVS activity by the area, intensity, and number of individual PVS events during the TC season. PVSI is also defined for in a shorter period (i.e., 30 days) to show intraseasonal variations in PVS activity and how this metric changes in active versus inactive TC seasons.

To compare PVSI to TC activity, another index is needed that combines intensity and duration of TC events. One such index is accumulated cyclone energy (ACE; Bell et al. 2000), which we use to directly compare to PVS activity. ACE is defined as:

$$ACE = 10^{-4} \sum {v_{max}}^{2} \tag{5.1}$$

where v_{max} is the maximum sustained surface winds of a TC, which is squared and summed for every 6-h period for all named TCs (≥ 35 kt; 1 kt = 0.51 m s^{-1}) in the NATL basin. Since both the PVSI and ACE are similarly defined at 6-h intervals when PVSs or TCs are present, it is possible to compare these two metrics over a TC season (1 June–30 November). The top and bottom eight years of total seasonal ACE (roughly representing the top and bottom 20th percentiles) will be used as a subset for active and inactive TC seasons which will be compared to PVS activity. A similar division is conducted for the top and bottom eight PVS activity years (using PVSI) to show how ACE is modulated in active and inactive PVSI years. Seasonal averages of environmental variables in the NATL basin (i.e., VWS, precipitable water, thickness, sea level pressure) are also computed to show how these quantities change in bottom minus top ACE years and top minus bottom PVSI years. Bootstrap resampling using 1000-permutations, sampling the top and bottom ACE and PVSI years, is conducted to deduce statistical significance between these year subsets, with the 5th and 95th percentile confidence limits used for negative and positive variable differences respectively, unless otherwise stated.

The above calculations investigate seasonal PVS and TC relationships, but not necessarily when PVSs and TCs occur at the same time. To investigate these instances, composites of TC positions relative to PVS cases will be created, where the centroid of PVS cases is used to center the composites. This composing is done to reveal where TCs are located at the time of PVS identification. This will allow us to determine if TC clustering occurs, and at what intensities or direction of motion, relative to PVS locations. These composites are created for all PVSs cases, and for the PVSs in the top and bottom 20th percentile in intensity, similar to the methodology described in Chapter 4. In this analysis, all tilts and areas are considered together for brevity.

5.3. Results: Comparison of PVS activity and TC activity on annual timescales

5.3.1. Statistical overview of yearly PVS activity and TC activity

Figure 5.1 shows a series of scatter plots that compare different PVS metrics to yearly ACE. In general, there is a negative relationship between the total number of PVS events identified each year and ACE (r = -0.48; Fig. 5.1a), and a slightly weaker negative relationship between average PVS area and ACE (r = -0.41; Fig. 5.1b). These relationships are similar to the results in Zhang et al. (2016, 2017), who found an even higher negative correlation between RWB frequency and ACE. Their analysis differs in subtle ways, however, namely by using a smaller climatological period to correlate ACE and RWB activity (July–October), a smaller region to identify RWB events (Zhang et al. 2017; see D0 in their Fig. 1), and a different methodology to identify PVS-like features (i.e., Abatzoglou and Magnusdottir 2006). While this study finds a negative correlation between PVS frequency and ACE, the relationship is dependent on the intensity of the PVS (Fig. 5.1c,d). For example, yearly ACE is more negatively correlated to the number of strong PVSs (r = -0.54, Fig. 5.1c) than to all PVS events. Conversely, yearly ACE has a weak *positive* correlation with the number of weak PVSs (r = 0.33, Fig. 5.1d). These results suggest that PVS intensity strongly dictates the overall relationship between PVS and TC activity.

Given that PVS intensity modifies the relationship between ACE and TC activity, it is beneficial to compare ACE to a metric that accounts for changes in PVS intensity. PVSI is defined in this dissertation to combine the effects of PVS frequency, area, and intensity, and is correlated to seasonal ACE in Fig. 5.2. Overall, PVSI possesses a negative correlation with ACE (r = -0.55), which is a greater negative correlation than using the number, area, or intensity of PVSs alone. While a linear trend line is used to assess this correlation (black solid line), the scatter plot in Fig. 5.2 suggests the relationship between the PVS activity index and ACE may be closer to exponential (red dashed line) since the exponential curve explains 3.3% more variance than the linear trend line. In general, ACE exhibits higher spread for lower PVS activity index values (standard deviation $\pm 60.8\times10^4$ kt^2 for PVSI < 65×10^4 σ), but lower spread for high PVS activity index values (standard deviation ± 24.2 kt^2 10^4 for PVSI > 65×10^4 σ). This result is more striking when noting that all years with PVSI > 65×10^4 σ possess ACE under the 1979–2015 mean (102.4×10^4 kt^2). The change in ACE variance with increasing PVSI is credible, since in low PVSI years, PVSs are weaker, smaller, or less common, allowing other factors to impart a greater influence on TC activity (e.g., ENSO, MDR SSTs). For high PVSI years, however, PVSs are stronger, larger, and more common, which allows their associated increases in VWS and decreases in precipitable water to exert a greater negative influence on TC activity (see Fig. 4.8 in Chapter 4). While the yearly negative correlation between PVSI and ACE is only moderate, it is statistically significant and stronger than correlations related to other indices presented in Table 5.1 that have previously been used to project TC activity, such as ENSO, MDR SSTs, and the AMO, which will be discussed later in this chapter.

Another way to assess the relationship between PVS activity and TC activity is to compare the top and bottom eight ACE years (red and blue dots, Fig. 5.2) to see how PVS metrics change in these subsets. The years selected for the top and bottom ACE years are available in Table 5.2. The bar plot comparison in Fig. 5.3 help to illustrate which PVS variables (intensity, area, frequency) are changing the most between top and bottom ACE years. Compared to low ACE years, high ACE years have fewer PVSs (531 vs. 605; -12.2%), fewer large PVSs (> 80th percentile, 89 vs. 137; -35.1%), much fewer strong PVSs (82 vs. 141; -41.8%), and many more weak PVSs (141 vs. 96; +46.9%). These results are consistent with top ACE years having a lower overall PVSI (average 47.7×10^4 σ) compared to bottom ACE years (average 72.5×10^4 σ). Of note is how the percentage change between strong and weak PVS events is larger than the total difference in all PVS events. This provides additional evidence that yearly PVS intensity changes are a significant factor governing TC activity differences.

5.3.2. Spatial pattern of top and bottom ACE and PVS activity years

So far we have documented statistical correlations between PVSI and ACE, and how the number of PVSs change in top and bottom ACE years. It is also illuminating, however, to plot correlations between PVS frequency and ACE in a spatial sense (Fig. 5.4). Over most of the NATL basin, a negative correlation exists between PVS frequency and ACE, though this negative correlation increases in magnitude (between -0.3 to -0.6) and is statistically significant mainly equatorward of 30^{o}N in the western NATL basin. This area is associated with the most TC activity as evidenced by the wide swath of climatological ACE between 2–6×10^{4} kt^{2} spanning the region. The negative correlation in this region signifies that lower ACE is observed as PVS frequency increases over this part of the domain.

To further confirm the relationship between PVS frequency and ACE, Fig. 5.5 shows yearly PVS frequency anomalies relative to climatology for bottom and top ACE years. Not surprisingly, bottom ACE years exhibit an expansive area (70^{o}–30^{o}W) of statistically significant positive PVS frequency anomalies (between +3 to +6%) relative to climatology, mostly equatorward of the climatological PVS occurrence maximum (Fig. 5.4a). One interpretation of this map is that the time-mean TUTT axis in these seasons may be stronger and displaced equatorward closer to the MDR in the NATL basin, which is associated with enhanced VWS equatorward of the TUTT and suppressed moisture along the TUTT axis (Fitzpatrick et al. 1995; Knaff 1997). In contrast, top ACE years exhibit an expansive area (70^{o}–30^{o}W) of statistically significant negative PVS frequency anomalies (between -4 to -6%) relative to climatology, primarily equatorward of the climatological PVS occurrence maximum (Fig. 5.4a). In turn, the time-mean TUTT axis in these seasons may be weaker and displaced poleward away from the

MDR in the NATL basin, which is associated with reduced VWS downstream of the TUTT axis (Fitzpatrick et al. 1995; Knaff 1997).

To confirm the possible changes in environmental VWS and moisture described above, Fig. 5.6 illustrates composite difference plots of bottom ACE years minus top ACE years (see Table 5.2 for years used in each subset). The most prominent feature in Fig. 5.6a is the statistically significant dipole of enhanced westerly VWS between 10–20^{o}N across the NATL basin and a corresponding area of reduced VWS differences between 20–30^{o}N. This pattern depicts a cyclonic circulation of VWS vector differences, which is associated with the change from positive to negative PVS frequency anomalies between bottom and top ACE years in Fig. 5.5. In addition, this region is also associated with a statistically significant reduction in upper-tropospheric thickness (Fig. 5.6b), precipitable water (Fig. 5.6c), and an enhancement of the sea level pressure (Fig. 5.6d) associated with 925-hPa anticyclonic flow differences. These differences in thickness, moisture, and sea level pressure link back to the stronger and larger PVS composites presented in Chapter 4 (Fig. 4.4, 4.7, 4.11, 4.14), which were previously noted to occur in higher frequency in bottom ACE years (Fig. 5.3). A lingering question that remains is if the same spatial patterns of these environmental variables also exists between top minus bottom PVSI years.

Figure 5.7 shows the same four variables described in Fig. 5.6, except for differences between top PVSI years minus bottom PVSI years. Once again, statistically significant enhancement of VWS is observed between 10^{o}–20^{o}N with an associated reduction in precipitatble water, upper-tropospheric thickness, and enhanced sea level pressure centered around 20^{o}N. Note that while the variable differences between high minus low PVSI years are similar to bottom minus top ACE years, the yearly composite subsets are not identical, since only four years are shared between top ACE, bottom PVSI and bottom ACE, top PVSI. Subtle differences do exist in the VWS, thickness, precipitable water, and sea level pressure differences, which all appear to shift further east in the NATL basin versus what is observed in Fig. 5.6. The general pattern remains, however, where cyclonic VWS differences, lower thickness, lower precipitable water, and enhanced sea level pressure around 20^{o}N appear to occur in conjunction with increased PVS activity in the NATL basin.

Focusing on the region where TC activity is most prevalent, VWS and precipitable water for each year is averaged in a box between 10^{o}–30^{o}N and 20^{o}–90^{o}W to see if there are significant changes in this region associated with yearly PVSI. Figure 5.8 shows a scatter plot of both variables versus PVSI. For VWS (Fig. 5.8a) there is a moderate positive correlation (r = 0.49) where increasing PVSI generally results in an increase in VWS where TCs frequently occur in the NATL basin (Fig. 5.4, ACE climatology in black contours). In contrast, precipitable water in this same domain exhibits a moderate negative correlation (r = -0.43) where increasing PVSI generally results in a decrease in precipitable water where TCs frequently occur in in the NATL basin. The top and bottom ACE years are also depicted as red and blue dots in both plots in Fig. 5.8. These years illustrate that significant variability in VWS and precipitatble water can still occur, even among yearly subsets associated with top and bottom ACE, respectively.

Overall, the results presented in this section fall in line with the results presented in Zhang et al. (2017, see Fig. 1.9 in Chapter 1), with a few exceptions. For instance, PVS intensity variations can modify the relationship between PVS activity and TC activity (e.g., Fig. 5.1 c–d). Thus, using a metric such as PVSI provides added value by incorporating size and intensity of PVSs into its overall quantity, and produces the strongest negative correlation (Fig. 5.2), even though its relationship with TC activity is not linear. Higher PVSI years are associated with larger and stronger PVSs, which increase VWS and decrease precipitatble water in low latitudes (Figs. 5.7, 5.8). These negative environmental factors explain why the strongest negative correlation between PVS frequency and ACE occurs between 10–30^{o}N mostly west of 40^{o}W (Fig. 5.4). The latter result suggests that different modes and locations of TCG may influence the correlation between PVSs and TCs, which will be explored in section 5.6.

5.4 Results: Comparison of intraseasonal PVS activity and TC activity

5.4.1. Top and bottom ACE and PVS years

While yearly differences in PVSI exist between top and bottom ACE years, there are particular periods within the TC season, during which these differences are enhanced. Figure 5.9 shows the 30-day running sum of PVSI from 1 June–30 November, with averages of the top and bottom ACE years highlighted in red and blue, respectively. Beginning in late June, there is a statistically significant increase in PVSI for the bottom ACE years that moves well above climatology by mid-July. While there is also an increase in PVSI for the top ACE years, this increase is well below climatology, staying near the -1σ contour just above. This early period of PVS activity is important, because this is near the climatological peak in PVS frequency and overall activity. These PVSI differences are unlikely to be related to the presence of TC activity in the top ACE years because July is still well before the climatological peak in TC activity observed in September. In Chapter 3, we noted that the climatological maximum PVSI in mid-July exhibited a positive correlation with PVSI for the remainder of the TC season, with daily correlations ranging between 0.3 to 0.6 for the rest of the period (Fig. 3.11) While PVSI decreases for both bottom and top ACE years for the remainder of the TC season, it remains higher than climatology for bottom ACE years, and lower than climatology for top ACE years, with statistical significance ranging from the 80–95% confidence interval between the two subsets (Fig. 5.9). This result suggests that early PVS activity may act as a harbinger for later PVS activity, even on intraseasonal timescales.

To further establish this relationship, Fig. 5.10 presents a scatter plot of PVSI early in the TC season (June–July; x-axis) versus later in the TC season (August–November; y-axis). A strong positive correlation (r = 0.67) exists between early and late season PVSI, and this relationship is also clear when investigating the eight bottom and top PVSI years (Fig. 5.10, blue and red circles). It is still unclear, however, why years with enhanced PVSI activity early in the TC season also exhibit enhanced PVSI activity later in the TC season. On synoptic timescales, strong PVS events were more likely to be preceded by earlier PVS events due to changes in the upper-tropospheric circulation that favor continued RWB (Figs. 4.16 and 4.21). The positive PVSI correlation exhibited in Fig. 5.10 extends across the TC season (June–July vs. August–November), however, and not just time scales in the synoptic to sub-seasonal timeframe. One seasonally varying feature that is positively correlated with yearly PVSI is ENSO (Fig. 3.18). Removing years that exhibit positive or negative temperature anomalies in Nino 3.4 (greater than or less than 0.5^{o}C from June–November), however, only reduces the positive correlation of early and late PVSI to +0.62.

5.4.2. PVSI linkages to the AMO

Another possible explanation for the early and late PVSI positive correlation may be tied to slowly varying fields, such as sea surface temperatures. Figure 5.11 depicts sea surface temperature anomalies averaged for the month of July in bottom PVSI years (Fig. 5.11a) and top PVSI years (Fig. 5.11b). PVS frequency negative and positive anomalies for July are also depicted as dotted and solid black contours, respectively. In bottom PVSI years, positive SST anomalies are observed between 10^{o}–20^{o}N and again poleward of 40^{o}N in the NATL basin. Conversely, top PVSI years are associated with negative SST anomalies between 10^{o}–20^{o}N and again poleward of 40^{o}N.

The SST anomaly pattern in Fig. 5.11 bears remarkable similarity to the canonical Atlantic Multidecadal Oscillation (AMO), which is a coherent NATL SST oscillation with a return period between 40–60 years and is noted for its influence on NATL TC activity (Goldenberg et al. 2001; Trenberth and Shea 2006; Vimont and Kossin 2007; Klotzbach and Gray 2008; Martin and Thorncroft 2014; Klotzbach et al. 2015). Note that while general changes in the AMO occur in 40–60-y cycles, finer scale (i.e., monthly and yearly) oscillations in the AMO index do occur, and are used to forecast seasonal TC activity (Klotzbach and Gray 2008, 2009). Positive values of the AMO are associated with positive SST anomalies in both the NATL MDR and in the higher latitudes poleward of 40^{o}N, and favor increased TC activity. Conversely, negative values of the AMO indicate negative SST anomalies in the same regions favoring suppressed TC activity. The most recent negative-AMO period was from 1970–1994, while the most recent positive-AMO period is ongoing (1995–current), though debate exists whether the end of the current positive AMO period is near (Klotzbach et al. 2015). It is interesting to observe a pronounced AMO signal in composites of bottom and top PVSI years, since these relationships are not fully explained by the years selected in the low and high PVSI composites. For instance, four of the eight high PVSI years occur in the most recent positive AMO period (see Table 5.2), yet exhibit a negative SST anomaly pattern more reminiscent of a negative AMO.

None the less, the relationship between AMO and PVSI is illuminated by a scatter plot of the AMO index (Klotzbach and Gray 2008) versus PVSI (Fig. 5.12). A moderate negative correlation (r = -0.52) is observed between the two variables, as PVSI generally decreases as the AMO index increases. This correlation of PVSI and AMO is also stronger than the other indices noted in Chapter 3 (e.g., ENSO, r = 0.39; MDR SSTs, r = -0.43). The environmental changes associated with a positive AMO index are also consistent with bottom PVSI years, since positive AMO years are associated with environmental factors (i.e., warmer SSTs, low sea level pressure, and reduced VWS) that are beneficial for TC activity (Goldenburg et al. 2001). It may also be possible, however, that PVS activity is modulating SST patterns that map onto the negative AMO index, where stronger 925-hPa trade wind northeasterlies (observed in Fig. 5.7d in high minus low PVSI years) occur from enhanced surface ridging associated with large and strong PVSs (Fig. 4.9). Stronger northeasterly trade winds occurring in the drier atmosphere (Fig. 5.7c) could suppress the typical rapid increase in SSTs that occur in mid-July across the NATL MDR, resulting in negative SST anomalies (e.g., Fig. 5.11b). The relationship between the mid-latitude extratropical forcing resulting in enhanced trade winds and reduced SST anomalies in the tropical Atlantic basin has been described in boreal winter and spring (e.g., Czaja et al. 2002; Chaing and Vimont 2004, Rugg et al. 2016), though debate exists if SSTs force the atmospheric signal during the boreal summer (Gastineau and Frankignoul 2015). Deducing the direct influence, or direction of causation, between PVS activity and SST anomaly patterns in the NATL basin is beyond the scope of this study, but may be an interesting path of future research.

5.5. Results: TC composites relative to PVS occurrence

This chapter has compared PVS activity to yearly TC activity, and has shown how PVS activity varies interseasonally in the top and bottom ACE years. This subsection will now show the spatial relationship between PVSs and TC activity when they occur simultaneously. For the climatological period of this study in the NATL basin spanning 10°–100°W, 21,149 PVS instances are identified, while 8,875 total TC positions with ≥ 35 kt winds (for 6-h synoptic times) are obtained from IBTrACS. Based on these raw counts, PVSs are a more common atmospheric feature in the NATL basin than TCs. Overall, only 27% of all PVSs occur with a TC also present in the NATL basin. This low percentage is mainly due to the observation that a large portion of PVS activity occurs early in the TC season (i.e., July, Fig. 5.9) prior to most of the TC activity in the NATL basin. Conversely, 69% of all TC points occur with a PVS present somewhere in the NATL basin, after removing double counts from multiple PVS events occurring at the same time.

Figure 5.13 illustrates the spatial variability of TC position relative to the centroid of PVS events (31.6°N, 47.7°W). Of the 7048 periods identified (includes double counting TCs for multiple PVSs), most TCs appear to cluster west of the composite PVS trough axis (red line, Fig. 5.13a). A secondary maximum also appears about 20° south and 10° east of the PVS axis. Predictably, there is a distinct minimum in TC positions within the PVS trough axis. The highest TC density exceeds 300 points at 25°N, 75°W, or approximately 3000 km west of the PVS centroid (Fig. 5.13c). This places the maximum in TC density firmly in the upstream ridge axis, where negative VWS anomalies and positive precipitable water anomalies were generally observed in the PVS composites presented in Chapter 4 (Figs. 4.2–4.7). Interestingly, the mean TC motion in this location is to the north and northeast ranging from 2–6 m s^{-1} (Fig. 5.13b).

Thus, it is possible that a significant subset of TCs in this composite are moving towards the northeast, where their convectively driven outflow and moisture anomalies may aid ridge amplification upstream of the PVS trough axis. Such a process is a possible pathway for PVS formation, where the upstream ridge building from TCs moving into the mid-latitudes and undergoing extratropical transition induces ridge amplification as described in prior studies (Ferreira and Schubert 1999; Riemer et al. 2008; 2010; Grams et al. 2011; Grams and Archambault 2016). Finally, the average TC intensity composite (Fig. 5.13d) emphasizes regions far away from the PVS trough axis, where highest average intensities (~75–85 kt) occur well southwest and southeast of the PVS location, in regions well away from the negative environmental effects associated with the PVS trough axis. Closer to the PVS centroid, TC intensities were lower, between 50–60 kt, consistent with the expectation that TCs that are near PVSs may be adversely affected by enhanced VWS and reduced precipitatble water (see Chapter 4 Figs. 4.2–4.7).

In addition to describing spatial characteristics of all PVSs and TCs occurring simultaneously, we can divide the PVS cases into strong and weak categories to see how this impacts the location and intensity of TCs in the composite (Fig. 5.14). For weak PVSs (Fig. 5.14a,c) the highest increase in ACE occurs immediately southwest of the PVS trough axis, while the largest decrease in ACE occurs a bit further west near where the upstream ridge is positioned (25°N, 75°W). These observations are consistent with regions that are associated with decreased VWS anomalies and neutral to positive precipitable water anomalies in the weak PVS composites (Fig. 4.3, 4.6). Note that the composite trough axis in the weak PVS composite is ill-defined by the 2-PVU contour (blue contour) since all weak PVS cases are composited, regardless of tilt or area, washing out the composite PV signal.

In contrast, the strong PVS composite (Fig. 5.14b,d) shows a substantial decrease in area-averaged ACE immediately southwest of the PVS trough axis. This likely is due to the observation that strong PVSs have enhanced VWS and reduced precipitable water in a large area surrounding the PVS trough axis (Fig. 4.2, 4.5). There are two pockets, however, where increased area-averaged ACE is present, mainly away from the PVS trough axis to the northwest (35°N, 85°W) and southeast (15°N, 35°W). These regions are far enough away from the PVS that they reside in regions of anomalously low VWS and neutral to positive precipitatble water anomalies (Fig. 4.2, 4.5). In particular, the enhanced ACE located upstream of the strong PVS trough axis may be associated with recurving TCs, as illustrated in Fig. 5.13b, and could promote ridge-building associated with strong PVSs (Fig. 5.14b,d), though this assumes these recurving TCs are producing significant diabatic heating and irrotational outflow aiding ridge amplification.

5.6. PVS activity and TC development pathways

As discussed in section 5.2.2., this dissertation uses the MC13 TCG pathway dataset to sort between non-baroclinic and baroclinic type TCGs from 1979–2010. For this dataset, the top eight PVSI years are reselected using the 1979–2010 period, since three years in the original subset occur after 2010, which is not included in the MC13 TCG pathway dataset (see Table 5.2 for details).

Figure 5.15 shows the total number of non-baroclinic (blue), baroclinic (red), and all TCG events for the top and bottom PVSI years. Top PVSI years are associated with a significant reduction in overall TCG occurrence (85 vs. 126; -32.5%), but nearly all of the reduction is related to sharp decreases in non-baroclinic TCG (33 vs. 75; -56%), since the total amount of baroclinic TCG barely changes from top to bottom PVSI years (52 vs. 51). This suggests that non-baroclinc TCG is more adversely affected by negative environmental conditions produced when large and strong PVSs are more common in top PVSI years.

Figure 5.16 shows two scatter plots comparing PVSI versus non-baroclinic TCG ACE and baroclinic TCG ACE. Similar to Fig. 5.2, non-baroclinic TCG ACE exhibits a moderate negative correlation (r = -0.56), meaning that as PVSI increases, ACE decreases from non-baroclinic TCG cases (Fig. 5.16a). This result is not surprising, because most non-baroclinic TCG cases occur at low-latitudes (between 10^{o}–20^{o}N), where top PVSI years are frequently associated with enhanced VWS anomalies and decreased precipitable water anomalies relative to bottom PVSI years (Fig. 5.7). In contrast, baroclinic TCG ACE exhibits little correlation (r = -0.09) with PVSI (Fig. 5.16b). This result is a bit more surprising, since this study originally hypothesized that greater PVS activity would allow for more opportunities of baroclinic TCG occurrence. This correlation is for ACE, however, and not overall TCG frequency, noting that baroclinic TCG cases typically produce lower ACE due to their genesis generally occurring in a less favorable environment (McTaggart-Cowan et al. 2008).

Differences in ACE produced by non-baroclinic and baroclinic TCG can also be depicted spatially over the NATL basin. Figure 5.17 illustrates a series of seasonal ACE composites, highlighting the annual 1979–2015 climatology (Fig. 5.17a), and the average seasonal ACE for the top and bottom PVSI years (Fig. 5.17b–c). Consistent with the large reduction in non-baroclinic TCG events noted in Fig. 5.16, there is also a large reduction and poleward shift in where ACE occurs in the NATL basin for top PVSI years (Fig. 5.17b). This shift in top PVSI years occurs because a large fraction of the seasonal ACE is now produced by baroclinic TCG, which occur at higher latitudes (red dots). Conversely, in bottom PVSI years, a significant enhancement of ACE is noted in the MDR (Fig. 5.17c). This ACE enhancement in bottom PVSI years occurs from an abundance of non-baroclinic TCG events that are more likely to become intense, long-track TCs in characteristically higher SSTs, lower VWS, and enhanced precipitable water in the MDR (Fig. 5.7, 5.11).

5.7. Tables

Table 5.1. Correlations between Accumulated Cyclone Energy (ACE) and various indices used to forecast TC activity from June–November 1979–2015. Nino 3.4 SST anomaly defined from 5^{o}S–5^{o}N 120^o–170^{o}W, MDR SSTs are defined from 10^o–20^{o}N, 20^o–80^{o}W, and the AMO, which is defined following the methodology outlined in Klotzbach and Gray (2008). All correlations are statistically significant at the 95% confidence interval.

Index	Correlation
Nino 3.4 SST anomaly	-0.49
MDR SSTs	0.47
AMO	0.45
PVS Index	-0.55

Table 5.2. High and low eight years selected for compositing using the PVS Index (1979–2015), PVS Index for MC13 (1979–2010), and ACE.

Metric	PVS Index	PVS Index (for MC13)	ACE
Years	Top (Bottom)	Top (Bottom)	Top (Bottom)
	1984 (1998)	1984 (1998)	2005 (1983)
	2014 (1999)	1986 (1999)	1995 (1982)
	2013 (2010)	1982 (2010)	2004 (1994)
	1986 (1995)	1983 (1995)	1998 (1987)
	1982 (1988)	2002 (1988)	1999 (2013)
	2015 (2006)	2009 (2006)	2003 (1991)
	1983 (1979)	1992 (1979)	1996 (1986)
	2002 (2001)	1990 (2001)	2010 (1993)

5.8. Figures

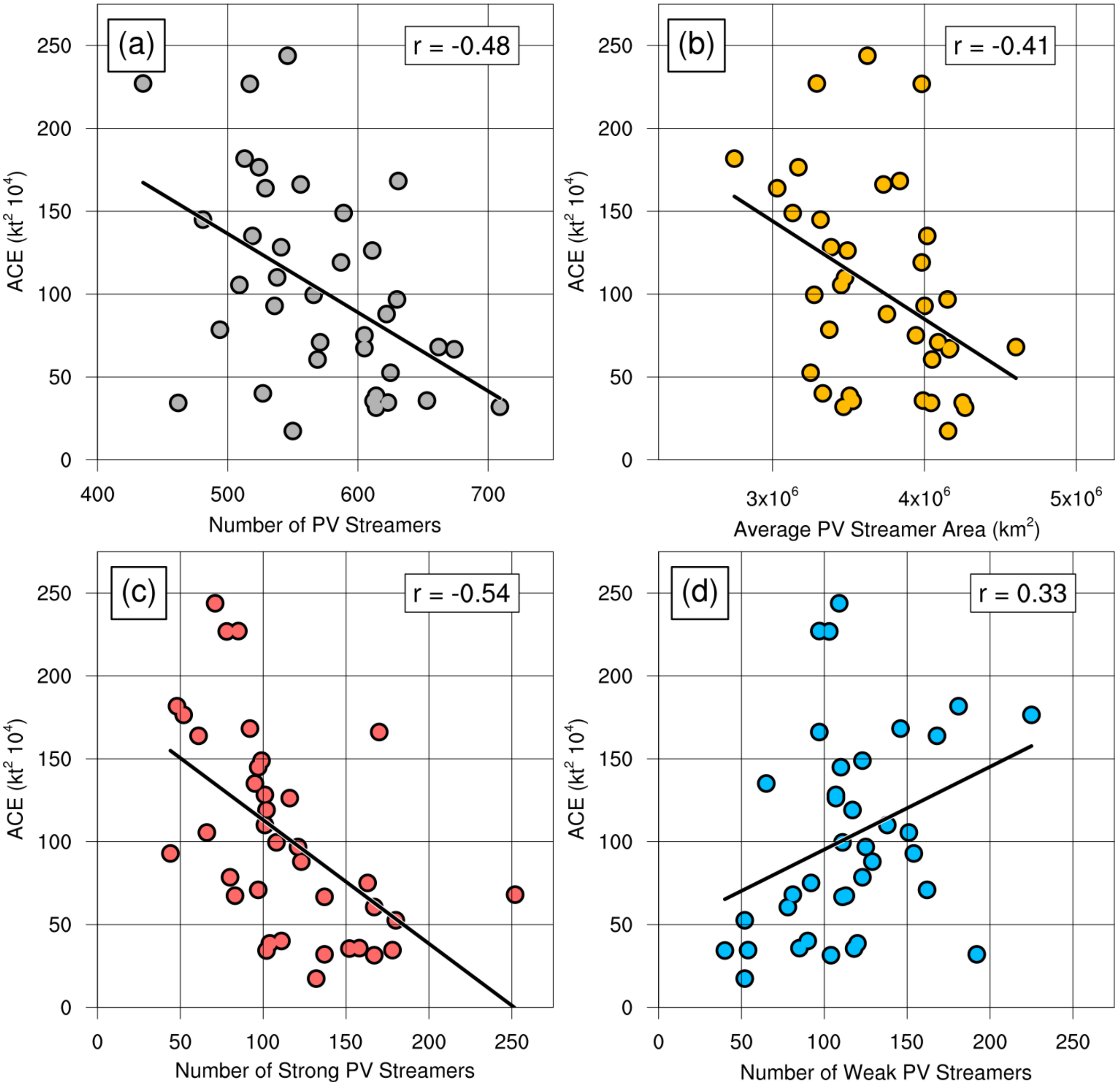

Fig. 5.1. Scatter plot of different yearly PVS metrics (x-axis) versus ACE (y-axis). Panel (a) compares the total number of PVSs versus ACE, panel (b) compares the average area of PVSs versus ACE, panel (c) compares the total number of strong PVS (top 20th percentile) versus ACE, and panel (d) compares the total number of weak PVSs (bottom 20th percentile) versus ACE. A linear trend line (black line) and correlation (top right) between the PVS metric and ACE is depicted in each scatter plot.

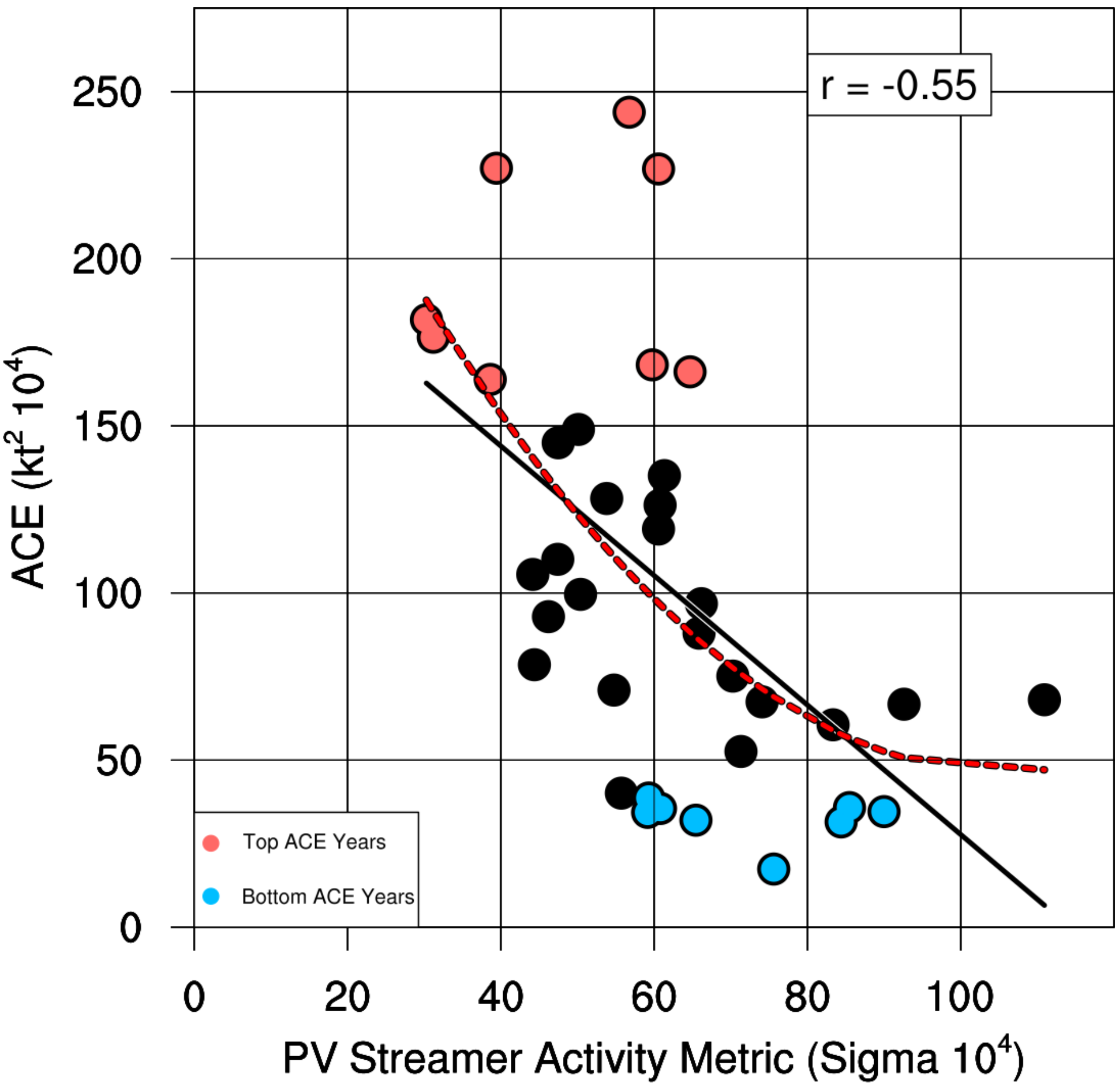

Fig. 5.2. Scatter plot of out PVS activity metric (x-axis) versus ACE (y-axis) on a yearly basis. A linear trend line (black line), exponential fit (red dashed line), and linear correlation (top right) between the PVS activity metric and ACE are also depicted. The top and bottom eight ACE years (representing top and bottom 20th percentiles) are illustrated as red and blue dots, respectively.

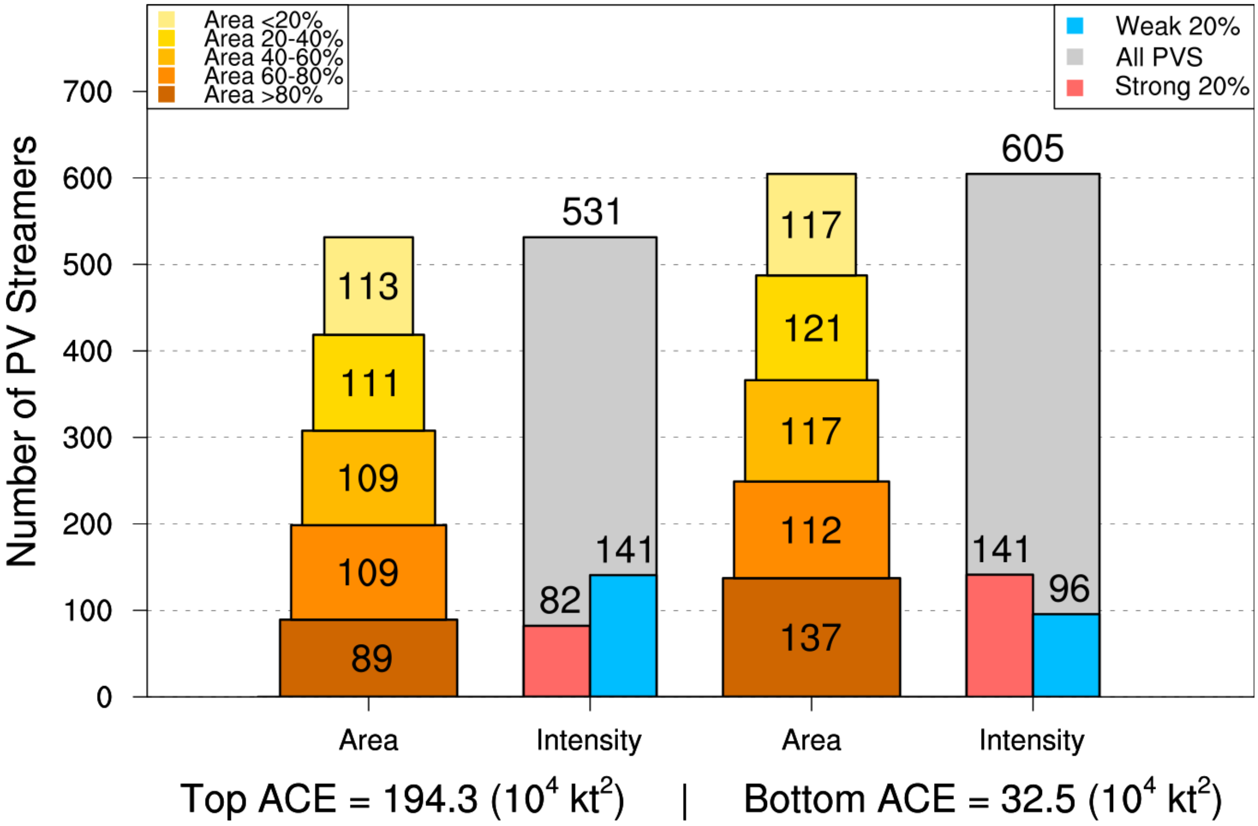

Fig. 5.3. Bar chart showing the average number of PVSs in different area and intensity percentiles associated with the top and bottom eight ACE years. The left bar plots depict the number of PVSs that fit in each area percentile (from largest to smallest percentile, legend at top left), with the size of the bar indicating the relative area percentile. The right bar plots depict the total number of PVSs, also divided into the total number of weak and strong PVS cases (legend at the top right). Area and intensity bar plots on the left are for the eight highest ACE years (with average ACE magnitude at the bottom), while area and intensity bar plots on the right are for the eight lowest ACE years (with average ACE magnitude at the bottom).

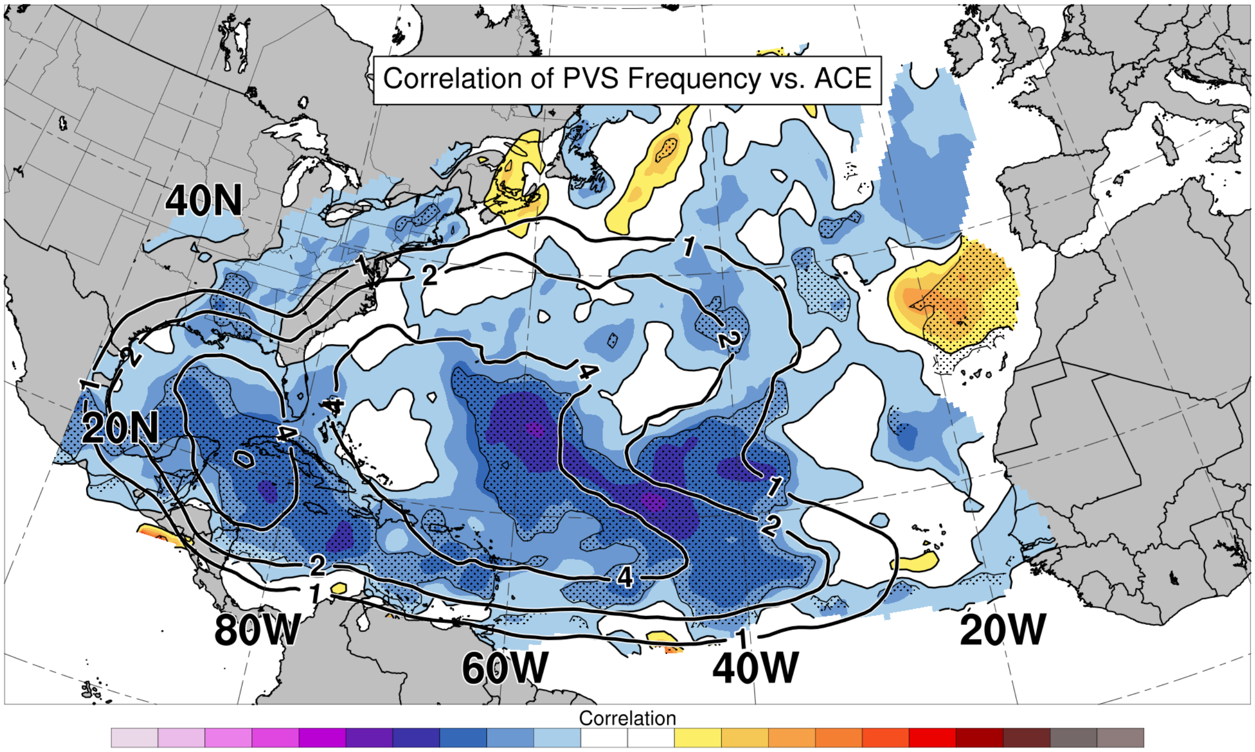

Fig. 5.4. Spatial correlation between PVS frequency and ACE on an annual basis (shading) and average annual ACE summed in 500 km radii (black contours, > 1×10^4 kt^2). Statistically significant correlations are stippled.

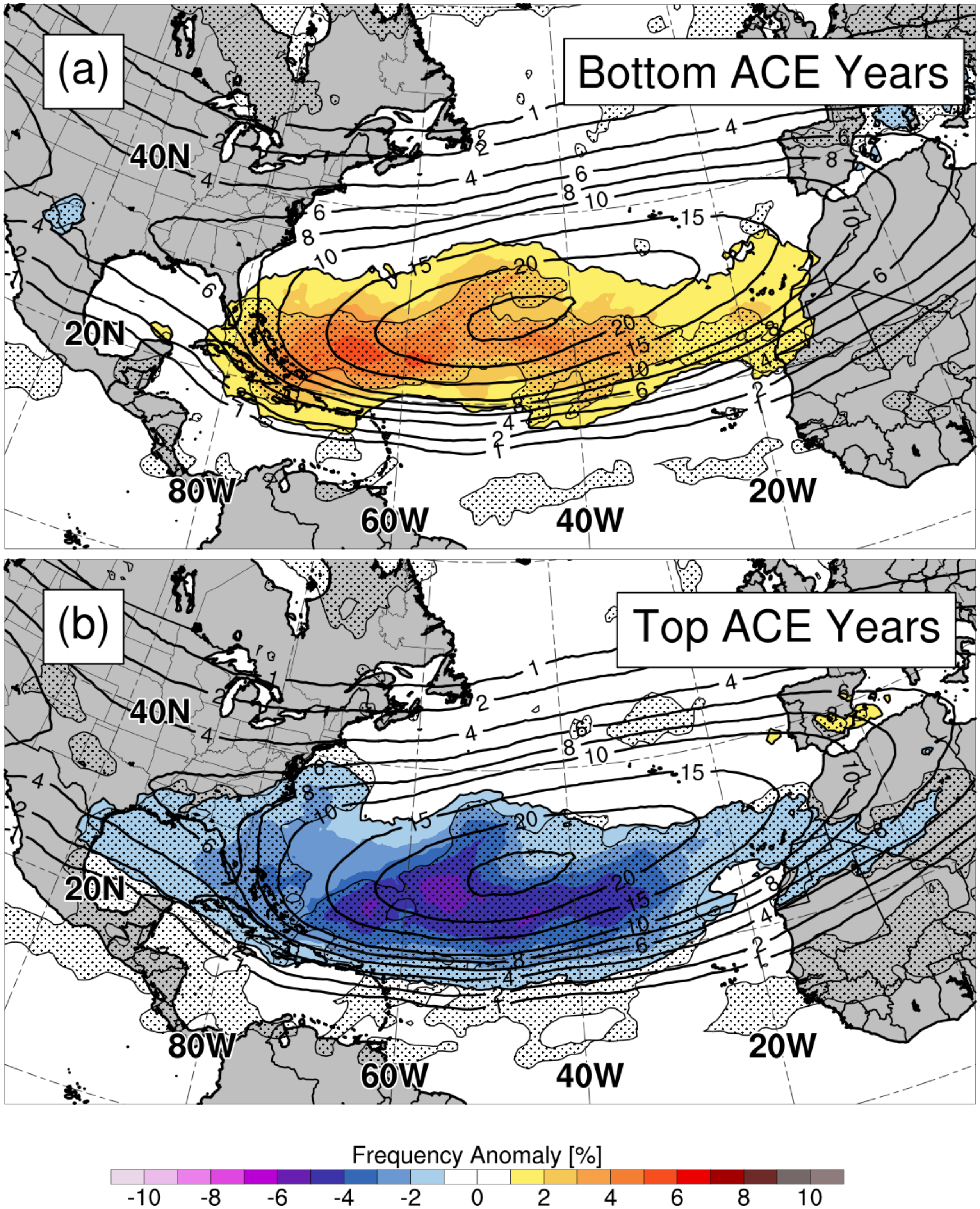

Fig 5.5. PVS frequency anomalies (shading, %) relative to the 1979–2015 climatology (black contours, %) for the (a) eight highest ACE years and (b) the eight lowest ACE years. Statistically significant differences relative to climatology are stippled.

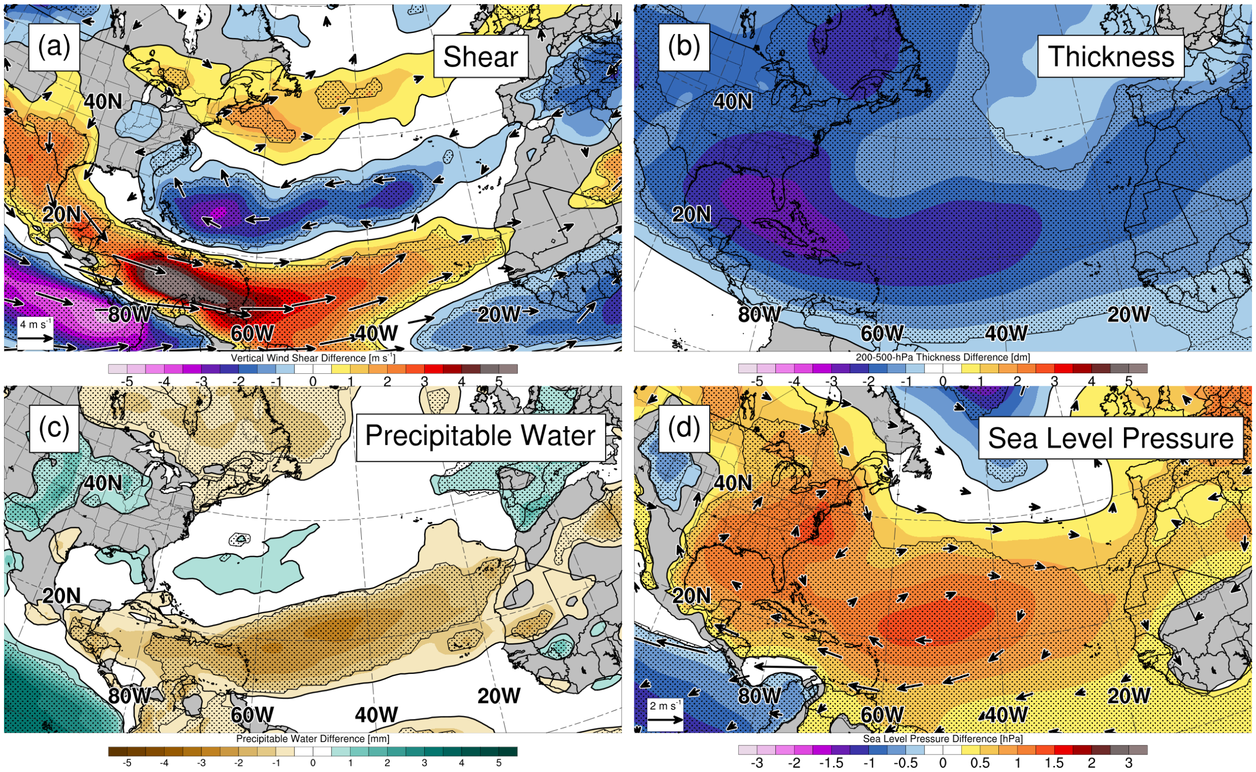

Fig. 5.6. Composite difference plots of the eight bottom ACE years minus the eight top ACE years. Panel (a) depicts 200-850-hPa VWS (shaded, m s^{-1}) and shear vector difference (vectors, > 1 m s^{-1}), (b) depicts 200-500-hPa thickness (shaded, dm), (c) depicts precipitable water (shaded, mm), and (d) depicts sea level pressure (shaded, hPa) and 925-hPa vector differences (vectors, > 0.5 m s^{-1}). Statistically significant differences of all the shaded quantities are stippled.

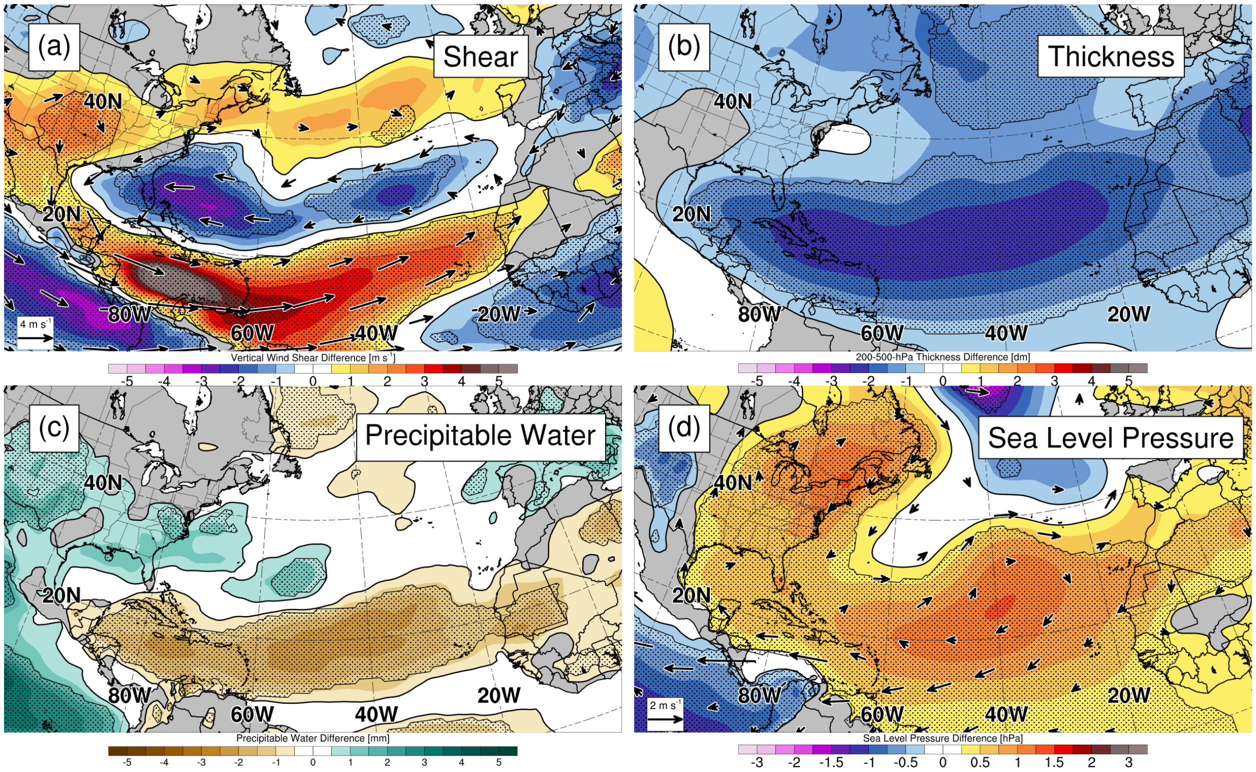

Fig. 5.7. As in Fig. 5.6, except for the eight top PVSI years minus the eight bottom PVSI years.

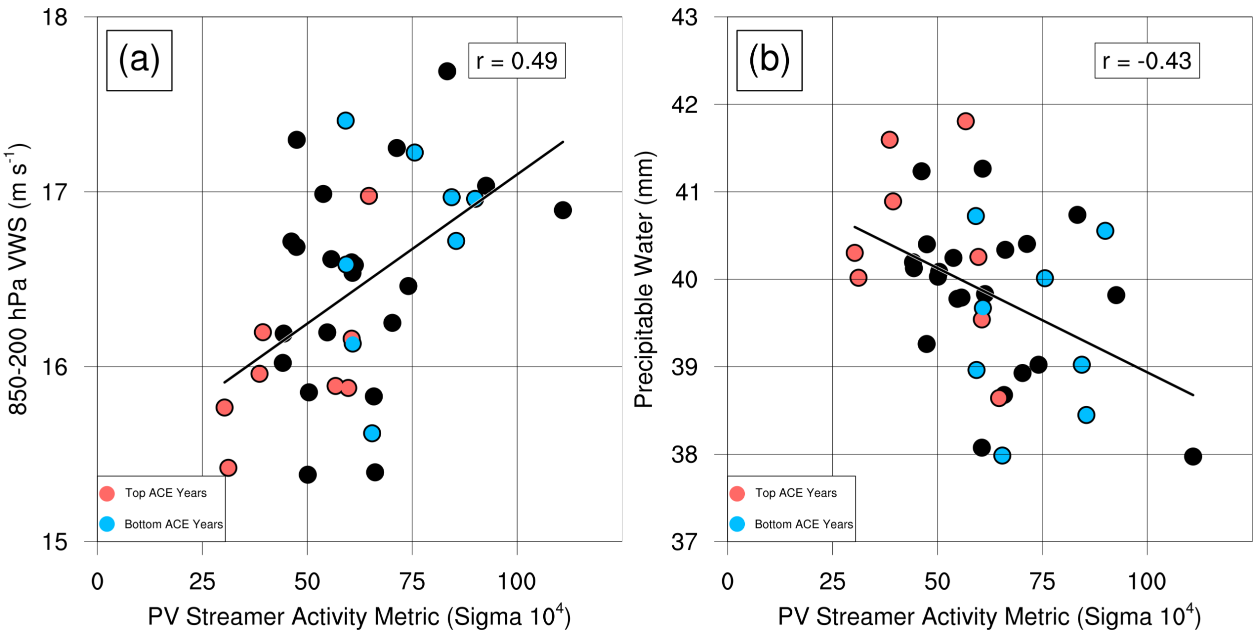

Fig. 5.8. Scatter plots of the yearly PVS activity metric (x-axis) with, (a) 200–850-hPa VWS (y-axis), and (b) precipitable water (y-axis). A linear trend line (black line) and correlation (top right) between the PVS activity metric and the compared variable are also depicted. The top and bottom eight ACE years are illustrated as red and blue dots, respectively.

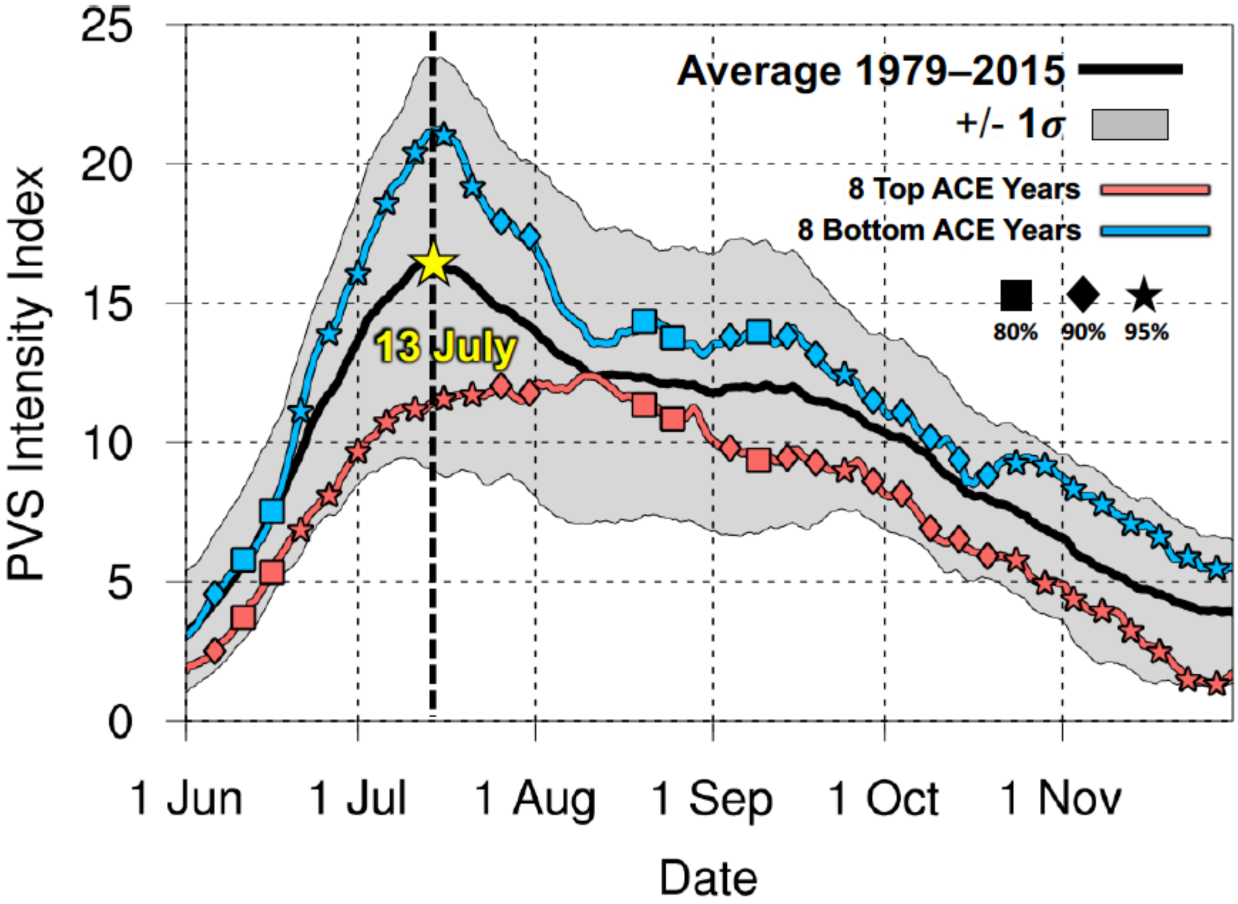

Fig. 5.9. 30-day centered moving sum of the PVS activity index from 1 June–30 November for the 1979–2015 average (black contour, 10^4 σ) and the +/- 1 standard deviation (gray shading, 10^4 σ). The top and bottom eight ACE years are depicted as red and blue lines, respectively, with shape (square, diamond, star) along the line denoting statistically significant differences between the two subsets at different confidence intervals (80%, 90%, 95%).

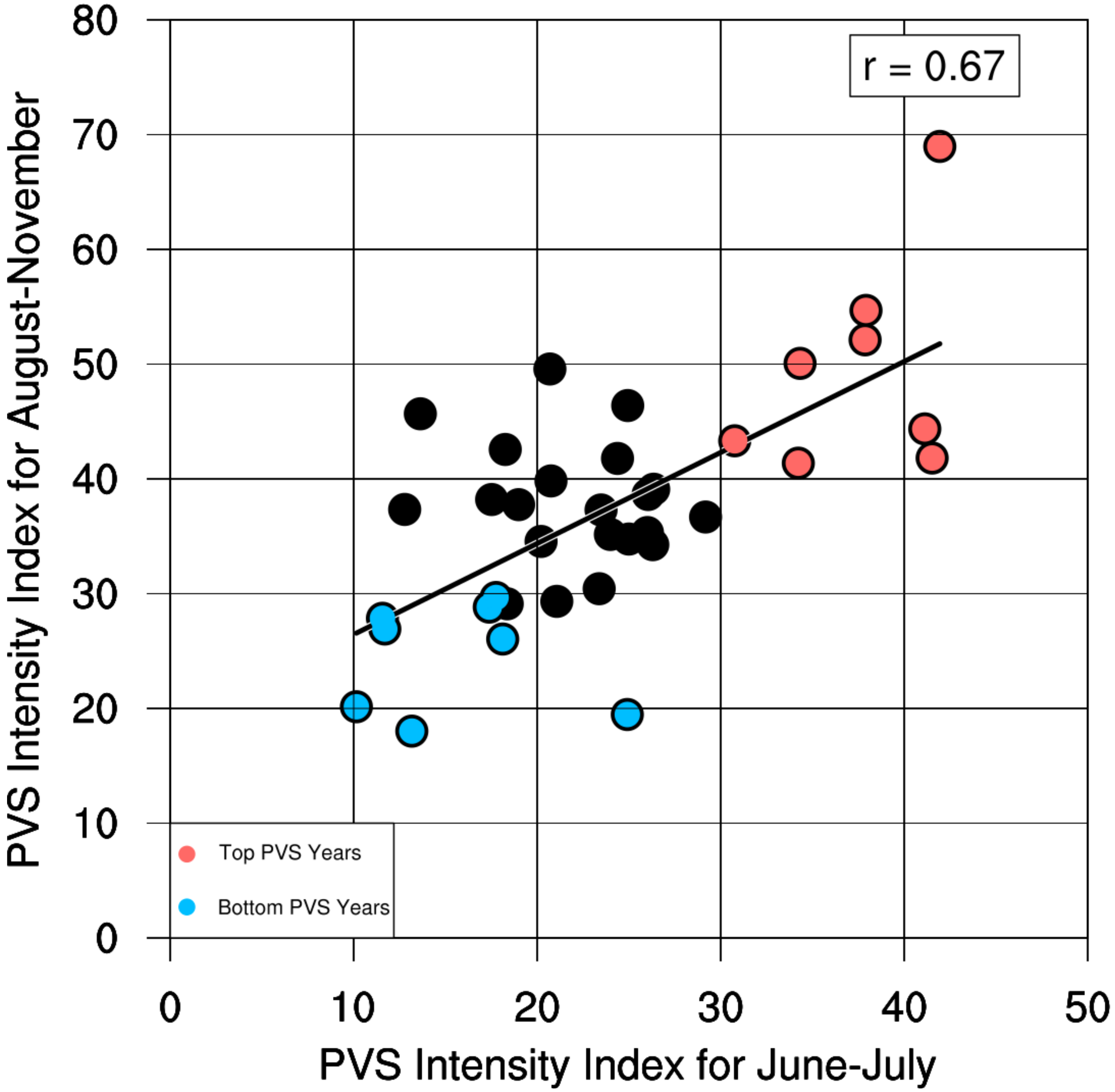

Fig. 5.10. Scatter plot of the yearly PVS activity index early in the TC season (June–July, x-axis) compared to total PVS activity index for later in the TC season (August–November, y-axis). A linear best-fit (black line) and correlation (top right) between the early and later PVS activity metrics are also depicted.

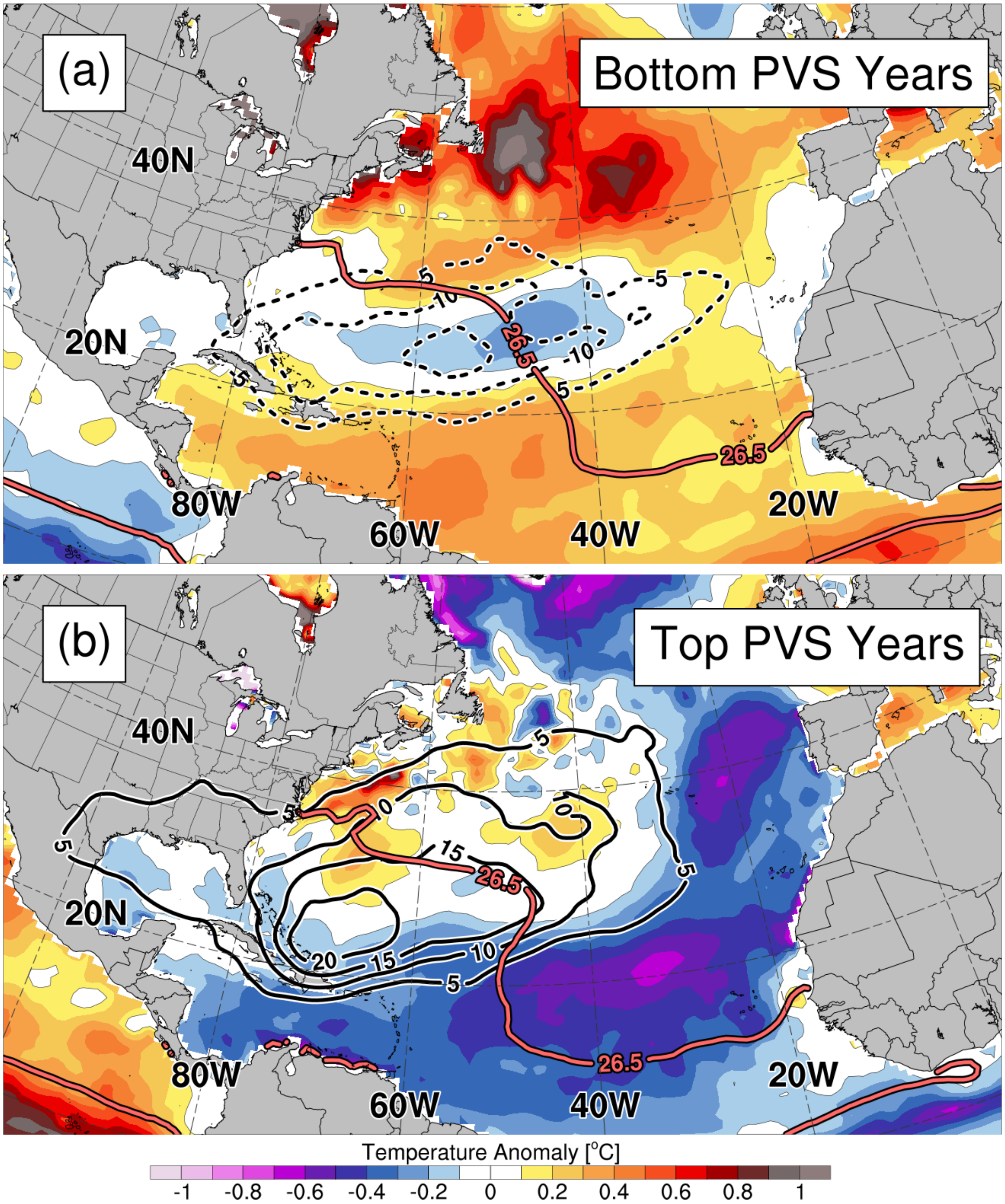

Fig. 5.11. Sea surface temperature anomalies (shaded, °C), PVS frequency anomalies (dashed and solid contours for negative and positive anomalies, every 5%), and the July 26.5°C sea surface temperature isotherm for the (a) eight lowest PVS activity years and (b) the eight highest PVS activity years.

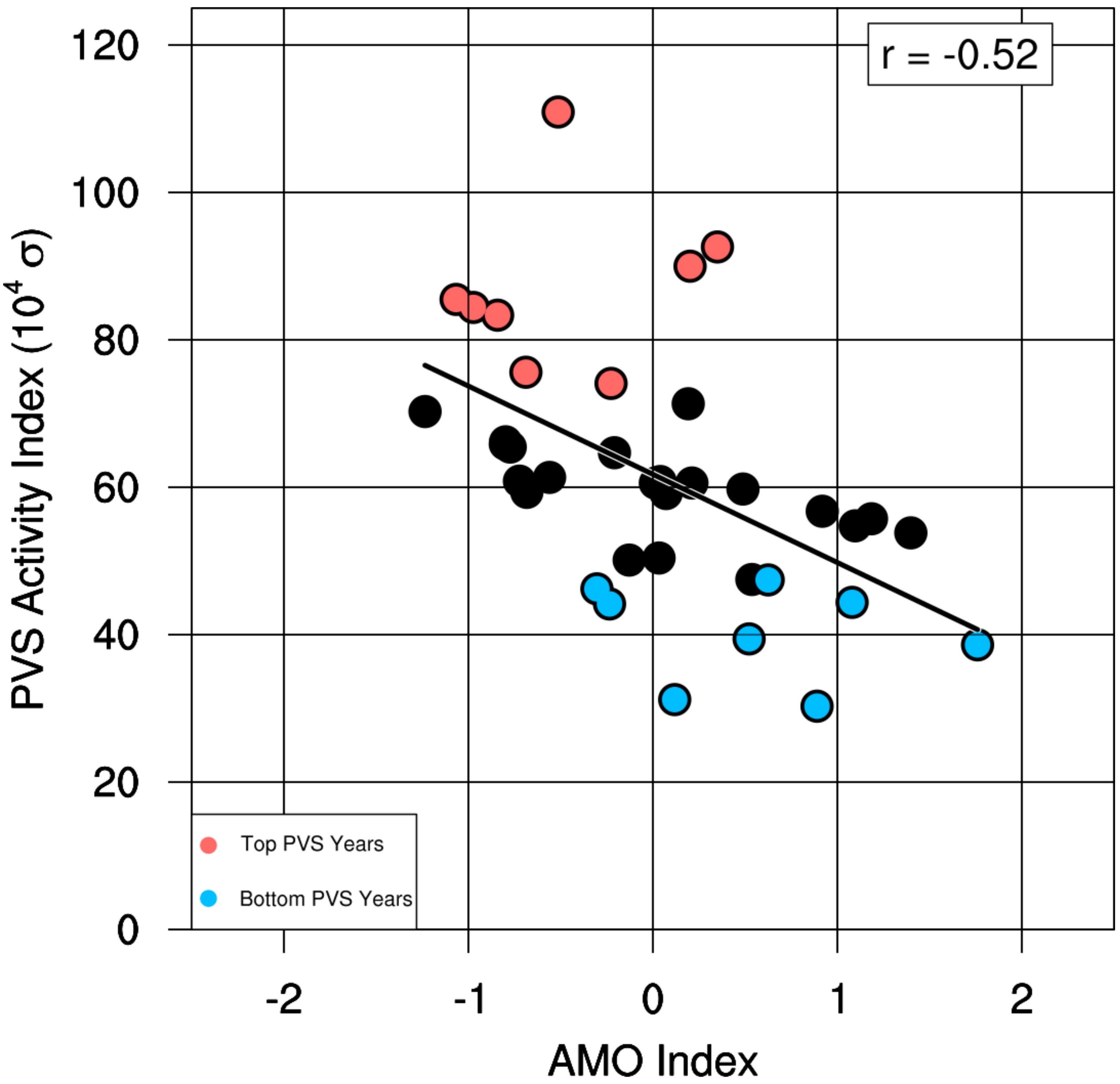

Fig. 5.12. Scatter plot of yearly averaged AMO index (from Klotzbach and Gray 2008, x-axis), and the PVS activity index (y-axis). A linear best-fit (black line) and correlation (top right) between the AMO and PVS activity index are also depicted.

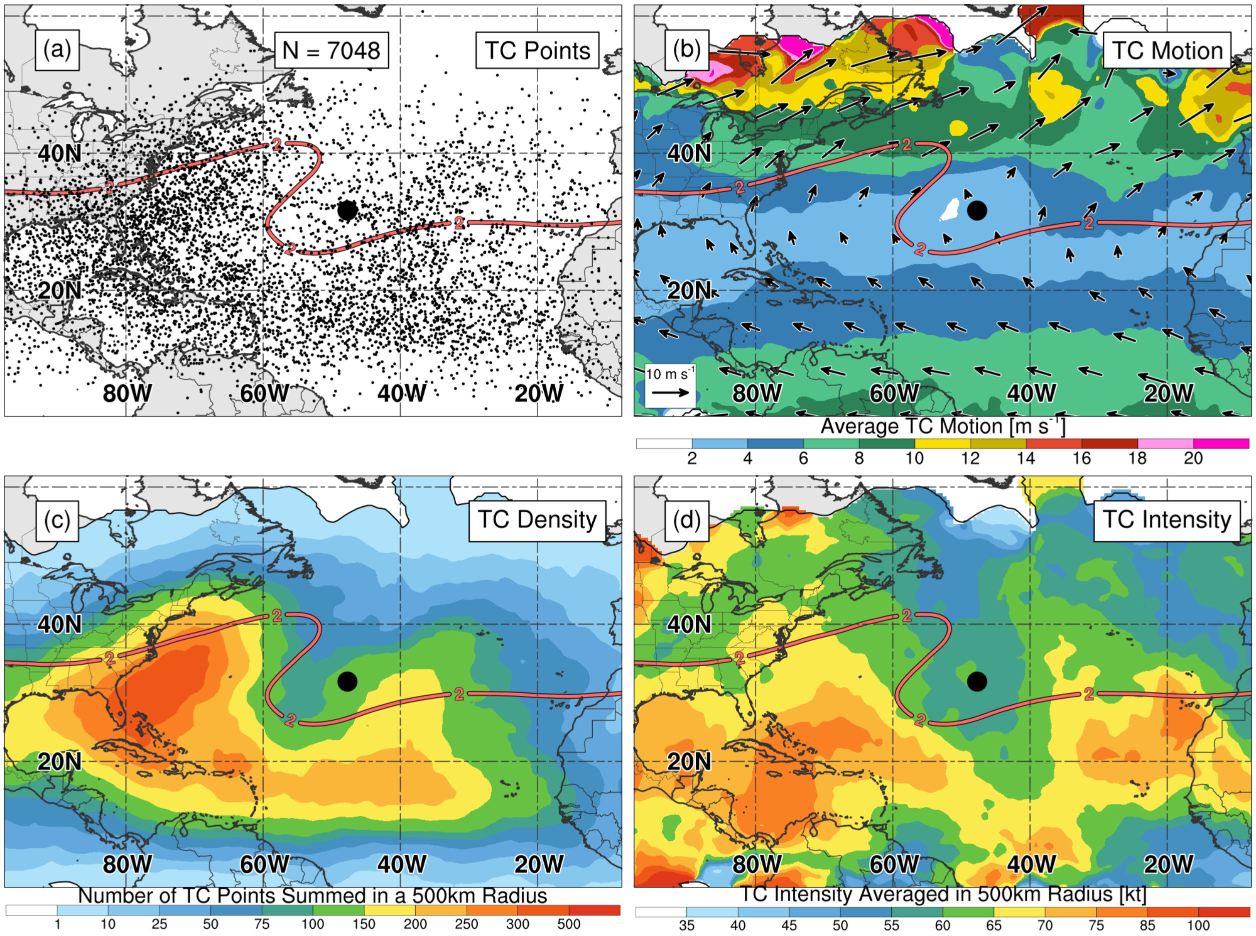

Fig. 5.13. TC positions relative to PVS centroid positions between 10°–100°W. Panel (a) shows the total number of TC points (small black dots, N = 7048) relative to the PVS centroid (big black dot), (b) shows the average TC speed (shaded, m s^{-1}) and direction (vectors, > 1 m s^{-1}), (c) shows the number of TCs summed in a 500-km radius at each grid point (shaded, #), and (d) shows the average TC intensity in a 500-km radius at each grid point (shaded, kt). The composite mean 350-K 2-PVU contour is depicted in each panel as a red contour. All plots are relative to the PVS centroid, but are also shifted onto the mean PVS centroid location (31.6°N, 47.7°W). As such, geography is provided as a scale reference only.

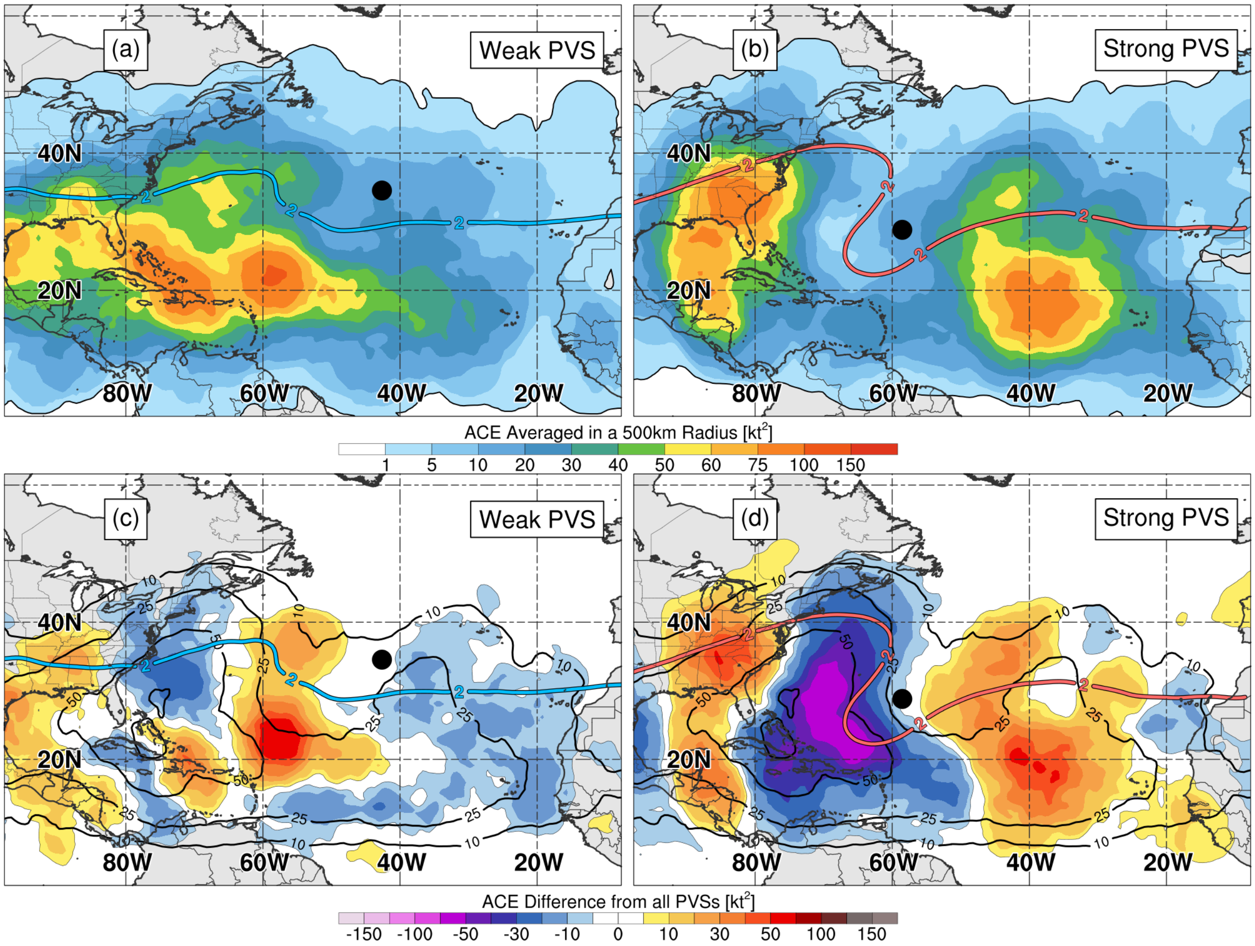

Fig. 5.14. Spatial ACE distribution averaged in 500-km radii at each grid point for (a) weak PVSs and (b) strong PVSs (shaded, kt^2). Panels (c,d) depict the spatial ACE difference (shaded, kt^2) relative to the spatial ACE of all PVSs (black contours, > 10 kt^2). The composite mean 350-K 2-PVU contour for all weak and strong PVSs is depicted as blue and red contours, respectively. The PVS centroid position in each PVS-relative plot is depicted as a large black dot. As in Fig. 5.13, geography is provided for scale reference only.

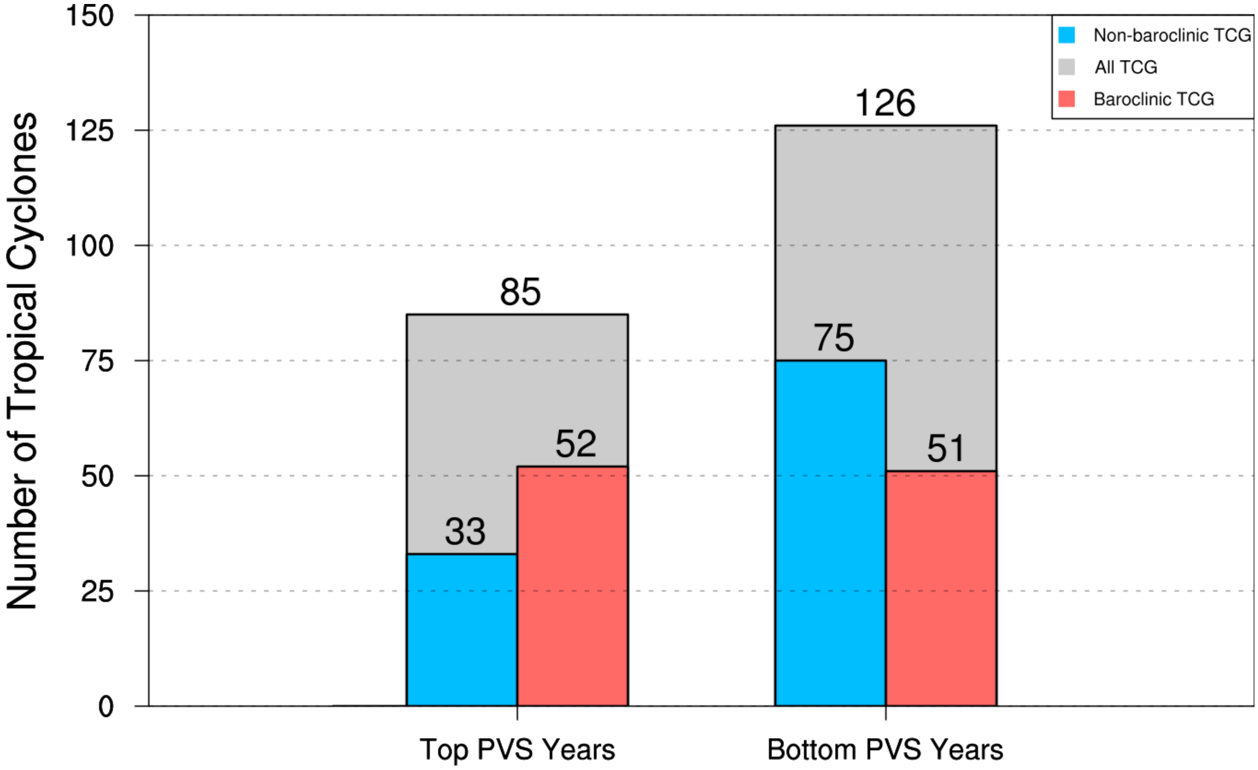

Fig. 5.15. Bar plots of the total number of baroclinic (red), non-baroclinic (blue), and all TCG cases (gray) for the top and bottom eight PVS activity years (left and right, respectively).

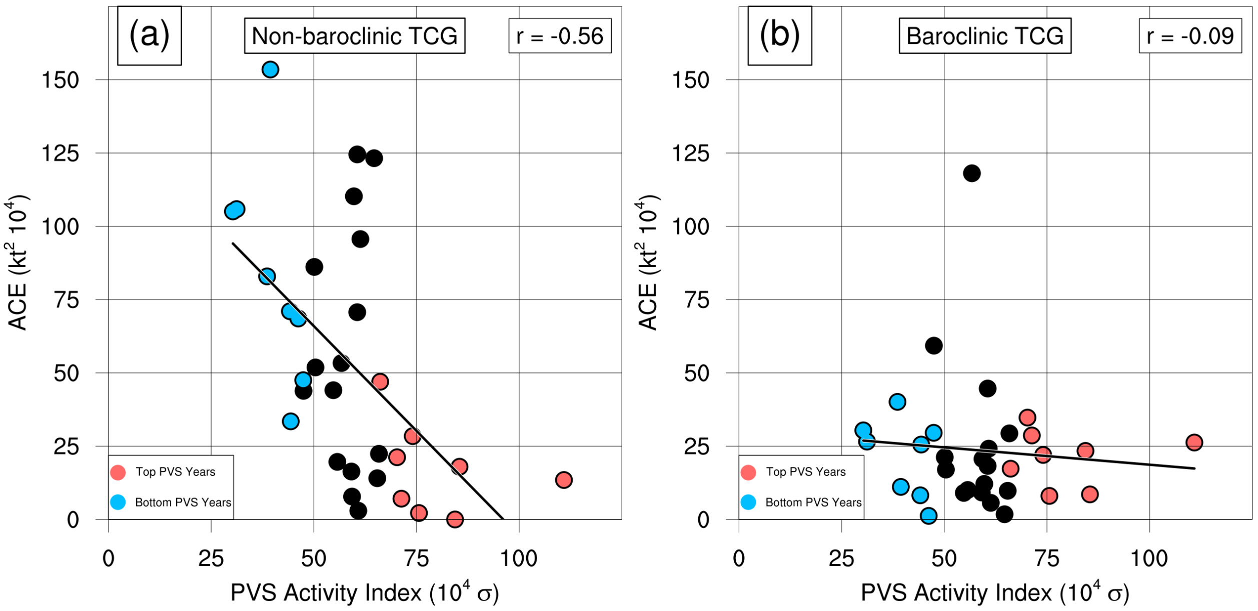

Fig. 5.16. Scatter plots of the yearly PVS activity index (x-axis) with (a) ACE from non-baroclinic TCG (y-axis), and (b) ACE from baroclinic TCG (y-axis). A linear best-fit (black line) and correlation (top right) between the PVS activity index and ACE in both scatter plots is also depicted.

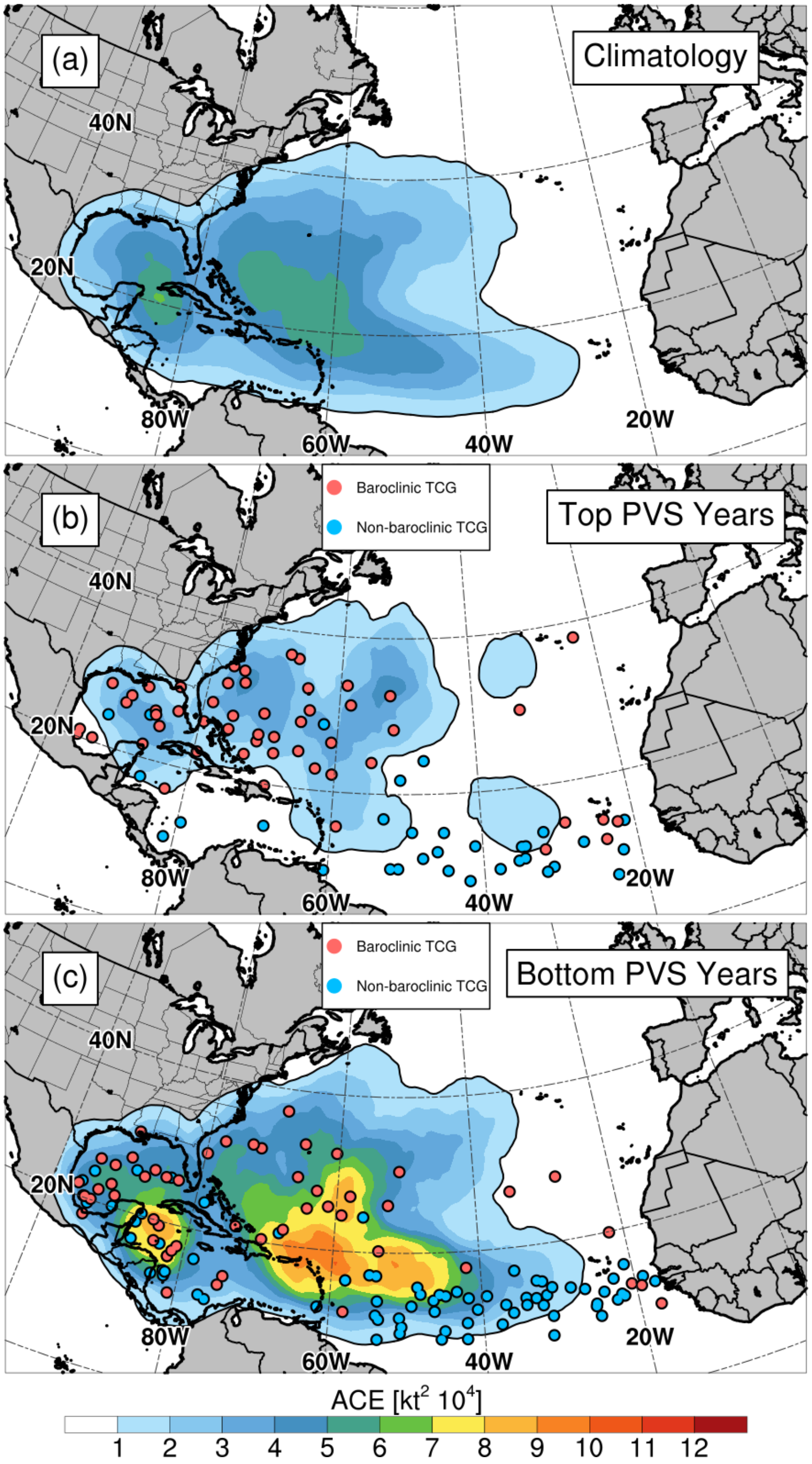

Fig. 5.17. Panel (a) depicts the 1979–2015 climatology of yearly ACE spatially averaged in 500-km radii at each grid point (shaded, kt^2 10^4). Panel (b) depicts ACE for the eight highest PVS activity years (shaded, kt^2 10^4) and panel (c) depicts ACE for the eight lowest PVS activity years (shaded, kt^2 10^4). Genesis locations for baroclinic and non-baroclinic TCG cases are depicted as red and blue dots for the highest and lowest PVS activity years, respectively.

6. Summary, conclusions, and recommendations for future work

6.1 Summary and conclusions

This dissertation examined warm season PVSs, which are elongated corridors of high-PV air that form from anticyclonic RWB events, and are defined along the 2-PVU contour on the 350-K surface in the NATL basin. This work investigated the overall PVS climatological distribution from June–November, their differing role in modifying environmental conditions based on changes in their intensity, area, and tilt, and, finally, their relationship with TC activity in the NATL basin. The analysis in this dissertation allows us to deduce the linkages between PVS events and changes in upstream and downstream environments, and to examine the overall PVS impact on TC activity.

6.1.1. The PVS climatology

The PVS climatology presented in this dissertation identified events from 1979–2015, between 1 June–30 November, in the NATL basin between 10^{o}–100^{o}W. These results complement the findings obtained in other PVS climatologies (e.g., Postal and Hitchman 1999; Wernli and Sprenger 2007; Zhang et al. 2016, 2017), but extend beyond these studies by including intensity, area, and tilt metrics associated with each PVS event.

The maximum PVS frequency (26%) is centered in the NATL basin at 28.5^{o}N, 47.5^{o}W, with slightly lower PVS frequencies oriented from the southwest-to-northeast. The PVS frequency maximum found in the ERAI climatology is three times the maximum found in Wernli and Sprenger (2007), which we attribute to differences in our PVS methodology that identify larger PVS features in the NATL basin. The southwest to northeast orientation of the PVS frequency maximum overlaps a broad cyclonic trough axis in 200-hPa streamlines, indicative of the position of the time-mean TUTT. Seasonally, the PVS frequency maximum shifts poleward and peaks in July, but then shifts southward and eastward and decreases in magnitude as the midlatitude jet accelerates. The TUTT follows this PVS frequency maximum, suggesting the climatological linkage between these two features. Annually, large year-to-year variations in the PVS frequency occur in the NATL basin, with some years showing a basin-wide increase in frequency (i.e., 2013), some years showing a basin-wide decrease in frequency (i.e., 2008), and other years having a distinct latitudinal shift in frequency anomalies (i.e., 1992). These year-to-year differences in the number of PVS events can be very abrupt (i.e., between 1994 to 1995), though there is little discernable long term trend in how PVS frequency is changing in the ERAI dataset.

There is large variability in PVS intensity, area, and tilt, both on an event by event basis, and in yearly PVS totals. PVS intensity is determined by averaging the standardized PV anomaly of all the grid points within a PVS area. Sorting all PVS by intensity reveals an approximately normal distribution, with an average PVS intensity of 0.85σ and a standard deviation of $\pm 0.62\sigma$. Years that have a similar number of PVS events, however, may not necessarily have the same total of strong or weak PVSs (i.e., 2005 vs. 2015). Most PVSs range in area between 1×10^6 km^2 and 1×10^7 km^2 with a mean 3.72×10^6 km^2, and range in tilt between 0° to 90° with a mean of 62.0°, consistent with a positively tilted trough axis that occurs downstream of an AWB event (e.g., Thorncroft et al. 1993).

This study created the PVS activity index (PVSI), which combines the intensity, area, and frequency of PVS events into a metric that better depicts overall PVS activity. The PVSI is capable of indicating overall activity in years where its component variables are not positively correlated. A good example is 2015, where despite only having the 19th most PVSs in the ERAI climatology, featured much higher than normal PVS intensity and area, which boosted the PVSI to the sixth highest in the ERAI climatology.

PVSI can also be defined for shorter intervals to investigate intraseasonal variations in PVS activity. Using a 30-day period, PVSI peaks in mid-July (13 July), consistent with the highest spatial frequency of PVSs. Another notable result is that this maximum in 30-day PVSI is positively correlated with PVSI for the rest of the TC season (August–November). These results suggest that early season PVS activity can be used as a predictor of late season PVS activity, which also has important implications for TC activity as described in Chapter 5.

PVS activity was also compared between the ERAI and CFSR datasets to show characteristic differences between the two reanalyses. In general, the CFSR climatology identified many more PVSs that were also larger in area, and mainly equatorward of the PVS frequency maximum identified in the ERAI. The CFSR climatology also exhibited a long-term trend in decreasing PVS count, intensity, and overall activity, which explained 45% of the variance in PVSI. These long-term changes are partially attributed to artifacts in how the CFSR uses time-evolving stratospheric bias correction of satellite observations, combined with the choice to run six separate streams to stitch together the 37-y CFSR climatology (Saha et al. 2010), which resulted in large stratospheric temperature discontinuities. In contrast, the ERAI was only run in two separate streams, with little discernable discontinuity in either satellite bias correction or temperature in the lower stratosphere. Given the issues presented in the CFSR dataset for stratospheric temperature, one should use the CFSR with caution for the purpose of PVS identification.

Using the ERAI PVS dataset, there were several seasonal and intraseasonal phenomena that were found to be correlated with PVS activity in the NATL basin. A yearly positive correlation was found between PVSI and ENSO (r = 0.39), while a yearly negative correlation was found between PVSI and MDR SST anomaly (r = -0.43). The positive correlation between PVSI and ENSO may potentially be related to changes in the Walker circulation (e.g., Lau and Yang 2002). In El Nino years, the descending branch of the Walker circulation is centered over the western NATL basin, which encourages upper-tropospheric subsidence that can warm the lower stratosphere and suppress convective activity. These changes are favorable for the occurrence of stronger PVSs that can penetrate equatorward in the NATL basin. In addition, enhanced convection over the eastern Pacific may also perturb the waveguide downstream, potentially promoting more AWB in the NATL basin. Conversely, warmer SSTs in the MDR in the NATL encourage enhanced convective activity in the NATL basin, which may act to suppress PVS activity by eroding positive PV anomalies present in the upper-troposphere associated with strong PVS events.

Another intraseasonal oscillation that modulates tropical convection in the NATL basin is the MJO, and changes in the RMM phase of the MJO appear to modulate PVS activity in the NATL basin. In particular, MJO phases 3–4 exhibit positive PVS frequency anomalies in the eastern NATL basin, when positive 200-hPa velocity potential (indicating large-scale subsidence) is also observed in the NATL basin (Ventrice et al. 2013). In contrast, MJO phases 7–8 feature positive PVS frequency anomalies in the western NATL basin, which may be present due to enhanced convective activity in the eastern Pacific (Ventrice et al. 2013), which perturbs the downstream waveguide, enhancing the probability of AWB in the western NATL basin. MacRitchie and Roundy (2016) found a similar relationship to AWB occurring downstream over the central North Pacific when an active MJO was observed over the Indian Ocean.

6.1.2. PVS composites: dynamics and environmental impact

6.1.2.1. Composites of strong and weak PVSs at identification-time (t_0)

Composite analysis was used to investigate changes in environmental variables associated with strong (top 20th percentile) and weak (bottom 20th percentile) PVS events, breaking down these results into different tilt and area percentiles. It was found that strong PVSs, regardless of tilt or area, feature significantly enhanced positive standardized VWS anomalies, downstream of their trough axis, over a much more expansive region than for weak PVSs. The size of the positive VWS anomalies appears to grow in extent as the PVS area increases, and the shear vector shifts from southwesterly to westerly as the PVS tilt increases. These results suggest that strong PVSs produce more unfavorable VWS environments for TCs in comparison to weak PVSs. The increase in positive VWS anomalies in strong PVSs is higher than that found in Zhang et al. (2017), though weak PVSs have lower positive VWS anomalies than that found in Zhang et al. (2017). These differences are mainly attributed to Zhang et al. (2017) combining all PVS-like events into one composite, rather than dividing them up into intensity-based subsets as was done in this study.

Precipitable water is another important variable for TC activity in the NATL basin, where decreases in precipitable water tend to inhibit TC activity in the NATL MDR. Strong PVSs feature significantly reduced standardized precipitable water anomalies within and just northwest of their trough axes in comparison to weak PVS cases. Strong PVSs also have more enhanced precipitable water anomalies flanking their ridges upstream. These differences in standardized precipitable water anomalies are most pronounced for low PVS tilt angles. The strong PVS composites bear the greatest similarity to the precipitable water composite depicted in Zhang et al. (2017), but the weak PVS composites are different, with little to no negative precipitable anomalies observed in the PVS trough axis. This implies that weak PVSs may be less detrimental for TC activity than strong PVSs since they are less likely to be associated with low precipitable water corridors.

Positive sea level pressure anomalies in the subtropical NATL basin on seasonal timescales have also been shown to be associated with reduced TC activity. In general, strong and large PVSs appear to be associated with the greatest, positive, sea level pressure anomalies embedded within, and west, of their trough axes. The size of the positive sea level pressure anomalies also appears to scale with the size of the PVS. Upper-tropospheric thickness was also composited, since this quantity provides a measure of upper-tropospheric stability. Regardless of tilt and area, strong PVSs have much lower upper-tropospheric thickness anomalies embedded in their trough axes. In contrast, weak PVSs have little to no change in their upper-tropospheric thickness relative to climatology in their trough axes. This result implies that strong PVSs have a stronger cold-core in the upper-troposphere, which is related to decreased static stability that may enable positive PV anomalies to have greater influence lower into the troposphere. The presence of higher sea level pressure and lower upper-troposphere thickness anomalies in strong and large PVSs are unfavorable factors for non-baroclinic TC activity, which traditionally occurs in low sea level pressure and high upper-tropospheric thickness environments (e.g., Gray 1968; Knaff 1997; McTaggart-Cowan et al. 2008).

Vertical differences between strong and weak PVSs were investigated in northwest to southeast cross-sections through the PVS trough axis. Strong PVSs were found to have much stronger cyclonic flow at the 350-K isentropic level, with flow differences decreasing moving lower into the troposphere, resulting in the much higher VWS noted in strong PVSs. Strong PVSs also have greater negative temperature anomalies in the troposphere, but greater positive temperature anomalies in the lower stratosphere. The flow and temperature anomaly differences of strong PVSs are consistent with the pattern expected from the inversion of greater positive PV anomalies within the strong PVS trough axis (Eliassen and Kleinschmidt 1957, HMR). Larger anomalous ascent and descent were also observed with strong PVSs, where ascent is observed downstream (southeast) near positive specific humidity anomalies between 850–300-hPa, and descent is observed upstream (northwest) near negative specific humidity anomalies between 500–1000-hPa. The negative specific humidity anomalies are more widespread, and occur in conjunction with stronger northeasterly flow. Dry air in the subtropics, either advected from higher latitudes or induced by subsidence, has been highlighted in PVS case studies and composites (e.g., Waugh 2005; Funatsu and Waugh 2008; Zhang et al. 2017), but the implication in this study is that these processes are enhanced in strong PVS events.

6.1.2.2. Time-lagged composites of strong and weak PVSs

Comparison of time-lagged composites of PV and wind anomalies between strong and weak PVS cases showed that strong PVSs have pre-existing positive PV anomalies in the same region where the strong PVSs develop. The upstream ridge rapidly amplifies 48–24-h before PVS identification, with the combination of negative PV anomalies in the ridge, and positive PV anomalies downstream combining to induce enhanced northeasterly flow. This northeasterly flow aids advection of high-PV air into the strong PVS trough axis. In contrast, weak PVSs have pre-existing negative PV anomalies in the region where the weak PVSs will develop. The upstream ridge slowly amplifies, as westerly wind anomalies spread further east, with less anomalous northeasterly flow. The weaker anomalous northeasterly flow is unable to advect as much high-PV air into the weak PVS trough axis. Consistent with these composites is the observation that strong PVSs are preceded by a statistically significant increase in prior PVS frequency, especially four to six days prior to PVS formation, while weak PVSs are associated with a statistically significant decrease in precursor PVS frequency in the same time frame. The enhanced PVS frequency manifests itself as an initial positive PV anomaly seen in the strong PVS composite, where the anomalous cyclonic flow associated with a prior PVS works jointly with the building ridge to aid positive PV advection into the subsequent strong PVS.

Comparison of time-lagged composites of precipitable water and IVT between strong and weak PVS cases show that strong-PVS events are typically preceded by upstream positive precipitable water anomalies that amplify as they are advected over the building ridge and downstream negative precipitable water anomalies that are advected into the strong PVS trough axis as AWB occurs. In contrast, weak PVSs possess few positive or negative precipitable water anomalies initially, but positive precipitable water anomalies develop later as the ridge builds and undergoes AWB with weak PVS formation on its equatorward flank. In the upstream ridge, strong PVSs have a statistically significant increase in mid-level diabatic heating 60–24-h before PVS occurrence, and negative PV advection by the irrotational wind 54–24h prior to PVS occurrence compared to weak PVSs. These results are consistent with strong PVSs initially having greater anomalous upstream moisture, which may support earlier condensation and diabatic heating. The associated negative PV advection by irrotational outflow thereafter enhances rapid ridge amplification. The positive role that LHR and irrotational outflow plays in ridge amplification along a waveguide has been documented in recent literature (e.g., Grams and Archambault 2016; Teubler and Riemer 2016), but the implication in this study is that stronger ridge amplification may feedback to induce a stronger downstream PVS through downstream development by quasi-barotropic flow (Teubler and Riemer 2016).

6.1.3. Impact of PVS activity on TC activity

The relationship between PVSs and TCs is investigated by correlating yearly PVS activity to TC activity, creating composites of TC position relative to PVS position, and, finally, by looking at distinct TCG pathways to determine if different TCG pathways display different sensitivities to between PVS activity and TC activity.

It is first found that the frequency of PVS events annually has moderate negative correlation with ACE (r = -0.48), as does the average annual area of PVSs (r = -0.41). These results are similar to the correlations in Zhang et al. (2016, 2017), who used a smaller region, period, and different methodology to correlate PVS frequency with TC activity. An important finding in this dissertation is that the relationship between PVSs and TCs depends on the intensity of the PVSs, where strong PVSs (top 20th percentile) have a stronger negative correlation (r = -0.54), but weak PVSs (bottom 20th percentile) have a weak *positive* correlation (r = 0.33).

Combining PVS intensity, area, and frequency over the TC season, PVSI is found to have the strongest negative correlation versus ACE (r = -0.55). The relationship between PVSI and ACE is not linear, however, but closer to an exponential decay curve, which explains more variance between PVSI and ACE. Low PVSI years are associated with high variance in seasonal ACE, but high values of PVSI are associated with low variance in seasonal ACE, which is itself consistently below climatology. High PVSI values are more likely to occur with bottom ACE years, because these years feature stronger, larger, and more frequent PVSs.

Spatially, the negative correlation between PVS frequency and ACE is pronounced across the NATL, but is strongest, and statistically significant, at low latitudes (< 30°N). This correlation is explained by noting that bottom ACE years exhibit a statistically significant increase (+2 to +6%) in PVS frequency, while top ACE years exhibit a statistically significant decrease (-3 to -6%) in PVS frequency equatorward of 30^{o}N. Subtracting the lowest ACE years from the highest ACE years reveals statistically significant increases in VWS between 10^{o}–20^{o}N, lower upper-tropospheric thickness between 20^{o}–30^{o}N, lower precipitable water between 15^{o}–25^{o}N, and higher sea level pressure with stronger northeasterly trade winds over the subtropical NATL basin. These environmental composite differences do not change drastically other than shift eastward when differencing the top minus bottom PVSI years. The decrease in upper-tropospheric thickness suggests that these environmental changes are occurring in conjunction with cold-core upper-tropospheric troughs that are consistent with more frequent, stronger PVSs. Supporting this finding, VWS is positively correlated with PVSI and precipitable water is negative correlated with PVSI in the region where most TC activity occurs (10^{o}–30^{o}N, 20^{o}–90^{o}W). In general, the seasonal increases in VWS, decreases in precipitable water, and increases in sea level pressure with stronger northeasterly trade winds in top PVSI years and bottom ACE years have all been noted as negative factors for TC activity in the MDR (e.g., Gray 1968; Knaff 1997; DeMaria et al. 2001; Zhang et al. 2017). The implication in this study is that these negative TC environmental factors are enhanced in years with large PVSI values.

On intraseasonal timescales, PVSI is significantly enhanced in July for bottom ACE years, but suppressed in top ACE years. While these differences in magnitude decrease later in the TC season, bottom ACE years maintain a PVSI that is above climatology, while top ACE years maintain a PVSI that is below climatology, with most of these differences statistically significant at the 80% confidence interval or greater. One reason why early TC season PVSI differences between top and bottom ACE years may also hold later in the TC season is due to the observation that early season PVSI (June–July) has a strong positive correlation (r = 0.67) with late season PVSI (August–November). This relationship may hold because strong PVS events tend to be associated with previous PVS occurrence, due to the favorable dynamics for additional AWB and higher equatorward PV advection as discussed in Chapter 4. Top PVSI years, however, are also associated with significant reductions in SST anomalies in the MDR, which has also been shown to be negatively correlated with PVS activity. The canonical SST anomaly pattern in the NATL basin between top and bottom PVS years bears remarkable similarities to the negative and positive phases of the AMO, and it is not surprising to see that PVSI is negatively correlated with the AMO (using the index methodology from Klotzbach and Gray 2008). It remains an open question, however, if PVSs are more frequent and/or intense under conditions that are characteristic of a negative AMO, or if PVS activity may modify the SST pattern to resemble the negative AMO pattern.

Composites of TC locations relative to PVS centroids reveal that TCs tend to be clustered well west of the PVS trough axis, in a position where VWS was anomalously low and precipitable water anomalously high in the PVS composites described in Chapter 4. TCs in this location tend to move to the north and northeast, which hints that these TCs may contribute to the ridge building that occurs upstream of the PVS. TCs are less common near the PVS trough axis, and tend to be weaker overall. When dividing these composites into the weakest (bottom 20th percentile) and strongest (top 20th percentile) PVSs, weak PVSs have increases in average TC ACE near the PVS trough axis, while strong PVSs have increases in TC ACE in two areas: northwest and southeast, away from the PVS trough axis. These differences are likely associated with where favorable low VWS and enhanced precipitable water is located relative to the centroid position of strong and weak PVSs.

When dividing TCG into non-baroclinic and baroclinic type pathways using the MC13 dataset, it was found that top PVSI years have a significant reduction in the number of non-baroclinic TCG, but little change in baroclinic TCG frequency compared to bottom PVSI years. This is consistent with yearly ACE from non-baroclinic TCG possessing significant negative correlation with PVSI (r = -0.56), but annual ACE from baroclinic TCG having little correlation with PVSI (r = -0.09). The negative PVSI correlation with ACE from non-baroclinic TCGs is not surprising, since increases in VWS and decreases in precipitable water at low-latitudes are common in top PVSI years. In contrast, ACE for baroclinic TCG in top PVSI years is not dramatically reduced compared to low PVSI years, because these TCs need initial upper-tropospheric forcing for ascent that can be produced by a PVS; however, negative environmental factors such as increased VWS and decreased precipitable water may still suppress their overall ACE (McTaggart-Cowan et al. 2008). This is confirmed by spatially depicting seasonal ACE in top and bottom PVSI years. In top PVSI years, ACE is shifted poleward near where baroclinic TCG is observed, but is lower than the typical climatological value in the NATL basin. In contrast, bottom PVSI years are associated with enhanced ACE values that are shifted equatorward, associated more low-latitude non-baroclinic TCG. These TCs can thrive and produce significant ACE in low-latitude environments of lower VWS and enhanced precipitable water more common in bottom PVSI years.

6.2 Summary schematic of strong and weak PVSs

One of the primarily results presented in this dissertation described the differences between strong and weak PVSs. To describe the evolution of strong and weak PVSs, two schematics are presented here to complement the analysis presented in the three prior result chapters.

Figure 6.1 presents a summary schematic that illustrates the evolution of a canonical strong PVS events from three days prior to their identification (t_0–72h) to the time of identification (t_0), highlighting the main features that are hypothesized to exist prior to, and at, strong PVS identification. At t_0–72h (Fig. 6.1a), pre-exiting areas of positive and negative precipitable water anomalies are located along the 350-K 2-PVU waveguide, where a prominent positive PV anomaly is located near the region where the strong PVS will develop. Over the subsequent 36-h period (Fig. 6.1b), the negative PV anomaly upstream increases in magnitude, expands westward, and is associated with positive precipitable water anomalies upstream that induce condensation with associated LHR and irrotational outflow, helping to spread negative PV anomalies along the upstream ridge. This negative PV anomaly has also strengthened the tropopause-based jet streak on its poleward flank, and this enhanced jet streak is beginning to interact with the positive PV anomaly downstream. The combined anticyclonic and cyclonic flow anomalies associated with the negative and positive PV anomalies then begin to advect high-PV air and low precipitable water air equatorward. By the time of PVS identification (Fig. 6.1c), the advection of high-PV air underneath the anticyclonic ridge has elongated the anomaly to the point that it now possesses PVS characteristics with a large aspect ratio. The high magnitude positive PV anomaly embedded within the PVS is resulting in a corridor of enhanced VWS to its southeast, which may inhibit non-baroclinic TCG pathways. Negative precipitable water anomalies are also located along and upstream of the strong PVS trough axis, which are being advected into the lower latitudes of the NATL basin.

The weak PVS environment (Fig. 6.2) initially features no significant positive or negative precipitable water anomalies, but is associated with an elongated, weak, negative PV anomaly that enhances westerly flow poleward of the waveguide (Fig. 6.2a). In the subsequent 36-h period (Fig. 6.2b), positive precipitable water anomalies appear as the ridge slowly intensifies, strengthening the westerly jet streak poleward of the 2-PVU contour. Unlike in the strong PVS evolution, however, the lack of positive PV anomalies downstream of the ridge reduces the anomalous northeasterly flow along the 2-PVU contour. By the time of weak PVS identification (Fig. 6.2c), the ridge propagates eastward and has significantly intensified due to more prominent LHR and irrotational outflow, but the weak PVS that has formed underneath is only composed of neutral to slightly positive PV anomalies. This weaker PVS is attributed to a lack of pre-existing positive PV anomalies and weaker anomalous northeasterly flow, preventing significant advection of high-PV air from higher latitudes. This weak positive PV anomaly has less enhanced southwesterly VWS and no negative precipitable water anomalies, which do little to prevent non-baroclinic TCG from occurring.

6.3. Recommendations for future work

The results presented in this dissertation motivate many future research directions. First, the methods applied in the current study to identify and quantify PVS characteristics in the NATL basin could be extended to other oceanic basins where PVSs are known to frequently occur (i.e., North Pacific basin, South Pacific basin, South Indian basin). In these basins, there may be different relationships between PVS activity and TC activity than those presented in the NATL basin. It is also possible the PVSs in these other oceanic basins are favored to occur at higher or lower isentropic surfaces than the 350-K surface used in this study. It would be relatively straightforward to adapt the current PVS algorithm to multiple isentropic surfaces to deduce the differences in PVS quantity and characteristics at these different levels, where PVSs on lower isentropic surfaces are more likely to have stronger lower-level influence of wind and temperature anomalies that enhance VWS and result in more pronounced precipitable water anomalies.

Two interesting results found in this dissertation were that early season PVS activity was positively correlated with later season PVS activity, and that strong PVSs appear to also be preceded by enhanced earlier PVS activity. These results suggest that PVS activity may have predictability ranging from synoptic to sub-seasonal scales. Therefore, a worthwhile future study could look at the synoptic to sub-seasonal predictability of PVSs using datasets available in The Observing system Research and Predictability Experiment (THORPEX) Interactive Grand Global Ensemble archive (TIGGE; https://software.ecmwf.int/wiki/display/TIGGE/Home) for predictability out to 15 days, or through the newly released sub-seasonal to seasonal (S2S) prediction project database (Vitart et al. 2017) for predictability in sub-seasonal time ranges. In particular, it may be useful to look at model frameworks that employ atmosphere–ocean coupling versus uncoupled atmospheric models that use static or climatologically varying SSTs to see if incorporating improved SST representation would also improve PVS forecasts, especially given the noted correlations that exist between PVS activity and ENSO, MDR SSTs, the MJO, and the AMO.

An important part of this dissertation was investigating the upstream ridge building that preceded strong and weak PVS events. While this dissertation opted to present a qualitative investigation into dynamic factors that influenced ridge building (i.e., mid-level diabatic heating; negative PV advection by the irrotational wind), a more quantitative investigation could conduct a PV budget (e.g., Boos et al. 2015; Teubler and Riemer 2016) for ridge building events associated with strong versus weak PVS events, to quantify the relative importance of LHR, baroclinic, barotropic, and irrotational wind effects on PV tendency in the upstream ridge. A similar PV budget may also be conducted for the PVS downstream to quantify how positive PV anomalies end up in the trough axis downstream of the ridge. Furthermore, instead of using coarse resolution global model data, which often parameterizes convection that may be important for generating negative PV anomalies in the upstream ridge, high resolution model simulations using the Weather Research and Forecasting (WRF) model (Skamarock et al. 2008) could be run on representative strong and weak PVS case studies. The model simulations from these cases could output model physics tendencies at the high-temporal resolution needed to close PV budgets.

The PVS composites produced at t_0 effectively showed differences in VWS, precipitable water, sea level pressure, and upper-tropospheric thickness between strong and weak PVSs. It would likely also be useful to employ piecewise PV inversion of the positive PV anomalies (e.g., Davis et al. 1991; Winters and Martin 2017) associated with strong and weak PVSs to quantify how the positive PV anomalies modify wind, temperature, and geopotential height anomalies in the tropospheric column below.

Finally, there are forecast applications for using the PVSI, which can be seen as an index used to measure aggregate PVS activity in much the same way as ACE is used to measure aggregate TC activity. Given the positive correlation between early season PVSI and later season PVSI, knowing the PVSI value early in the TC season can be a useful indicator of how PVSI activity may impact the TC season later on (after July). Years with enhanced early season PVSI may foreshadow negative environmental factors that are associated with enhanced PVSI later in the TC season. Studies evaluating the usefulness of PVSI as an operational predictor of TC activity would be useful exercises to see if it can provide additional skill to the current indices used to predict TC activity on intraseasonal to seasonal timescales (e.g., ENSO, AMO, MJO; Klotzbach and Gray 2009).

6.4 Figures

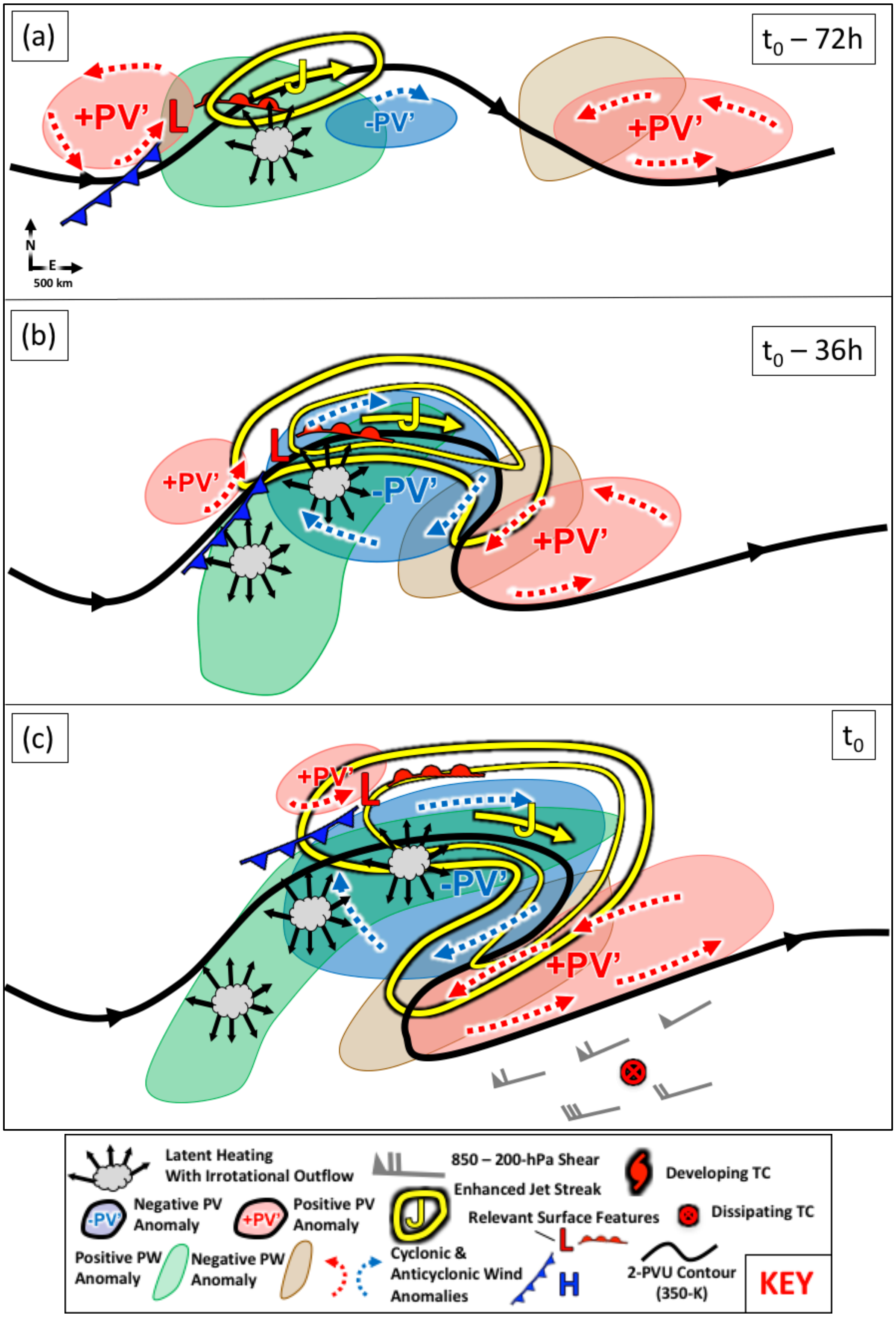

Fig. 6.1. Schematic depicting the development of a strong PVS from 72-h before (a), 36-h before (b), and then at the time of PVS identification (c). All relevant variables in the schematic are depicted in the key at the bottom.

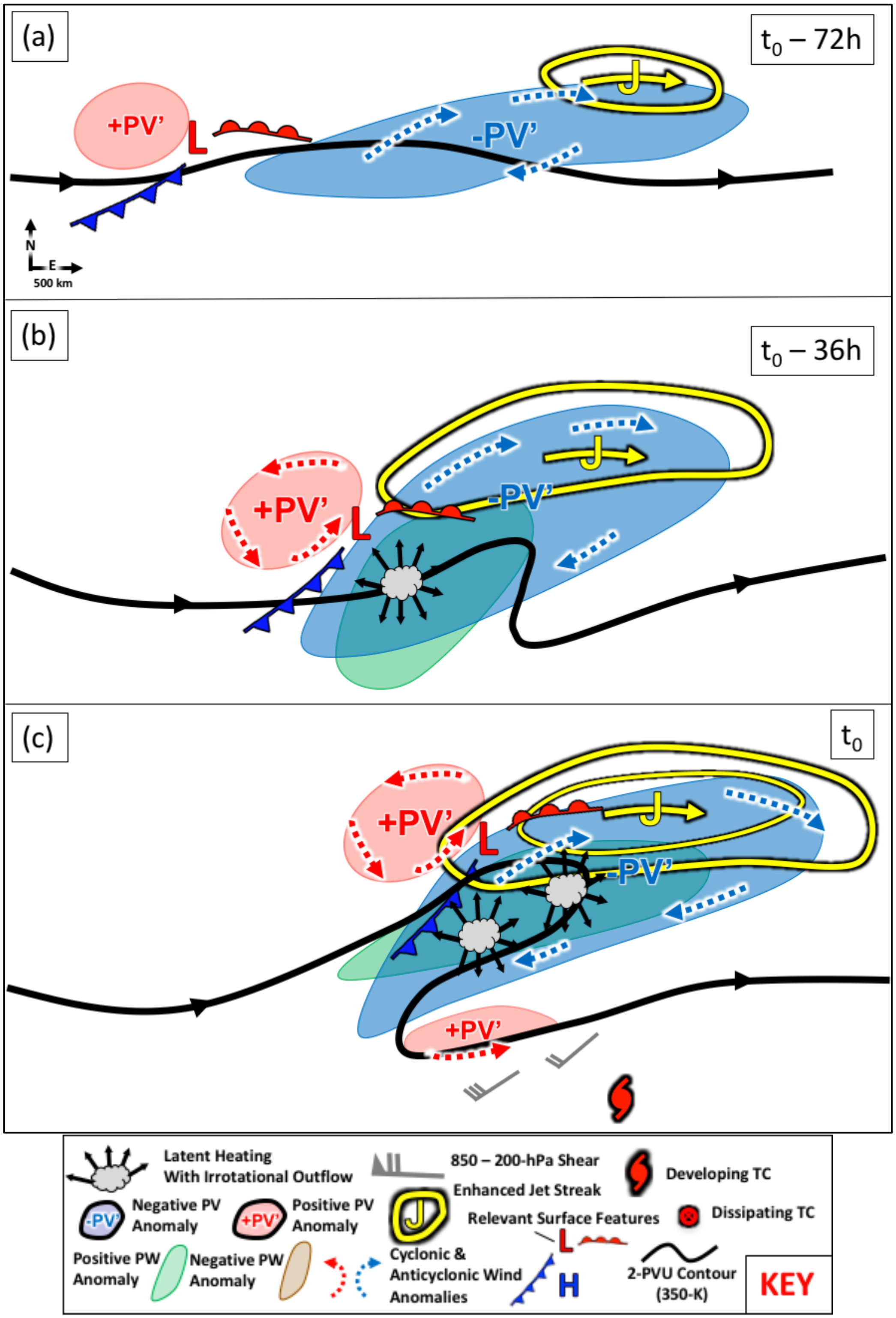

Fig. 6.2. As in Fig. 6.1, except for the development of weak PVSs.

REFERENCES

Abatzoglou, J. T., and G. Magnusdottir, 2006: Planetary wave breaking and nonlinear reflection: seasonal cycle and interannual variability. *J. Clim.*, **19**, 6139–6152.

Appenzeller, C., and H. C. Davies, 1992: Structure of stratospheric intrusions into the troposphere. *Nature*, **358**, 570–572.

Archambault, H. M., L. F. Bosart, D. Keyser, and J. M. Cordeira, 2013: A climatological analysis of the extratropical flow response to recurving western North Pacific tropical cyclones. *Mon. Wea. Rev.*, **141**, 2325–2346.

Archambault, H. M., L. F. Bosart, D. Keyser, Christopher A. Davis, and J. M. Cordeira, 2015: A composite perspective of the extratropical flow response to recurving western North Pacific tropical cyclones. *Mon. Wea. Rev.*, **143**, 1122–1141.

Baldwin, M. P., and J. R. Holton, 1988: Climatology of the stratospheric polar vortex and planetary wave breaking. *J. Atmos. Sci.*, **45**, 1123–1142.

Bell, G. D., M. S. Halpert, R. C. Schnell, R. W. Higgins, J. Lawrimore, V. E. Kousky, R. Tinker, W. Thiaw, M. Chelliah, and A. Artusa, 2000: Climate assessment for 1999. *Bull. Amer. Meteor. Soc.*, **81**, 1328–1328.

Bentley, A. M., and N. D. Metz, 2016: Tropical transition of an unnamed, high-latitude, tropical cyclone over the eastern North Pacific. *Mon. Wea. Rev.*, **144**, 713–736.

Bentley, A. M., D. Keyser, and L. F. Bosart, 2016: A dynamically based climatology of subtropical cyclones that undergo tropical transition in the North Atlantic Basin. *Mon. Wea. Rev.*, **144**, 2049–2068.

Bentley, A. M., L. F. Bosart, and D. Keyser, 2017: Upper-tropospheric precursors to the formation of subtropical cyclones that undergo tropical transition in the North Atlantic Basin. *Mon. Wea. Rev.*, **145**, 503–520.

Bijlsma, S. J., L. M. Hafkenscheid, and P. Lynch, 1986: Computation of the streamfunction and velocity potential and reconstruction of the wind field. *Mon. Wea. Rev.*, **114**, 1547–1551.

Bjerknes, J., 1966: A possible response of the atmospheric Hadley circulation to equatorial anomalies of ocean temperature. *Tellus*, **18**, 820–829.

Boos, W. R., J. V. Hurley, and V. S. Murthy, 2015: Adiabatic westward drift of Indian monsoon depressions. *Q. J. R. Meteorol. Soc.*, **141**, 1035–1048.

Bosart, L. F., and J. A. Bartlo, 1991: Tropical storm formation in a baroclinic environment. *Mon. Wea. Rev.*, **119**, 1979–2013.

Bosart, L. F., B. J. Moore, J. M. Cordeira, and H. M. Archambault, 2017: Interactions of North Pacific tropical, midlatitude, and polar disturbances resulting in linked extreme weather events over North America in October 2007. *Mon. Wea. Rev.*, **145**, 1245–1273.

Bracken, W. E., and L. F. Bosart, 2000: The role of synoptic-scale flow during tropical cyclogenesis over the North Atlantic Ocean. *Mon. Wea. Rev.*, **128**, 353.

Czaja, A., P. Van Der Vaart, and J. Marshall, 2002: A diagnostic study of the role of remote forcing in tropical atlantic variability. *J. Clim.*, **15**, 3280–3290.

Chaing, J. C. H., and D. J. Vimont, 2004: Analogous Pacific and Atlantic meridional modes of tropical atmosphere – ocean variability. *J. Clim.*, **17**, 4143–4158.

Davies, H. C., C. Schar, and H. Wernli, 1991: The palette of fronts and cyclones within a baroclinic wave development. *J. Atmos. Sci.*, **48**, 1666–1689.

Davis, C. A., and K. A. Emanuel, 1991: Potential vorticity diagnostic of cyclogenesis. *Mon. Wea. Rev.*, **119**, 1929–1953.

Davis, C. A., 2010: Simulations of subtropical cyclones in a baroclinic channel model. *J. Atmos. Sci.*, **67**, 2871–2892.

Davis, C. A., and T. J. Galarneau, 2009: The vertical structure of mesoscale convective vortices. *J. Atmos. Sci.*, **66**, 686–704.

Davis, C. A., and L. F. Bosart, 2001: Numerical simulations of the genesis of Hurricane Diana (1984). Part 1: Control simulation. *Mon. Wea. Rev.*, **129**, 1859–1881.

Davis, C., and L. F. Bosart, 2002: Numerical simulations of the genesis of Hurricane Diana (1984). Part II: Sensitivity of track and intensity prediction. *Mon. Wea. Rev.*, **130**, 1100–1124.

Davis, C. A., and L. F. Bosart, 2003: Baroclinically induced tropical cyclogenesis. *Mon. Wea. Rev.*, **131**, 2730–2747.

Davis, C. A., and L. F. Bosart, 2004: The TT problem: Forecasting the tropical transition of cyclones. *Bull. Amer. Meteor. Soc.*, **85**, 1657–1662.

Davis, C. A., and L. F. Bosart, 2006: The formation of Hurricane Humberto (2001): The importance of extra-tropical precursors. *Q. J. R. Meteorol. Soc.*, **132**, 2055–2085.

Dee, D. P., and Coauthors, 2011: The ERA-Interim reanalysis: Configuration and performance of the data assimilation system. *Q. J. R. Meteorol. Soc.*, **137**, 553–597.

DeMaria, M., J. A. Knaff, and B. H. Connell, 2001: A tropical cyclone genesis parameter for the tropical atlantic. *Wea. Forecasting.*, **16**, 219–233.

Eliassen, A., and E. Kleinschmidt, 1957: *Dynamic meteorology. In "Handbuch der Physik."* S. Flügge, Ed. Springer, Berlin, 48,1-154.

Ertel, H., 1942: Ein neuer hydrodynamischer Erhaltungssatz (A new hydrodynamic conservation law). *Meteor. Z.*, 59, 277–281.

Ferreira, R. N., and W. H. Schubert, 1999: The role of tropical cyclones in the formation of tropical upper-tropospheric troughs. *J. Atmos. Sci.*, **56**, 2891–2907.

Fischer, M. S., B. H. T. Tang, and K. L. Corbosiero, 2017: Assessing the influence of upper-tropospheric troughs on tropical cyclone intensification rates after genesis. *Mon. Wea. Rev.*, **145**, 1295–1313.

Fitzpatrick, P. J., J. A. Knaff, C. W. Landsea, and S. V. Finley, 1995: Documentation of a systematic bias in the Aviation Model's forecast of the Atlantic tropical upper-tropospheric trough: implications for tropical cyclone forecasting. *Wea. Forecasting.*, **10**, 433–446.

Funatsu, B. M., and D. W. Waugh, 2008: Connections between potential vorticity intrusions and convection in the eastern tropical Pacific. *J. Atmos. Sci.*, **65**, 987–1002.

Galarneau, T. J., R. McTaggart-Cowan, L. F. Bosart, and C. A. Davis, 2015: Development of North Atlantic tropical disturbances near upper-level potential vorticity streamers. *J. Atmos. Sci.*, **72**, 572–597.

Gastineau, G., and C. Frankignoul, 2015: Influence of the North Atlantic SST variability on the atmospheric circulation during the twentieth century. *J. Clim.*, **28**, 1396–1416.

Goldenberg, S. B., C. W. Landsea, A. M. Mestas-Nunez, and W. M. Gray, 2001: The recent increase in Atlantic hurricane activity: causes and implications. *Science.*, **293**, 474–480.

Gray, W. M., 1968: Global view of the origin of tropical disturbances and storms. *Mon. Wea. Rev.*, **96**, 669–700.

Gray, W. M., 1984: Atlantic seasonal hurricane frequency. Part II: Forecasting its variability. *Mon. Wea. Rev.*, **112**, 1669–1683.

Grams, C. M., and Coauthors, 2011: The key role of diabatic processes in modifying the upper-tropospheric wave guide: A North Atlantic case-study. *Q. J. R. Meteorol. Soc.*, **137**, 2174–2193.

Grams, C. M., and H. M. Archambault, 2016: The key role of diabatic outflow in amplifying the midlatitude flow: A representative case study of weather systems surrounding western North Pacific extratropical transition. *Mon. Wea. Rev.*, **144**, 3847–3869.

Grody, N. C., K. Y. Vinnikov, M. D. Goldberg, J. T. Sullivan, and J. D. Tarpley, 2004: Calibration of multisatellite observations for climatic studies: Microwave Sounding Unit (MSU). *J. Geophys. Res. D Atmos.*, **109**, 1–12.

M. H. Hitchman, and A. S. Huesmann, 2007: A seasonal climatology of Rossby wave breaking in the 320–2000-K Layer. *J. Atmos. Sci.*, **64**, 1922–1940.

Holton, J. R., 1995: Stratosphere-tropopsphere exchange. *Rev. Geophys.*, **33**, 403–439.

Holton, J. R., 2004: *An Introduction to Dynamic Meteorology*. 4th ed. R. Dmowska, J.R. Holton, and H.T. Rossby, Eds. Elsevier Academic Press, 535 pp.

Homeyer, C. R., and K. P. Bowman, 2013: Rossby wavebreaking and transport between the tropics and extratropics above the subtropical jet. *J. Atmos. Sci.*, **70**, 607–626.

Hoskins, B. J., M. E. McIntyre, and A. W. Robertson, 1985: On the use and significance of isentropic potential vorticity maps. *Q. J. R. Meteorol. Soc.*, **111**, 877–946.

Hu, H., F. Dominguez, W. Zhuo, D. A. Lavers, G. Zhang, and F. M. Ralph, 2017: Linking atmospheric river hydrological impacts on the U.S. West Coast to Rossby wave breaking. *J. Clim.*, doi:10.1175/JCLI-D-16-0386.1.

Juckes, M., 1999: The structure of idealized upper-tropospheric shear lines. *J. Atmos. Sci.*, **56**, 2830–2845.

Juckes, M., and R. K. Smith, 2000: Convective destabilization by upper-level troughs. *Q. J. R. Meteorol. Soc.*, **126**, 111–123.

Kaplan, A., M. A. Cane, Y. Kushnir, A. C. Clement, M. Benno Blumenthal, and B. Rajagopalan, 1998: Analyses of global sea surface temperature 1856-1991. *J. Geophys. Res.*, **103**, 567–589.

Kaplan, J., M. DeMaria, and J. A. Knaff, 2010: A revised tropical cyclone rapid intensification index for the Atlantic and eastern North Pacific Basins. *Wea. Forecasting.*, **25**, 220–241.

Klotzbach, P. J., 2011: The influence of El Niño-Southern Oscillation and the Atlantic Multidecadal Oscillation on Caribbean tropical cyclone activity. *J. Clim.*, **24**, 721–731.

Klotzbach, P. J., and W. M. Gray, 2008: Multidecadal variability in North Atlantic tropical cyclone activity. *J. Clim.*, **21**, 3929–3935.

Klotzbach, P. J., and W. M. Gray, 2009: Twenty-five years of Atlantic basin seasonal hurricane forecasts (1984-2008). *Geophys. Res. Lett.*, **36**, 1–5.

Klotzbach, P., W. Gray, and C. Fogarty, 2015: Active Atlantic hurricane era at its end? *Nat. Geosci.*, **8**, 737–738.

Knaff, J. A., 1997: Implications of summertime sea level pressure anomalies in the tropical Atlantic region. *J. Clim.*, **10**, 789–804.

Knapp, K. R., M. C. Kruk, D. H. Levinson, H. J. Diamond, and C. J. Neumann, 2010: The International Best Track Archive for Climate Stewardship (IBTrACS). *Bull. Amer. Meteor. Soc.*, **91**, 363–376.

Knippertz, P., 2005: Tropical–extratropical interactions associated with an Atlantic tropical plume and subtropical jet streak. *Mon. Wea. Rev.*, **133**, 2759–2776.

Knippertz, P., and J. E. Martin, 2005: Tropical plumes and extreme precipitation in subtropical and tropical West Africa. *Q. J. R. Meteorol. Soc.*, **131**, 2337–2365.

Knippertz, P., 2007: Tropical-extratropical interactions related to upper-level troughs at low latitudes. *Dyn. Atmos. Ocean.*, **43**, 36–62.

Knippertz, P., and J. E. Martin, 2007: A Pacific moisture conveyor belt and its relationship to a significant precipitation event in the semiarid southwestern United States. *Wea. Forecasting.*, **22**, 125–144.

Kunz, A., P. Konopka, R. Müller, and L. L. Pan, 2011: Dynamical tropopause based on isentropic potential vorticity gradients. *J. Geophys. Res. Atmos.*, **116**, 1–13.

Kunz, A., M. Sprenger, and H. Wernli, 2015: Climatology of potential vorticity streamers and associated isentropic transport pathways across PV gradient barriers. *J. Geophys. Res.*, 3802–3821.

Lau K-M, and S. Yang, 2002: Walker Circulation, in *Encyclopedia of Atmospheric Sciences*, edited by J. Holton, J. P. Pyle, and J. Curry, pp. 2505–2509, Academic, San Diego, Calif., 2002

Ling, J., and C. Zhang, 2013: Diabatic heating profiles in recent global reanalyses. *J. Clim.*, **26**, 3307–3325.

MacRitchie, K., and P. E. Roundy, 2016: The two-way relationship between the Madden-Julian oscillation and anticyclonic wave breaking. *Q. J. R. Meteorol. Soc.*, **142**, 2159–2167.

Madden, R. A., and P. R. Julian, 1971: Detection of a 40–50 day oscillation in the zonal wind in the tropical Pacific. *J. Atmos. Sci.*, **28**, 702–708.

Madonna, E., H. Wernli, H. Joos, and O. Martius, 2014: Warm conveyor belts in the ERA-Interim dataset (1979–2010). Part I: Climatology and potential vorticity evolution. *J. Clim.*, **27**, 3–26.

Madonna, E., S. Limbach, C. Aebi, H. Joos, H. Wernli, and O. Martius, 2014: On the co-occurrence of warm conveyor belt outflows and PV streamers. *J. Atmos. Sci.*, **71**, 3668–3673.

Maloney, E. D., and L. Hartmann, 2000: Modulation of hurricane activity in the Gulf of Mexico by the Madden-Julian Oscillation. *Science*, **287**, 2002–2004.

Martin, E. R., and C. D. Thorncroft, 2014: The impact of the AMO on the West African monsoon annual cycle. *Q. J. R. Meteorol. Soc.*, **140**, 31–46.

Martin, J. E., 2006: *Mid-Latitude Atmospheric Dynamics: A First Course*. Wiley, 324 pp.

Martínez-Alvarado, O., H. Joos, J. Chagnon, M. Boettcher, S. L. Gray, R. S. Plant, J. Methven, and H. Wernli, 2014: The dichotomous structure of the warm conveyor belt. *Q. J. R. Meteorol. Soc.*, **140**, 1809–1824.

Martius, O., C. Schwierz, and H. C. Davies, 2007: breaking waves at the tropopause in the wintertime Northern Hemisphere: climatological analyses of the orientation and the theoretical LC1/2 classification. *J. Atmos. Sci.*, **64**, 2576–2592.

Martius, O., C. Schwierz, and H. C. Davies, 2010: Tropopause-level waveguides. *J. Atmos. Sci.*, **67**, 866–879.

Masarik, M. T., and W. H. Schubert, 2013: Analytical solutions of the potential vorticity invertibility principle. *J. Adv. Model. Earth Syst.*, **5**, 366–381.

Massacand, A. C., H. Wernli, and H. C. Davies, 2001: Influence of upstream diabatic heating upon an Alpine event of heavy precipitation. *Mon. Wea. Rev.*, **129**, 2822–2828.

McIntyre, M. E., and T. N. Palmer, 1983: Breaking planetary waves in the stratosphere. *Nature*, **305**, 593–600.

McTaggart-Cowan, R., L. F. Bosart, C. A. Davis, E. H. Atallah, J. R. Gyakum, and K. A. Emanuel, 2006a: Analysis of Hurricane Catarina (2004). *Mon. Wea. Rev.*, **134**, 3029–3053.

McTaggart-Cowan, R., E. H. Atallah, J. R. Gyakum, and L. F. Bosart, 2006b: Hurricane Juan (2003). Part I : a diagnostic and compositing life cycle study. *Mon. Wea. Rev.*, **134**, 1725–1747.

McTaggart-Cowan, R., L. F. Bosart, J. R. Gyakum, and E. H. Atallah, 2007a: Hurricane Katrina (2005). Part I: complex life cycle of an intense tropical cyclone. *Mon. Wea. Rev.*, **135**, 3905–3926, doi:10.1175/2007MWR1875.1.

McTaggart-Cowan, R., L. F. Bosart, J. R. Gyakum, and E. H. Atallah, 2007b: Hurricane Katrina (2005). Part II: evolution and hemispheric impacts of a diabatically generated warm pool. *Mon. Wea. Rev.*, **135**, 3927–3949.

McTaggart-Cowan, R., G. D. Deane, L. F. Bosart, Christopher A. Davis, and T. J. Galarneau, 2008: Climatology of tropical cyclogenesis in the North Atlantic (1948–2004). *Mon. Wea. Rev.*, **136**, 1284–1304.

McTaggart-Cowan, R., T. J. Galarneau, L. F. Bosart, R. W. Moore, and O. Martius, 2013: A global climatology of baroclinically influenced tropical cyclogenesis. *Mon. Wea. Rev.*, **141**, 1963–1989.

Meier, F., and P. Knippertz, 2009: Dynamics and predictability of a heavy dry-season precipitation event over West Africa—Sensitivity experiments with a global model. *Mon. Wea. Rev.*, **137**, 189–206.

Methven, J., 2015: Potential vorticity in warm conveyor belt outflow. *Q. J. R. Meteorol. Soc.*, **141**, 1065–1071.

Moore, R. W., O. Martius, and T. Spengler, 2010: The modulation of the subtropical and extratropical atmosphere in the Pacific Basin in response to the Madden–Julian Oscillation. *Mon. Wea. Rev.*, **138**, 2761–2779.

Ndarana, T., and D. W. Waugh, 2011: A climatology of Rossby wave breaking on the Southern Hemisphere tropopause. *J. Atmos. Sci.*, **68**, 798–811.

Neiman, P. J., F. M. Ralph, G. A. Wick, J. D. Lundquist, and M. D. Dettinger, 2008: Meteorological characteristics and overland precipitation impacts of atmospheric rivers affecting the West Coast of North America based on eight years of SSM/I satellite observations. *J. Hydrometeorol.*, **9**, 22–47.

Nielsen-Gammon, J. W., and R. J. Lefevre, 1996: Piecewise tendency diagnosis of dynamical processes governing the development of an upper-tropospheric mobile trough. *J. Atmos. Sci.*, **53**, 3120–3142.

Orlanski, I., and J. Sheldon, 1993: A case of downstream baroclinic development over western North America. *Mon. Wea. Rev.*, **121**, 2929–2950.

Pantillon, F., J. P. Chaboureau, C. Lac, and P. Mascart, 2013: On the role of a Rossby wave train during the extratropical transition of hurricane Helene (2006). *Q. J. R. Meteorol. Soc.*, **139**, 370–386.

Pantillon, F., J.-P. Chaboureaua, and E. Richarda, 2015: Remote impact of North Atlantic hurricanes on the Mediterranean during episodes of intense rainfall in autumn 2012. *Q. J. R. Meteorol. Soc.*, **141**, 967–978.

Patla, J. E., D. Stevens, and G. M. Barnes, 2009: A Conceptual model for the influence of TUTT cells on tropical cyclone motion in the northwest Pacific Ocean. *Wea. Forecasting.*, **24**, 1215–1235.

Peduzzi, P., B. Chatenoux, H. Dao, A. De Bono, C. Herold, J. Kossin, F. Mouton, and O. Nordbeck, 2012: Global trends in tropical cyclone risk. *Nat. Clim. Chang.*, **2**, 289–294.

Peirano, C. M., K. L. Corbosiero, and B. H. Tang, 2016: Revisiting trough interactions and tropical cyclone intensity change. *Geophys. Res. Lett.*, **43**, 5509–5515.

Postel, G. A., and M. H. Hitchman, 1999: A climatology of Rossby wave breaking along the subtropical tropopause. *J. Atmos. Sci.*, **56**, 359–373.

Postel, G. A., and M. H. Hitchman, 2001: A case study of Rossby wave Breaking along the subtropical tropopause. *Mon. Wea. Rev.*, **129**, 2555–2569.

Rabier, F., J.-N. Thépaut, and P. Courtier, 1998: Extended assimilation and forecast experiments with a four-dimensional variational assimilation system. *Q. J. R. Meteorol. Soc.*, **124**, 1861–1887.

Raiber, F., H. Jarvian, E. Klinker, J. F. Mahfouf, and A. Simmons, 2000: The ECMWF operational implementation of four-dimensional variational assimilation. I: Experimental results with simplified physics. *Q. J. R. Meteorol. Soc.*, **126**, 1143–1170.

Ralph, F. M., P. J. Neiman, G. N. Kiladis, K. Weickmann, and D. W. Reynolds, 2011: A multiscale observational case study of a Pacific atmospheric river exhibiting tropical–extratropical connections and a mesoscale frontal wave. *Mon. Wea. Rev.*, **139**, 1169–1189.

Rappaport, E. N., and Coauthors, 2009: Advances and challenges at the National Hurricane Center. *Wea. Forecasting.*, **24**, 395–419.

Reed, R. J., 1955: A study of a characteristic type of upper-level frontogenesis. *J. Meteorol.* **12**, 226–237.

Riemer, M., and S. C. Jones, 2010: The downstream impact of tropical cyclones on a developing baroclinic wave in idealized scenarios of extratropical transition. *Q. J. R. Meteorol. Soc.*, **136**, 617–637.

Riemer, M., S. C. Jones, and C. A. Davis, 2008: The impact of extratropical transition on the downstream flow: An idealized modelling study with a straight jet. *Q. J. R. Meteorol. Soc.*, **134**, 69–91.

Rossby, C. G., 1939: Relation between variations in the intensity of the zonal circulation of the atmosphere and the displacements of the semi-permanent centers of action. *J. Mar. Res.*, **2**, 38–55.

Rossby, C.-G., 1940: Planetary flow patterns in the atmosphere. *Q. J. R. Meteorol. Soc.*, **66**, 68–87.

Rotunno, R., and K. A. Emanuel, 1987: An air–sea interaction theory for tropical cyclones. Part II: evolutionary study using a nonhydrostatic axisymmetric numerical model. *J. Atmos. Sci.*, **44**, 542–561.

Rugg, A., G. R. Foltz, and R. C. Perez, 2016: Role of mixed layer dynamics in tropical North Atlantic interannual sea surface temperature variability. *J. Clim.*, **29**, 8083–8101.

Sadler, J. C., 1967: The tropical upper tropospheric trough as a secondary source of typhoons and a primary source of trade-wind disturbance. Hawaii Institute of Geophysics, University of Hawaii, HIG-67-12 and AFCRL-67-0203. 44 pp.

Sadler, J. C., 1976: A Role of tropical upper tropospheric trough in early season typhoon development. *Mon. Wea. Rev.*, **104**, 1266–1278.

Saha, S., and Coauthors, 2010: The NCEP Climate Forecast System Reanalysis. *Bull. Amer. Meteor. Soc.*, **91**, 1015–1057.

Sardeshmukh, P. D., and B. J. Hoskins, 1988: The generation of global rotational flow by steady idealized tropical divergence. *J. Atmos. Sci.*, **45**, 1228–1251.

Schwierz, C., S. Dirren, and H. C. Davies, 2004: Forced waves on a zonally aligned jet stream. *J. Atmos. Sci.*, **61**, 73–87.

Simmons, A. J., P. Poli, D. P. Dee, P. Berrisford, H. Hersbach, S. Kobayashi, and C. Peubey, 2014: Estimating low-frequency variability and trends in atmospheric temperature using ERA-Interim. *Q. J. R. Meteorol. Soc.*, **140**, 329–353.

Skamarock, W. C., and Coauthors, 2008: A description of the Advanced Research WRF version 3. *Tech. Rep.*, 113.

Slingo, J. M., 1998: Extratropical forcing of tropical convection. *Q. J. R. Meteorol. Soc.*, **124**, 27–51.

Song, J., C. Li, J. Pan, and W. Zhou, 2011: Climatology of anticyclonic and cyclonic Rossby wave breaking on the dynamical tropopause in the Southern Hemisphere. *J. Clim.*, **24**, 1239–1251.

Sprenger, M., O. Martius, and J. Arnold, 2013: Short communication cold surge episodes over southeastern Brazil – a potential vorticity perspective. *Int. J. Climatol.*, **33**, 2758–2767, doi:10.1002/joc.3618.

Stoelinga, M. T., 2003: Comments on "The evolution and dynamical role of reduced upper-tropospheric potential vorticity in intensive observing period one of FASTEX." *Mon. Wea. Rev.*, **131**, 1944–1947.

Strong, C., and G. Magnusdottir, 2008: Tropospheric Rossby wave breaking and the NAO/NAM. *J. Atmos. Sci.*, **65**, 2861–2876.

Teubler, F., and M. Riemer, 2016: Dynamics of Rossby wave packets in a quantitative potential vorticity-potential temperature framework. *J. Atmos. Sci.*, **73**, 1063–1081.

Thépaut, J.-N., P. Courtier, G. Belaud, and G. Lemaître, 1996: Dynamical structure functions in a four-dimensional variational assimilation: A case study. *Q. J. R. Meteorol. Soc.*, **122**, 535–561.

Thorncroft, C. D., B. J. Hoskins, and M. E. McIntyre, 1993: Two paradigms of baroclinic-wave life-cycle behaviour. *Q. J. R. Meteorol. Soc.*, **119**, 17–55.

Thorpe, A. J., and H. Volkert, 1997: Potential vorticity: A short history of its definitions and uses. *Meteorol. Zeitschrift*, **6**, 275–280.

Torn, R. D., 2010: Diagnosis of the downstream ridging associated with extratropical transition using short-term ensemble forecasts. *J. Atmos. Sci.*, **67**, 817–833.

Trenberth, K. E., 1978: On the Interpretation of the Diagnostic Quasi-Geostrophic Omega Equation. *Mon. Wea. Rev.*, **106**, 131–137.

Trenberth, K. E., and D. J. Shea, 2006: Atlantic hurricanes and natural variability in 2005. *Geophys. Res. Lett.*, **33**, 1–4.

Vecchi, G. A., and G. Villarini, 2014: Next season's hurricanes. *Science*, **343**, 618–619.

Ventrice, M. J., M. C. Wheeler, H. H. Hendon, C. J. Schreck, C. D. Thorncroft, and G. N. Kiladis, 2013: A modified multivariate Madden–Julian Oscillation index using velocity potential. *Mon. Wea. Rev.*, **141**, 4197–4210.

Vimont, D. J., and J. P. Kossin, 2007: The Atlantic Meridional Mode and hurricane activity. *Geophys. Res. Lett.*, **34**, 1–5.

Vitart, F., and Coauthors, 2017: The sub-seasonal to seasonal prediction (S2S) project database. *Bull. Amer. Meteor. Soc.*, 163–173.

Waugh, D. W., and L. M. Polvani, 2000: Climatology of intrusions into the tropical upper troposphere. *Geophys. Res. Lett.*, **27**, 3857–3860.

Waugh, D. W., and B. M. Funatsu, 2003: Intrusions into the tropical upper troposphere : three-dimensional structure and accompanying ozone and OLR distributions. *J. Atmos. Sci.*, **60**, 637–653.

Waugh, D. W., 2005: Impact of potential vorticity intrusions on subtropical upper tropospheric humidity. *J. Geophys. Res. D Atmos.*, **110**, 1–11.

Wheeler, M. C., and H. H. Hendon, 2004: An all-season real-time multivariate MJO Index: development of an index for monitoring and prediction. *Mon. Wea. Rev.*, **132**, 1917–1932.

Wernli, H., and H. C. Davies, 1997: A Lagrangian-based analysis of extratropical cyclones I: The method and some applications. *Q. J. R. Meteorol. Soc.*, **123**, 467–489.

Wernli, H., and M. Sprenger, 2007: Identification and ERA-15 climatology of potential vorticity streamers and cutoffs near the extratropical tropopause. *J. Atmos. Sci.*, **64**, 1569–1586.

Whitaker, J. S., G. P. Compo, and J.-N. Thépaut, 2009: A comparison of variational and ensemble-based data assimilation systems for reanalysis of sparse observations. *Mon. Wea. Rev.*, **137**, 1991–1999.

Whitfield, M. B., and S. W. Lyons, 1992: An upper-tropospheric low over Texas during summer. *Wea. Forecasting.*, **7**, 89–106.

Wilks, D. S., 1997: Resampling hypothesis tests for autocorrelated fields. *J. Clim.*, **10**, 65–82.

Wilks, D. S., 2006: *Statistical Methods in the Atmospheric Sciences*. 2nd ed. R. Dmowska, D. Hartmann, and H.T. Rossby, Eds. Elsevier Academic Press, 627 pp.

Winters, A. C., and J. E. Martin, 2017: Diagnosis of a North American polar–subtropical jet superposition employing piecewise potential vorticity inversion. *Mon. Wea. Rev.*, **145**, 1853–1873.

Yanai, M., and T. Tomita, 1998: Seasonal and interannual variability of atmospheric heat sources and moisture sinks as determined from NCEP–NCAR reanalysis. J. Climate, 11, 463–482.

Yoneyama, K., and D. B. Parsons, 1999: A proposed mechanism for the intrusion of dry air into the tropical Western Pacific region. *J. Atmos. Sci.*, **56**, 1524–1546.

Zehr, R. M., 1992: Tropical cyclogenesis in the western North Pacific. NOAA Tech. Rep. NESDIS 61, NOAA/NESDIS, 181 pp.

Zhang, G., Z. Wang, T. J. Dunkerton, M. S. Peng, and G. Magnusdottir, 2016: Extratropical impacts on Atlantic tropical cyclone activity. *J. Atmos. Sci.*, **73**, 1401–1417.

Zhang, G., Z. Wang, M. S. Peng, and G. Magnusdottir, 2017: Characteristics and impacts of extratropical Rossby wave breaking during the Atlantic hurricane season. *J. Clim.*, **30**, 2363–2378.

APPENDIX

Figure A1 shows the 1979–2015 yearly PVS frequency for each year of the ERAI climatology. Note the large variability that can occur from year to year and how this PVS activity modulates the 200-hPa streamlines that indicate the time-mean TUTT axis.

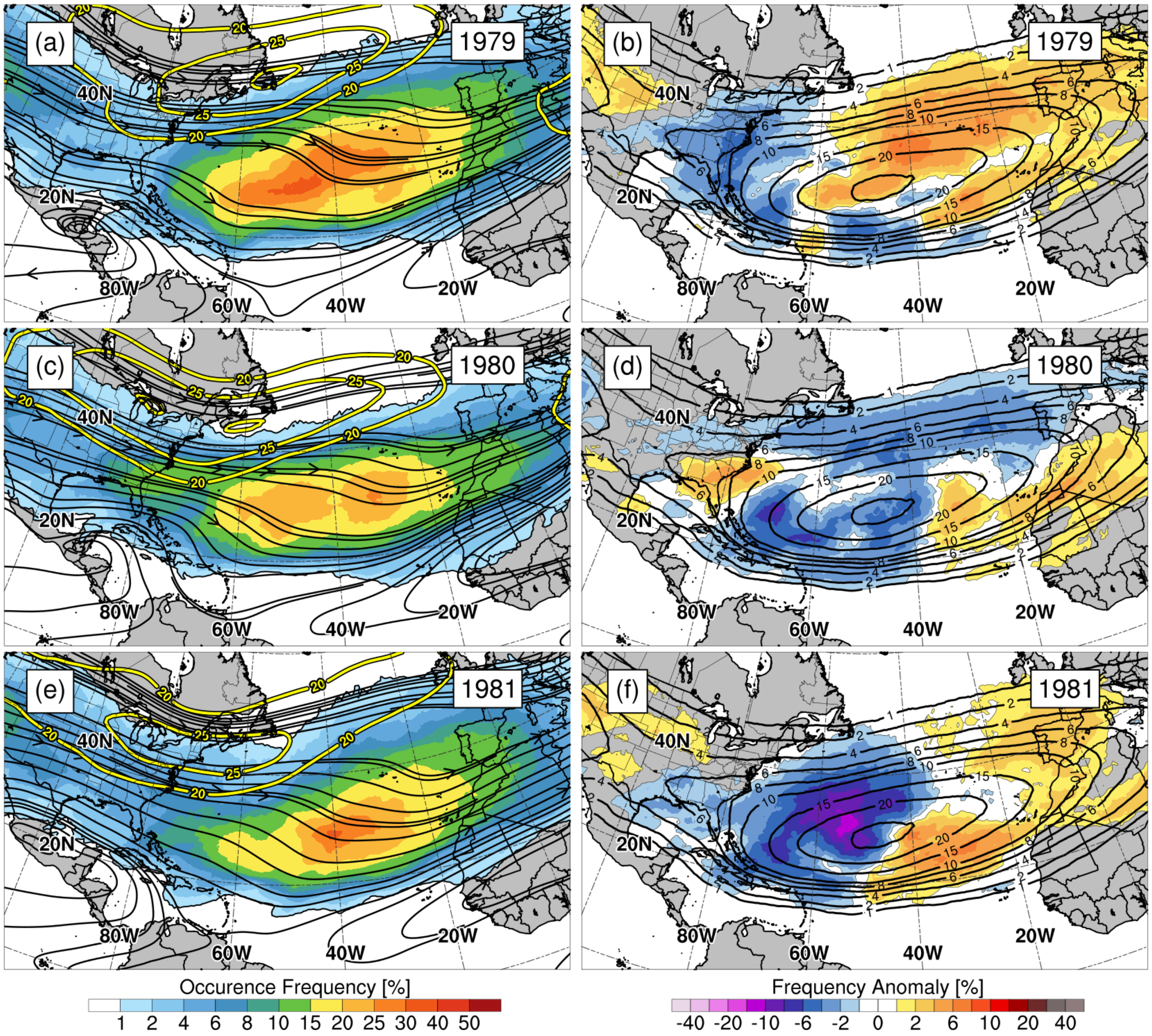

Figure A1. (left panels) PVS frequency (shaded,%), 200-hPa wind magnitude (yellow contours, > 20 m s^{-1}), and 200-hPa streamlines (black lines). (Right panels) PVS frequency anomaly (shaded, %) relative to climatology (black contours, %). Years are (a–b) 1979, (c–d) 1980, and (e–f) 1981.

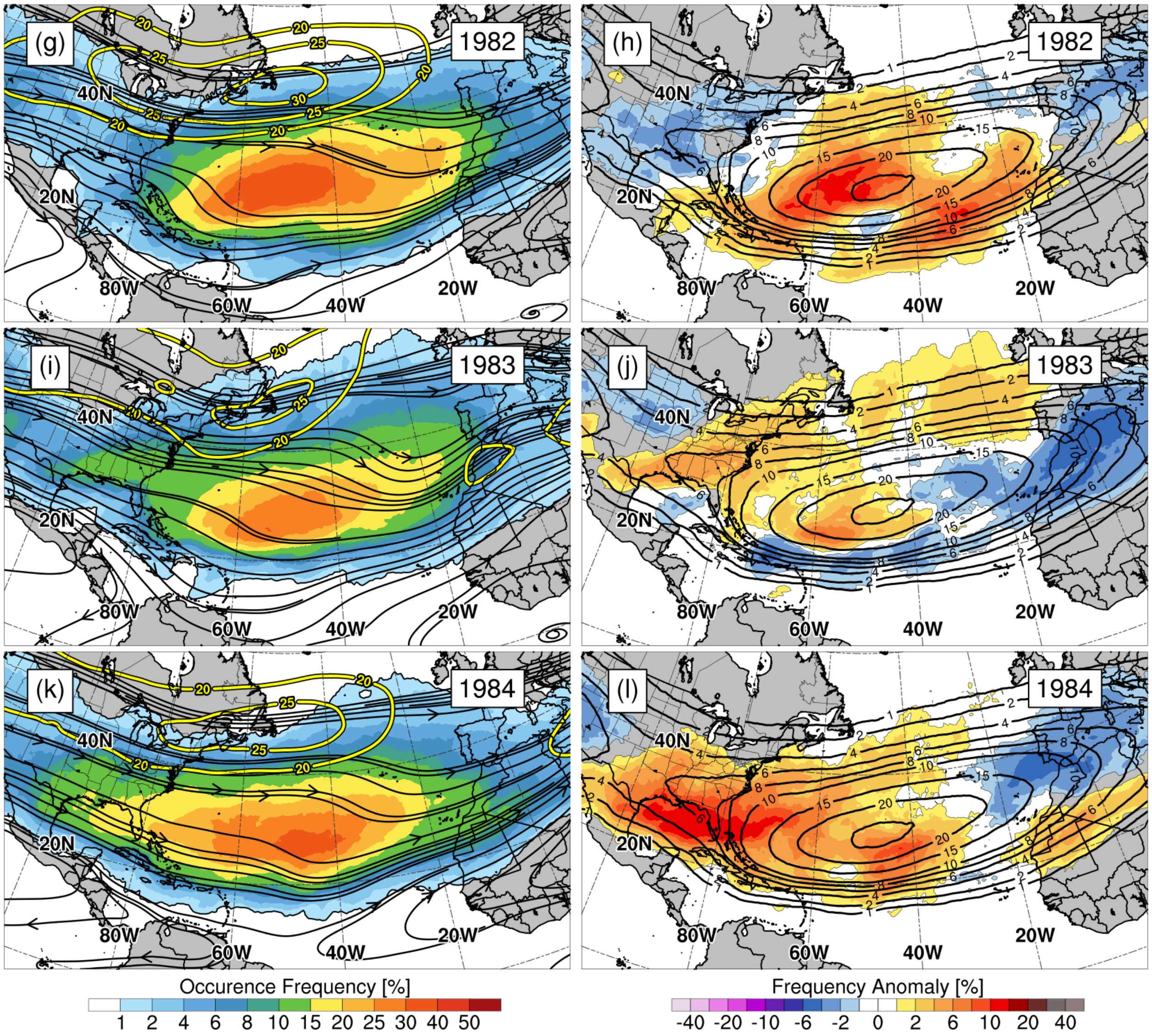

Fig. A1 Cont. for (g–h) 1982, (i–j) 1983, and (k–l) 1984.

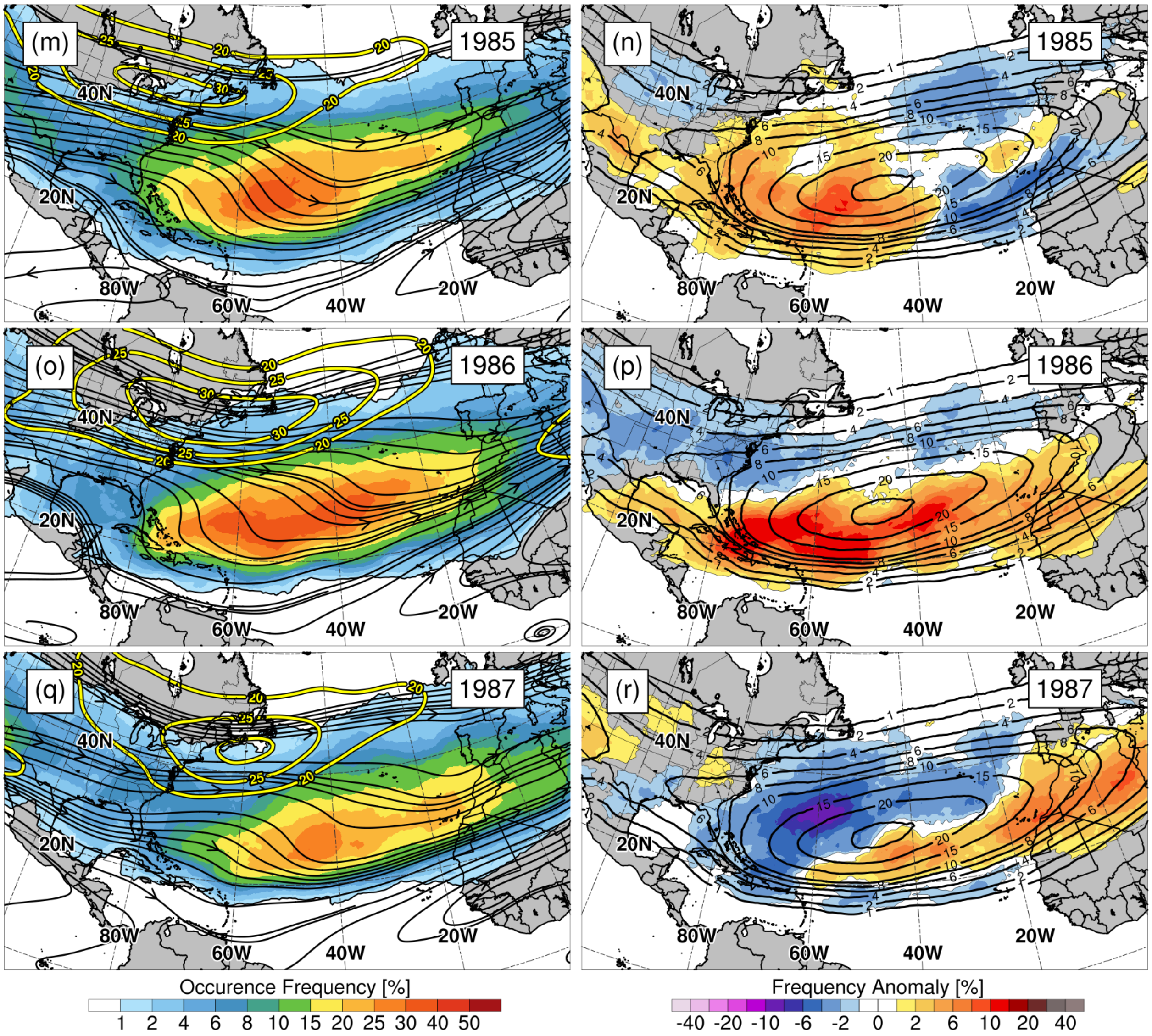

Fig. A1 Cont. for (m–n) 1985, (o–p) 1986, and (q–r) 1987.

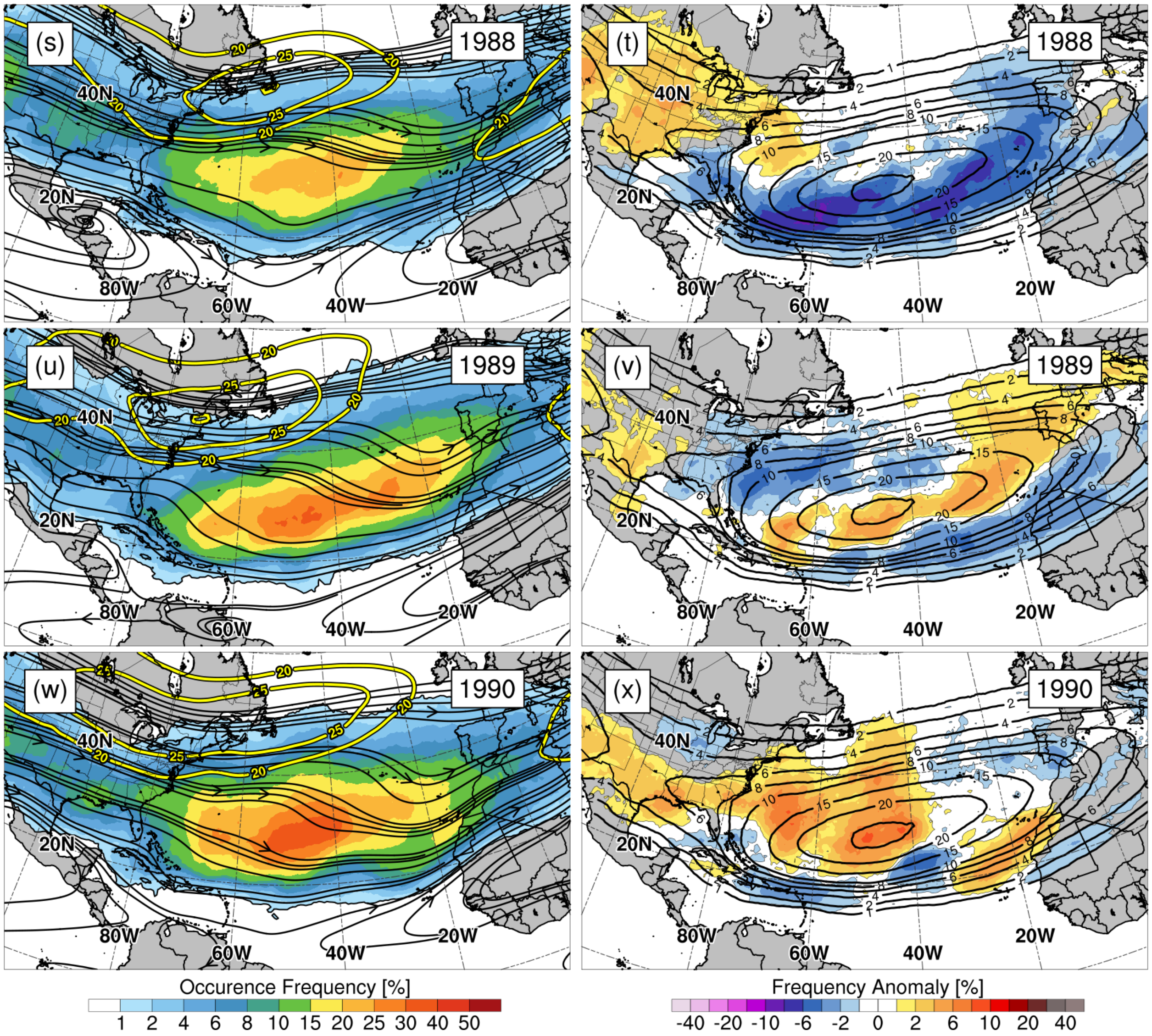

Fig. A1 Cont. for (s–t) 1988, (u–v) 1989, and (w–x) 1990.

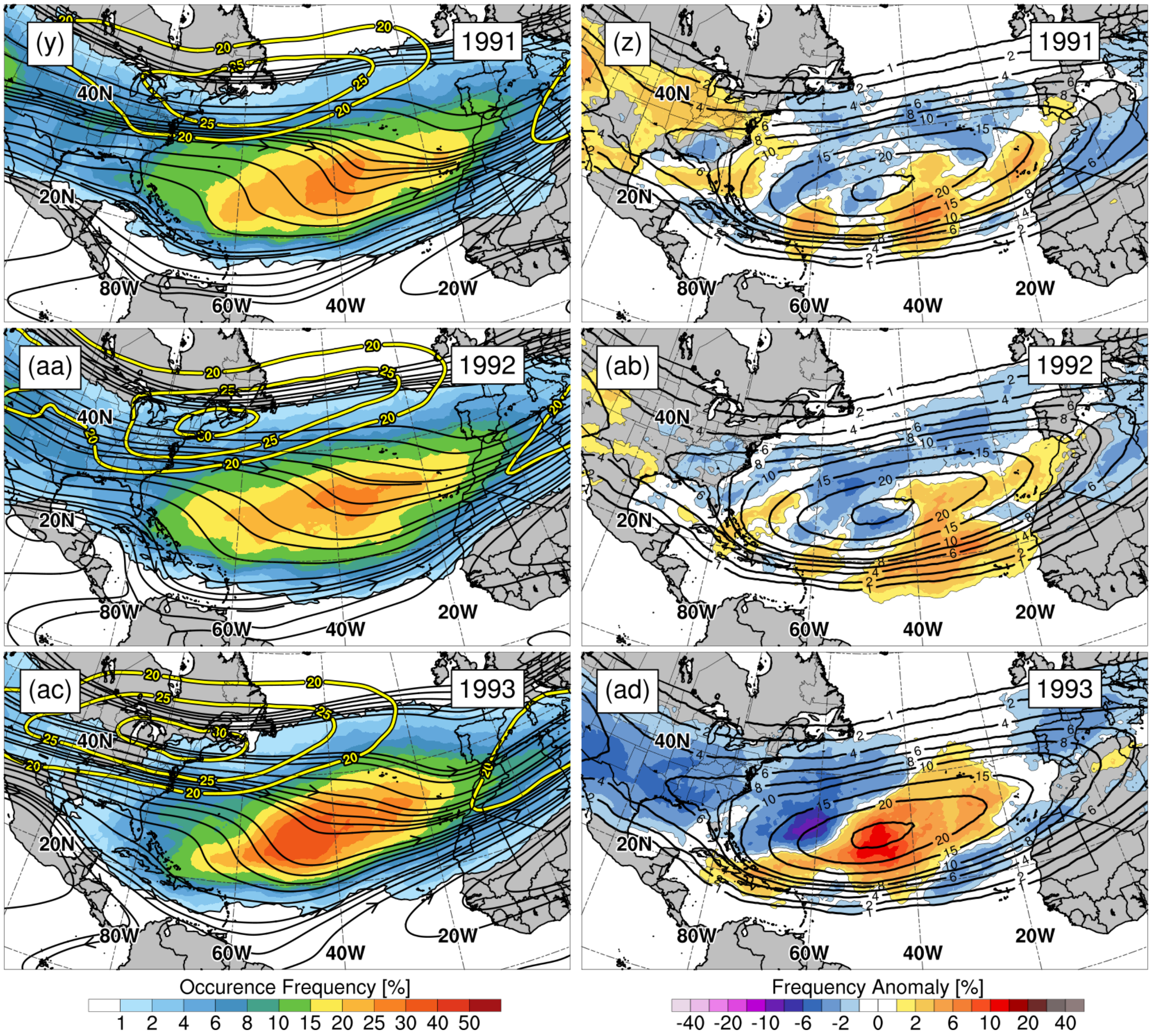

Fig. A1 Cont. for (y–z) 1991, (aa–ab) 1992, and (ac–ad) 1993.

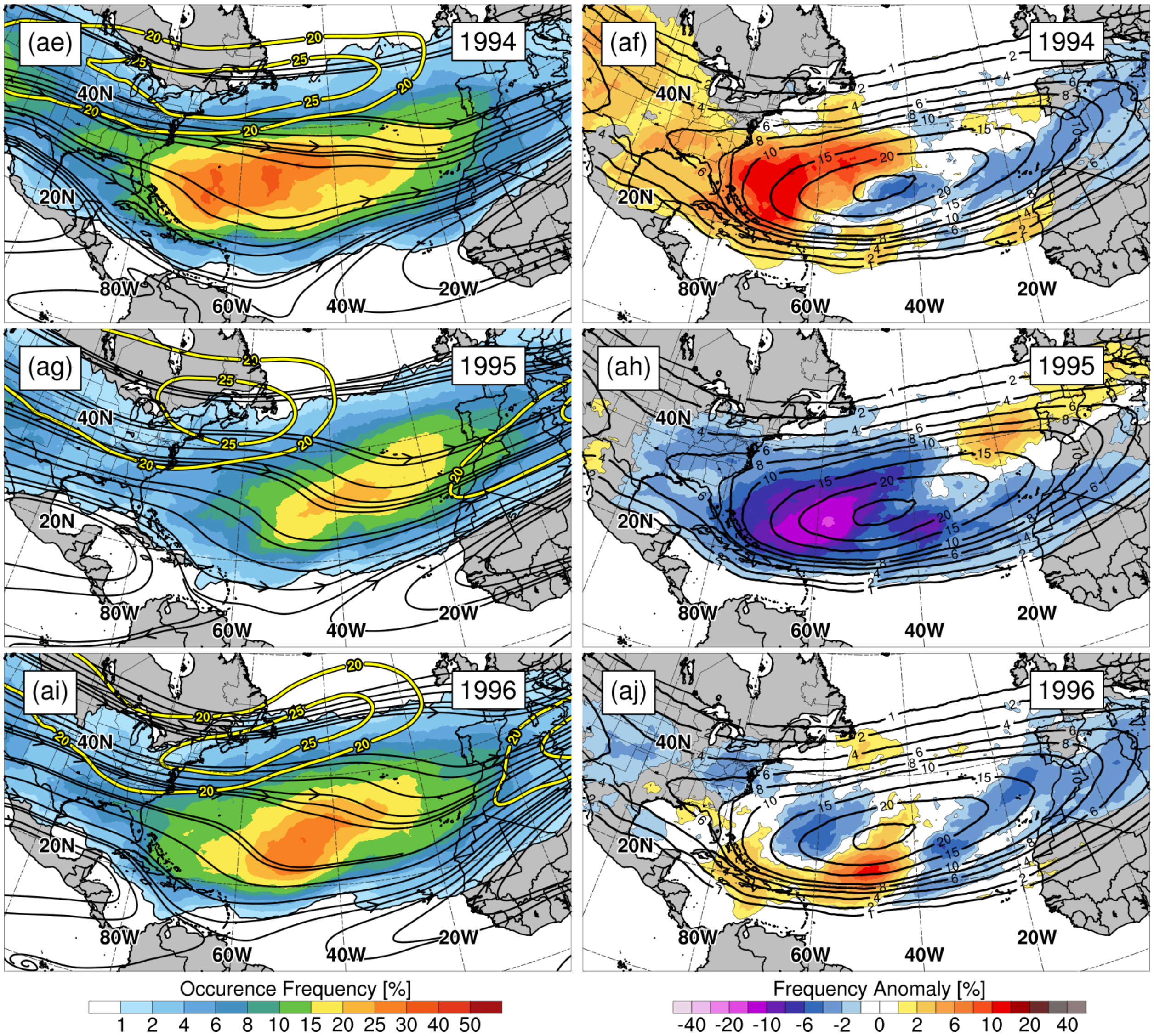

Fig A1 Cont. (ae–af) 1994, (ag–ah) 1995, and (ai–aj) 1996.

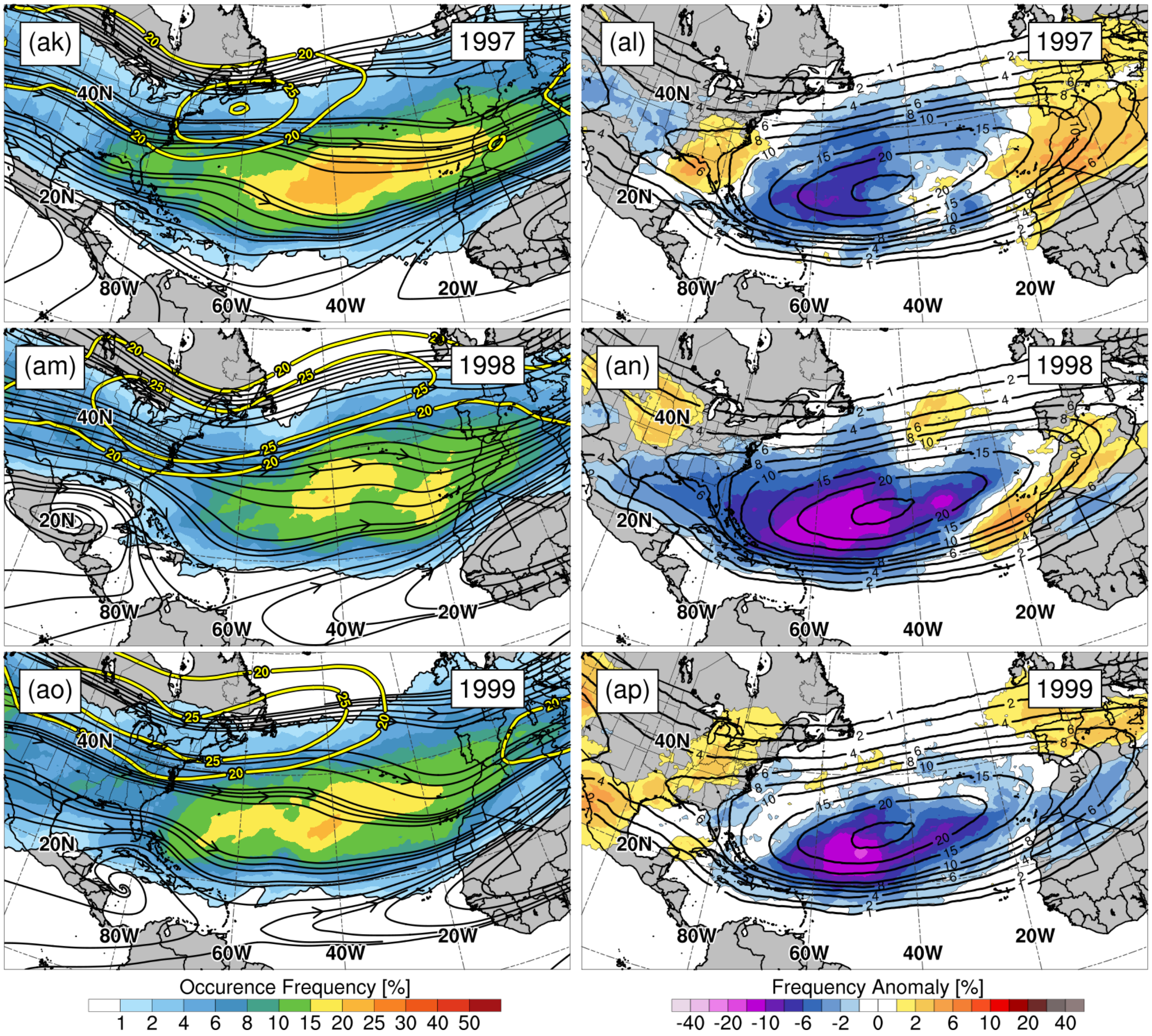

Fig A1 Cont. (ak–al) 1997, (am–an) 1998, and (ao–ap) 1999.

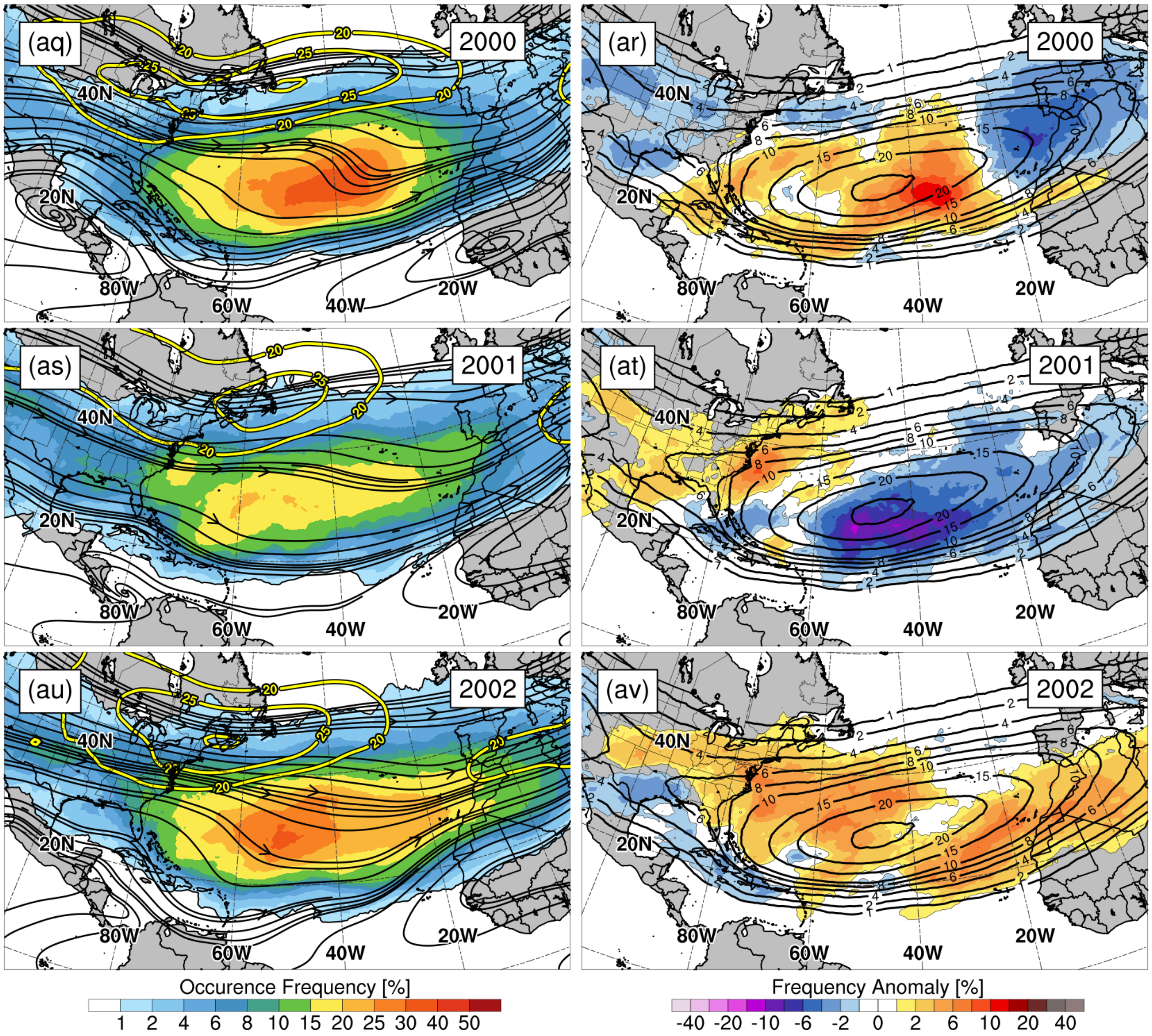

Fig. A1 Cont. (aq–ar) 2000, (as–at) 2001, and (au–av) 2002.

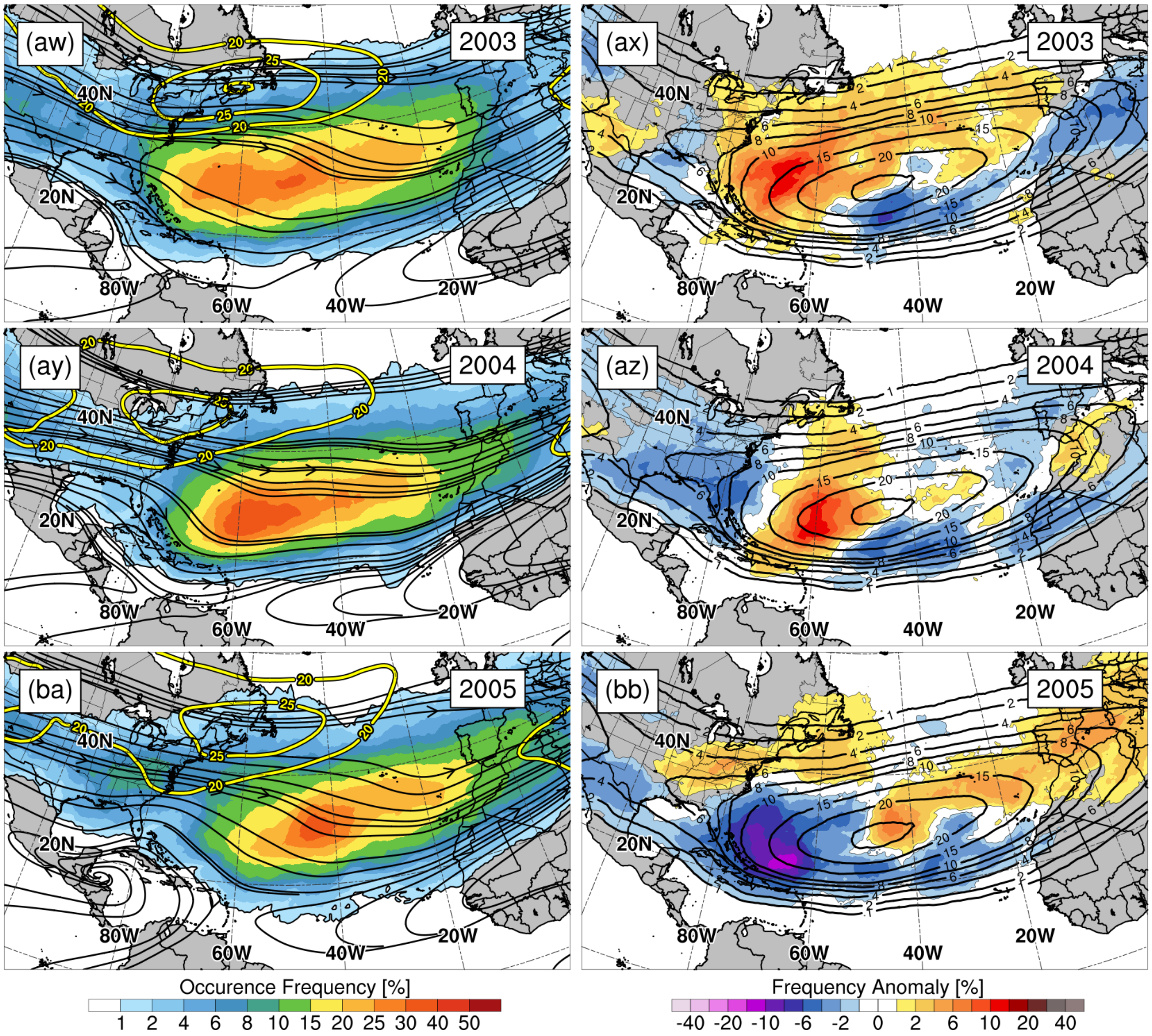

Fig A1 Cont. (aw–ax) 2003, (ay–az) 2004, and (ba–bb) 2005.

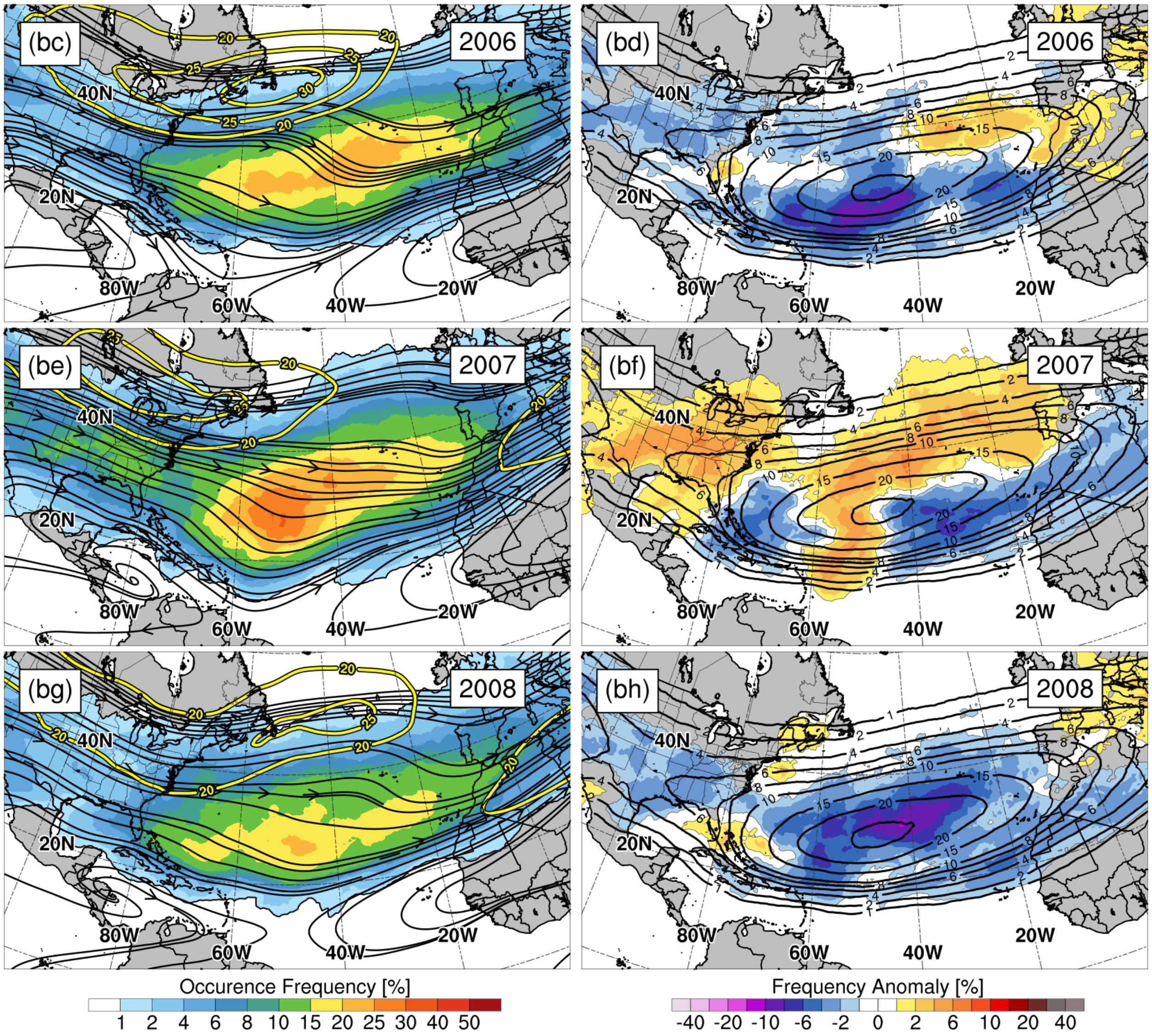

Fig. A1 Cont. (bc–bd) 2006, (be–bf) 2007, and (bg–bh) 2008.

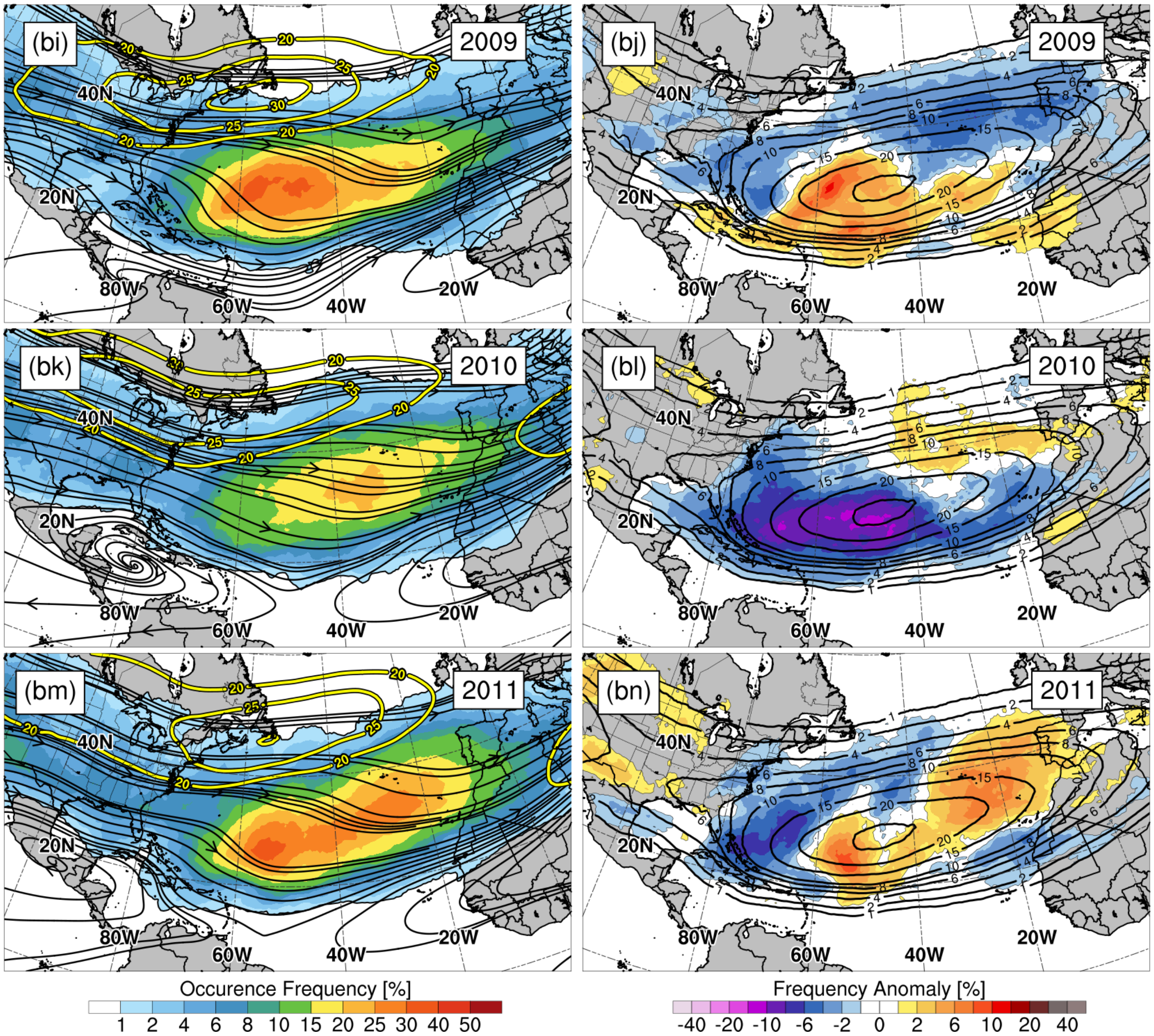

Fig. A1 Cont. (bi–bj) 2009, (bk–bl) 2010, and (bm–bn) 2011.

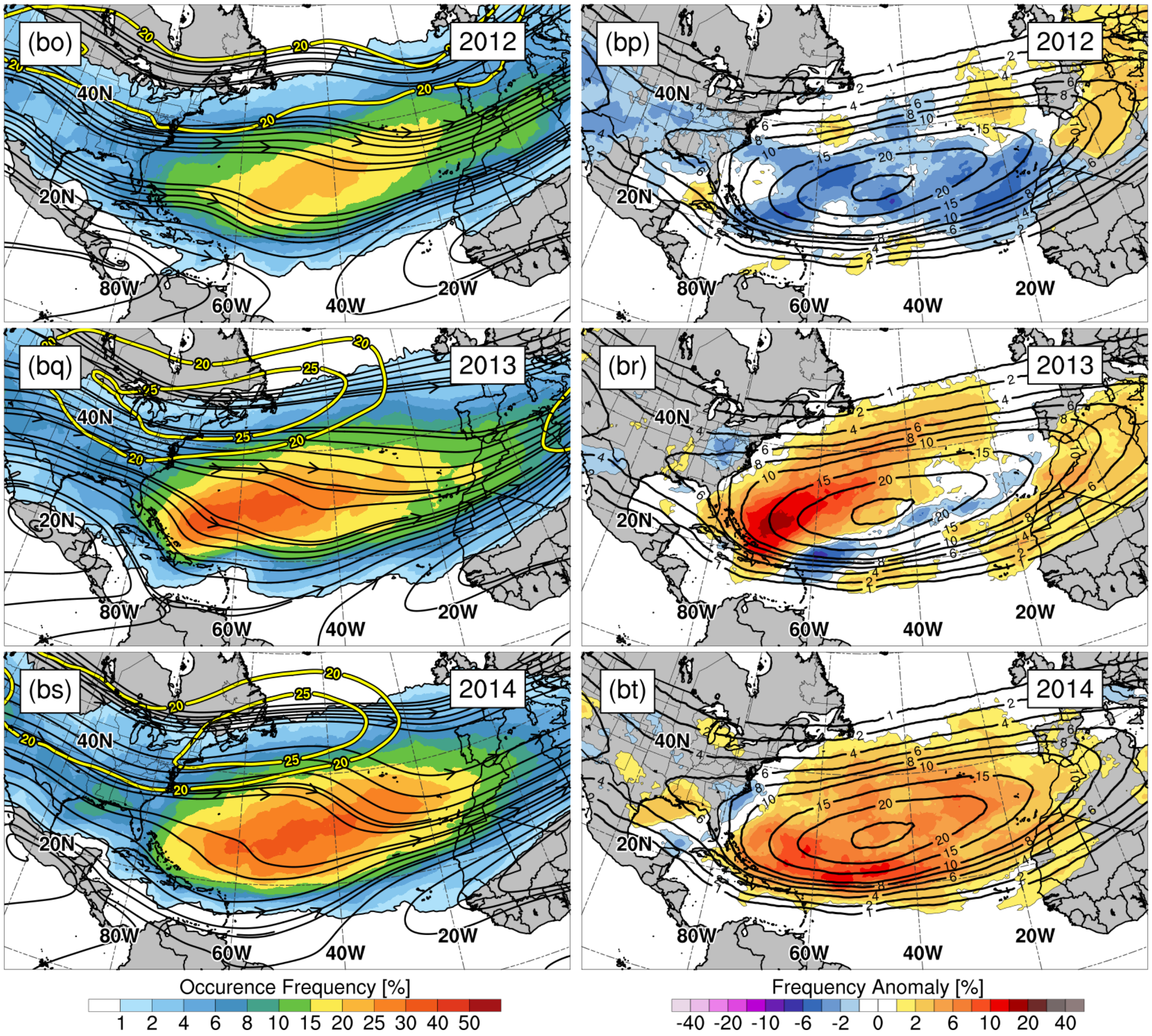

Fig. A1 Cont. (bo–bp) 2012, (bq–br) 2013, and (bs–bt) 2014.

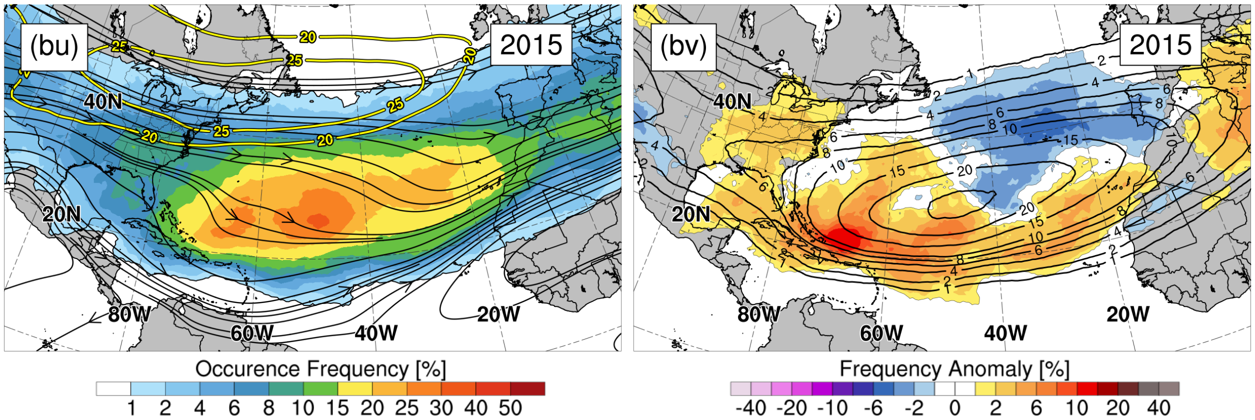

Fig. A1 Cont. (bu–bv) 2015.